

Multi-scale investigation of winter balance on alpine glaciers

by

Alexandra Pulwicki

B.Sc., University of Calgary, 2014

Dissertation Submitted in Partial Fulfillment of the
Requirements for the Degree of
Master of Science

in the
Earth Science
Faculty of Science

**© Alexandra Pulwicki 2017
SIMON FRASER UNIVERSITY
Summer 2017**

Copyright in this work rests with the author. Please ensure that any reproduction or re-use is done in accordance with the relevant national copyright legislation.

Approval

Name: **Alexandra Pulwicki**

Degree: **Master of Science (Earth Science)**

Title: **Multi-scale investigation of winter balance on alpine glaciers**

Examining Committee: Chair: ??
??

Gwenn Flowers
Senior Supervisor
Associate Professor

Valentina Radic
Committee Member
Associate Professor

Kirsten Zickfeld
Committee Member
Associate Professor

??
External Examiner
Professor
Department of Quantum Fields
Mars University

Date Defended: ??

Abstract

Accurately estimating winter surface mass balance on glaciers is central to assessing glacier health and predicting glacier runoff. However, measuring and modelling snow distribution is inherently difficult. Here we explore rigorous statistical methods of estimating winter balance and its uncertainty from multiscale measurements of snow depth and density. In May 2016 we collected over 9000 manual measurements of snow depth across three glaciers in the St. Elias Mountains, Yukon, Canada. Linear regression, combined with cross correlation and Bayesian model averaging, as well as simple kriging are used to interpolate point-scale values. Elevation and a wind-redistribution parameter exhibit the highest correlations with winter balance, but the relationship varies considerably between glaciers. A Monte Carlo analysis reveals that the interpolation itself introduces more uncertainty than the assignment of snow density or the representation of grid-scale variability. Despite challenges associated with estimating winter balance, our results are consistent with a regional-scale winter-balance gradient.

Keywords: glacier; snow; winter balance; spatial statistics; regression

Dedication

Acknowledgements

Table of Contents

Approval	ii
Abstract	iii
Dedication	iv
Acknowledgements	v
Table of Contents	vi
List of Tables	x
List of Figures	xiv
1 Introduction	1
1.1 Accumulation variability	1
1.1.1 Topographic scales	2
1.1.2 Snow drift and preferential deposition	2
1.2 Snow distribution models	3
1.2.1 Dynamic models	4
1.2.2 Statistical models	5
1.3 Measuring accumulation	7
1.3.1 Snow probing	8
1.3.2 GPR	14
1.3.3 DEM subtraction	15
1.3.4 Comparison of methods	17
1.3.5 Temporally resolved methods	18
1.4 Snow distribution on glaciers	18
1.5 Glaciers in the St. Elias Mountains	21
1.6 Research scope	24
1.7 Summary	26
1.8 Thesis overview	27

2 Field methods and data processing	28
2.1 Experimental design	29
2.1.1 Sampling Scheme and Naming System	29
2.2 Field methods	34
2.2.1 Linear and Curvilinear Transects	34
2.2.2 Zigzag	42
2.2.3 Federal Snow Sampler	42
2.2.4 Firn Corer	45
2.2.5 Snowpit	46
2.3 Data processing	48
2.3.1 Snow depth measured with graduated avalanche probe	48
2.3.2 Snow density	50
2.3.3 Snow water equivalent (SWE)	51
2.4 Topographic parameters	53
2.4.1 Obtaining digital elevation models (DEMs) for study glaciers	53
2.4.2 Calculating topographic parameters	56
2.4.3 DEM smoothing	61
2.4.4 Parameter correlations	62
2.4.5 Maps of topographic parameters and distribution of parameters sampled	63
2.5 Summary	74
3 Sampling	76
3.1 Density	76
3.1.1 Basic statistics	76
3.1.2 Federal Sampler measurements and snow depth	76
3.1.3 Density uncertainties	77
3.1.4 Comparing density from snowpit and Federal Sampler measurements	80
3.1.5 Density and elevation	82
3.2 Linear and curvilinear transect snow depth data	85
3.3 Zigzag snow depth data	86
3.4 Snow water equivalent (SWE)	88
3.5 Variability at multiple scales	94
3.5.1 Point scale	95
3.5.2 Grid cell scale	96
4 Interpolation	102
4.1 Linear topographic regressions	102
4.1.1 Background	102
4.1.2 Importance of variables in regression models	103
4.1.3 Snow density estimation methods	103

4.1.4	Multiple Linear Regression (MLR)	104
4.1.5	Bayesian Model Averaging (BMA)	117
4.1.6	MLR and BMA comparison	128
4.1.7	Number of cross validation runs	130
4.2	Kriging	131
4.2.1	Background	131
4.2.2	Methods	132
4.2.3	Results	132
4.3	Regression kriging	135
4.3.1	Background	135
4.3.2	Methods	136
4.3.3	Results	136
4.4	Comparison of interpolation methods	138
4.5	Summary	142
5	Winter Balance	143
5.1	Background	143
5.2	Methods	143
5.2.1	SWE uncertainty	144
5.2.2	Density uncertainty	144
5.2.3	Interpolation uncertainty	144
5.3	Results	145
5.3.1	Winter balance uncertainty	145
5.3.2	Spatial patterns of winter balance uncertainty	145
5.4	Discussion	147
6	Regional Controls	149
6.1	Transferability of linear regression coefficients	149
6.1.1	Results	149
6.1.2	Accumulation gradient	153
6.1.3	Limitations and future work	153
6.2	Conclusion	155
Bibliography		157
Appendix A GPS Waypoint Creation and Upload to GPS Device		168
Appendix B Field Maps		170
Appendix C Data Processing Scripts		183
C.1	Snow depth measured with graduated avalanche probe	183

C.1.1	Linear and curvilinear transect surveys	183
C.1.2	Zigzag surveys	184
C.2	Snow density	185
C.3	Snow water equivalent (SWE)	186
Appendix D	Topographic parameters from QGIS to Matlab	188
Appendix E	MLR software	189
Appendix F	BMA software	191
Appendix G	Kriging software	193
Appendix H	Variability of data at various scales	194
H.1	Point Scale	194
H.1.1	Data normality	194
H.1.2	Observer differences	194
H.1.3	Standard deviation of snow depth along linear and curvilinear transects	195
H.1.4	Standard deviation of SWE in DEM cell	196
Appendix I	Winter surface mass balance distribution	200
I.1	Linear regression winter balance distribution	201
I.2	Simple kriging winter balance distribution	205

List of Tables

Table 1.1	Relevant spatial scales for snow variability on glaciers. Information from [21].	3
Table 1.2	Area, length, and elevation descriptors of three chosen glacier.	25
Table 2.1	Summary information for snow depth transects. Transect shapes completed include Lower Hourglass (LH), Lower Circle (LC), Lower Midline (LM), Upper Hourglass (UH), Upper Circle (UC), Upper Midline (UM), Upper Transect (UT), and Bonus Transect (BT). The first observer was navigating to waypoints and the remaining three were taking depth measurements.	39
Table 2.2	Summary information for zigzag measurements	40
Table 2.3	Summary information for SWE measurements with the Federal Snow Sampler	43
Table 2.4	Statistics of integrated densities measured using Federal Sampler or vertical density profiles (of snow wedge measurmenets) in snow pits. Mean, standard deviation (std), and number (n) of snow density (kg m^{-3}) measurements on study glaciers is shown.	50
Table 2.5	Description of density interpolation methods used to calculate SWE used in the topographic regression. Abbreviations with ‘S’ used snowpit-derived densities and abbrviations with an ‘F’ used Federal Sampler-derived densities.	52
Table 2.6	Values of azimuth (A) and maximum search distance (d_{\max}), that correspond to the Sx that had the highest absolute correlation to observed SWE.	61
Table 2.7	Pearson correlation coefficients between topographic parameters at sampled locations. Topographic parameters are distance from centreline (d_C), elevation (z), aspect (α), slope (m), northness (N), curvature (κ), and Sx.	63

Table 2.8	Descriptive statics of topographic parameter full and sampled distribution. Mean and standard deviation are in units of meters for distance from centrelne (d_C) and elevation (z), in units of m^{-1} for profile (κ_P) and tangential (κ_T) curvature, and are unitless for cosine of aspect (α), “northness” (N), slope (m), and Sx. Skewness is a measure of the data asymmetry about the mean, with positive values indicating data that are more spread to the right of the mean and zero indicating a perfectly symmetric distribution. Kurtosis is a measure of how prone a distribution is to outliers. A normal distribution has a kurtosis value of 3 and larger values indicate distributions that are more prone to outliers.	67
Table 3.1	Summary of reference and range of integrated snow density calculated from snowpit measurements. The reference density values are calculated with an ice layer density of 917 kg m^{-3} and a ‘hard’ snow density of 600 kg m^{-3} . To determine the error in estimating integrated snow density, ice density, ice thickness, and the ‘hard’ layer density are varied between 700 and 917 kg m^{-3} , $\pm 1 \text{ cm}$, and 500 and 600 kg m^{-3} , respectively.	79
Table 3.2	Range of densities estimated from Federal Sampler measurements. The number (n) of reliable measurements, as well as the minimum, maximum, and mean density are shown. The density range, given as a percent of the mean density, is also shown. Location refers to the snowpit name as shown in Figure 2.9.	81
Table 3.3	Summary of linear regressions between integrated density and elevation (m a.s.l.).	82
Table 3.4	2σ values of SWE variability (%) distributions at the point and grid cell scale.	95
Table 4.1	Description of density interpolation methods used to calculate SWE used in the topographic regression. Abbreviations with ‘S’ used snowpit-derived densities and abbrviations with an ‘F’ used Federal Sampler-derived densities.	104

Table 4.2	Mean MLR and BMA coefficients for topographic regression between measured SWE and standardized topographic parameters. Topographic parameters are distance from centreline (d_C), elevation (z), aspect (α), slope (m), northness (N), curvature (κ), and Sx. Since parameters are standardized, the magnitude of the coefficients is representative of their importance in predicting SWE. The root-mean-squared error (RMSE) between modelled SWE using those coefficients and observed SWE is also given. Semi-partial correlation is a metric that describes the increase in R^2 from the addition of a parameter to a regression that contains all other regressors. Raw correlation is the square of the Pearson correlation between a parameter and SWE.	106
Table 4.3	MLR coefficients for topographic regression between measured SWE and standardized topographic parameters. Topographic parameters are distance from centreline (d_C), elevation (z), aspect (α), slope (m), northness (N), curvature (κ), and Sx. Since parameters are standardized, the magnitude of the coefficients is representative of their importance in predicting SWE. The root-mean-squared error (RMSE) between modelled SWE using those coefficients and observed SWE is also given. See Table 4.1 for description of density options.	107
Table 4.4	BMA coefficients for topographic regression between measured SWE and standardized topographic parameters. Topographic parameters are distance from centreline (d_C), elevation (z), aspect (α), slope (m), northness (N), curvature (κ), and Sx. Since parameters are standardized, the magnitude of the coefficients is representative of their importance in predicting SWE. The root-mean-squared error (RMSE) between modelled SWE using those coefficients and observed SWE is also given. See Table 4.1 for description of density options.	121
Table 4.5	ANOVA p-values between estimated SWE found using MLR and BMS regression coefficients for various density options. Significance is taken to be $p < 0.05$	129
Table 4.6	Nugget ($\times 10^{-3}$ m w.e.) and range length (m) values for SWE data with various snow density interpolation schemes estimated using maximum likelihood in DiceKriging package. S = Snowpit density values, F = Federal Sampler density values. See Section 4.1.3 for details on density options.	134

Table 5.1 Standard deviation ($[\times 10^{-2} \text{ m w.e.}]$) of winter balance distributions arising from SWE (σ_{SWE}), density (σ_ρ) and interpolation (σ_{INT}) uncertainty. Result for Glacier 4 (G4), Glacier 2 (G2) and Glacier 13 (G13) are shown.	145
Table 6.1 Elevation regression coefficients and intercepts used in linear regression transferability. The mean RMSE for all glaciers is also shown.	152
Table H.1 Normality of data with various subgroups. χ^2 values are shown and normally distributed data is bold ($p < 0.05$). Data for each glacier are divided into lower hourglass (LH), lower circle (LC), lower midline (LM), upper hourglass (UH), upper circle (UC), upper midline (UM), and upper transect (UT).	195
Table H.2 Mean standard deviation (cm) of snow depth measurements for the entire glacier (Overall Glacier), different transects (Overall Transect), and each observer. Standard deviation as a percent of the mean snow depth is shown in brackets. Data for each glacier are divided into lower hourglass (LH), lower circle (LC), lower midline (LM), upper hourglass (UH), upper circle (UC), upper midline (UM), and upper transect (UT).	198
Table H.3 Overall standard deviation (cm) of snow depth measurements for the entire glacier (Overall Glacier), different transects (Overall Transect), and each observer. Standard deviation as a percent of the mean snow depth is shown in brackets. Data for each glacier are divided into lower hourglass (LH), lower circle (LC), lower midline (LM), upper hourglass (UH), upper circle (UC), upper midline (UM), and upper transect (UT). The standard deviation of all transect data was 64.6 cm.	199

List of Figures

Figure 1.1	Digging a snowpit in the accumulation area of Haig Glacier, Rocky Mountains	8
Figure 1.2	Examples of snow sampling schemes. Figures (a), (b), (c), and (e) from [111]. Figure (d) from [109]. Figure (f) from Parr, C., (2016 personal communication).	12
Figure 1.3	Schematic diagram of a helicopter-borne radar snow survey. The travel time for the signal to interact with the snow surface is shown as a solid line and the signal travel time of the interaction with the ice is shown as a dashed line. Together, these values can be used to determine snow depth. The inset (a) is an example waveform that would be recorded from these two events. Figure taken from [52].	14
Figure 1.4	Radargram from the accumulation area of Findelengletscher, Valais, Switzerland. (a) The reflection at the air-snow interface. (b) The reflection at the snow-ice interface. Figure taken from [114].	15
Figure 1.5	Schematic of airborne LiDAR system geometry. Scan angle (θ), height (h), and swath width (SW) are shown. Figure from [33].	16
Figure 1.6	Map of the St. Elias Mountains and surrounding area. Figure taken from [29].	22
Figure 1.7	Visualization of four spatial scales investigated in project. The lower panels show examples of the amount of data analyzed at each scale.	25
Figure 1.8	Visual representation of research project. General scope is described on the left (ovals) and specific investigations are shown on the right (squares).	26
Figure 2.1	Study glaciers in the Donjek Range, Yukon (see inset). The topographic divide is shown as a dashed line.	31
Figure 2.2	Target waypoints for snow depth transects, snow pits, and SWE measurements on three study glaciers.	32
Figure 2.3	Randomly assigned locations for zigzag measurements in the ablation area (divided into seven zones).	33

Figure 2.4	Example of zigzag. Vertices are labelled and measurements are taken at random intervals along the dashed lines between vertices. The randomly chosen location of the SWE measurement is shown as a diamond.	35
Figure 2.5	Implementation of transect probing. The first person navigated to the intended waypoint using the GPS device. The second, third, and fourth (not seen) observers are probing using 3.2 m long avalanche probes. There is approximately 10 m between observers. Photo credit: G. Flowers	37
Figure 2.6	Schematic of the snow depth measurement configuration. Blue circles indicate depth measurement and orange squares indicate waypoint (WP) location.	38
Figure 2.7	Snow depth values measured along a zigzag pattern (G04_Z3A)	41
Figure 2.8	Using the Federal Sampler to measure SWE	44
Figure 2.9	Locations and labels for all snowpits dug on Glaciers 4, 2 and 13 (left to right).	46
Figure 2.10	Taking snow density measurements in a snowpit. An expandable ruler is used to measure snow depth and determine sampling locations. A 250cc wedge cutter is used to extract a known volume of snow and a spring scale is used to weigh the snow. The dial-stem thermometer is used for measuring snow temperature. Note that the sampling wall is shaded, has an undisturbed snow surface above it, and has a smoothed face. Photo credit: A. Criscitiello	48
Figure 2.11	Example of estimating snow depth measurement locations in one area (indicated by black box) on Glacier 13. Numbered waypoint (WP) locations are shown in blue and estimated measurement locations are shown in orange at a distance of 10, 20, and 30 m from the WP. Measurement locations are taken to be along a straight line between subsequent WPs. For the first WP of a transect, the measurement locations are assumed to be along the same line as that between the first and second WPs of a transect. For example, the measurement locations behind WP 660 fall along the same line as those between WP 660 and WP 661. The same is true for WP 745.	49

Figure 2.12 Example of zigzag survey measurement locations calculated using difference reference vertices for each section of the zigzag. Black squares show measurement locations calculated using the original GPS coordinates of vertices (Option 1). Blue circles show measurement locations calculated using the last measurement location from the previous section as the reference vertex (Option 2). For the first and fifth vertices (located at (0, 40 m) and (0, 4 m)) the original GPS coordinates were used for both options.	50
Figure 2.13 Relationship between various ways to interpolate between density measurements for the calculation of SWE. The bottom row shows the code for each density interpolation option as described in Section 2.3.3.	51
Figure 2.14 SPOT-5 DEMs available for the Donjek Range. Study glaciers are shown as red outlines. The DEM made from imagery collected on September 3, 2007 (GES 08-029) is shown in (a) and the DEM made from imagery collected on September 13, 2007 (GES 07-044) is shown in (b). Imagery that contains cloud cover result in a distorted DEM, as seen in the boxed area of (a).	53
Figure 2.15 Landsat 7 ETM images of study glaciers on September 13, 2007. Snow cover is shown as light blue and ice is shown as dark blue. . .	54
Figure 2.16 Vertical difference between DEMs in overlapping area. Difference was found by subtracting GES 08-029 from GES 07-044. Positive values indicate that GES 07-044 values are higher than GES 08-029 values.	54
Figure 2.17 Histogram of the vertical difference between GES 08-029 and GES 07-044 before (dark blue) and after (light blue) correction.	55
Figure 2.18 Outlines of the cropped GES 07-044 DEM (pink, left) and cropped GES 08-029 DEM (blue, right) used for merging. There is a slight overlap between the two DEMs that cannot be seen at this scale. .	56
Figure 2.19 Merged DEM of the Donjek range from two corrected SPOT-5 DEMs, plotted with 10 m contour lines. Study glaciers are shown in red. Discrepancies between the DEMs along the merge line can be seen as anomalous linear features in the contour map (yellow boxes). Distorted contours in the eastern regions (white box) are a result of errors in the DEM.	57
Figure 2.20 Labelling of DEM grid cells surrounding the cell of interest. The eight surrounding cells are used for estimating topographic parameters in QGIS. The cell of interest, which is located at row i and column j of the DEM, is shown as a shaded cell and is labelled z_5	58

Figure 2.21	Image and description from [130]. Example of Sx calculations for three cells of interest along a 270° search vector. As depicted, with dmax set equal to 300 m, the shelter-defining pixel for cells 1 and 2 is cell A, producing positive Sx values. The shelter-defining cell for cell 3 is cell B, producing a negative Sx. Had dmax been equal to 100 m, the search for the shelter- defining pixel for cell 1 would not extend across the valley, thus producing a negative Sx for cell 1, while Sx for cell 2 would remain the same and that for cell 3 would be slightly lower.	61
Figure 2.22	Curvature found using the orginal DEM (a) and the smoothed (7×7 window moving average) DEM (b).	62
Figure 2.23	Distributions of elevation (z) used in the topographic regressions for the study glaciers. This DEM is derived from a SPOT5 satellite image and has a grid size of 40×40 m. Subsequent topographic parameters were derived from this DEM. Arrows indicate glacier flow direction and black dots show snow depth sampling locations.	68
Figure 2.24	Histograms of elevation (z) sampled (black) as compared to total range of elevation (white) of study glaciers.	68
Figure 2.25	Distributions of distance from centreline (d_C) used in the topographic regressions for the study glaciers. Centreline was drawn by hand in QGIS. Arrows indicate glacier flow direction and black dots show snow depth sampling locations.	69
Figure 2.26	Histograms of distance from centreline (d_c) sampled (black) as compared to total range (white) of distance from centreline of study glaciers.	69
Figure 2.27	Distributions of the sine of aspect (α), which indicates north-south component of a slope (+1 defined as north), used in the topographic regressions for the study glaciers. Values are derived from a smoothed DEM. Arrows indicate glacier flow direction and black dots show snow depth sampling locations.	70
Figure 2.28	Histograms of aspect (α) sampled (black) as compared to total range (white) of aspect of study glaciers.	70
Figure 2.29	Distributions of slope (m) used in the topographic regressions for the study glaciers. Values were derived from a smoothed DEM (grid size of 40×40 m) in QGIS. Arrows indicate glacier flow direction and black dots show snow depth sampling locations.	71
Figure 2.30	Histograms of slope (m) sampled (black) as compared to total range (white) of slope of study glaciers.	71

Figure 2.31	Distributions of “northness” (N) used in the topographic regressions for the study glaciers. “Northness” is defined as the product of the cosine of aspect and sine of slope. A value of -1 represents a steep, south facing slope, a value of +1 represents a steep, north facing slope, and flat surfaces yield 0. Values were derived from a smoothed DEM (grid size of 40×40 m) in QGIS. Arrows indicate glacier flow direction and black dots show snow depth sampling locations.	72
Figure 2.32	Histograms of “northness” (N) sampled (black) as compared to total range (white) of “northness” of study glaciers.	72
Figure 2.33	Distributions of curvature (κ) used in the topographic regressions for the study glaciers. Values were derived from a smoothed DEM (grid size of 40×40 m) in QGIS. Colour axis has been scaled to better resolve values close to zero. Arrows indicate glacier flow direction and black dots show snow depth sampling locations.	73
Figure 2.34	Histograms of curvature (κ) sampled (black) as compared to total range (white) of profile curvature of study glaciers.	73
Figure 2.35	Distributions of S_x , which is a wind redistribution parameter, used in the topographic regressions for the study glaciers. See section 2.4.2 and the original paper by [130] for more details on calculation. See Table 2.6 for values of best correlated azimuth and maximum search distance for each glacier. Arrows indicate glacier flow direction and black dots show snow depth sampling locations.	74
Figure 2.36	Histograms of S_x sampled (black) as compared to total range (white) of S_x of study glaciers.	74
Figure 3.1	Relationship between measured density and snow depth for all Federal Sampler and snowpit locations. A linear regression of depth and density for Federal Sampler (FS) measurements is shown as a solid line and for snowpits (SP) is shown as a dashed line.	78
Figure 3.2	Comparison of integrated density estimated using wedge cutters in a snowpit and density estimated using Federal Sampler measurements for Glacier 4 (G04), Glacier 2 (G02) and Glacier 13 (G13). Error bars are minimum and maximum values for each estimate as reported in Table 3.1 and 3.2.	80
Figure 3.3	Relationship between measured snow depth and elevation at all sampling locations.	83
Figure 3.4	Relationship between snowpit-derived density and elevation for all study glaciers.	83

Figure 3.5	Relationship between Federal Sampler-derived density and elevation for all study glaciers.	84
Figure 3.6	Boxplots of snow depth measured on study glaciers. All snow depth values shown in (a) and snow depth values only from transects (zigzag, snowpit and Federal Sampler measurements excluded) shown in (b). Red line indicates median, blue box shows first quartiles, bars indicate minimum and maximum values (excluding outliers), and red crosses show outliers, which are defined as being outside of the range of 1.5 times the quartiles (approximately $\pm 2.7\sigma$).	85
Figure 3.7	Boxplots of snow depth data measured at each zigzag location. See Figure 3.8 for locations of each zigzag.	86
Figure 3.8	Map of zigzag locations on Glaciers 4, 2 and 13 (left to right).	86
Figure 3.9	Snow depths measured in zigzags on Glacier 4. Mean depth (\bar{z}) is also reported. Zigzag elevations (left to right) are 2162, 2229 and 2360 m a.s.l. See Figure 3.8 for locations of each zigzag.	87
Figure 3.10	Snow depths measured in zigzags on Glacier 2. Mean depth (\bar{z}) is also reported. Zigzag elevations (left to right) are 2172, 2332 and 2403 m a.s.l. See Figure 3.8 for locations of each zigzag.	87
Figure 3.11	Snow depths measured in zigzags on Glacier 13. Mean depth (\bar{z}) is also reported. Zigzag elevations (a-d) are 2156, 2206, 2271 and 2297 m a.s.l. See Figure 3.8 for locations of each zigzag.	88
Figure 3.12	Boxplots of estimated SWE at sampling locations for Glacier 4 (a), Glacier 2 (b) and Glacier 13 (c). The density options using snowpit (S) or Federal Sampler (F) derived densities are mean from all glaciers (1), mean for individual glaciers (2), elevation regression (3) and inverse-distance weighting (4). SWE estimations using various density options were tested for differences using ANOVA ($p < 0.05$). SWE estimates that were not significantly different for each glacier are labelled with the same letter (e.g. all estimates with A on Glacier 4 are significant different than all estimates with B).	90
Figure 3.13	Estimated snow water equivalent (SWE) at measurement locations. Density was taken to be the mean value of all snowpit-derived densities from all glaciers (S1). Arrows show ice-flow direction and dashed lines show approximate ELA. Note that the individual measurement locations overlap on the figure.	91

Figure 3.14	Estimated snow water equivalent (SWE) at measurement locations. Density was taken to be the mean value of all Federal Sampler-derived densities from all glaciers (F1). Arrows show ice-flow direction and dashed lines show approximate ELA. Note that the individual measurement locations overlap on the figure.	91
Figure 3.15	Estimated snow water equivalent (SWE) at measurement locations. Density for each glacier was taken to be the mean value of snowpit-derived densities from that glacier (S2). Arrows show ice-flow direction and dashed lines show approximate ELA. Note that the individual measurement locations overlap on the figure.	92
Figure 3.16	Estimated snow water equivalent (SWE) at measurement locations. Density for each glacier was taken to be the mean value of Federal Sampler-derived densities from that glacier (F2). Arrows show ice-flow direction and dashed lines show approximate ELA. Note that the individual measurement locations overlap on the figure.	92
Figure 3.17	Estimated snow water equivalent (SWE) at measurement locations. Density was determined by using a linear fit between snowpit-derived density and elevation for each glacier (S3). Arrows show ice-flow direction and dashed lines show approximate ELA. Note that the individual measurement locations overlap on the figure.	93
Figure 3.18	Estimated snow water equivalent (SWE) at measurement locations. Density was determined by using a linear fit between Federal Sampler-derived density and elevation for each glacier (F3). Arrows show ice-flow direction and dashed lines show approximate ELA. Note that the individual measurement locations overlap on the figure.	93
Figure 3.19	Estimated snow water equivalent (SWE) at measurement locations. Density was calculated using inverse distance weighting using all snowpit-derived densities (S4). Arrows show ice-flow direction and dashed lines show approximate ELA. Note that the individual measurement locations overlap on the figure.	94
Figure 3.20	Estimated snow water equivalent (SWE) at measurement locations. Density was calculated using inverse distance weighting using all snowpit-derived densities (F4). Arrows show ice-flow direction and dashed lines show approximate ELA. Note that the individual measurement locations overlap on the figure.	94
Figure 3.21	SWE variability at one measurement location. Three to four snow depth measurement were taken at each location and converted to SWE values using S1 density option.	96

Figure 3.22	Coefficient of variation of observations at one measurement location. Three to four snow depth measurement were taken at each location and converted to SWE values using S1 density option.	96
Figure 3.23	SWE variability for each set of zigzag measurements.	98
Figure 3.24	SWE variability at the grid cell scale based on zigzag measurements.	99
Figure 3.25	Number of measurements locations within DEM grid cells.	99
Figure 3.26	SWE variability at the grid cell scale based on multiple measurements in a DEM grid cell.	100
Figure 3.27	SWE variability at the grid cell scale based on zigzag measurements.	100
Figure 3.28	SWE variability at the grid cell scale based on eight different density interpolation methods in a DEM grid cell.	101
Figure 3.29	SWE variability at the grid cell scale based on eight different density interpolation methods.	101
Figure 4.1	Top panel shows comparison of estimated (MLR) and observed (original) snow water equivalent (SWE) for three study glaciers. The SWE values were calculated using inverse-distance weighted snowpit densities (S4). Bottom panel shows plots of all linear fits between estimated and observed SWE using eight options for calculating density. Mean R^2 value is shown for each sub-plot and a reference 1:1 line is also provided. Black line highlights the S4 option from the top panel. See Figure 4.11 for a plot of all estimated SWE values.	110
Figure 4.2	Summary of estimated SWE values found using MLR coefficients. Red line indicates median, blue box shows first quantiles, bars indicate minimum and maximum values (excluding outliers), and red crosses show outliers, which are defined as being outside of the range of 1.5 times the quartiles (approximately $\pm 2.7\sigma$).	111
Figure 4.3	Residuals of SWE predicted using MLR for all options of estimating density.	111
Figure 4.4	Summary of residuals from estimated SWE values found using MLR coefficients (S4). Red line indicates median, blue box shows first quantiles, bars indicate minimum and maximum values (excluding outliers), and red crosses show outliers, which are defined as being outside of the range of 1.5 times the quartiles (approximately $\pm 2.7\sigma$).	112
Figure 4.5	Map of the residuals from estimated SWE values found using MLR coefficients (S4) for each measurement location.	112

Figure 4.6	Boxplot showing the range of regressor coefficients explained by each topographic parameter for each option of estimating snow water equivalent (SWE). Topographic parameters are distance from centreline (d_C), elevation (z), aspect (α), slope (m), northness (N), curvature (κ), and Sx. Within each box, the mean is shown as a circle, the median as a horizontal line, the interquartile range (IQR) as a coloured box, two times the IQR as dashed lines beyond the box, and outliers as single points.	113
Figure 4.7	Boxplot showing the range of semi-partial correlation explained by each topographic parameter for each option of estimating snow water equivalent (SWE). Topographic parameters are distance from centreline (d_C), elevation (z), aspect (α), slope (m), northness (N), curvature (κ), and Sx. Within each box, the mean is shown as a circle, the median as a horizontal line, the interquartile range (IQR) as a coloured box, two times the IQR as dashed lines beyond the box, and outliers as single points.	114
Figure 4.8	Modelled SWE using coefficients determined using MLR and density interpolated with inverse-distance weighting from snowpits (S4). Observed SWE values are overlain on the maps.	115
Figure 4.9	Map of the difference between maximum and minimum SWE values for each DEM cell between all density options using MLR coefficients. Observed SWE values are overlain on the maps.	115
Figure 4.10	Map of the difference between maximum and minimum SWE values, expressed as a percent of the maximum SWE, for each DEM cell between all density options using MLR coefficients. The colours have been scaled to highlight difference in the main part of the glaciers. Values of zero are found where the minimum estimated SWE is zero m w.e. Observed SWE values are overlain on the maps.	116
Figure 4.11	Map of modelled SWE using the MLR coefficient values for all density options. Measured SWE is plotted as overlain filled circles. Glacier flow directions are indicated by black arrows and mean estimated SWE values for each glacier are shown.	117
Figure 4.12	Uniform model prior for eight topographic regressors used in BMA.	118
Figure 4.13	Comparison of predicted (BMA) and observed (original) snow water equivalent (SWE) for three study glaciers. The SWE values were calculated inverse distance weighted snowpit densities (S4).	122

Figure 4.14	Plot of all linear fits between modelled (BMA) and observed SWE using eight options for calculating density. Mean R ² value is shown for each sub-plot and a reference 1:1 line is also provided. See Figure 4.13 for a plot of the data.	122
Figure 4.15	Residuals of SWE predicted using BMA for all options of estimating density.	123
Figure 4.16	Summary of residuals from estimated SWE values found using BMA coefficients (S4). Red line indicates median, blue box shows first quantiles, bars indicate minimum and maximum values (excluding outliers), and red crosses show outliers, which are defined as being outside of the range of 1.5 times the quartiles (approximately $\pm 2.7\sigma$).	123
Figure 4.17	Map of the residuals from estimated SWE values found using BMA coefficients (S4) for each measurement location.	124
Figure 4.18	Summary of estimated SWE values found using BMA coefficients (S4). Red line indicates median, blue box shows first quantiles, bars indicate minimum and maximum values (excluding outliers), and red crosses show outliers, which are defined as being outside of the range of 1.5 times the quartiles (approximately $\pm 2.7\sigma$).	124
Figure 4.19	Boxplot showing the range of regressor coefficients explained by each topographic parameter for each option of estimating snow water equivalent (SWE) using BMA. Topographic parameters are distance from centreline (d_C), elevation (z), aspect (α), slope (m), northness (N), curvature (κ), and Sx. Within each box, the mean is shown as a circle, the median as a horizontal line, the interquartile range (IQR) as a coloured box, two times the IQR as dashed lines beyond the box, and outliers as single points.	125
Figure 4.20	Boxplot showing the range of semi-partial correlation explained by each topographic parameter for each option of estimating snow water equivalent (SWE) using BMA. Topographic parameters are distance from centreline (d_C), elevation (z), aspect (α), slope (m), northness (N), curvature (κ), and Sx. Within each box, the mean is shown as a circle, the median as a horizontal line, the interquartile range (IQR) as a coloured box, two times the IQR as dashed lines beyond the box, and outliers as single points.	126
Figure 4.21	Modelled SWE using coefficients determined using BMA and density interpolated with inverse-distance weighting from snowpits (S4). Observed SWE values are overlain on the maps. Arrows indicate glacier flow direction and black dots show snow depth sampling locations.	127

Figure 4.22	Map of the difference between maximum and minimum SWE values for each DEM cell between all density options using BMA coefficients. Arrows indicate glacier flow direction and black dots show snow depth sampling locations.	127
Figure 4.23	Map of the difference between maximum and minimum SWE values, expressed as a percent of the mean SWE, for each DEM cell between all density options using BMA coefficients. The colours have been scaled to highlight difference in the main part of the glaciers. Arrows indicate glacier flow direction and black dots show snow depth sampling locations.	128
Figure 4.25	Boxplot showing the range of values of coefficients for each topographic parameter from both MLR and BMA analysis for Glacier 4 (left), Glacier 2 (middle), and Glacier 13 (right). Note the different y axes for the three glaciers. Topographic parameters are distance from centreline (d_C), elevation (z), aspect (α), slope (m), northness (N), curvature (κ), and Sx. Within each box, the mean is shown as a circle, the median as a horizontal line, the interquartile range (IQR) as a coloured box, two times the IQR as dashed lines beyond the box, and outliers as single points.	129
Figure 4.26	(a) Mean winter balance and (b) elevation regression coefficient found with varying number of runs for cross validation.	130
Figure 4.27	SWE distributions estimated by kriging. Arrows indicate glacier flow direction and black dots show snow depth sampling locations.	133
Figure 4.29	Simple-kriging winter-balance confidence interval (95%) as a percent of distributed SWE, found using kriging. The SWE value were estimated using density S4. Arrows indicate glacier flow direction and black dots show snow depth sampling locations.	134
Figure 4.28	Comparison of estimated (simple kriging) and observed (original) snow water equivalent (SWE) for three study glaciers. The SWE values were calculated using inverse-distance weighted snowpit densities (S4).	135
Figure 4.30	Distributed BMA residuals estimated by simple kriging. Arrows indicate glacier flow direction and black dots show snow depth sampling locations. Dashed line indicates approximate ELA.	137
Figure 4.31	SWE distributions estimated by adding the kriged residuals to the SWE distributions estimated using topographic regression with BMA. Observed SWE values are overlain on the maps. Arrows indicate glacier flow direction.	137

Figure 4.32 Comparison of estimated (regression kriging) and observed (original) snow water equivalent (SWE) for three study glaciers. The SWE values were calculated using inverse-distance weighted snowpit densities (S4).	138
Figure 4.33 Mean observed SWE and estimated winter balance using topographic regression, kriging, and regression kriging , averaged over density options.	139
Figure 4.34 Mean correlation coefficient (R^2) between observed SWE and estimated winter balance using topographic regression, kriging, and regression kriging at sampling locations, averaged over all density options.	139
Figure 4.35 Mean SWE and mean estimated winter balance using topographic regression, kriging, and regression kriging.	141
Figure 4.36 Correlation coefficient (R^2) between observed SWE and mean estimated winter balance using topographic regression, kriging, and regression kriging at sampling locations.	141
Figure 5.1 Probability density functions (PDFs) fitted to distributions of specific winter balance values that arise from (left) SWE uncertainty (σ_{SWE}), (middle) interpolation uncertainty (σ_{INT}) and (right) all three sources of uncertainty. Results from a linear regression interpolation (top panels) and simple kriging (bottom panels) are shown. Each PDF is calculated using one of eight density interpolation methods for Glacier 4 (G4), Glacier 2 (G2) and Glacier 13 (G13).	146
Figure 5.2 Uncertainty of SWE estimated using linear regression (top) and simple kriging (bottom). Uncertainty is a relative quantity measured by taking the sum of differences between one hundred estimates of distributed winter balance that include SWE uncertainty and, in the case of linear regression, regression uncertainty. The sum is then normalized for each glacier. Glacier flow directions are indicated by arrows.	147
Figure 6.1 Transfer of LR coefficients to estimate distributed winter balance on study glaciers. winter balance found using Glacier 4 (top), Glacier 2 (middle) and Glacier 13 (bottom) regression coefficients. The mean SWE from all density interpolation options is shown. Arrows indicate glacier flow direction.	151

Figure 6.2	Transfer of LR coefficients to estimate distributed winter balance on study glaciers. Winter balance found using coefficients determined from all available SWE observations. The mean SWE from all density interpolation options is shown. Arrows indicate glacier flow direction.	152
Figure 6.3	Root mean squared error (RMSE) at sampling locations when LR coefficients are transferred between glaciers. The mean RMSE from all density interpolation options is shown.	153
Figure 6.4	Relation between SWE and linear distance from St. Elias mountain divide, located at the head of the Kaskawulsh Glacier. Blue dots are snow pit derived SWE values from [115]. Orange dots furthest from the divide are mean winter balance from Glaciers 4, 2 and 13, with 95% confidence interval using a linear regression interpolation. Orange dots close to the divide are snow pit derived SWE value at two locations in the accumulation area of the Kaskawulsh Glacier collect in May 2016. Black line indicates line of best fit ($R^2 = 0.85$).	154
Figure H.1	Variability in all snow depth measurements taken at each glacier. Red line indicates median, blue box shows first quantiles, bars indicate minimum and maximum values (excluding outliers), and red crosses show outliers, which are defined as being outside of the range of 1.5 times the quartiles (approximately $\pm 2.7\sigma$).	196
Figure H.2	Standard deviation (a) and standard deviation as percent of mean (b) of all snow depth measurements binned in elevation bands of 10 m. Bars at the top of the figure indicate the elevation ranges of the three study glaciers. The regression of elevation and standard deviation of snow depth is shown as a coloured line within the data.	197
Figure H.3	Boxplot of the standard deviation of measured SWE in one DEM grid cell. Red line indicates median, blue box shows first quantiles, bars indicate minimum and maximum values (excluding outliers), and red crosses show outliers, which are defined as being outside of the range of 1.5 times the quartiles (approximately $\pm 2.7\sigma$).	198

Figure I.1	Distribution of winter balance obtained using linear regression. (Top) Winter balance values obtained from a Monte Carlo sampling of normally distributed SWE variation (obtained from zigzag measurements) about the local SWE value. (Middle) Winter balance values obtained from a Monte Carlo sampling of normally distributed regression coefficients. (Bottom) Winter balance values obtained using both SWE variability and regression coefficient variability. Eight different density interpolation methods are used to obtain SWE values used in the regression.	201
Figure I.2	Winter surface mass balance distribution obtained using linear regression for eight density interpolation options when variation due to SWE measurement (σ_{ZZ}) is included.	202
Figure I.3	Winter surface mass balance distribution obtained using linear regression for eight density interpolation options when variation due to regression coefficient estimation (β) is included.	203
Figure I.4	Winter surface mass balance distribution obtained using linear regression for eight density interpolation options when variation due to regression coefficient estimation and SWE measurement (β and σ_{ZZ}) is included.	204
Figure I.5	Distribution of winter balance obtained using simple kriging. (Top) Winter balance values obtained from a Monte Carlo sampling of normally distributed SWE variation (obtained from zigzag measurements) about the local SWE value. (Middle) Winter balance values obtained from a Monte Carlo sampling of normally distributed regression coefficients. (Bottom) Winter balance values obtained using both SWE variability and regression coefficient variability. Eight different density interpolation methods are used to obtain SWE values used in the regression.	205
Figure I.6	Winter surface mass balance distribution obtained using simple kriging for eight density interpolation options when variation due to SWE measurement (σ_{ZZ}) is included.	206
Figure I.7	Winter surface mass balance distribution obtained using simple kriging for eight density interpolation options when variation due to regression coefficient estimation (β) is included.	207
Figure I.8	Winter surface mass balance distribution obtained using simple kriging for eight density interpolation options when variation due to regression coefficient estimation and SWE measurement (β and σ_{ZZ}) is included.	208

Chapter 1

Introduction

Snow accumulation, as the dominant input of mass to alpine glaciers, plays an important role in governing their mass balance and the hydrology of alpine catchments more broadly. This has implications not only for the availability of water for local ecological and human use [8, 97], but also for rates of global sea-level rise [44]. It is therefore necessary to understand the spatial distribution of snow on glaciers. However, achieving such an understanding is complicated by the fact that snow distribution in alpine regions is not uniform or static, but rather highly variable and influenced by diverse and dynamic processes operating on multiple spatial and temporal scales. Although previous research has attempted to account for these processes through the development of various techniques of measurement and modelling, little is known about how they operate in glacierized alpine environments. This severely limits possibilities of quantifying and predicting snow distribution on glaciers, particularly in remote locations where frequent empirical measurements are difficult [95].

Chapter 1 examines what is currently known and unknown about the topic of snow accumulation on glaciers and its spatial variability. The following section begins with an overview of accumulation variability within alpine regions in general, as there is a considerably greater breadth of studies devoted to snow in non-glacierized alpine basins. Section 1.3 reviews different ways of modelling the distribution of snow in alpine environments, while Section 1.4 describes methods for measuring accumulation and their relative merits and challenges. Section 1.5 compiles studies that specifically look at accumulation variability on glaciers and summarizes their key findings. Section 1.6 section focuses on the St. Elias Mountains, a large glacierized region where little is known about snow distribution and its effects on glacier mass balance.

1.1 Accumulation variability

The spatial distribution of seasonal snow accumulation can vary significantly. This is a result of interactions between spatially and temporally variable atmospheric conditions and heterogeneous topography [33, 74]. Understanding and predicting snow distribution there-

fore requires accounting for factors that include atmospheric circulation, precipitable water, air pressure, air temperature, wind speed and direction, elevation, slope exposure, presence of orographic barriers, surface slope and aspect, surface roughness, and relief [110, 83].

1.1.1 Topographic scales

Snow accumulation is spatially variable on point scales (<5 m), hillslope scales (1–100 m), watershed scales (100–10,000 m) and regional scales (10–1000 km) [21]. The features and conditions that lead to variability at these scales differ (see Table 1.1) and their relative importance depends on the topography and climate of the study area. Inclusion of parameters that describe relevant processes at multiple scales has been shown to improve models that aim to explain measured snow distribution [80, 21].

Point-scale variability is generally associated with surface roughness effects and the presence of small obstacles. These effects can be significant in vegetated landscapes or when the surface is very rough (e.g. boulder field) [78]. Many parts of a glacier though are characterized by a relatively smooth surface, with roughness lengths on the order of centimetres [57]. In these areas, point-scale variability of snow depth is low. However, in heavily crevassed regions, point-scale variability can be large and thus have a significant impact on snow distribution in the area [83].

Hillslope-scale variability is caused by variations in the surface topography of the glacier. The curvature and slope of the surface as well as the presence of local ridges or depressions can affect where snow is located [15, 114]. Avalanching can also redistribute snow, especially on the margins of a glacier [17, 91].

Watershed-scale variability results mainly from interaction between changing elevation and aspect with a basin and the atmospheric conditions [21]. In particular, orographic lifting and shading can result in higher elevation and north-facing areas of the glacier having more snow than other areas [91, 114]. Gradients in temperature from elevation changes also affect the freezing level, which determines whether precipitation falls as snow or rain [17].

Regional-scale variability occurs when areas within a mountain range have differing amounts of snow. Often, this results from horizontal precipitation gradients and rain shadows forming on the lee side of topographic divides. Areas with large, steep mountains are especially affected by these processes.

Generally, spatial variability increases with spatial scale [21]. Extent and spacing of measurements must therefore capture variability both across the study area and at smaller scales. [21] note that studies of snow water equivalent (SWE) that have been conducted in alpine environments vary considerably in the extent and spacing of their measurements.

1.1.2 Snow drift and preferential deposition

Snow drift and preferential deposition are crucial factors that influence the distribution of snow [71, 130, 21]. Sharp changes in topography create convergent and divergent airflows

Table 1.1: Relevant spatial scales for snow variability on glaciers. Information from [21].

Scale	Length	Associated glacier feature
Point	<5 m	Crevasses
Hillslope	1–100 m	Local surface topography (curvature, slope), avalanching
Watershed	100–10,000 m	Elevation, aspect
Regional	10–1000 km	Horizontal precipitation gradient across mountain range

close to the surface, leading to turbulence and vorticity. This terrain-induced turbulence modifies mean wind (and snow particle) velocities, and can thus influence snow distribution [91, 71, 28].

Snow drift is the erosion and deposition of already deposited snow [28]. In general, erosion on the windward side is caused by increased wind speeds and deposition on the lee side of ridges is due to decreased wind speeds [75, 91, 28]. [92] found that creep, which is the rolling of snow particles on the snow surface, and saltation, which is the bouncing and dislodging of snow particles, are primarily responsible for the formation of cornice-like features.

Preferential deposition is inhomogeneous precipitation in the absence of local erosion [71]. It is mainly governed by winds, where higher wind velocities and updrafts on the windward side of ridges cause reduced deposition while reduced wind velocities on the lee side enhance deposition. This process can occur at relatively low wind speeds because it does not require the lifting of already deposited snow — instead, it only needs to act with or against the falling snow [91, 28]. For example, [90] found that the spatial structure of snow distribution in an alpine bowl was dominated by the preferential deposition of precipitation due to altered air flow fields.

Both snow drift and preferential deposition can occur at multiple spatial scales. Enhanced accumulation has been observed at the point scale in small depressions and near obstacles, at the hillslope scale along ridges, and at the watershed scale in areas with sheltered aspects [54, 16, 91, 130, 21].

1.2 Snow distribution models

The distribution and variability of snow distribution can be estimated using either dynamic or statistical models. These models help to determine relevant processes that affect accumulation, generally by relating its spatial distribution to meteorological and topographic descriptors. Inferences made from these models drive the direction of future studies and provide valuable insight into understanding how snow variability arises. Accounting for wind in snow distribution models is especially important because it plays a dominant role in spatial patterns of accumulation [131].

1.2.1 Dynamic models

Deposition and redistribution of snow can be represented using physically based, spatially distributed models. The general aim of these models is to simulate surface processes and how they vary spatially and temporally [91]. These models usually consider atmospheric conditions including freezing level, precipitation rates, relative humidity, and wind speed and direction, as well as processes such as orographic lifting, cloud formation, downslope evaporation, advection and fallout, snow metamorphism, and wind redistribution of snow (erosion, saltation) due to terrain induced turbulence [112, 74, 71, 91]. Modelling the dynamically induced flows of these components together describes the preferential deposition and redistribution of snow in alpine environments [71, 91, 28].

Many models have been developed to describe preferential deposition and redistribution. Early models were developed for flat or gently rolling terrain where boundary layer flow is better understood [28]. Boundary layer flow in steep terrain is generally non-linear [91, 28], so a number of different approaches have been applied. For example, [28] and [71] modelled wind-flow velocities by solving non-hydrostatic, compressible Navier-Stokes equations in 3-D and aimed to conserve momentum, heat, mass, and states of water. [112] employed Fourier transforms in a linear orographic model, which allowed for a more accurate representation of complex terrain.

Dynamic models are a valuable way to determine accumulation variability. Since they use physically consistent processes, they can be applied to any site. Dynamic models can also be used in different climatic conditions meaning that they can be applied to past and projected accumulation regimes [21]. Furthermore, a historic data set of variables is not needed to generate meaningful output. Another advantage of dynamic models is that they allow for high temporal resolution (e.g. [91] have a 1 hour time step), which allows for snowpack evolution to be examined.

Application of dynamic models is however operationally complex and computationally expensive, and also requires a diverse set of observations. A large number of input parameters, such as precipitation, wind speed and direction, air temperature, and relative humidity, need to be measured frequently and extensive sampling within a study region is required for accurate modelling[74]. For example, [28] used meteorological data from three automatic weather stations located throughout the study basin, while in the study done by [91] monthly stake measurements were needed. Such a well-monitored basin can be difficult to achieve in remote or inaccessible areas. A number of other dynamic models, such as those described in [42], use general circulation model values to drive local circulation models, but model output strongly depends on model boundary choice. Even with sufficient and appropriate input data, the models must assume a number of parameters and simplify parameter relationships (e.g. constant mean wind speed [91]) to characterize the atmosphere, which may not realistically describe air movement and stability. Additionally, the models do not

account for all modes of snow transport. For example, snow deposition due to avalanching can be an important process of snow transport that is not captured in current models [91].

1.2.2 Statistical models

Statistical models of snow variability establish empirical relationships between snow distribution and external variables [42]. These models assume that local distribution is forced by external factors, such as meteorological conditions or topography, which can be described by proxy parameters.

Statistical downscaling

Statistical downscaling is the process of determining an empirical relationship between large-scale atmospheric conditions and regional climates [42]. In general, this relationship is expressed as a function F such that regional variables R are found by $R = F(X)$ where X encompasses large-scale climate variables [42]. These models are trained and validated using gridded reanalysis data from global climate models (X) and point observations (R). Performance of these models is measured using correlation coefficients, distance measures (e.g. root mean squared error), or explained variance [42].

There are three main types of statistical models [42]. The first is a regression model, which directly quantifies a relationship between a local variable and a number of large-scale variables. Statistical methods such as multiple linear regressions [53], principal component analysis [63], canonical-correlation analysis [20], neural networks [138], and singular value decomposition [128] can be employed. The second type of model is a weather typing scheme, which relates the occurrence of a particular ‘weather class’ to local variables. Weather classes can be found using empirical orthogonal functions or cluster analysis [42]. The third model uses weather generators that simulate local precipitation using a prescribed distribution of precipitation [42].

Large-scale input variables that are usually chosen (e.g. sea-level pressure, geopotential heights) for statistical downscaling are representative of large-scale circulation. Increasingly, other variables such as humidity are being incorporated into analyses to account for mechanisms that rely on thermodynamics and vapour content [42]. When focusing on precipitation, integrated vapour transport (IVT) can be used as a proxy for precipitable water in the atmosphere and can be used to identify corridors of large water vapour transport that correlate with intense precipitation events [93].

Statistical models are a simple way to examine variability. They are computationally efficient and comparatively easy to apply because they are based on standard and accepted statistical procedures [42]. Furthermore, predicting variables does not require prior knowledge of all the processes that affect the variable. Functions can therefore be calculated for situations where all processes are currently not accounted for or where many processes are equally important.

Although the application of statistical downscaling is simple, it has a number of disadvantages. The method is difficult to apply in areas that have minimal historical data, as model performance is better when a long and reliable data set is used for calibration [42]. Statistical downscaling also assumes that the relationship between large-scale and local variables is stationary in time, limiting the ability of models to project into the future [42]. Furthermore, an empirical relationship assumes that there is no climate system feedback and the data generated through the empirical function are subject to the same biases as those of the original data set [42]. [129] also notes that the choice of large-scale variable domain (location and spatial extent) exerts a strong effect on the accuracy of the empirical function.

Terrain-based parametrization

Terrain-based parametrization determines empirical relationships between topographic indices and observed data. To determine topographic indices, the terrain in the study area is divided into grid cells where terrain parameters (e.g. slope, curvature, aspect, “northness”, wind exposure, topographic similarity) are calculated [2, 83]. The variable of interest is then measured in the study area and a relationship between grid-cell terrain parameters and observed data can be established [e.g. 17, 75, 3, 83].

Terrain-based parametrization requires a good terrain model and a meaningful network of observed data. For example, [88] found that that there were significant differences in modelled snow distribution when different terrain models were used. This is likely because the terrain-model grid size affects the value of the calculated terrain parameter for the cell. Terrain-based parameterization also requires sufficiently high resolution and spatial extent of observed data. When measuring accumulation, the variability within the study area needs to be captured and all areas should be well represented.

Relating terrain model parameters with observed data is often accomplished with simple statistical methods. Multiple linear regressions [80, 114, 83], mixed-effects multiple regression [61], parametric probability distributions [21], bivariate screening [3], probability distribution functions [62], and regression tree models [37, 130, 88, 105, 126] are among the more popular models. These models relate snow distribution to terrain parameters with varying success. For example, the multiple linear regression model developed by [114] explained about 50% of the variance of snow depth while the model developed by [3] explained 70–80% of the variance in snow water equivalent. A number of studies have found that elevation and wind redistribution parameters explain the majority of the variance in observed snow depth or snow water equivalence [e.g. 38, 117, 108, 48, 83]. Interaction parameters (e.g. *slope* × *orientation*) have also been found to be significant predictors for precipitation distribution in alpine areas [9]. [39] and [88] note that many relationships between accumulation and controlling parameters are nonlinear so use of regression tree models yields better results. Combining statistical models has also been seen to improve model accuracy.

Examples include combining linear regressions with generalized additive models [77] as well as binary decision trees with kriging [7].

Relating topographic parameters and observed data is a simple approach to understanding processes that affect variability. Although no physically-based relations are employed, terrain parameters can act as proxies for processes that are known to occur [83]. In this way, dominant processes can be inferred through easy to find statistical relationships. This approach is especially powerful in alpine environments, where topography strongly affects local snow distribution.

While terrain-based parametrization is easy to employ, its usefulness in understanding snow distribution can be limited. This method assumes that variability between cells is larger than within cell variability, which may not necessarily apply to all cells, especially in steep terrain or where grid size is comparatively large. [80] found that the standard deviation within the 30 m by 30 m grid cells used in the study was slightly larger than the between-grid variability. Additionally, [50] observed that local statistical models are able to perform well but that they cannot be transferred to different regions and that regional-scale models are not able to explain the majority of variance. The temporal transferability of terrain-based parameterization is also not reliable. [50] found that local models could be applied between years while [105] found that snow distribution variability could not be explained by their model in low snow years. Furthermore, the use of terrain parameters as proxies does not provide meaningful insight into relevant processes. This is important when attempting to predict distribution of variables in a different climate or location.

1.3 Measuring accumulation

Estimating accumulation requires snow density and depth measurements. Measuring these parameters within a glacierized basin has many challenges. Basin location and topography affect accessibility, while the cost and time required to conduct measurements can be prohibitive. In most cases, the resolution of measurements over a large area is insufficient to approximate the true variability [15, 32].

Snow density can be measured directly or with models of snow density change. To measure bulk density, a column of snow with a known volume is excavated (in a snow pit or with a firn corer) and weighed [114, 113]. Usually, a number of snow-column densities are measured and the average density is taken as representative of glacier-wide density [e.g. 79, 49, 83]. This can result in error when calculating snow water equivalence (SWE) because density can vary spatially and temporally (due to total snow depth, elevation, solar radiation, and wind effects) in a way that is not captured by a limited number of snow density measurements [49, 126]. However, snow density has been seen to vary over greater spatial scales than snow depth so fewer density measurements than depth measurements are usually made [37, 21]. Snow and firn density can also be calculated using models that

account for relevant processes such as compaction from overlaying snow and refreezing of meltwater [56, 113]. Densification processes are difficult to capture in models though, so they should be applied with caution [84].

Three main methods are currently used to measure snow depth. Probing involves taking *in situ* point measurements of snow depth, ground-penetrating radar (GPR) surveying involves using radar to detect the snow depth along continuous lines, and digital elevation model (DEM) subtraction involves taking the difference between the glacier surface at the end of the ablation and end of the accumulation seasons to find snow depth. Methods are selectively applied based on desired spatial resolution, cost effectiveness, and equipment availability. Each is prone to different sources of error and there is ongoing research to reconcile these approaches [113].

1.3.1 Snow probing

Measurement

The most direct way of measuring snow depth is by probing. To determine the snowpack thickness, the height of the snow above the end of the previous year's ablation surface is measured. Usually, a number of snow height measurements are obtained close to each other and the mean value is taken to be representative of that location. For example, [79] took the mean of nine snow probe measurements within a 7 m radius as representative of a measurement location.

In the ablation zone, snow depth is easy to measure because the interface between the end of summer melt surface and the beginning of winter accumulation is well defined (i.e. glacier ice) [83]. In the accumulation zone however, the snow surface at the end of the melt season may not be easily distinguishable from the winter accumulation [49]. It is common for the accumulation zone to have a heterogeneous surface at the end of the melt season — some areas do not experience any melt, while other areas experience some melt and the melt water percolates through the snow and firn. Melt water generated from warm weather or rain events, especially in the early and late parts of the accumulation season, can refreeze in the snowpack to form ice lenses [113]. As a result, the interface can be difficult to observe and



Figure 1.1: Digging a snowpit in the accumulation area of Haig Glacier, Rocky Mountains

contain a combination of dense or compacted snow, ice lenses, and/or firn. Probing in the accumulation zone can therefore result in erroneous depth measurements — penetration into the dense snow or firn will make it seem like a deeper snowpack exists and probing to an ice lens within the snowpack can make it seem like shallower snow is present [114]. Snow pits and firn cores are therefore used to examine snow and firn layers and to determine where the current season's snow begins.

To determine the basin-wide snow distribution, point snow depth measurements from probing need to be interpolated and extrapolated. This is often done using a statistical regression on parameters such as slope, aspect, curvature, and susceptibility to wind redistribution [e.g. 127, 83]. A regression generates an equation that is site specific and is used to estimate accumulation for each grid cell based on the values of its topographic parameters.

Snow probing is the simplest and oldest method used to determine accumulation. At the most basic level, it requires little more than a probe to determine depth, a way to determine location (such as a hand-held GPS), and a shovel to dig snow pits (see Figure 1.1). Furthermore, this method directly measures snow depth so no data processing or corrections are needed and depth uncertainty is simple to quantify (often multiple depth measurements are taken close together) [114].

There are however many drawbacks to this method. *In situ* probing and digging snow pits is incredibly time-consuming [33]. This limits the number of measurements that can be made, which means that accumulation distribution is under-represented and spatial variability in accumulation is difficult to capture [113]. Measurement is also limited to areas that are both accessible and safe for researchers. In complex terrain many areas cannot be surveyed, resulting in data gaps. [114] noted that this systematic bias can

result in incorrect values of glacier-wide accumulation — particularly because inaccessible areas such as cliffs and ridges have relatively shallow accumulations (due to wind erosion), while heavily crevassed areas can accumulate deep snow packs.

Sampling Design

Optimal sampling schemes for snow probing are central for accurately estimating snow distribution and mass balance from *in situ* measurements. Measuring snow depth and travelling between measurement locations is both time consuming and can disturb the snow so care must be taken to choose a sampling scheme that avoids bias, allow for the greatest variability to be measured, and minimizes distance travelled [111]. A design that maximizes accuracy and minimizes effort is therefore desired [36] and both theoretical [116] and applied [69, 111] investigations of various sampling designs have been pursued. There are a number of different designs that have been employed to obtain point measurements, including pure random, linear random, nested, gridded random, and gridded.

A purely random distribution of points is favourable because it avoids all bias, has the best correlation with true distribution, and is likely to capture the most variability [68, 111]. Logistically though, it is difficult to successfully measure all points in the study area because some may be impossible to access and some may be disrupted during travel or measurement. This design often results in inefficient travelling routes, which decreases the number of possible point measurements. [36] show a simple basin-wide random sample is a less optimal sampling scheme than a stratified random sample that accounts for known variation. One instance of a purely random sampling scheme can be seen in Figure 1.2(a).

Linear-random sampling schemes impose a structure to traverse as much of the study area as possible

but allow for a random distance between sampling points. An example of this scheme is the ‘star’, created by [111]. A significant advantage of this scheme is that it was designed to minimize distance travelled while still measuring snow properties in various orientations and various distances apart, which reduces bias. However, since the observer travels in straight transects there is still a potential to miss smaller features or ones that parallel the transects (spatial autocorrelation). [111] used comparative Monte Carlo simulations to validate that the star scheme performs equivalently or better than other (more structured) sampling methods and that it converges to the true distribution as well as a purely random scheme. One instance of a linear-random sampling scheme can be seen in Figure 1.2(b). Linear-random sampling can also be done in an ‘hourglass’ shape with an inscribed circle (referred to as an hourglass sampling scheme). As seen in Figure 1.2(f), this pattern allows sampling in all directions and captures a wide range of snow depths from the underlying snow distribution (Parr, C., 2016 personal communication).

Gridded-random designs involve dividing the study area into equal sized areas and then sampling randomly within each area. The L-grid is an example of this scheme [11, 35, 12]. In this scheme, the study area is divided into a grid and in each cell a random location is chosen as the start of the transect. The cardinal direction and measurement spacing of the transect are chosen randomly. Transects consist of five measurements, with three in the first direction selected and two perpendicular to this, forming an ‘L’ shape. This scheme has a small error bias (maintains randomness), while allowing for more efficient measurement [111]. Compared to the star scheme, the L-grid does not have a consistent travel distance and involves constant reorientation and finding of transect start locations, which decreases its efficiency. One

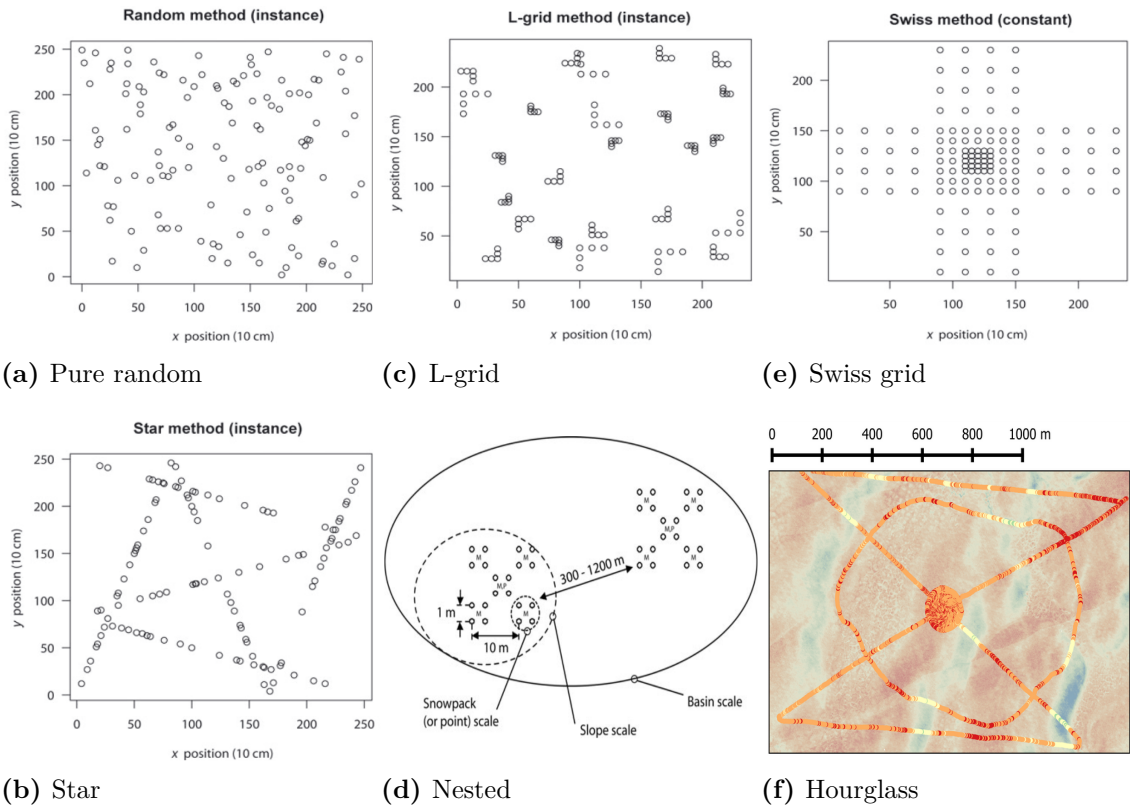


Figure 1.2: Examples of snow sampling schemes. Figures (a), (b), (c), and (e) from [111]. Figure (d) from [109]. Figure (f) from Parr, C., (2016 personal communication).

instance of a gridded-random sampling scheme can be seen in Figure 1.2(c).

Nested sampling is a scheme that maintains a certain sampling pattern and applies it at various length scales. For example, [109] took four point measurement in a 1 m square and did this 10 m apart to form another square. The set of measurements was then repeated 300–1200 m away to capture basin scale values. Hierarchical trees that incorporate selected parameters are often used to determine nested sampling locations. [124] and [61] use hierarchical sampling to divide the study area into regions (often discontinuous) that are likely to have a similar snow distribution and low variance, which means they require fewer sampling locations. Nested sampling requires that the observer predetermine parameters that affect the spatial pattern of the variable. Often, remote sensing is used to obtain these parameters so the resolution of regions is limited to that of the remote sensing images (typically 30 m resolution). The variability that exists at scales less than the grid-size of the images is classified as being caused by ‘random’ effects, which are assumed to be unbiased and unpredictable [124]. Nested sampling is well suited for regions with many complex and interacting parameters. For example, [124] used a hierarchical tree with time (traveling between locations), elevation, vegetation, and solar radiation at various length scales to create subgroup to sample. A nested sampling scheme can be seen in Figure 1.2(d).

Gridded sampling designs use regular measurement intervals in a grid pattern. Many variations of this scheme exist [87, 68, 78] with the most popular one being the Swiss cross [69]. This nested arrangement allows for a larger area to be covered than a fully quadratic grid and measures at various spatial scales, leading to more reliable geospatial statistics. This method allows for easy measurement and reveals details at various scales. However, measurements are biased by regular spaced intervals and linear ori-

tation, which could result in an under representation of the snow distribution further from the centre. A gridded sampling scheme can be seen in Figure 1.2(e).

1.3.2 GPR

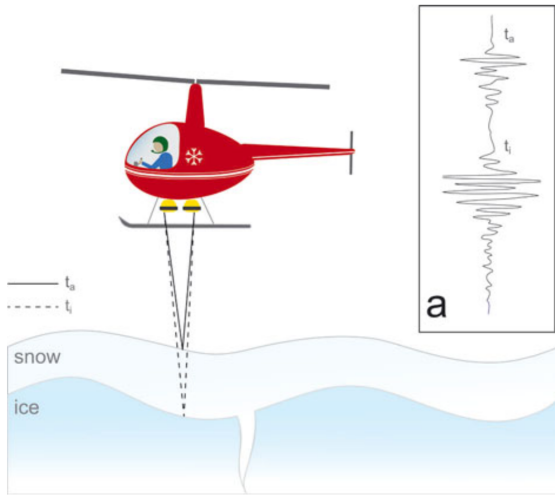


Figure 1.3: Schematic diagram of a helicopter-borne radar snow survey. The travel time for the signal to interact with the snow surface is shown as a solid line and the signal travel time of the interaction with the ice is shown as a dashed line. Together, these values can be used to determine snow depth. The inset (a) is an example waveform that would be recorded from these two events. Figure taken from [52].

then done to find the glacier-wide accumulation. [83] describe this process in five steps: (i) acquisition of GPR and probing data (ground truthing), (ii) calculation of snow density and radar velocity, (iii) calculation of snow thickness and resulting snow water equivalent (SWE), (iv) application of a correction to measured accumulation based on ground truth data, and (v) use of a multiple regression model to extrapolate SWE across the glacier. The extrapolation of SWE can also be done using an inverse approach with a coupled surface energy-balance snow model [119].

GPR is an effective tool for measuring accumulation. It provides continuous snow depth transects, which means that spatial variability is well represented along the radar lines. Surveys also need to be conducted only once to gain depth observations, which makes data collection fast and reduces logistical efforts [79]. GPR snow depth estimates are not

Ground penetrating radar (GPR) can be used to find snow depth along continuous lines. This method is used to calculate the distance from the radar source to a boundary with a strong contrast in dielectric permittivity, which corresponds to a change in material properties [114]. When the speed of the radar wave through the material is known, the travel time can be measured and from this the distance calculated. On a glacier, the radar wave is able to penetrate snow and ice at MHz frequencies and the strongest reflections arise when water is present [114]. To measure snow depth, GPR units are mounted on aircrafts or snowmobiles that then travel over snow covered areas (see Figure 1.3) [79, 83]. The resulting processed radargram (e.g. Figure 1.4) gives a continuous snow depth profile. Processing of the radargrams involves using tracking algorithms that are able to trace continuous layers. Interpolation between transects is

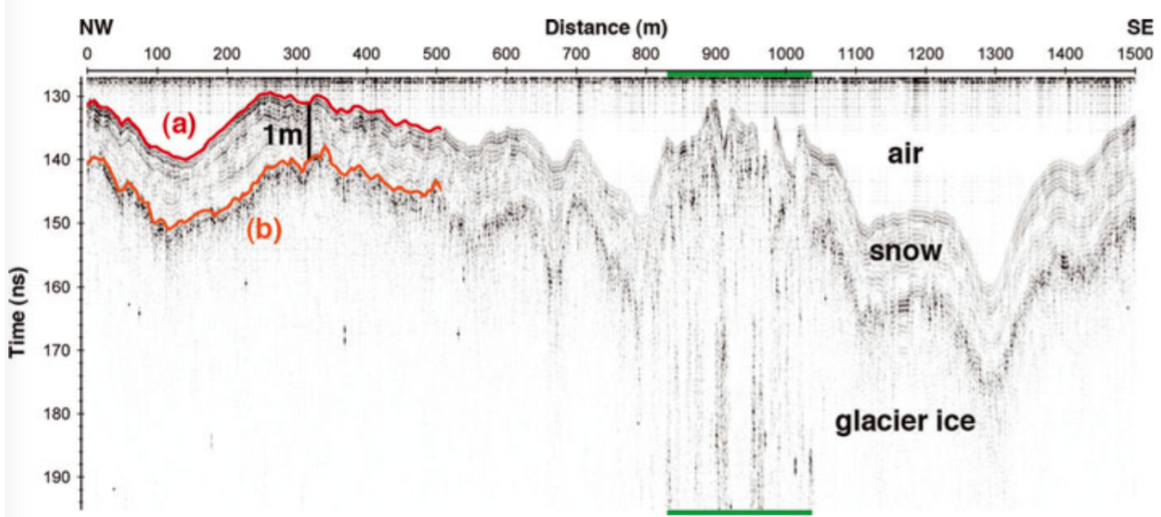


Figure 1.4: Radargram from the accumulation area of Findelengletscher, Valais, Switzerland. (a) The reflection at the air-snow interface. (b) The reflection at the snow-ice interface. Figure taken from [114].

affected by glacier dynamics and the ability to fly over steep or inaccessible regions means that all areas of a glacier can be measured.

A large limitation of GPR is the difficulty of processing radargrams. Areas where the snow–ice boundary is not well defined (i.e. the accumulation area) lack clearly contrasted material properties, which can lead to misinterpretation of their internal layers [83]. In the ablation area, the presence of crevasses can also result in radargram misinterpretation [79]. Variation and uncertainty in radar wave speed due to differing snow density and liquid water content can also affect depth calculations [114]. Often, wave speed is only measured in a few reference locations so changes in snow pack properties cannot be accounted for. Lastly, there is no universal procedure for processing GPR data. Selection of parameters and processing algorithms is dependent on available equipment, field conditions, survey design and intention [114], which hampers the reproducibility of surveys.

1.3.3 DEM subtraction

Digital elevation model (DEM) subtraction involves taking two detailed surface topography scans — one at the end of the melt season and one at the end of the accumulation season — and subtracting them from each other to find the snowpack height. The largest advantage of this remote sensing method is that it provides a highly resolved spatial measurement of snow depth over an entire basin [33, 114]. Data collection is fast, although two surveys must be conducted. This technique is sensitive to other processes that change the glacier surface elevation, including vertical displacement due to ice flow (positive in the ablation area and negative in the accumulation area), firn compaction, and surface lowering due

to melt after the acquisition of the end of melt season DEM [114]. For example, [114] found that a first-order approach (where the observed elevation change was interpreted as snow accumulation) was inconsistent with snow depth probing — DEM subtraction showed decreasing accumulation with an increase in elevation. Corrections can be made to account for these discrepancies but they rely on *in situ* measurement of snow depth, knowledge of long-term mass balance, or information about the vertical displacement of ice from GPS towers [114].

Lidar and photogrammetry are the two main methods of producing DEMs. Lidar produces a surface elevation model by calculating the distance to a target (by measuring the time between an emitted and return laser signal) [33, 114]. Terrestrial lidar systems involve stationary units placed in vantage points from which they are able to scan the basin surface [49]. Large basins require multiple overlapping scans to acquire a complete surface profile. Airborne lidar systems (see Figure 1.5) can also only scan a certain size footprint so the aircraft must fly over all parts of the basin to acquire a full surface profile. These systems also require an accurate global positioning system (GPS) — which is often corrected by referencing to a stationary GPS — to determine the 3D locations of the surface [33]. Airborne systems are widely applied and favourable in large basins or ones where no vantage point exists or is inaccessible. However, these systems are expensive so terrestrial scanners, which are comparatively more cost effective, are becoming popular [49].

Complex topography and multiple laser reflections can cause problems when producing a DEM from lidar data [33]. Significant vertical changes result in the spreading of the laser footprint and an incorrect interpretation of distance. [33] shows that an error of 50 cm can result from lidar scans of 45° terrain from 1000 m flight height. Careful planning of flight paths can reduce this error. Scattering of laser light and penetration into the snow pack can also introduce error into height calculations, although its magnitude is small (\sim cm) [33]. When subtracting the two measured DEMs, misclassification of corresponding point locations can occur, resulting in error in the final accumulation value [33].

Photogrammetry uses photographs to produce a series of DEMs that can be subtracted to find snow depth. Early attempts in the 1960s at applying this technique in snow covered areas suffered from poor vertical resolution due to overexposed photographs and the

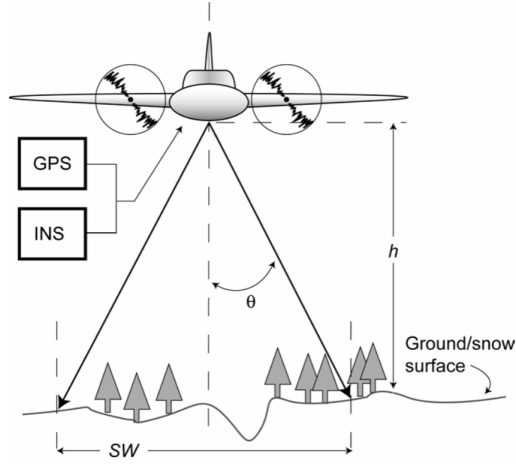


Figure 1.5: Schematic of airborne LiDAR system geometry. Scan angle (θ), height (h), and swath width (SW) are shown. Figure from [33].

necessity of manual differencing [95]. Modern photography equipment, GPS, and software technology have allowed for an increase in accuracy and lowering of costs associated with photogrammetry [95]. Current photogrammetry software is able to determine a snow surface profile relative to stable, snow-free points within the mapped area [41]. The photos collected for DEM creation can also be used to identify suspect changes in the snow pack [95]. Errors in photogrammetric measurements arise from sensor noise and poor lighting. Camera sensor noise is present in all digital photographs and its location changes from picture to picture. These erroneous pixels can be misinterpreted by the software as actual differences in height and thus lead to significant topographic noise, especially in steep mountainous terrain [95]. Additionally, having sufficient contrast in the photographed snow surface is critical for determining surface profile. Flat light conditions can reduce the resolution of the DEM or result in an absence of data in those parts of the photograph [95]. These effects can be avoided by waiting for better lighting.

1.3.4 Comparison of methods

The three methods of measuring accumulation differ in the extent of spatial information, collection techniques, costs, and processing needs. Spatial footprint is lowest for probing, which means that data must be interpolated. Although the actual measurement is simple and has relatively low uncertainty, the interpolation of points can lead to misrepresentation of spatial variability and significant errors that are difficult to quantify. GPR provides continuous snow depth profiles, but interpolation is still needed between lines. Further, significant errors can arise from misinterpretation of layers in radargrams. DEM differencing has the advantage of allowing for the measurement of surface topography across the whole basin, but error can result when glacier dynamics affect surface height changes.

Large differences in data collection time and cost also exist. Probing has low equipment costs but requires a large amount of human hours for ground-based measurements. GPR and DEM subtraction both require the use of aircrafts and expensive electronic equipment. However, these methods require lower logistical effort and data collection occurs quickly.

The three methods also have different data processing requirements. Simple statistical relations can be used for interpolating accumulation found by probing. However, GPR and DEM subtraction both require specialized software and knowledge of image processing methods, which increases the likelihood that misinterpretations of observations will occur. GPR has an advantage over DEM subtraction because it is not subject to elevation changes due to glacier dynamics and firn compaction. However, DEM subtraction has the advantage of more easily detecting the previous year's surface in the accumulation area and provides complete coverage of the study area [114].

In general, [79] and [114] found good correlations between probing measurements, GPR, and DEM subtraction. However, [114] found that the methods did not always corroborate each other, particularly in crevassed areas and marginal regions. In crevassed areas, accu-

mulation has large variation on small scales. The footprint of the GPR was usually too large to detect changes in snow depth and the movement of crevasses with time affected the lidar-derived snow depth. Marginal regions were misrepresented in the probing-derived profile because measurement was often not conducted in these areas. This area also included the uppermost part of the glacier where wind erosion had a significant effect on accumulation.

Choice of measurement technique for a snow survey is therefore dependent on project specific needs. Resolution, cost, and equipment availability need to be considered when selecting the most appropriate method. To reduce errors and misrepresentation of measurements, multiple methods can also be applied [79].

1.3.5 Temporally resolved methods

Temporally resolved methods take continuous measurements to provide a time series of snow accumulation. Usually, these methods involve relatively few measurement locations so they do not represent spatial variability well. However, they are especially useful for identifying large snowfall events (rapid increases in accumulation) and wind erosion (gradual decreases in accumulation).

There are a number of methods of measuring accumulation with time. Snow depth sensors, such as the SR50, measure the time between emission and return of an ultrasonic pulse [107]. As snow accumulates, the distance between the sensor and the snow surface decreases. Snow pillows, which are large (3 m diameter) bladders filled with antifreeze solution, directly measure changes in snow water equivalent with time [4]. As snow accumulates on the pillow, the weight of the snow forces an equivalent amount of the solution from the pillow to a standpipe. The height of the solution in the pipe is then recorded. Another method for measuring snow depth involves using multipath modulation of GPS signals [70, 82]. Multipath modulation involves isolating GPS signals that are reflected from horizontal, planar reflectors, such as a snow surface. The distance between the geodetic GPS receivers and the reflection point will change during the accumulation season, thus recording changes in snow depth. This method allows for the measurement of average snow depth in a ~ 1000 m^2 area around the antenna [82].

1.4 Snow distribution on glaciers

While studies of snow distribution in alpine regions are plentiful [21, and sources within] there are comparatively few studies on the distribution of snow on glaciers. Although glaciers are often found in alpine environments, they present a different setting for accumulation. The freezing temperatures of glacier ice allow for snow to stick earlier than on the surrounding rocks, which can be above freezing especially in the early part of the accumulation season. Additionally, the surface of a glacier is often less steep than the surrounding peaks, which allows for snow to deposit more easily. The margin of the glacier can also

accumulate snow from avalanches released from the surrounding peaks [17, 91]. Further, most glaciers do not support vegetation, which has significant effects on snow accumulation in many alpine basins [101]. [1] found that in open alpine areas with snow fields and small cirque glaciers there was a wide range of SWE values over a relatively small range of elevation, while in the montane areas there was a strong relationship between elevation and SWE where SWE values increased rapidly with elevation. Since few studies have been done on this topic, it is difficult to say whether snow distribution on glaciers is fundamentally different than that of an alpine basin. This lack of snow variability quantification points to a significant gap in the literature.

[132] conducted one of the first accumulation variability studies on a glacier. A GPR system was used to measure snow depth along three large transects on Spitsbergen, Svalbard. It was found that the accumulation-elevation gradients varied considerably and that regional variability was large, with almost 50% more accumulation on the eastern coast and a minimum in accumulation in the inland locations. A number of subsequent accumulation studies in Svalbard have since been conducted. [98] used GPR along longitudinal profiles of Nordenskjöldbreen and found 40 – 60% spatial variability over short distances. [45] compared snow distribution on four types of glaciers in Svalbard. It was observed that the land-terminating mountain glacier had a simple altitudinal gradient while the outlet glacier had a much weaker correlation and more wind-redistributed snow. It was thought that the orientation and shape of the glacier also had a significant impact on snow accumulation, with the glaciers that were oriented parallel to the dominant wind direction having stronger altitudinal gradients. Another glacier that was observed had no altitudinal gradient, so its distribution was determined by complex local conditions. The ice cap that [45] studied had all of these types of distributions in different areas.

[79] conducted an airborne GRP survey of two adjacent glaciers in Switzerland. The lower part of the larger valley glacier showed a clear correlation between altitude and snow accumulation. The upper part of the glacier and the adjacent smaller glacier had no altitudinal trend and the fluctuations in depth were large. Additionally, the accumulation was 40% lower on the smaller glacier. The altitudinal trend is a well documented pattern and was thought to be a result of melt that occurred during warmer weather, which is more pronounced at lower elevations. Spatial variability of precipitation and redistribution of snow were believed to have resulted in the high spatial variability in higher parts of the study area. Since the majority of the precipitation events originated from one direction and the large glacier was on the lee side of a ridge, it experienced preferential deposition. Meanwhile, the smaller glacier was further along the storm track so it received less precipitation. Overall, [79] showed that snow distribution on glaciers is not simply a function of altitude, which corroborated research done in other alpine catchments.

The most recent and comprehensive study of snow distribution on glaciers was done by [83]. This study focused on seven Alaskan glaciers of various sizes, orientations, and

distances from the Pacific Ocean. [83] found that SWE was highly variable (40% differences) at the hillslope-scale and was especially large in the ablation area (which has a rough surface due to the presence of crevasses). The dominant control on SWE distribution was altitude, but multiple terrain parameters were needed to capture most of the variance — after elevation, wind exposure explained the most variance. [83] also plotted mean SWE difference against distance and found that four of the study glaciers exhibited a rapid increase in variability over the first \sim 150 m and a slow increase in variability beyond but the three other study glaciers exhibited a gradual increase in variability over the entire range. Although this was not a detailed investigation of observed length scales, it potentially points to a heterogenous nature of snow distribution length scales on glaciers and the need for their increased measurement.

The study done by [122] contains the longest record of spatial distribution of snow accumulation. [122] analyzed 48 and 44 year records of two Norwegian glaciers for inter-annual stability in distribution patterns. It was found that snow accumulation is spatially heterogeneous yet it exhibits robust time stability in distributions. Reliability maps were then used to reduce the sampling scheme to one index site as well as a transect with 50 m elevation intervals for each glacier. Although winter balance reconstructions produced values within 0.15 m water equivalent, it was determined that a centreline transect underestimated winter balance. Transverse transects were therefore recommended as an addition to the sampling scheme to improve reliability. Additionally, several strongly irregular snow spatial distribution years were identified, which were inconsistent with the overall reduced sampling schemes.

The majority of studies that have examined snow distribution on glaciers have been done with either airborne or ground-based radar [e.g. 132, 79, 45, 119, 83]. In general, the radargrams provided valuable information but ground truthing by probing was always conducted. [52] also did a small GPR survey on an Alaskan glacier and found that GPR reflections were difficult to identify in areas of the glacier that had high debris content on the surface or in the upper part of the accumulation area. [114] did an extensive study that compared snow distribution values obtained by using probing, GPR, and DEM subtraction with lidar. All three methods showed an overall altitudinal trend but with significant small-scale variability (for a comparison of the three methods and their relative benefits, see Section 1.3.4). [119] used GPR and a surface-energy balance model coupled with a snow model to examine accumulation variability. It was found that terrain parameters such as slope and curvature were good representations of preferential deposition. Additionally, [119] calculated that small-scale variability of snow accumulation had a negligible effect on the mean net mass balance in the accumulation zone and a negative impact of -0.09 m w.e. a^{-1} in the ablation area.

[28] is the only study thus far that has examined snow distribution on glaciers using a dynamic model. This study specifically looked at the effect of wind on snow accumulation

and found that glacierized areas with the largest accumulation also experienced the lowest horizontal wind speeds and highest downward wind velocity. Preferential deposition was highest (positive or negative) in troughs located close to steep slopes, where updrafts and down drafts led to decreased and enhanced deposition, respectively. In general, the wind speed was controlled by small-scale topography and had a significant impact on accumulation.

Although there are still relatively few studies of snow distribution on glaciers, the work described above provides a good starting point for such investigations. Comparisons of variability between neighbouring glaciers and within a basin are both important areas of research.

1.5 Glaciers in the St. Elias Mountains

Snow data are generally sparse in mountain regions, especially those that are far from population centres [81]. The St. Elias Mountains (Figure 1.6) are one such area. These mountains contain the largest non-polar ice field and the longest valley glaciers outside of Greenland and Antarctica [81, 29]. Steep climatic gradients across the mountains create sharp changes in glacier cover and mass balance [22]. This region currently has the most negative mass budget and is the largest contributor to sea-level rise in the world [60, 44]. Understanding how local glacier mass balance is affected by distribution of snow is therefore critical for accurate predictions of glacier response to a warming climate.

The weather in the St. Elias varies considerably over the range. The west side of the mountains is characterized by a cool, Marine West Coast climate due to the influence of the Pacific Ocean, while the eastern side (just 250 km from the coast) is considered subarctic [81]. [115] studied the relationship between synoptic weather conditions and basin weather conditions across the St. Elias Mountains. It was observed that the mountains are oriented perpendicular to frequent and intense storms that originate in the ocean, which results in considerable interaction between weather and topography. When weather moves from the Gulf of Alaska, it is orographically lifted, which creates significant precipitation. If the front is perpendicular to the mountains, it can be deflected north or south, depending on the upper atmospheric flow. Fronts that are more or less aligned parallel to the mountains or very strong perpendicular fronts travel without deflection. The fronts can also stall on the west side of the mountains. Occasionally, the fronts spill over the mountain divide (located to the west of the Kaskawulsh Glacier) and descend along the eastern side, which often results in decreased precipitation. The rain shadow is likely a major cause of differences in accumulation and equilibrium line altitude (ELA) between the two sides of the mountains — the marine side has an ELA of \sim 1100 m and the continental side has an ELA of \sim 2100 m, while at the same elevation there is three times more accumulation on the marine side [81].

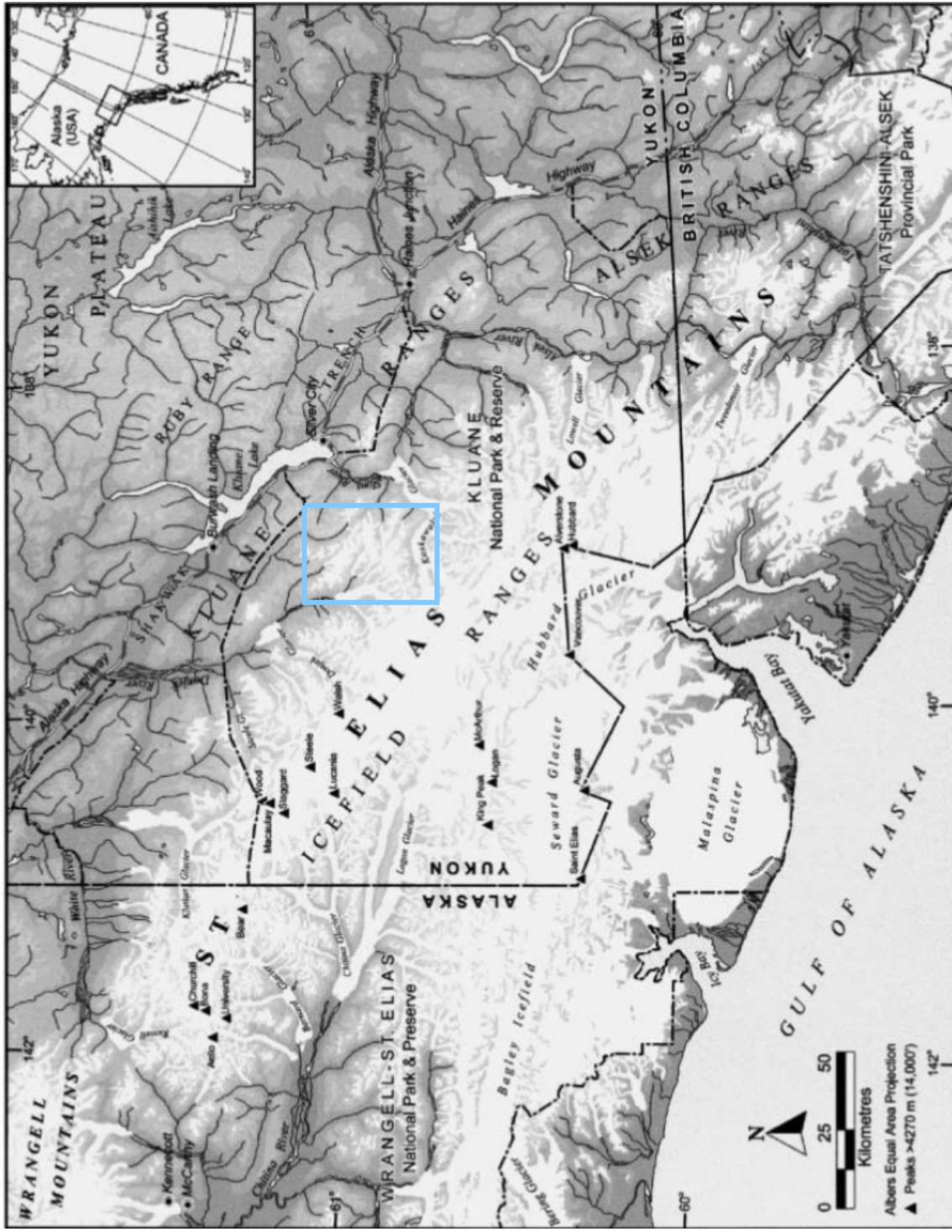


Figure 1.6: Map of the St. Elias Mountains and surrounding area. Figure taken from [29].

Although the characterization of synoptic conditions by [115] is useful, it was conducted during the summer when weather conditions are considerably different than during winter. [115] does note though that the weather patterns observed would likely be strengthened during winter because many of the spatial gradients are enhanced. The synoptic air masses present during the winter produce a strong temperature and moisture gradient, with warm, moisture-laden air coming from the Pacific Ocean and cold, dry air coming from the Mackenzie Basin. These gradients would likely result in even more precipitation and stronger winds. The presence of a high pressure Arctic system could decrease the ability of low-pressure systems to pass over the divide, leading to a further enhancement of precipitation on the western side of the mountains.

The study done by [115] also identified weather patterns at multiple scales. Synoptic conditions, including front movement, affected regional-scale differences in weather and precipitation patterns. Watershed-scale topography was responsible for differences in weather between nearby basins and affected wind speed and direction most significantly. Point-scale topography had strong effects on snow accumulation. Orographic effects were found to be significant on all scales.

Research on snow distribution and glacier mass balance in the St. Elias is limited. The first significant investigations took place under Project Snow Cornice [134]. Researchers looked at snow accumulation and ice formation as well as ice-mass thermal regime, density, and depth. Studies were conducted primarily on large glaciers such as the Kaskawulsh and Seward Glaciers, and thus provided insights into large-scale accumulation patterns. This initiative was then followed by the Icefield Ranges Research Project (IRRP), which was established in 1961 [29]. A number of subsequent long-term studies have been established in the St. Elias since IRRP [e.g. 23, 99]. For example, [127] determined the end-of-winter accumulation for the mass balance of a small alpine glacier in the Donjek Range. The study measured snow depth at a number of fixed stakes and used a multiple linear regression model — that accounted for slope, curvature, and elevation — to extrapolate these points and estimate basin-wide winter balance. [5] also briefly studied the mass balance of a number of glaciers in the St. Elias.

Two ice cores have been retrieved from the St. Elias Mountains. The first one was taken from the summit of Mt. Logan (5340 m) in 1980 and was 103 m long. The accumulation history in this core has been used to study the local [59] and regional [89] climate history. A second core, called the Eclipse core, was taken from a site 45 km northeast of Mt. Logan, 2 km lower in altitude, with an accumulation almost five times as large [121]. This core is 160 m and has also been used for studying local and regional climate history [121].

A study done by [101] looked at snow mass balance in a non-glacierized alpine basin within the St. Elias. It was found that wind had a significant impact on the distribution of snow — up to 79% of the snow was redistributed from alpine areas to (primarily) hillsides, where accumulation was tripled. In the study basin, measured accumulation ranged from

54% to 419% of the actual snowfall. However, in a subsequent study year, which had two large wet snow events, the redistribution of snow was minimal and accumulation variability was much lower. The type of snow and how susceptible it is to wind effects therefore also plays a critical role in distribution. Additionally, areas within the basin can have different accumulation patterns throughout the winter. One area within the basin studied by [101] had almost no redistribution (despite heavy winds) from the beginning of winter through to March. After this, all of the snow was lost even though additional accumulation events occurred in the basin. This could indicate a dependence of redistribution on weather conditions such as temperature, or that a critical depth was reached that allowed for redistribution to occur. Sublimation was also observed to occur throughout the study period and since sublimation is several orders of magnitude faster when blowing snow is present (~20% of winter days in this study), it could have a significant impact.

There is clearly a strong need for a more comprehensive understanding of snow accumulation in the St. Elias Mountains. Although a few studies have examined accumulation, no studies have examined the distribution of snow and how it varies spatially. This is especially true of small alpine glaciers in the St. Elias Mountains, since most of the accumulation differences have been observed on large glaciers. It is likely that orographic lifting as well as wind redistribution and preferential deposition play major roles in determining accumulation on small alpine glaciers, so future studies should focus on the impact of these factors.

1.6 Research scope

There is a need for a multi-scale investigation of snow accumulation on glaciers. The goal of this project is to improve understanding of processes and parameters that affect snow accumulation on glaciers. The snow distribution is characterized by identifying relevant length scales and by investigating the uncertainty, techniques, and controlling factors associated with calculating spatial patterns of winter balance. Throughout the thesis, winter balance refers to the winter surface mass balance, which is the net accumulation and ablation of snow over the winter season [24].

The thesis work aims to examine the spatial variability of snow distribution in the St. Elias Mountains using direct measurements and statistical models. Four spatial scales that are relevant to accumulation on glaciers will be considered: point, gridcell, basin and regional scale (Figure 1.7). An extensive snow survey is conducted, using a combination of snow-depth probing and two snow density measurement techniques, on three alpine glaciers in the Donjek Range. The Donjek Range is located on the continental side of the St. Elias Mountains (Table 1.2). A combination of statistical techniques, including basic statistics and regressions, is used to investigate spatial variability at multiple scales.

SCALES OF VARIABILITY

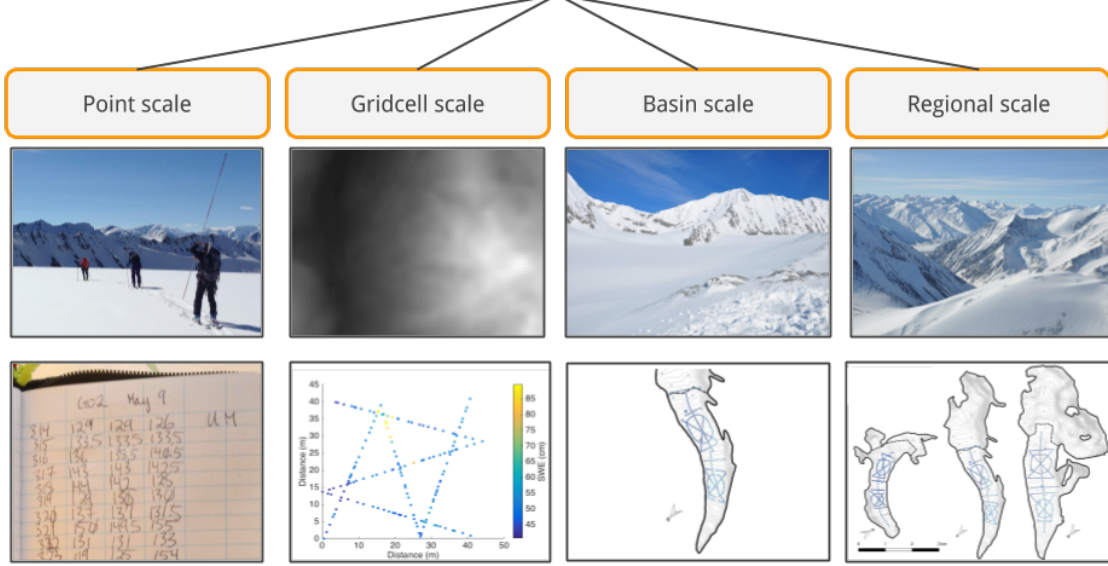


Figure 1.7: Visualization of four spatial scales investigated in project. The lower panels show examples of the amount of data analyzed at each scale.

The project is structured in four main stages (Figure 1.8). First, observations are described using basic statistics and a variety of density assignment methods are investigated. Second, regression and kriging methods are used to interpolate winter balance data. An evaluation of the various interpolation techniques is then done and significant topographic parameters are identified. Third, a Monte Carlo approach is used to investigate the effects of variability and uncertainty associated with the conversion of gridcell-scale winter balance values to an estimate of glacier-wide winter balance. Fourth, the transferability of statistical relationships between glaciers is examined and an winter-balance gradient on the continental side of the St. Elias Mountains is identified.

Table 1.2: Area, length, and elevation descriptors of three chosen glacier.

	Area (km ²)	Length (km)	Elevation (m)		
			Minimum	Maximum	Mean
Glacier 4	3.8	6.2	1958	2809	2344
Glacier 2	7.0	7.4	1899	3103	2495
Glacier 12	12.6	9.5	1923	3067	2428

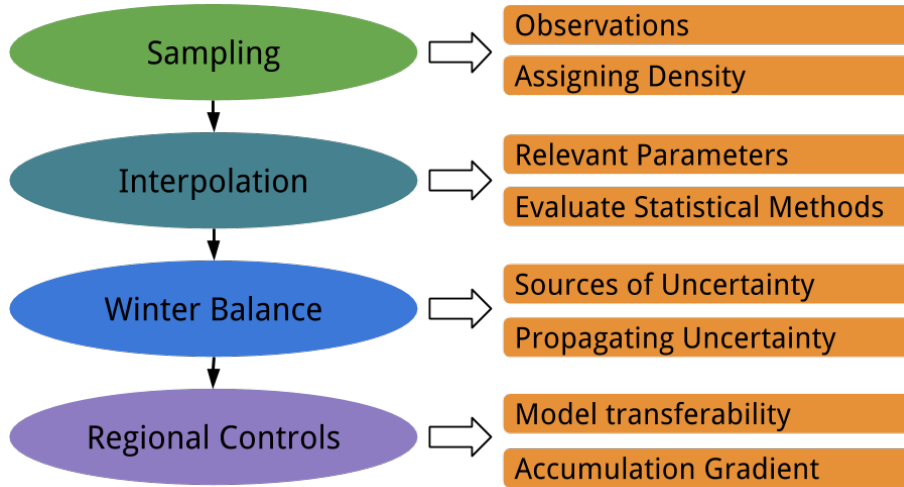


Figure 1.8: Visual representation of research project. General scope is described on the left (ovals) and specific investigations are shown on the right (squares).

1.7 Summary

Snow accumulation plays a central role in alpine hydrology and has a prominent impact on glacier mass balance. In mountainous regions, accumulation is highly variable on point, hillslope, watershed, and regional scales. The contribution of accumulation to glacier mass balance is controlled mainly by the distribution of snow. Processes such as orographic lifting, preferential deposition, and wind redistribution, all arising from the interaction of atmospheric conditions and topography, strongly affect snow distribution. Statistical models have been used to relate meteorological and topographic variables to snow accumulation in order to better understand the effects of these processes. These models rely on accurate measurement of snow distribution, which can be achieved by determining snow water equivalent values from snow density and depth. Results from previous studies of accumulation on glaciers have shown considerable spatial variability at many scales resulting from interactions between topography and atmospheric conditions.

Accumulation in the St. Elias Mountains is poorly understood, largely because the glaciers are remote. There is a need to quantify snow accumulation in this region and how it varies both between glaciers and within glacierized basins. Our study is the first within the St. Elias Mountains to examine accumulation variability at the point, gridcell, basin, and regional scale. Well-established methods are applied to measure accumulation variability. These measurements are used to investigate the role of topography in determining snow distribution, uncertainty in estimating glacier-wide winter balance, the transferability of statistical relationship and regional differences in distributed winter balance. This comprehensive approach to examining spatial patterns in snow distribution on glaciers con-

tributes to the current understanding of processes and parameters that affect winter balance variability on glaciers.

1.8 Thesis overview

The thesis is structured to follow the visual representation of the research scope presented in Figure 1.8. Chapter 2 provides a detailed description of the intended and executed experimental design as well as a description of how the observations are processed to produce data that can be analysed. Chapter 3 focuses on presenting snow depth and density observations as well as subsequent data processing, which includes various methods of assigning density values, converting snow depth and density to winter-balance as well as calculating topographic parameters used for interpolation. Chapter 4 details three interpolation methods used to obtain a distributed estimate of winter balance. Linear regression, simple kriging and regression kriging are compared and insights gained through the interpolation processes about controls on winter balance are discussed. Chapter 5 examines estimates of winter balance and how snow variability, data error and our methodological choices interact to create uncertainty in estimates of winter balance. Chapter 6 examines winter balance at the regional-scale. The transferability of linear regression models between glaciers is examined and glacier-wide winter balances are related to the regional accumulation gradient within the continental side of the St. Elias Mountains.

Chapter 2

Field methods and data processing

The thesis work is centred around data collected during a snow survey on three glaciers within the Donjek Range, St. Elias Mountains, Yukon, Canada during a two week period in May 2016. The intention of the survey design was to capture spatial variability, at various scales, of end-of-winter snow accumulation. Measurement locations are concentrated in the ablation area of the glacier, where a clearly defined boundary between snow and ice allows for accurate measurement of accumulation during the 2015–2016 winter season. Snow depth was measured using avalanche probes and snow density was measuring using a Federal Sampler and attempts were made to use a firn corer in the accumulation areas. Data was manually recorded in the field and photo back ups of the data were taken. Waypoints were recorded using a single band GPS and snow measurement locations estimated from these waypoints.

The following sections describe the design of the snow survey, how the survey was implemented in the field and how the data was digitized as well as initial processing to obtain data for future analysis. Section 2.1 describes the survey naming scheme we employed and shows locations of planned snow measurement. Section 2.2 provides detailed steps of how we executed the snow survey with four people and how we used snow measurement tools. Section 2.3 focuses on how the data is processed to obtain the full data set that is used for analysis in subsequent sections. Section 2.4 documents how we obtain topographic parameters from a given DEM of our study region. Processing steps such as DEM stitching, smoothing, and raster calculations are described in detail. Appendices 1, 2, 3, and 4 contain more details on GPS waypoint creation, maps used in the field, as well as in depth description of steps used in the data processing and topographic parameter calculation scripts.

2.1 Experimental design

2.1.1 Sampling Scheme and Naming System

Three glaciers within the Donjek Range were chosen as study sites and can be seen in Figure 2.1. Glaciers in the Donjek Range are unnamed but working names have been employed by [27] and are adopted for this work. Glacier 4, Glacier 2, and Glacier 13 were selected. These glaciers were chosen because these glaciers are spread throughout the Donjek Range and are located increasingly further from the large-scale topographic divide (located at the head of the Kaskawulsh Glacier [115]). The three glaciers are also located on different sides of the range-scale topographic divides, which run roughly from west to east in the southern area and from south to north in the eastern area and form an ‘L’ shape. Glacier 4 is located on the southern side of the first arm, Glacier 2 is located on the northern side of the first arm and the western side of the second arm, and Glacier 13 is located on the eastern side of the second arm. The selected glaciers also have similar orientations and one central glacier-filled valley (similar shape). Within the Donjek Range, these glaciers have good SPOT5 DEM coverage, which provides the highest resolution DEM available for this area. Additionally, the majority of the three glaciers is accessible on foot and the total area is small enough (see Table ??) to allow for reasonable coverage using point measurements.

The sampling scheme for each glacier was chosen to be similar so that comparison between glaciers could be done more readily. Each glacier was divided into the accumulation area, upper ablation area, and lower ablation area. In the accumulation area, a central snowpit location was chosen. Additionally, a series of approximately ten snow coring locations was chosen throughout the accumulation area. Steep sections and glacier margins were avoided. In both the upper and lower ablation area a number of linear and curvilinear transects were mapped, which included an ‘hourglass and circle’ (Parr, C., 2016 personal communication) as well as a transverse (below the hourglass) and midline transect. The length and width of each transect was adjusted to span the full dimension of its corresponding area. Snowpit locations in the ablation area were chosen to be at the centre of each hourglass. An overview of the sampling design can be seen in Figure 2.2.

The full ablation area was also divided into seven zones of approximately equal elevation intervals. Three locations within each zone were then randomly selected for zigzag [111] measurements (Figure 2.3) and the three locations were randomly labelled as different priorities. The goal was to complete one zigzag in each zone. If possible, the measurement would be completed at the ‘Priority A’ location but if it was not possible due to dangerous conditions then the ‘Priority B’ or ‘Priority C’ locations would be chosen. This allowed for random locations to be used but with the flexibility to adjust locations in the field. SWE measurements would be taken within each zigzag, and at snowpit locations with the ablation area.

The location of each snow depth and density measurement is imported into hand-held GPS devices (Garmin GPSMAP 64s) as a waypoint with a unique name. Points that are part of a transect have a name with the glacier number, the transect and area that the point belongs to, and a three-digit sequential number. The code for the transect area and type includes two letters. The first letter is either ‘A’ for ‘accumulation area’, ‘U’ for ‘upper ablation area’, or ‘L’ for ‘lower ablation area’. The second letter indicates the transect type, with ‘H’ for ‘hourglass’, ‘T’ for ‘transverse transect’, ‘C’ for ‘circle’, and ‘M’ for ‘midline’. For example, the name G04_UM023 is the 23rd point on the Midline transect in the Upper ablation area of Glacier 4, and G13_LC134 is the 134th point on the circle in the lower ablation area of Glacier 13. Other points that are not part of a transect also follow a similar naming convention. The snowpit locations use the code ‘SP’ (e.g. G04_LSP is the snowpit located in the lower ablation zone of Glacier 4) and the firn coring locations have the code ‘FC’ and a two digit number (e.g. G02_AFC04 is the fourth firn core location in the accumulation area of Glacier 2).

The zigzag points have a name with the glacier number, the zone that they were located in, the zigzag priority, and the vertex number. The zone and priority (A, B, C) are indicated by a ‘Z’, then the zone number, and then an ‘A’, ‘B’, or ‘C’. The vertex number is indicated by a ‘ZZ’ and then a sequential number. For example, the vertex labelled G02_Z2C_ZZ04 is on Glacier 2 in zone 2 and the fourth point of a priority C zigzag. The vertex labelled G13_Z7A_ZZ08 is on Glacier 13 in zone 7 and the eighth point of a priority A zigzag. An example of a zigzag sampling scheme can be seen in Figure 2.4.

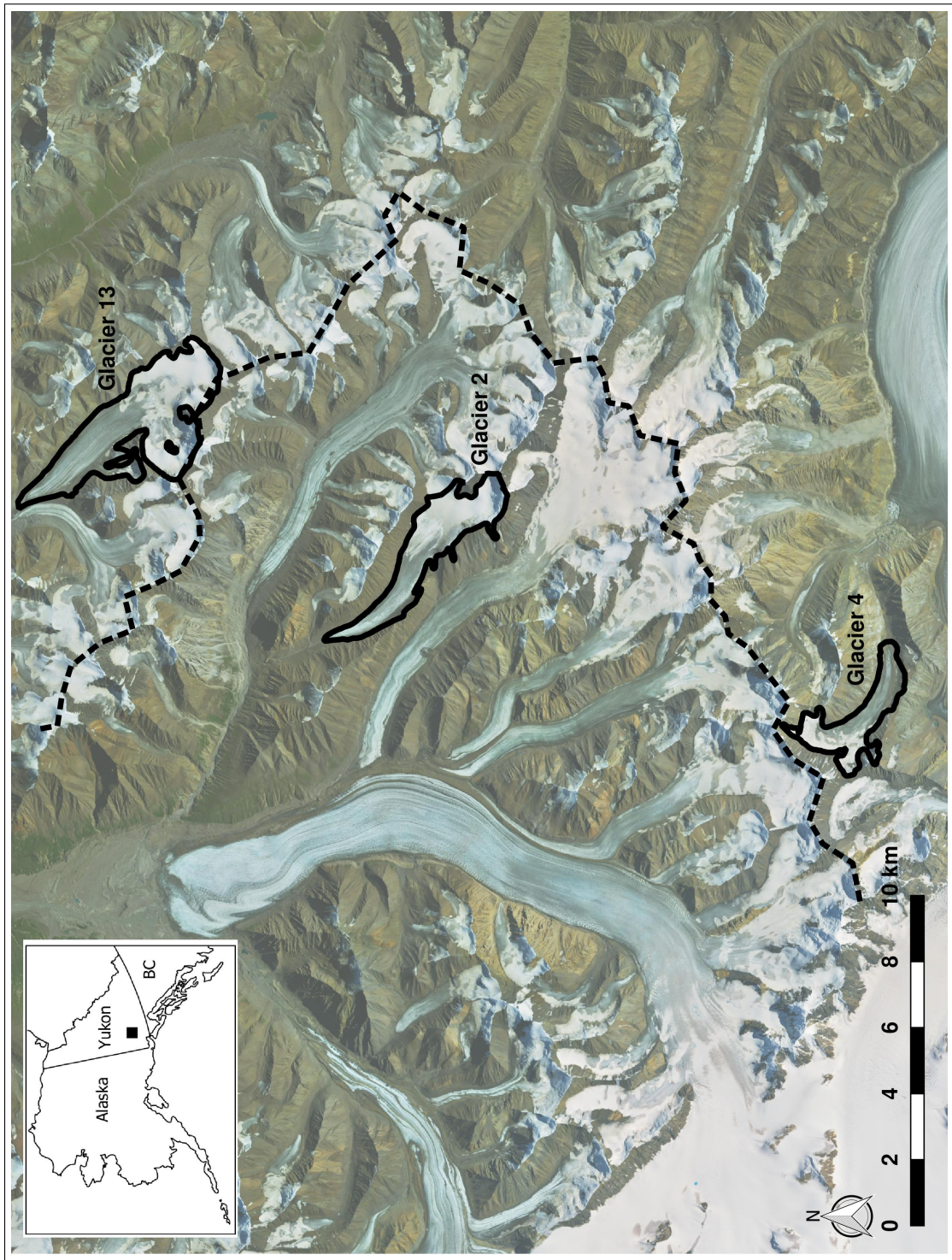


Figure 2.1: Study glaciers in the Donjek Range, Yukon (see inset). The topographic divide is shown as a dashed line.

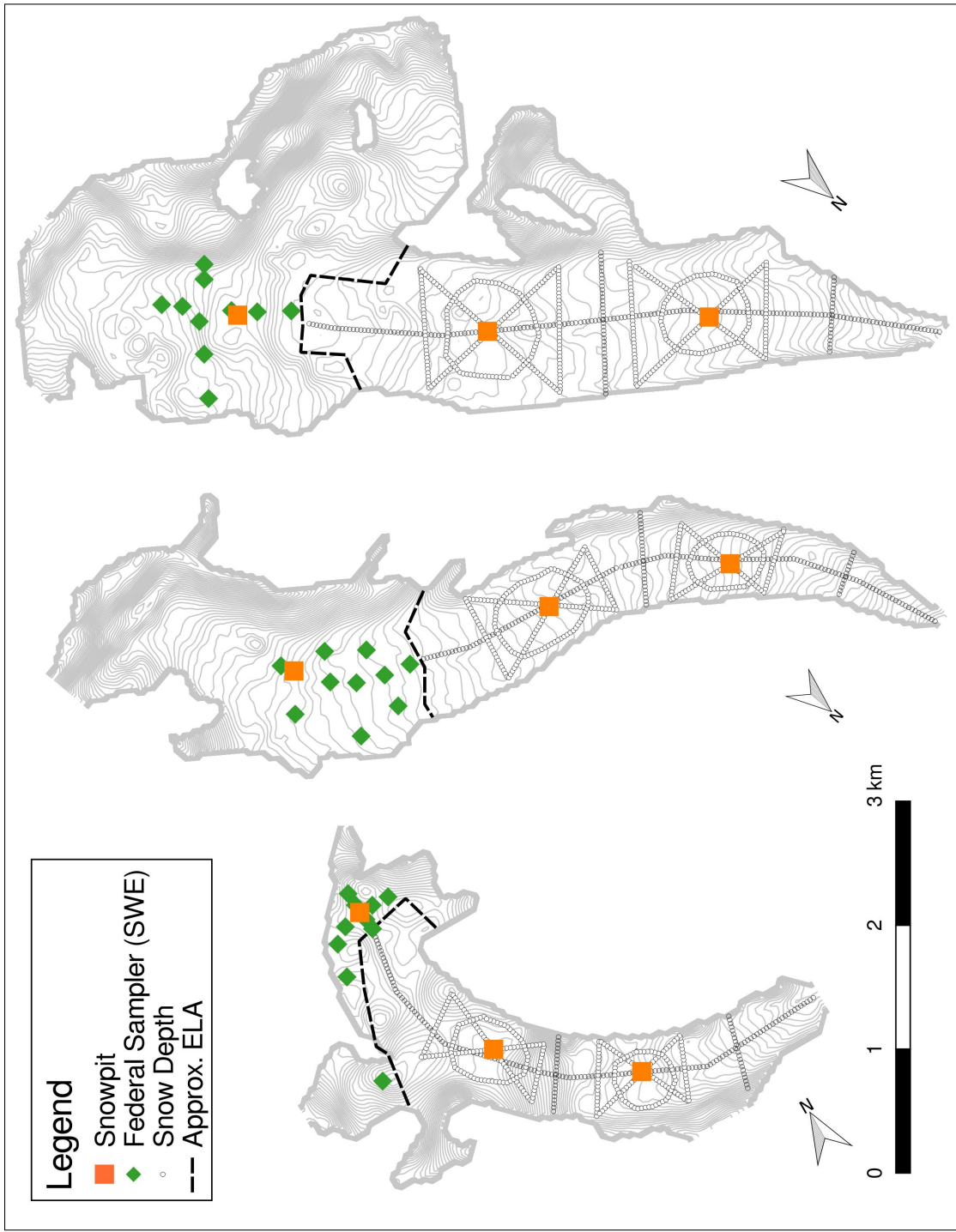


Figure 2.2: Target waypoints for snow depth transects, snow pits, and SWE measurements on three study glaciers.

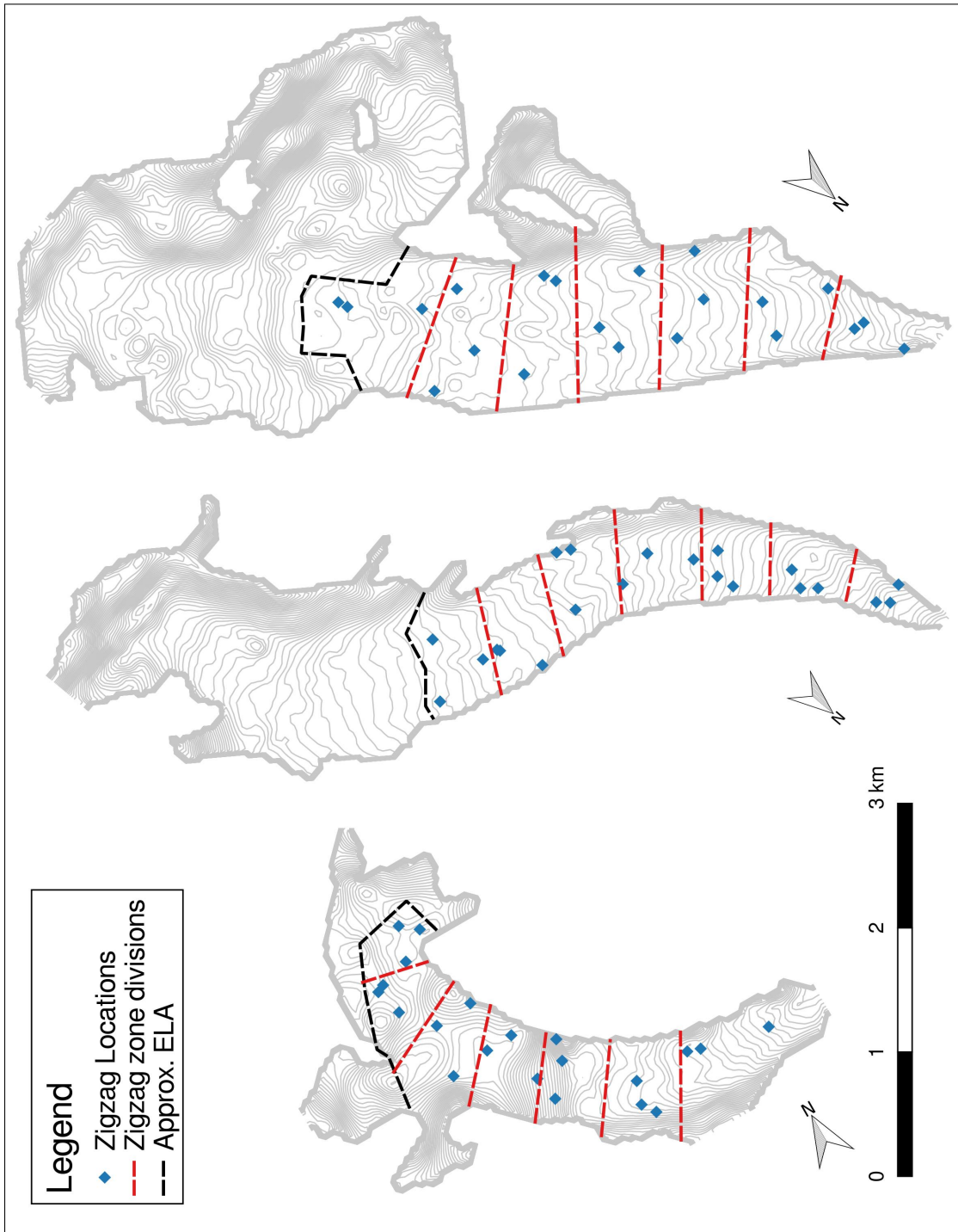


Figure 2.3: Randomly assigned locations for zigzag measurements in the ablation area (divided into seven zones).

2.2 Field methods

2.2.1 Linear and Curvilinear Transects

The transects, which include the hourglass, circle, transverse transect, and midline, were all executed in a similar way. Along each transect, waypoints were marked every 30 m. To sample these locations, a team of four people was used in the configuration shown in Figure 2.5 and schematically in Figure 2.6. The four people were roped together so that during typical glacier travel there was approximately 10 m separating each person (likely ranged between 9.5 and 11 m). The front person was responsible for navigation and waypoint marking and would follow these steps for each measurement location:

1. Use the GPS device to locate each intended waypoint
2. Navigate to that location using the GPS device
3. Stop and inform the team when they had arrived at the location
4. Mark a new waypoint on the GPS device as the real location of the measurement (allow for auto labelling of waypoint, which was a three digit number that increased by one with subsequent waypoints). When needed, call out the waypoint label to the team.
5. In one line of a field book, write the labels ‘Intended’ for the waypoint that was being navigated to (code created during planning stage), ‘Real’ for the name of the newly created waypoint on the GPS device (three digit number), as well as the easting, northing, and elevation for that location. This served as the backup for locating measurement points in the event of GPS device failure.

The remaining three people took snow depth measurement using a graduated 3.2 m avalanche probe. Upon arriving at the waypoint they would follow these steps:

1. Insert the probe into the snow until the snow/ice interface was reached. Read the depth of the snow pack on the probe to 0.5 cm. Repeat two (or three) more times (total of three (or four) measurements) within a 1 m² area of the first measurement and in a way that the three (or four) measurements are approximately equidistant.
2. In one line of a field book, record the ‘Real’ waypoint label (three digit number), as well as the three (or four) depth measurements.

Note that the snow/ice interface could often be differentiated from an ice lens. Typically, glacier ice felt hard, had a thin, low density (empty feeling) layer above, and created a bright ‘ping’ sound in the probe. Ice lenses felt sticky and the probe would make a dull ‘thud’ sound. In some locations this differentiation was obvious while in other locations it was difficult to be determine what was at the end of the probe. Often, layers in the snowpack could be felt with the probe. For example, the probe would move easily through low density

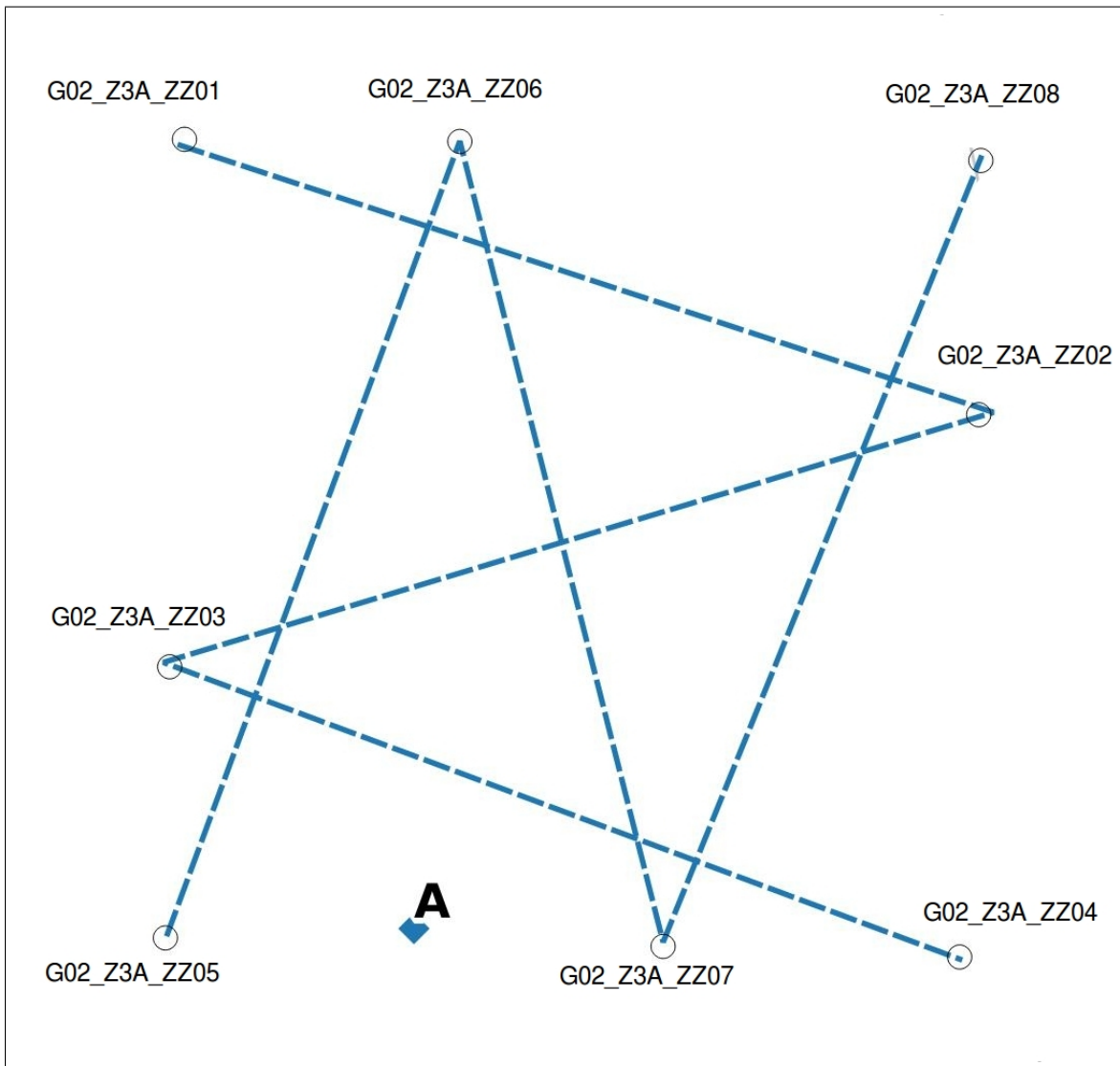


Figure 2.4: Example of zigzag. Vertices are labelled and measurements are taken at random intervals along the dashed lines between vertices. The randomly chosen location of the SWE measurement is shown as a diamond.

layers such as depth hoar and would ‘stick’ to hard layers or ice lenses. Increasing the force applied to the probe would usually allow the probe to penetrate through hard layers. In cases where the ‘sticky’ layer could not be penetrated, the observer would place a question mark next to the recorded depth or simply omit that measurement. A question mark was also placed beside measurements that were notably smaller than adjacent measurements, which suggested much deeper snow. Note that the probe was inserted vertically, which was not necessarily perpendicular to the snow surface.

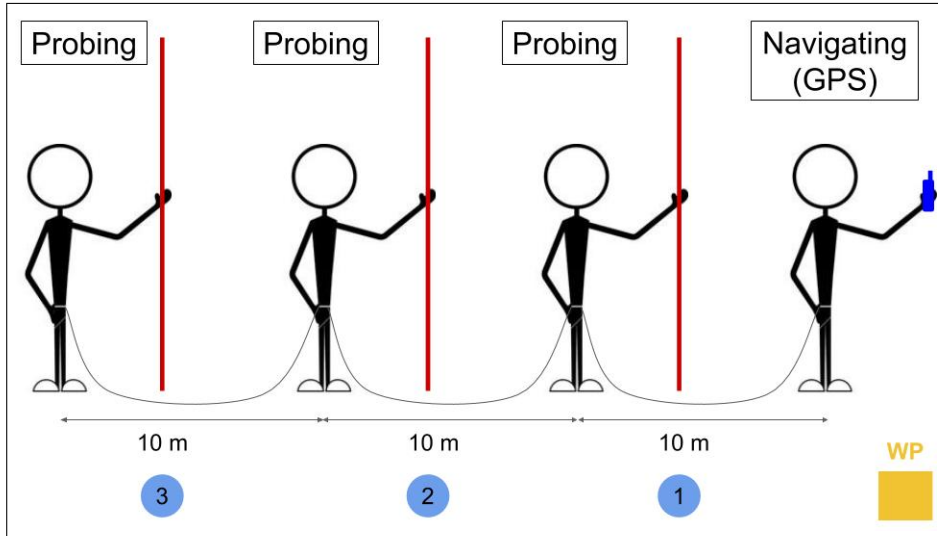
It was originally planned for each observer to take four depth measurements in a square pattern. However, during the first transect the observers found time consuming and difficult to remember and record four depths. The observers found that the most efficient way to collect data was to take three depth measurements, remember the values, and then write them all down in the field book. When four measurements were taken it was too difficult to remember all the values simultaneously so the whole process would take much longer. The decision was made to decrease the number of measurements so that we could increase the number of locations measured.

There were dedicated field books for each type of measurement rather than each observer. The first person had the ‘Navigation’ field book, the second person had ‘Snow depth #1’, the third person had ‘Snow depth #2’, and the fourth person had ‘Snow depth #3’. In this way, the location of each measured value can be inferred from its location relative to the navigation person (where the location was being recorded). For example, the ‘Snow depth #3’ value was located ~30 m behind the waypoint location along the trajectory between the previous and current waypoint. This arrangement was preferred to having a field book for each observer because it minimized confusion and potential errors when entering and processing data.

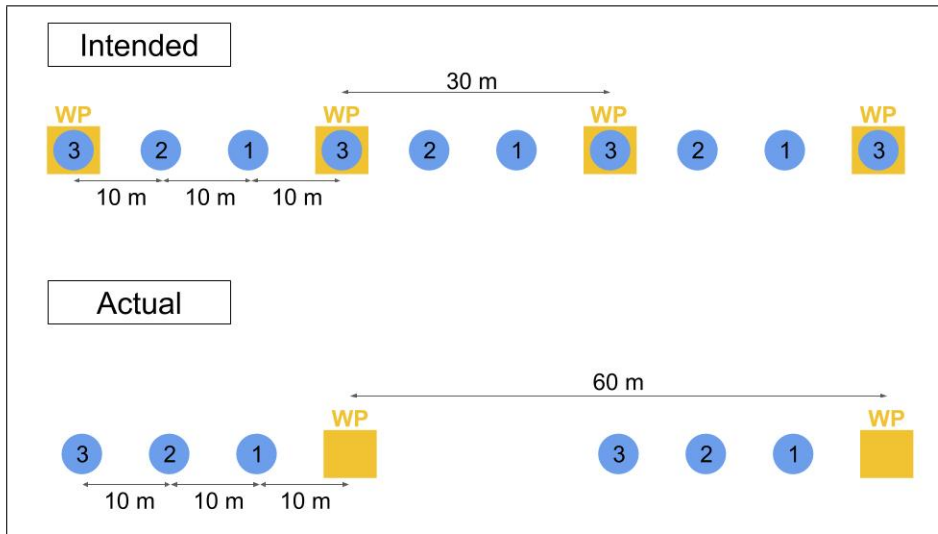
In this arrangement, snow depth measurements could be taken every 10 m along a transect if a waypoint was marked every 30 m. For the first two transects, measurements were completed at every waypoint. However, this also proved to be too time consuming so measurements were taken at every second waypoint for subsequent transects (exceptions include the midline on Glacier 4 and the lower hourglass on Glacier 2, see Table 2.1). A schematic of this arrangement can be seen in Figure 2.6b. Waypoints that were too dangerous to access were omitted. Additional waypoints (not originally uploaded to GPS devices) were created in some instances when travelling from the last accessible waypoint to the next accessible waypoint. A summary of information about the completed snow depth transects can be seen in Table 2.1.



Figure 2.5: Implementation of transect probing. The first person navigated to the intended waypoint using the GPS device. The second, third, and fourth (not seen) observers are probing using 3.2 m long avalanche probes. There is approximately 10 m between observers. Photo credit: G. Flowers



(a) Relative location of four people taking depth measurements at desired locations.



(b) Intended and actual transect depth measurement spacing. In the intended design, there was continuous measurement with 10 m sampling interval. In the actual implementation, every second waypoint was accessed so there was 60 m between subsequent measurements.

Figure 2.6: Schematic of the snow depth measurement configuration. Blue circles indicate depth measurement and orange squares indicate waypoint (WP) location.

Table 2.1: Summary information for snow depth transects. Transect shapes completed include Lower Hourglass (LH), Lower Circle (LC), Lower Midline (LM), Upper Hourglass (UH), Upper Circle (UC), Upper Midline (UM), Upper Transect (UT), and Bonus Transect (BT). The first observer was navigating to waypoints and the remaining three were taking depth measurements.

Glacier	Shape	Measurement Interval	Date	GPS Waypoint Labels	Observer Order	Comments
Glacier 4 (G04)	LH	30 m (60 m for upper part)	4 May 2016	021 – 070	GF–AP–CA–AC	4 depth measurement/location along upper part
	LC	60 m	6 May 2016	159 – 184	GF–AP–CA–AC	
	LM	90 m	7 May 2016	185 – 207	AP–GF–CA–AC	
	UH	60 m	5 May 2016	072 – 126	CA–GF–AP–AC	
	UC	60 m	5 May 2016	127 – 157	CA–GF–AP–AC	
	UM	90 m	7 May 2016	208 – 221	AP–GF–CA–AC	Additional measurement at WP 158 (6 May 2016)
	UT	30 m	4 May 2016	004 – 020	GF–AP–CA–AC	4 depth measurement/location
Glacier 2 (G02)	LH & LC	30 m	11 May 2016	371 – 518	GF–AP–CA	Only two probers. Avoided crossing main channel so LH & LC were combined and done together on glacier right and then glacier left off the channel. Almost all measurements in the dune area.
	LM	~60 m	10 May 2016	355 – 370	AP–GF–CA–AC	Original points along supraglacial stream bed so points moved to glacier right and locations were approximated
	UH	60 m	8 May 2016	223 – 275	AC–AP–CA–GF	Many corner points avoided due to crevasse danger
	UC	60 m	8 May 2016	276 – 313	AC–AP–CA–GF	
	UM	60 m	9 May 2016	313 – 343	AC–AP–CA–GF	
	UT	60 m	11 May 2016	519 – 528	GF–AP–CA	Only two probers
	BT	~60 m	19 May 2016	344 – 354	GF–AP–CA–AC	
Glacier 13 (G13)	LH	60 m	15 May 2016	745 – 811	AC–AP–CA–GF	
	LC	60 m	15 May 2016	812 – 847	AC–AP–CA–GF	
	LM	60 m	14 May 2016	714 – 743	AC–AP–CA–GF	
	UH	60 m	12 May 2016	571 – 650	AC–GF–CA–AP	
	UC	60 m	12 May 2016	529 – 570	AC–GF–CA–AP	
	UM	60 m	14 May 2016	678 – 713	AC–AP–CA–GF	
	UT	60 m	14 May 2016	660 – 677	AC–AP–CA–GF	

Table 2.2: Summary information for zigzag measurements

Glacier	Zone	Priority	Date	Observers	Number of Measurements	Comments
G04	3	A	5 May 2016	AP/CA	168	
G04	2	A	7 May 2016	CA/AC	135	
G04	5	B	7 May 2016	AP/GF	146	Sticky layer - many points not collected Snowing during measurements
G02	5	C	10 May 2016	CA/GF	152	Extra line measured
G02	7	A	10 May 2016	CA/GF/AP/AC	191	Vertex labelling error in GPS device
G02	3	B	10 May 2016	GF/AP	160	Channel present
G13	7	C	14 May 2016	AC/AP	167	Vertex labelling error in GPS device
G13	4	C	14 May 2016	GF/CA	143	Channel present
G13	3	B	15 May 2016	GF/CA	164	Vertex labelling error in GPS device
G13	5	A	15 May 2016	AP/AC	157	Mushy snow that collapses
						Vertex labelling error in GPS device

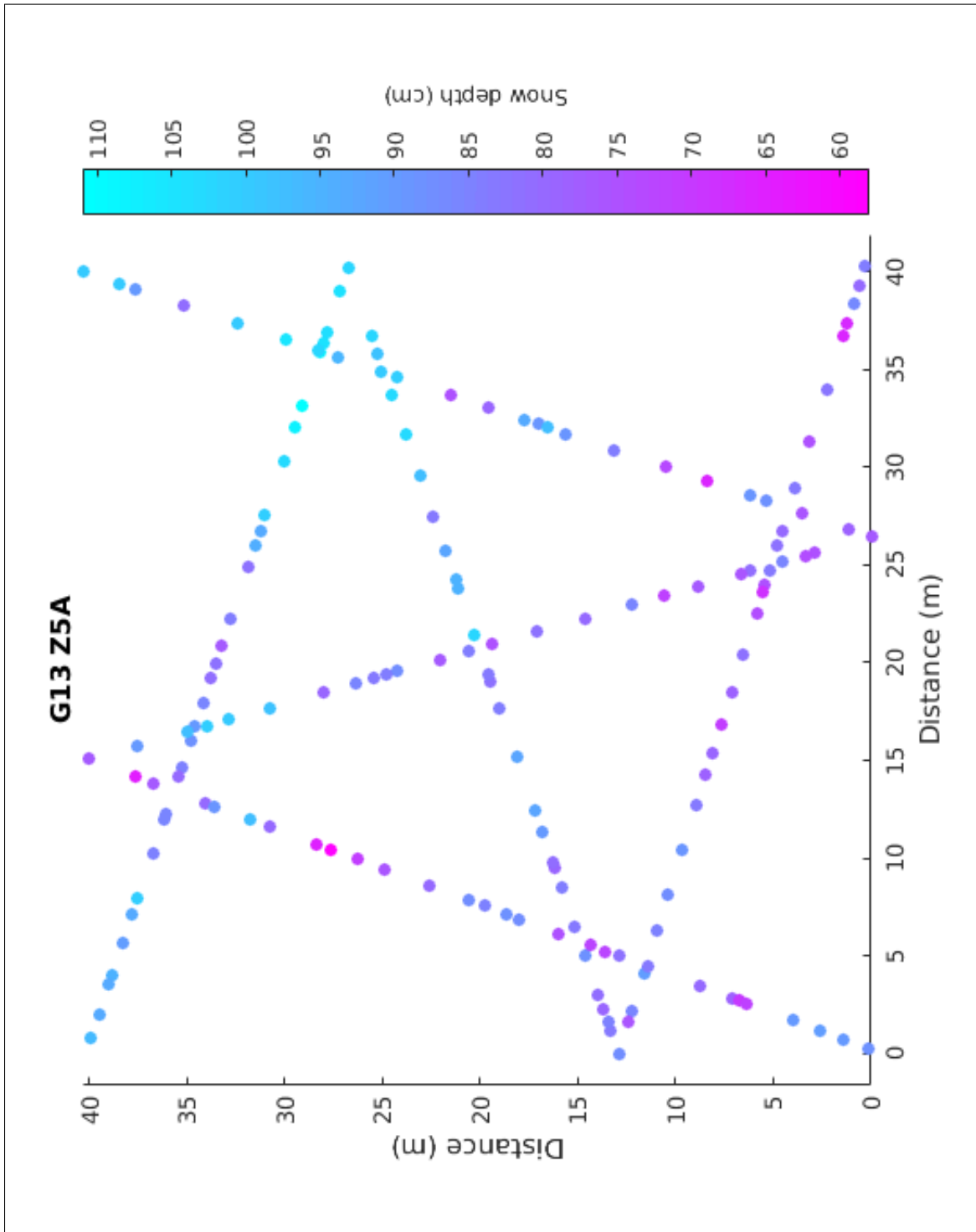


Figure 2.7: Snow depth values measured along a zigzag pattern (G04_Z3A)

2.2.2 Zigzag

The zigzag sampling pattern was used to obtain many measurements within a 40 x 40 m area. The pattern consisted of two intersecting ‘Z’ shaped transects. Snow depth was measured with random spacing between 0.3 m and 3.0 m.

Two teams of two people were used to complete each zigzag. The first team would navigate to the vertices of the zigzag using the GPS device and place wands at each vertex. Often the tracks would not be straight between two vertices so the second team would use the wands to travel between vertices in as straight a line as possible. The first person would use the avalanche probe to measure out the distance to the next measurement spot and then probe at that point (Sturm, M., 2016 personal communication). Probing protocol was exactly the same as for transect measurements (see Section 2.2.1). The first person would call out the depth to the second person, who was responsible for recording the distance between measurements and the depth at the measurement point. A field book was dedicated to zigzag measurements and each page would have the name of the vertex where measurements started, the distance from the previous measurement point and the depth at that point. The second person also had a sheet with random numbers from a uniform distribution between 0.3 and 3.0 m (generated used Matlab) and would call out these numbers in order as the distance between measurement points. While the second team was measuring snow depth, the first team took three SWE measurements with a ~1 m area around the predetermined location within the zigzag area (see Section 2.2.3 for protocol). An example of a completed zigzag pattern can be seen in Figure 2.7 and a summary of information about completed zigzags can be seen in Table 2.2.

2.2.3 Federal Snow Sampler

A metric Federal Snow Sampler from Geo Scientific Ltd. was used to measure snow depth and snow water equivalent (SWE). At the predetermined locations, three measurements (within 50 cm of each other) were made using the sampler. At the snowpit locations, a total of eight measurements were made, with two measurements on each side of the snowpit. Density calculated from these values will be compared with density determined from sampling within the snow pit (see Section 2.2.5).

The Federal Snow Sampler consists of four 0.83 m sections that could be screwed together. One end of the sampler has cutter teeth and the other end has a removable thread protector that can be screwed onto the top section of the tube. The sampler has graduations in units of 1 cm and slits along the side of the tube allow the observer to determine the length of the core when it is in the tube. The spring scale that comes with the Federal Sampler is in units of cm SWE.

To take a measurement with the Federal Sampler the following steps were taken:

Table 2.3: Summary information for SWE measurements with the Federal Snow Sampler

Glacier	Location	Total Values	Number of Tube Lengths	Date	Observers	Comments
G04	Z3A	5	3	5 May 2016	GF/AC	
	USP	2+2+2+3	3	5 May 2016	GF/CA	
	Z2A	3	3	7 May 2016	GF/AP	
	LSP	3+2+2+2	3	7 May 2016	GF/CA	
	Z5B	3	3	7 May 2016	CA/AC	
	Z5A	3	3	7 May 2016	CA/AC	
	Z5C	3	2	7 May 2016	CA/AC	
G02	Z5C	3	2	10 May 2016	AP/AC	
	USP	3+2+2+2	2	10 May 2016	AP/AC	
	Z7A	3	3	10 May 2016	CA/GF	
	Z7B	3	3	10 May 2016	CA/GF	
	Z7C	3	2	10 May 2016	AP/CA	
	LSP	2+2+2+2	1	10 May 2016	CA/AC	Used snowpit spring scale (grams)
	Z3B	3	1	10 May 2016	CA/AC	Used snowpit spring scale (grams)
G13	ASP	2+2+2+2	3	13 May 2016	AP/AC	
	AFC05	3	3	13 May 2016	AP/CA	Probe depth \neq tube depth
	WP 651	3	3	13 May 2016	AP/CA/GF	
	WP 652	4	3	13 May 2016	AP/CA/GF	
	WP 653	3	3	13 May 2016	AP/CA/GF	
	WP 654	3	3	13 May 2016	AP/CA/GF	
	WP 655	3	3	13 May 2016	AP/CA/GF	
	WP 656	3	3	13 May 2016	AP/CA/GF	
	WP 657	3	3	13 May 2016	AP/CA/GF	
	WP 658	3	3	13 May 2016	AP/CA/GF	
	WP 659	3	3	13 May 2016	AP/CA/GF	
	Z7C	3	2	13 May 2016	CA/GF	
	USP	2+2+2+2	2	14 May 2016	AP/AC	Ice layer near bottom
	Z4C	3	3	14 May 2016	AP	In stream channel
WP 744	WP 744	3	2	14 May 2016	AP	In Z4C zigzag
	Z3B	3	2	15 May 2016	AP/AC	
	Z4B	3	2	15 May 2016	AP/AC	
	Z5C	3	2	15 May 2016	CA/GF	
	Z5B	3	2	15 May 2016	CA/AC	



(a) Inserting the Federal Sampler into the snow. Photo credit: C. Ariagno



(b) Weighing the Federal Sampler using the spring scale (units of cm SWE). Photo credit: G. Flowers

Figure 2.8: Using the Federal Sampler to measure SWE

1. Three depth measurements (within ~50 cm of each other) were made using an avalanche probe and the depths were recorded.
2. The weight (in cm SWE) of the assembled empty tube was measured using the spring scale and then recorded (tare).
3. The tube was placed vertically into the snow and then pushed and twisted clockwise so that the cutters at the end of the tube would penetrate the snow pack. If this proved to be too difficult, the T-handle was added onto the tube to aid in pushing the tube further into the snow.
4. When the bottom of the snow pack was reached, the observer would measure the snow depth by using the graduation on the outside of the tube.
5. The tube was then gently pulled out of the snow (so as not to lose any snow from the bottom). The length of the snow core inside the tube was then measured by using the side slits to see the top of the core and lining it up with the graduation on the outside of the tube. This value was then recorded. If the length of the snow core was much less than the snow depth (typically a result of lost snow), the sample measurement was redone.
6. The snow and tube were weighed together using the spring scale and the value was recorded.

7. The tube was then emptied and wiped using a soft cloth on a pole to remove any moisture.

When the T-handle was used, the tube segments often became difficult to take apart. The small handles provided in the kit aided in disassembling the Federal Sampler. However, if a significant force was applied to the T-handle during sampling and the tube segments seized then longer handles (accomplished by attaching snow shovel handles to provided tools) helped in disassembling the sampler. Anti-seizing compound was included in the kit and was applied when needed. A summary of information about completed SWE measurements can be seen in Table 2.3.

2.2.4 Firn Corer

The firn corer was intended to be used in the accumulation area to extract a snow/firn core. The coring device would be beneficial in the accumulation area because the core can be extracted and used to determine the location of the snow/firn transition. From that, the snow depth and the mass of the snow core, which included only the past year of accumulation, could be determined. The Federal Sampler was thought to be ineffective in the accumulation area because the snow/firn transition may not have been felt and the core cannot be examined to establish where the transition occurs.

When the corer was used in the field however, a number of problems were encountered that prevented the collection of accurate measurements. The first was that the snow core would get stuck inside the core barrel. Warm temperatures meant that the barrel would get wet from snow melt and when it was inserted into the snow pack, the snow would freeze onto the side of the barrel. This meant that the core was destroyed in the extraction process. The second problem (which was connected to the first problem) was that the coring chips in the hole could not be discriminated from the core itself. Coring chips are loose snow crystals that fall to the bottom of the drilling hole when the barrel is taken out. When the barrel is reinserted for the second (or third) core, the snow in the subsequent core will contain these coring chips, which are not part of the intended core. The mass of the core will be incorrect (overestimate) because of this additional snow. This problem is typically avoided by extracting the in-tact core and identifying and removing the coring chips. However, since the core could not be extracted as one piece, this step was not possible and the masses of the cores were incorrect.

In a few locations, sections of the core could be exacted without breaking them apart. In these areas the snow/firn transition could be identified. This means that in principal, the firn corer could be used to determine the depth of this transition. The main challenge is therefore being able to identify chips. In firn core trials that occurred after this field work, it was found that the the cores could be pulled out easily if the barrel was not totally full. However, in these less compacted cores the chips were difficult to identify so the problem persists.

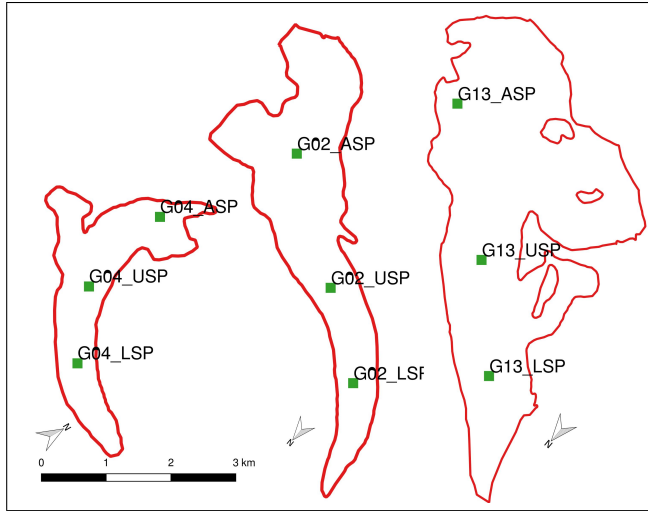


Figure 2.9: Locations and labels for all snowpits dug on Glaciers 4, 2 and 13 (left to right).

As a result of these complications, many accumulation area measurements on Glacier 4 and Glacier 2 were abandoned. On Glacier 13, the Federal Sampler was successfully used to take SWE measurements. The snow/firn transition could be felt with the Federal Sampler because of the large density change, which made it almost impossible to further insert the tube into the snow pack.

2.2.5 Snowpit

Three snowpits were excavated on each glacier (Figure 2.9) and snow density sampled every 10 cm using a wedge cutter (Snow Metrics RIP 2 Cutter (250 cc)). The snow temperature was also measured at 10 cm intervals. The snowpit was oriented so that the sampling face was in the shade (typically south edge of snowpit), which reduces melt.

The measurement procedure in the snowpit was as follows:

1. The face of the wall that was chosen for sampling was smoothed and a ruler was placed against the wall with the 0 cm mark at the bottom of the snowpit. The ruler was used to measure sampling heights within the snow pack. The snow surface directly above this wall was undisturbed during the digging process so that the true snow depth could be determined.
2. Air and snow surface temperature were measured by placing the thermometer (dial-stem thermometer ($\pm 0.5^\circ$)) in the shade of a shovel or ski.
3. A snow density sample was taken in 10 cm intervals through the full depth of the snow pack. Samples were offset horizontally from each other so that the snow was not affected by previous measurements.

- (a) The wedge cutter was inserted into the snow vertically (to sample 10 cm intervals) and the top was slid onto the wedge to isolate the sample. The wedge was taken out and inspected. If the sample appeared to fill the entire wedge (no obvious voids) then the wedge was emptied into a small plastic bag. If the sample was poor then the snow was discarded and a new sample was taken at the same height in the snow pit.
 - (b) A spring scale (± 2.5 g) was then used to weigh the bag with the snow sample and the weight was recorded. The snow sample was then discarded. Note that the spring scale was tared with an empty bag.
4. Snow temperatures were also measured and recorded every 10 cm. The thermometer was inserted into the snow at the desired location and left to equilibrate for several minutes. The temperature was then recorded.

Modifications to this procedure occurred when snow samples could not be taken because the snow was too dense. This would often occur when ice layers or lenses were present in the snow, which could not be cut by the wedge. In these cases, the measured thickness was recorded. A sample would then be taken using the wedge cutter but aligned horizontally so that a 5 cm tall sample was taken. Additionally, the sample interval closest to the ice surface (0–10 cm) would be difficult to obtain because the ice was rough and the snow above was faceted. Sometimes, this sample could not be obtained or a 5 cm sample needed to be taken.

After the majority of snowpit measurements were completed, a spring scale with finer resolution was found. For Glacier 4 and 2 the coarse resolution (10 g) scale had been used but for Glacier 13 the fine resolution (2 g) scale was used. Future measurements should use the finer resolution spring scale when using the small wedge sampler. As a result, the snow-density uncertainty is larger for Glacier 4 and 2 than for Glacier 13.

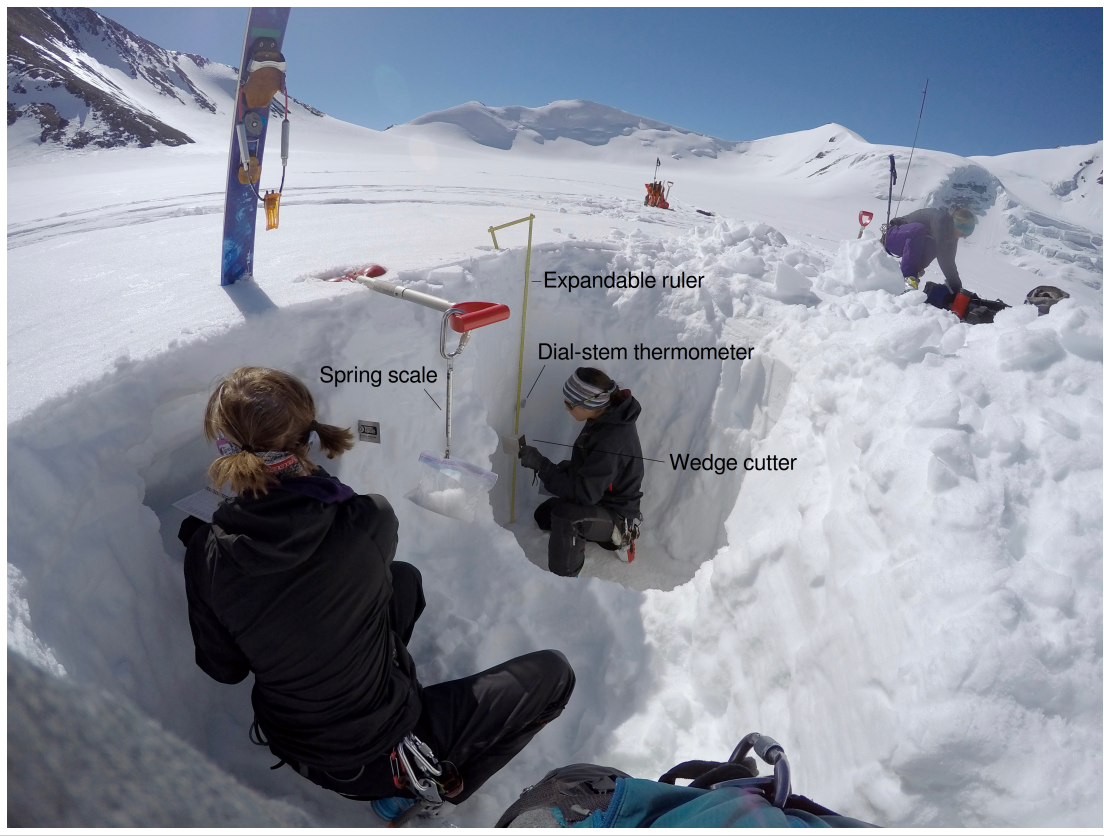


Figure 2.10: Taking snow density measurements in a snowpit. An expandable ruler is used to measure snow depth and determine sampling locations. A 250cc wedge cutter is used to extract a known volume of snow and a spring scale is used to weigh the snow. The dial-stem thermometer is used for measuring snow temperature. Note that the sampling wall is shaded, has an undisturbed snow surface above it, and has a smoothed face. Photo credit: A. Criscitiello

2.3 Data processing

2.3.1 Snow depth measured with graduated avalanche probe

Linear and curvilinear transect surveys

Snow depth measurements along the linear and curvilinear transects were taken at locations a certain distance from marked waypoints. Since only the coordinates of the waypoints (WP) were recorded, the measurement coordinates need to be estimated. The measurement locations were assumed to be 10, 20, and 30 m behind the marked WP, in a straight line between the marked WP and the previous WP (Figure 2.11). In cases with only two observers, locations were assumed to be 10 and 20 m behind the marked WP. For the first marked WP of a transect, it was assumed that the measurement locations were along the same line as that between the first and second WPs. Details of the methodology used to estimate measurement locations can be found in Appendix C.1.1.

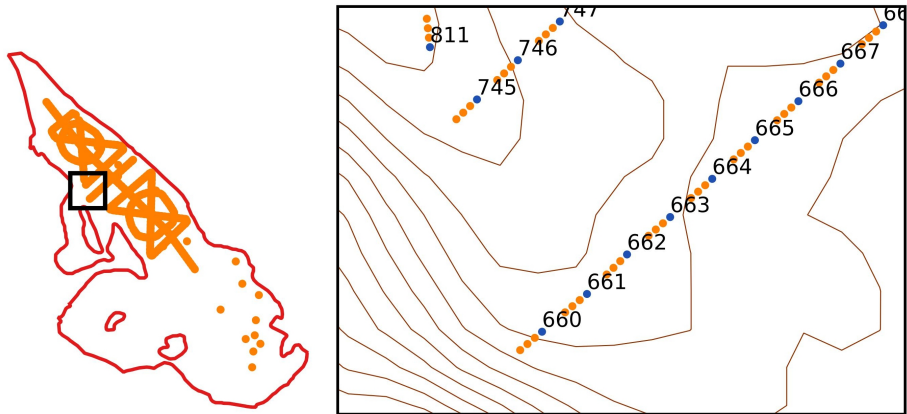


Figure 2.11: Example of estimating snow depth measurement locations in one area (indicated by black box) on Glacier 13. Numbered waypoint (WP) locations are shown in blue and estimated measurement locations are shown in orange at a distance of 10, 20, and 30 m from the WP. Measurement locations are taken to be along a straight line between subsequent WPs. For the first WP of a transect, the measurement locations are assumed to be along the same line as that between the first and second WPs of a transect. For example, the measurement locations behind WP 660 fall along the same line as those between WP 660 and WP 661. The same is true for WP 745.

Zigzag surveys

Depth measurements in zigzag surveys were taken along six sections that connected eight vertices. GPS coordinates of vertices were predetermined. The survey involved navigating to the first vertex, then taking measurements at random distances from this vertex along a straight line between that vertex and the next one. The location of each measurement was measured, using the avalanche probe, and recorded as the distance from the previous measurement location. Each section was recorded separately and identified by its start, or reference, vertex.

Originally, the location of measurements was found by taking the cumulative distance of a measurement from its reference vertex along a straight line between the reference and the next vertices. However, it was found that the cumulative distance (measured using an avalanche probe) of each zigzag section was not equivalent to the distance between UTM coordinates of each vertex (due to error in GPS and/or walking between vertices not along a straight line). Therefore, a second option for calculating the measurement locations was established. This second option still assumes the measurement was along a straight line between two vertices but the location is relative to the end of the previous section, not the reference vertex. Vertices 1 and 5 were used as reference vertices for their respective section because they began a section with no prior measurements. An example of differences between these two location estimation methods can be seen in Figure 2.12.

2.3.2 Snow density

The snowpit and Federal Sampler measurements were entered into a spreadsheet and the snow density from each measurement was calculated. For snowpit measurements the snow density was calculated by multiplying the measured density from each wedge sample by the thickness of the sample and summing these values. This is known as an integrated snow density and it encompasses the whole snow column. A density of 917 kg m^{-3} was applied to ice layers and a density of 600 kg m^{-3} was applied to layers that were described as ‘hard’ and were too difficult to sample. To determine the error in estimating integrated snow density, the values of ice density, ice-layer thickness, and the ‘hard’ layer density were varied between 700 and 917 kg m^{-3} , $\pm 1 \text{ cm}$ (representing 20-100% of the ice-layer thickness), and 500 and 600 kg m^{-3} , respectively. A summary of density values and ranges is shown in Table 2.4.

Density values determined from Federal Sampler measurements that were deemed to be unrepresentative of the local snow pack, including measurements where the inner core length was less than 70% of the snow depth or where density values were exceptionally high (e.g. 490 kg m^{-3}), were flagged as poor

Table 2.4: Statistics of integrated densities measured using Federal Sampler or vertical density profiles (of snow wedge measurements) in snow pits. Mean, standard deviation (std), and number (n) of snow density (kg m^{-3}) measurements on study glaciers is shown.

	Snowpits			Federal Sampler		
	Mean	Std	n	Mean	Std	n
Glacier 4	348	13	3	327	32	7
Glacier 2	333	26	4	326	23	7
Glacier 13	349	26	10	307	32	31
All	342	26	10	316	31	31

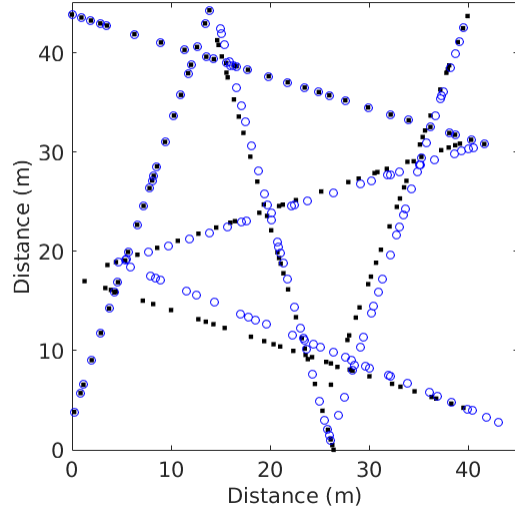


Figure 2.12: Example of zigzag survey measurement locations calculated using difference reference vertices for each section of the zigzag. Black squares show measurement locations calculated using the original GPS coordinates of vertices (Option 1). Blue circles show measurement locations calculated using the last measurement location from the previous section as the reference vertex (Option 2). For the first and fifth vertices (located at $(0, 40 \text{ m})$ and $(0, 4 \text{ m})$) the original GPS coordinates were used for both options.

quality and removed. The remaining Federal Sampler density values were then averaged for each measurement location.

2.3.3 Snow water equivalent (SWE)

The conversion of measured snow depth to snow water equivalent (SWE) could not be done at all measurement locations because snow density was not measured at all locations where snow depth was measured. This meant that the density measurements need to be interpolated. A subset of appropriate interpolation methods was chosen for this project. In the absence of a clear justification for choosing one option over the other, all options were carried forward in the analysis. A schematic of the interpolation method choices is shown in Figure 2.13.

Four main interpolation methods are used [83, 36]. The first assumes a uniform spatial distribution of density, calculated as the mean from all measurement locations on all three glaciers, over the entire study area. The second also assumes a uniform spatial distribution of density but uses a mean density for individual glaciers (different value for each glacier). The third and fourth methods involve spatially variable density values. One of these methods involves using a regression of elevation and measured density values to interpolate between measurement locations. The other spatially variable interpolation method uses an inverse-distance weighted mean for interpolation.

Since the snowpit-derived densities and Federal Sampler-derived densities had no discernible relationship, the two density datasets are kept separate. This means that for each density interpolation option, there are two outputs. In the end, there are eight different interpolations of density that are carried forward throughout the study, which allows for a range of SWE estimates to be made.

The eight density distributions can be classified as using either snowpit-derived densities (SP) or Federal Sampler-derived densities (FS) and as using a certain method, indicated by a number (Table 4.1).

S1 Calculates the mean density of all snowpit measurements.



Figure 2.13: Relationship between various ways to interpolate between density measurements for the calculation of SWE. The bottom row shows the code for each density interpolation option as described in Section 2.3.3.

- F1 Calculates the mean density of all Federal Sampler measurements.
- S2 Calculates the mean density for each glacier using the snowpit measurements.
- F2 Calculates the mean density for each glacier using the Federal Sampler measurements.
- S3 Calculates the slope and intercept of the best-fit regression line of snowpit densities with elevation for each glacier using the ‘fit’ function and then uses slope and intercept to determine density for all elevations associated with each measurement location.
- F3 Calculates the slope and intercept of the best-fit regression line of Federal Sampler densities with elevation for each glacier using the ‘fit’ function and then uses the slope and intercept to determine density for all elevations associated with each measurement location.
- S4 Determines the distance between each measurement location and each snowpit and then calculates the inverse-distance weight. For each measurement location, each snowpit density is then multiplied by its weight and these values are added together and divided by the sum of all weights.
- F4 Determines the distance between each measurement location and each Federal Sampler and then calculates the inverse-distance weight. For each measurement location, each Federal Sampler density is then multiplied by its weight and these values are added together and divided by the sum of all weights.

Table 2.5: Description of density interpolation methods used to calculate SWE used in the topographic regression. Abbreviations with ‘S’ used snowpit-derived densities and abbreviations with an ‘F’ used Federal Sampler-derived densities.

	Source of snow density	Estimation method
	<i>Snowpit</i>	<i>Federal Sampler</i>
S1	■	
F1		■
S2	■	
F2		■
S3	■	
F3		■
S4	■	
F4		■

2.4 Topographic parameters

2.4.1 Obtaining digital elevation models (DEMs) for study glaciers

Topographic parameters can be derived from a digital elevation model (DEM) of the study area. The DEM used in this project was created from imagery collected by the SPOT-5 satellite and it was provided at no cost by the French Space Agency (CNES) through the SPIRIT International Polar Year project [67]. The DEM has a cell size of 40×40 m. The DEM was created using a set of correlation parameters fit for steeper slopes (E. Berthier personal communication, 2016).

Two DEMs were available for the Donjek Range. The first DEM (GES 08-029) was made from images collected on September 3, 2007 and the second DEM (GES 07-044) was made from images collected on September 13, 2007. The snow extent on September 13, 2007, as imaged by a Landsat 7 satellite can be seen in Figure 2.15. Since the images were collected in September, the surface would likely be at a seasonal minimum with minimum snow cover. Therefore, the surface described by the DEM in the ablation area represents the topography below the snow. A limitation in using this DEM is that the DEM is from 2007 and there have almost certainly been changes in the end-of-summer glacier surface. However, the SPOT-5 DEM is the best resolution and most current DEM available for the study area.

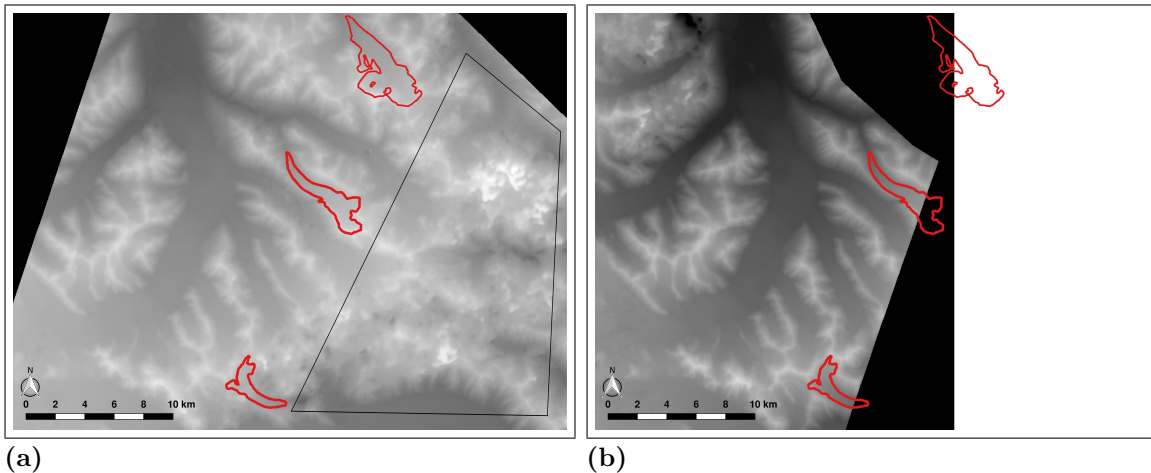


Figure 2.14: SPOT-5 DEMs available for the Donjek Range. Study glaciers are shown as red outlines. The DEM made from imagery collected on September 3, 2007 (GES 08-029) is shown in (a) and the DEM made from imagery collected on September 13, 2007 (GES 07-044) is shown in (b). Imagery that contains cloud cover result in a distorted DEM, as seen in the boxed area of (a).

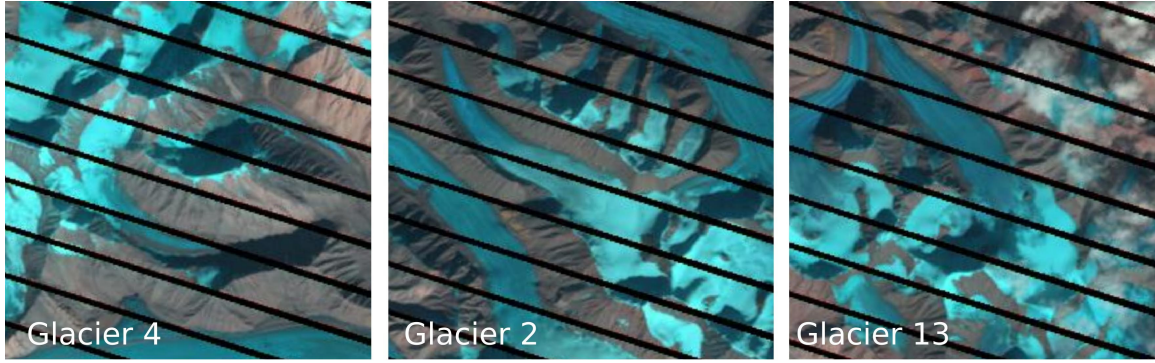


Figure 2.15: Landsat 7 ETM images of study glaciers on September 13, 2007. Snow cover is shown as light blue and ice is shown as dark blue.

The GES 08-029 DEM covers all three study glaciers (see Figure 2.14a) but a large part of Glacier 4 and some areas of Glacier 2 were masked by clouds and/or showed limited contrast in the original stereoimage pairs, resulting in incorrect elevation data (E. Berthier personal communication, 2016). The cloudy areas appear as black regions on the DEM mask (not shown) and as distortion in the DEM, as seen in the boxed area of Figure 2.14a. The second DEM (GES 07-044) spans only part of the Donjek Range, covering most of Glacier 4 and ~60% of Glacier 2 (see Figure 2.14b). This DEM had no masked areas over Glaciers 2 and 4. The two DEMs were therefore merged to create a cloud free DEM that spanned all three glaciers.

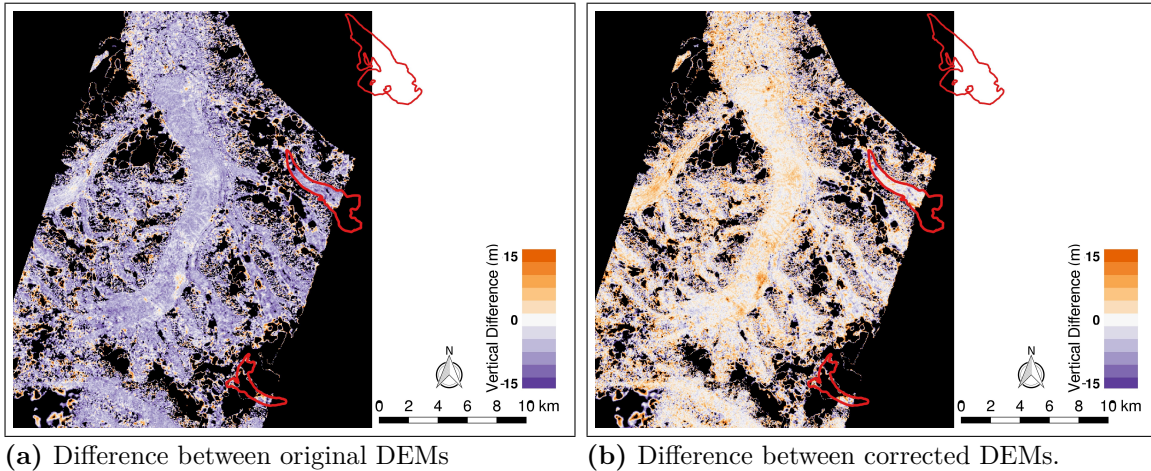


Figure 2.16: Vertical difference between DEMs in overlapping area. Difference was found by subtracting GES 08-029 from GES 07-044. Positive values indicate that GES 07-044 values are higher than GES 08-029 values.

The merging process was complicated by the fact that there was a horizontal and vertical discrepancy between the two DEMs. Although the discrepancy was not consistent throughout the study area, the GES 07-044 DEM was generally higher than the first, as

can be seen by the overall purple colour in Figure 2.16a and the positive skew of the vertical difference between the two DEMs in Figure 2.17. The mean vertical difference is +6.3 m.

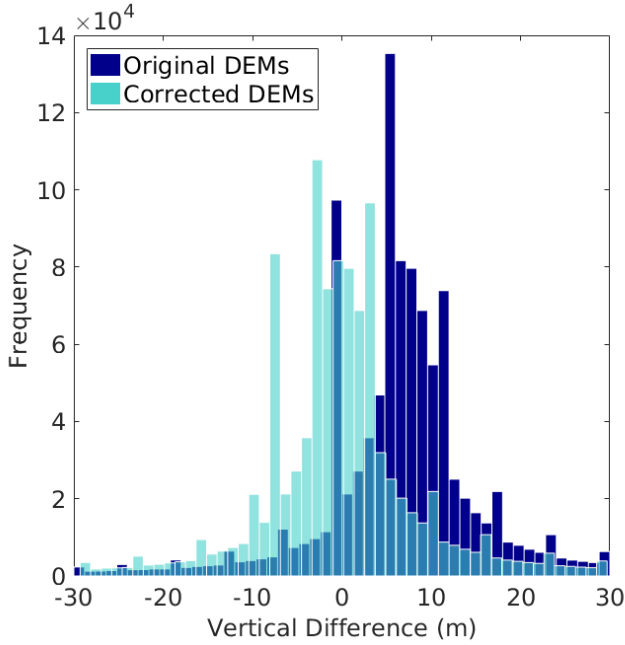


Figure 2.17: Histogram of the vertical difference between GES 08-029 and GES 07-044 before (dark blue) and after (light blue) correction.

The discrepancy was corrected by E. Bertier (2016, personal communication) using an iterative 3D-coregistration algorithm [13]. The GES 07-044 DEM was arbitrarily chosen to be used as the reference DEM. Note that the absolute value of the elevation is not necessarily important for the topographic regression, as long as the relative elevations are correct. The reference DEM, GES 07-044, was first shifted vertically by +5.4 m, estimated using ICESat data [14]. Then, the mean horizontal and vertical (X, Y, Z) shift between the reference DEM and the GES 08-029 DEM was found by minimizing the standard deviation of the elevation differences between the DEMs. Using this correlation, the GES 08-029 DEM was shifted ~ 2 m east, ~ 4 m north, and ~ 1.9 m vertically. The GES 08-029 DEM was then reprojected in the same projection as the reference DEM (GES 07-044). The difference map between the two shifted DEMs is shown in Figure 2.16b. Difference values are not uniform but do show both positive and negative values. The distribution of vertical difference values (Figure 2.17) after correction is centred at zero with a mean difference of -0.2 m.

Merging of the corrected DEMs was completed in QGIS. First, the rasters were cropped to overlap by a few cells. The crop line was chosen by hand to include as much of the reference DEM as possible (fewer areas of poor data) but was a relatively small distance from the edge of the DEM (see Figure 2.18). The second DEM was cropped to follow the same merge line but overlap with the first DEM by a few cells. This was done to avoid

gaps in cell values that arise from cropping across a DEM cell. The merging was completed using the built in QGIS tool ‘Merge’ and in areas where the two DEMs overlapped, the GES 08-029 DEM values were chosen.

The final DEM used for subsequent analysis can be seen in Figure 4. Despite the corrections, there were still discrepancies along the intersection of the DEMs, which can be seen as sharp boundaries in the contour lines. However, these discrepancies are not present on the study glaciers and are located more than 250 m from the edge of the glacier so this DEM was used as the final version for the Donjek Range.

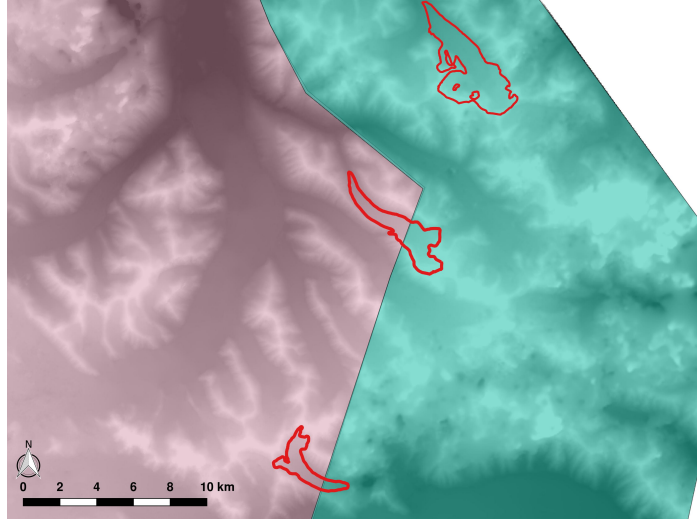


Figure 2.18: Outlines of the cropped GES 07-044 DEM (pink, left) and cropped GES 08-029 DEM (blue, right) used for merging. There is a slight overlap between the two DEMs that cannot be seen at this scale.

Topographic parameters are used to describe characteristics of the local topography that may affect snow distribution and can act as proxies for physical processes that determine snow deposition and redistribution. Topographic parameters used in snow accumulation studies on glaciers include elevation (z), distance from centreline (d_C), slope (m), tangential (κ_T) and profile (κ_P) curvature, “northness” (N), aspect (α) and Sx, which is a proxy for wind redistribution [9, 105, 83].

A number of programs are used to calculate topographic parameters from the DEM. Distance from centreline and “northness” were calculated in Matlab. Sx was determined using a executable obtained from Adam Winstral that follows the procedure outlined in [130]. The remaining parameters were calculated using the `r.slope.aspect` module in GRASS GIS software run through QGIS as described in [86] and [58]. Note that topographic parameters were calculated using the full DEM and then trimmed to Randolph Glacier Inventory defined glacier outlines so as to avoid errors that arise at the edge of the DEM when taking derivatives.

Details about the calculation of topographic parameters are described below.

Elevation

Elevation (z) values were taken from the (corrected) SPOT-5 DEMs directly (Figure 2.23).

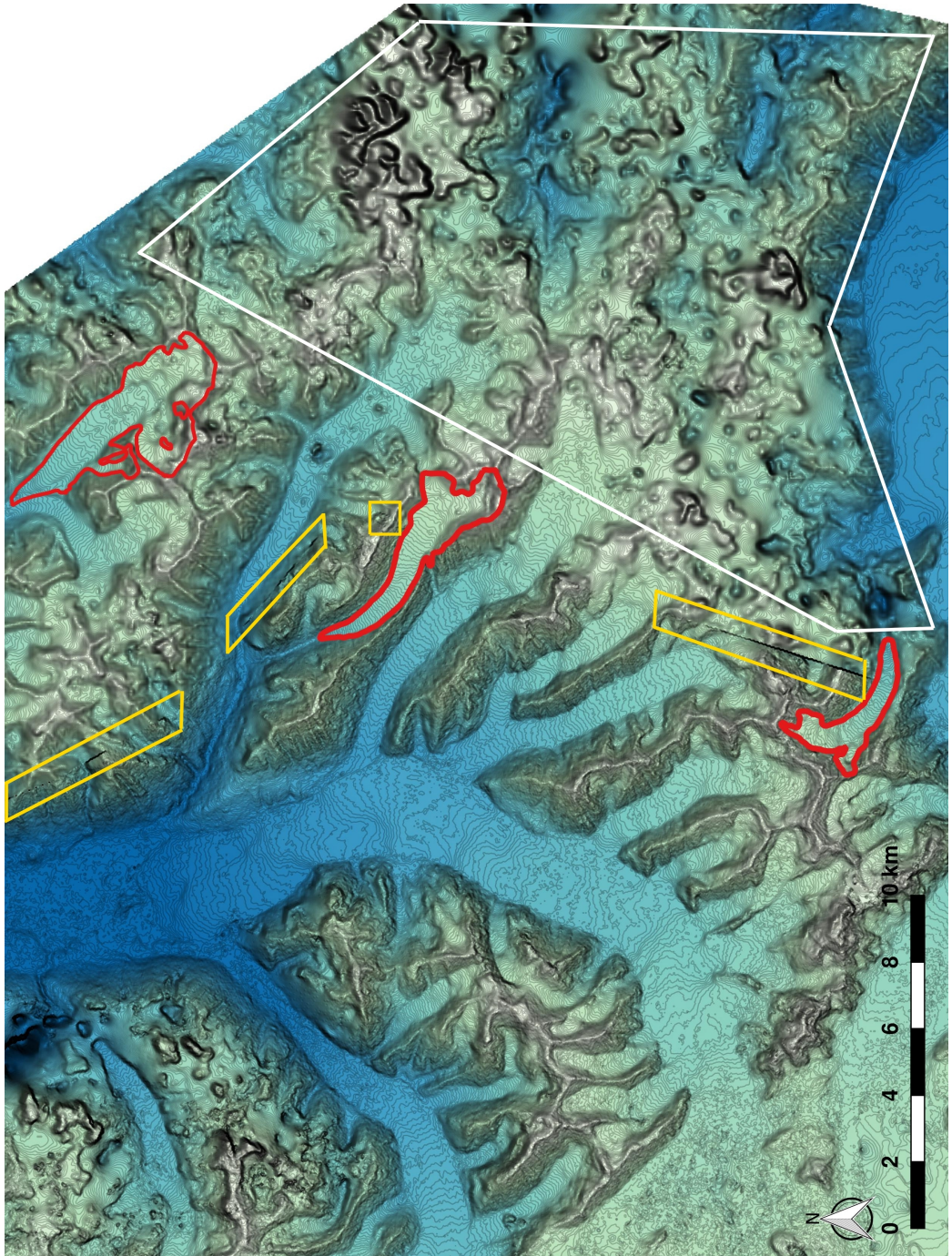


Figure 2.19: Merged DEM of the Donjek range from two corrected SPOT-5 DEMs, plotted with 10 m contour lines. Study glaciers are shown in red. Discrepancies between the DEMs along the merge line can be seen as anomalous linear features in the contour map (yellow boxes). Distorted contours in the eastern regions (white box) are a result of errors in the DEM.

Distance from centreline

Distance from centreline (d_C) was calculated as the minimum distance between the Easting and Northing of the northwest corner of each cell and a manually defined centreline (Figure 2.25).

Slope

Slope (m) is the maximal rate of change of elevation and is defined as the angle between a plane tangential to the surface (gradient) and the horizontal [96] (Figure 2.29). Slope (m) is calculated according to

$$m = \arctan \sqrt{\left(\frac{\partial z}{\partial x}\right)^2 + \left(\frac{\partial z}{\partial y}\right)^2}, \quad (2.1)$$

where the partial derivatives can be approximated by [86, 94, 58]

$$\begin{aligned} \frac{\partial z}{\partial x} &\approx \frac{(z_7 - z_9) + (2z_4 - 2z_6) + (z_1 - z_3)}{8\Delta x}, \\ \frac{\partial z}{\partial y} &\approx \frac{(z_7 - z_1) + (2z_8 - 2z_2) + (z_9 - z_3)}{8\Delta y}. \end{aligned} \quad (2.2)$$

Here, z_k refers to one of the grid cells surrounding the cell of interest, which is located at row i and column j of the DEM. So $z_3 = z_{i+1,j+1}$, $z_7 = z_{i-1,j-1}$, and so on (Figure 2.20). The grid spacing (resolution) of the DEM is Δx and Δy in the east-west and north-south direction, respectively [94].

z_1	z_2	z_3
z_4	z_5	z_6
z_7	z_8	z_9

Figure 2.20: Labelling of DEM grid cells surrounding the cell of interest. The eight surrounding cells are used for estimating topographic parameters in QGIS. The cell of interest, which is located at row i and column j of the DEM, is shown as a shaded cell and is labelled z_5 .

Curvature

Curvature describes the convexity or concavity of a surface. The curvature of a surface is different in different directions, so there are various types of curvature. Profile and tangential curvature are the most common types to consider in geophysical systems. For this study, the mean curvature (κ), found by taking the average of profile and tangential curvature, is used. The mean curvature emphasizes mean-concave (positive values) areas with relative accumulation and mean-convex (negative values) terrain with relative scouring [96].

Profile curvature is the curvature in the direction of the surface gradient and it describes the change in slope angle. The equation for profile curvature (κ_p [m^{-1}]) is [94]

$$\kappa_p = \frac{\frac{\partial^2 z}{\partial x^2} \left(\frac{\partial z}{\partial x}\right)^2 + 2 \frac{\partial^2 z}{\partial x \partial y} \frac{\partial z}{\partial x} \frac{\partial z}{\partial y} + \frac{\partial^2 z}{\partial y^2} \left(\frac{\partial z}{\partial y}\right)^2}{\left[\left(\frac{\partial z}{\partial x}\right)^2 + \left(\frac{\partial z}{\partial y}\right)^2\right] \sqrt{\left[\left(\frac{\partial z}{\partial x}\right)^2 + \left(\frac{\partial z}{\partial y}\right)^2 + 1\right]^3}} \quad (2.3)$$

where first-order partial derivatives are found using Equation 2.2. Second-order partial derivatives can be approximated by [58, 94]

$$\begin{aligned} \frac{\partial^2 z}{\partial x^2} &\approx \frac{z_1 - 2z_2 + z_3 + 4z_4 - 8z_5 + 4z_6 + z_7 - 2z_8 + z_9}{6(\Delta x)^2}, \\ \frac{\partial^2 z}{\partial y^2} &\approx \frac{z_1 - 4z_2 + z_3 - 2z_4 - 8z_5 - 2z_6 + z_7 + 4z_8 + z_9}{6(\Delta y)^2}, \\ \frac{\partial^2 z}{\partial x \partial y} &\approx \frac{(z_7 - z_9) - (z_1 - z_3)}{4\Delta x \Delta y}. \end{aligned} \quad (2.4)$$

Tangential Curvature represents the curvature in the direction of the contour tangent. The equation for profile curvature (κ_t [m^{-1}]) is [94]

$$\kappa_t = \frac{\frac{\partial^2 z}{\partial x^2} \left(\frac{\partial z}{\partial y}\right)^2 - 2 \frac{\partial^2 z}{\partial x \partial y} \frac{\partial z}{\partial x} \frac{\partial z}{\partial y} + \frac{\partial^2 z}{\partial y^2} \left(\frac{\partial z}{\partial x}\right)^2}{\left[\left(\frac{\partial z}{\partial x}\right)^2 + \left(\frac{\partial z}{\partial y}\right)^2\right] \sqrt{\left[\left(\frac{\partial z}{\partial x}\right)^2 + \left(\frac{\partial z}{\partial y}\right)^2 + 1\right]}}, \quad (2.5)$$

where first- and second-order partial derivatives are approximated using Equation 2.2 and 2.4.

“Northness”

“Northness” (N) is a solar radiation parameter that has been shown to increasingly affect accumulation distribution during the spring [105]. It is also likely that this parameter may be related to sun induced snow metamorphosis and/or sun crusts, both of which affect SWE [83]. “Northness” (N) is defined as the product of the cosine of aspect and sine of slope [88]. A value of -1 represents a vertical, south facing slope, a value of +1 represents a vertical, north facing slope, and a flat surface yields 0.

Aspect

Aspect (α) represents the orientation of the steepest slope, with 0° defined as North and no value given to cells that have zero slope. The equation for aspect in degrees is [94]

$$\alpha = \arctan\left(\frac{\partial z}{\partial y} / \frac{\partial z}{\partial x}\right), \quad (2.6)$$

where the partial derivatives are approximated by Equations 2.2. Here, $\alpha = 0$ is in the west direction but the computed values were transformed to reflect 0° as north (clockwise).

Aspect is a circular parameter (0° is the same as 360°) but regressions (Section 4.1) require that a parameter is linear. Therefore, only the sine of aspect was used in topographic analysis. The sine of aspect is representative of the relative amount of direct solar radiation incident on a slope, which can affect SWE by metamorphosis of snow.

Sx

Sx represents wind exposure/shelter and is based on selecting a cell within a certain angle and distance from the cell of interest that has the greatest upward slope relative to the cell of interest [130]. This cell is referred to as the maximum upwind slope. Negative Sx values represent exposure relative to the shelter-defining pixel, which means that the cell of interest is higher than the cell with greatest upward slope. Conversely, positive values represent sheltered cells. To determine Sx values, we use the equation

$$Sx_{A,d\max}(x_i, y_i) = \max \left[\tan^{-1} \left(\frac{z(x_v, y_v) - z(x_i, y_i)}{[(x_v - x_i)^2 + (y_v - y_i)^2]^{1/2}} \right) \right], \quad (2.7)$$

where A is the azimuth of the search direction, (x_i, y_i) are the coordinates of the cell of interest, and (x_v, y_v) are the set of all cell coordinates located along the search vector defined by (x_i, y_i) , the azimuth (A), and maximum search distance ($d\max$). Code for this calculation was provided by Adam Winstral (2016, personal communication). As done by [83], we compute Sx at 5° azimuth increments for $d\max$ distances of 100, 200 and 300 m. These values are then correlated (Pearson correlation) with observed values of SWE and the Sx values from the combination of azimuth and $d\max$ input values that have the highest correlation are used for subsequent analysis (Table 2.6). The code for calculating Sx requires a UTM raster formatted to ASCII in ArcGIS.

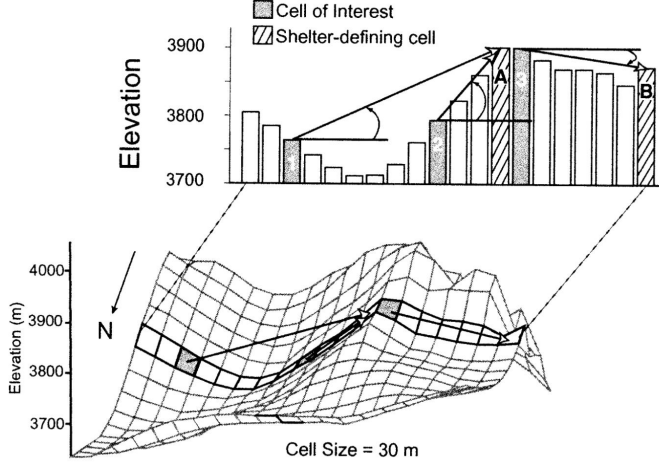


Figure 2.21: Image and description from [130]. Example of Sx calculations for three cells of interest along a 270° search vector. As depicted, with d_{\max} set equal to 300 m, the shelter-defining pixel for cells 1 and 2 is cell A, producing positive Sx values. The shelter-defining cell for cell 3 is cell B, producing a negative Sx. Had d_{\max} been equal to 100 m, the search for the shelter-defining pixel for cell 1 would not extend across the valley, thus producing a negative Sx for cell 1, while Sx for cell 2 would remain the same and that for cell 3 would be slightly lower.

Table 2.6: Values of azimuth (A) and maximum search distance (d_{\max}), that correspond to the Sx that had the highest absolute correlation to observed SWE.

	A ($^\circ$ from North)	d_{\max} (m)	Correlation Coefficient
Glacier 4	85	300	-0.26
Glacier 2	330	300	0.56
Glacier 13	280	200	0.28

2.4.3 DEM smoothing

Visual inspection of the curvature fields calculated using the DEM showed noisy spatial distribution that did not vary smoothly. [96] states that the curvature calculation is sensitive to noisy data and a smoothing filter often needs to be applied to the DEM prior to calculation. Curvature, as well as slope, aspect and “northness”, are all sensitive to noise because calculating these parameters involves calculating the first and second derivatives of the elevation, which are highly dependent on the size of the DEM cell. To minimize the effect of noise on these four parameters, a smoothing filter was applied to the DEM and this smoothed DEM was used to calculate curvature, slope, aspect and “northness”. The non-smoothed DEM was used to determine elevation and Sx because these parameters do not depend on a topographic length scale and their values are not sensitive to the size of the DEM cell size.

To choose a smoothing algorithm and window size, a number of smoothing algorithms was applied and the one that resulted in topographic parameters that had the highest correlation with SWE was chosen. Window sizes of 3×3 , 5×5 , 7×7 and 9×9 were used. For all sizes, inverse-distance weighted smoothing and Gaussian smoothing were poorly correlated with SWE. An average value smoothing with a 7×7 window resulted in the highest correlation between curvature (second derivative) and SWE as well as slope (first derivative) and SWE. The window size that produced the highest correlation of SWE values and curvature for each glacier differed, but for all SWE values taken together, the 7×7 window resulted in the highest correlation. For slope, the highest correlation for individual glaciers was from the DEM with a 7×7 smoothing window but the overall correlation was not the highest with this window. To maintain consistency between parameters, the 7×7 smoothing window was chosen and applied to the DEM for calculation of curvature, slope, aspect and “northness”.

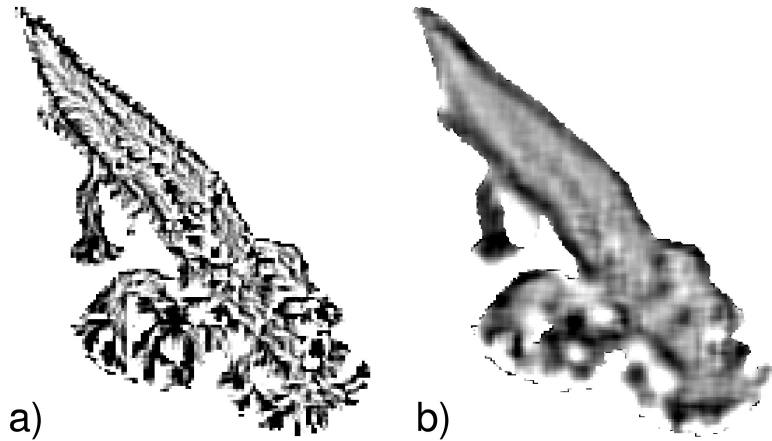


Figure 2.22: Curvature found using the orginal DEM (a) and the smoothed (7×7 window moving average) DEM (b).

2.4.4 Parameter correlations

The correlation between topographic parameters at sampling locations on each glacier is shown in Table 2.7. Correlation values are generally low, with the exception of the correlation between northness and aspect on Glacier 2 and northness and Sx on Glacier 13, which were both larger than 0.7. Since there is little correlation between parameters and the correlations vary between glaciers, the use of a linear regression with these topographic parameters as predictor variables is warranted.

Table 2.7: Pearson correlation coefficients between topographic parameters at sampled locations. Topographic parameters are distance from centreline (d_C), elevation (z), aspect (α), slope (m), northness (N), curvature (κ), and Sx.

	z	d_C	α	m	N	κ	Sx	
Glacier 4	z	1	0.16	-0.57	-0.08	-0.51	0.17	0.43
	d_C		1	0.13	0.56	0.16	-0.43	0.35
	α			1	0.57	0.95	-0.61	-0.58
	m				1	0.64	-0.58	-0.10
	N					1	-0.59	-0.59
	κ						1	0.05
	Sx							1
Glacier 2	z	1	0.06	-0.52	-0.58	-0.62	0.45	0.57
	d_C		1	0.06	0.13	0.11	-0.27	0.01
	α			1	0.33	0.86	-0.42	-0.45
	m				1	0.74	-0.67	-0.41
	N					1	-0.67	-0.48
	κ						1	0.28
	Sx							1
Glacier 13	z	1	0.15	0.19	-0.15	0.10	0.02	0.27
	d_C		1	-0.05	0.18	0.10	-0.45	0.06
	α			1	-0.07	0.68	<0.01	0.45
	m				1	0.63	-0.22	-0.22
	N					1	-0.21	0.23
	κ						1	-0.30
	Sx							1

2.4.5 Maps of topographic parameters and distribution of parameters sampled

Elevation maps (Figure 2.23) show that both Glacier 2 and 13 have small areas with high elevation, which correspond to steep headwalls. Mean elevation is the same for all glaciers for the full and sampled distribution within one standard deviation (Table 2.8). However, maximum elevation values are lower for Glacier 4 than the other two glaciers (Figure 2.24) and the sampled elevation means are approximately 200 m less than that of the full distribution. Standard deviations are smaller for sampled ranges for all glaciers. The skewness of sampled and full distributions is different for all glaciers. Elevation full distributions are similar for the study glaciers, with kurtosis for all distributions, except sampled elevation on Glacier 13, being less than 3 (value for normal distribution). Kurtosis of sampled dis-

tributions show that Glacier 13 had a broader distribution and Glacier 2 has a narrower distribution.

The distribution of sampled distance from centreline (Figure 2.26) is different from that of the full distribution. Generally, large distances were not sampled. Larger values of skewness and kurtosis in the full distribution indicate that these distributions are broader and span a larger range of values (Table 2.8). This is also seen in the mean and standard deviation values, which are also larger for the full distribution. Large values of distance from centreline are located at the edges of the glacier in the accumulation area (Figure 2.25), which constitute steep, inaccessible terrain. Within the ablation area, the hourglass sampling pattern allowed for locations across the whole width of the glacier to be measured. Note that Glacier 13 has two centrelines in the accumulation area because of the confluence of two major arms of the glacier.

The aspect of Glaciers 2 and 13 indicate that the majority of these two glaciers is north facing, while the majority of Glacier 4 is south facing (Figure 2.27). This is also highlighted in the mean values of aspect, which are positive for Glaciers 2 and 13 and negative for Glacier 4 (Table 2.8). Sampled mean aspect is similar to the full distribution, although the standard deviation of sampled aspects is much lower. Further, the skewness and kurtosis of the sampled distributions differs considerably from the full distribution and there are many aspects that were not sampled (Figure 2.28).

Slope of the three study glaciers (Figure 2.29) is generally less than 20° , with only the margins of the accumulation area and a few steps on Glacier 13 having steep slopes. The full and sampled distributions of slope are similar between glaciers (Table 2.8), with mean values of $\sim 13^\circ$ for the full distribution and 5° to 8° for the sampled distribution. The sampled distributions are all different than the full range, as indicated by the lower means, standard deviations, and skewness, as well as larger kurtosis. This shows that the sampled distributions are generally narrower than full distributions and severely under sample steep slopes (Figure 2.30).

The mean “northness” values for all glaciers were close to zero and the majority of cells have values close to zero, which is likely due to their low slope values (Figure 2.31). Even for Glacier 4, which is largely south facing and should thus have lower values of “northness”, has a distribution with a mean close to zero (Table 2.8). The low slope values mean that the values of “northness” were determined largely by the aspect, which can be seen by the resemblance between the “northness” map and the aspect map and their high correlation (Table 2.7). Sampled distributions of “northness” did not resemble the full distributions. Although the mean values were similar, the skewness and kurtosis values were higher for all glaciers, indicating that the sampling was biased.

Curvature values on all glaciers are largely negative, indicating that concave topography is more prevalent than convex topography (Figures 2.33 and 2.34). The sampled distribution of curvature is a poor representation of the full distribution as shown by the dramatically

different values of skewness, which are positive for the full distribution and negative for the sampled distribution (Table 2.8).

S_x maps over the study glaciers are shown in Figure 2.35 and the wind direction and maximum search distance with the highest correlation to SWE for each glacier are shown in Table 2.6. For Glacier 4, an approximately east wind and 300 m search distance were most strongly correlated. The correlation was negative, which means that negative values of S_x (exposure) correspond to areas with larger SWE (more snow). This is counter intuitive and perhaps indicates that S_x is not an appropriate topographic parameter to correlate with SWE on Glacier 4. Despite this, S_x was retained in future analysis for consistency between glaciers. For Glacier 2, a north wind with a 300 m search distance was most strongly correlated and for Glacier 13, a west wind with a 200 m search distance produced the strongest correlation. Both of these correlations were positive, so a more positive S_x value (sheltered) corresponds to higher values of SWE (more snow). The correlation values for Glacier 4 and 2 are low (<0.3) which indicates that S_x will likely be insignificant in estimating snow accumulation. The correlation between S_x and SWE on Glacier 2 is higher at 0.56.

The full distribution of S_x (Figure 2.36) is different for each glacier and differs greatly between sampled and full distributions. Glacier 2 has a mean less than zero, indicating that a large portion of the glacier has exposed topography (Table 2.8). Glacier 4 and 13 have positive mean values of S_x , indicating more sheltered topography. Extreme values of S_x are generally located along the edges of the accumulation areas (Figure 2.35). The sampled distribution mean for Glacier 2 is close to that of its full distribution, while the sampled distribution means of Glacier 4 and 13 are different (negative) than that of the full distribution means (positive). The sampled distribution are more sharply peaked, as indicated by the smaller standard deviation values and larger kurtosis when compared to the full distributions. The skewness also differs for Glaciers 4 and 2, with the sampled distributions skewed more to the right than full distributions. Overall, the sampled distribution of S_x is a poor representation of the full distribution.

Overall, the sampled topographic parameters are poor representatives of the full distribution of parameters. Extreme values of all parameters are grossly under sampled and the distribution of the sampled parameters generally differs from the full distribution. This was largely do to dangerous travel conditions and an inability to quickly and accurately measure snow depth in the accumulation area. As a result, extrapolation of regression models will likely result in large errors. These errors are especially relevant in the accumulation area, which has extreme values for all parameters. Errors in the accumulation area are especially important to acknowledge because this area has the highest values of SWE and is likely to heavily influence final winter mass balance values. Improvements to this study could include using an air-borne GPR to collect a dense network of SWE measurements in difficult to access areas [e.g. 83] (see Section 1.3.2 for more details). Generally, the sampled values do

not fully capture the variance in topographic parameters but a regression is still valuable since topographic regressions are common when estimating winter mass balance. Acknowledging that this methodology is limited and prone to extrapolation errors is paramount to capturing uncertainty in accumulation studies.

Table 2.8: Descriptive statics of topographic parameter full and sampled distribution. Mean and standard deviation are in units of meters for distance from centreline (d_C) and elevation (z), in units of m^{-1} for profile (κ_P) and tangential (κ_T) curvature, and are unitless for cosine of aspect (α), “northness” (N), slope (m), and Sx. Skewness is a measure of the data asymmetry about the mean, with positive values indicating data that are more spread to the right of the mean and zero indicating a perfectly symmetric distribution. Kurtosis is a measure of how prone a distribution is to outliers. A normal distribution has a kurtosis value of 3 and larger values indicate distributions that are more prone to outliers.

		Full			Sampled		
		Mean	Standard Deviation	Skewness	Kurtosis	Mean	Standard Deviation
Glacier 4	z	2343.76	178.36	-0.17	2.13	2242.63	89.52
	d_C	258.95	233.49	1.82	6.52	124.33	89.56
	α	-0.35	0.61	0.75	2.23	-0.37	0.53
	m	12.81	7.03	1.11	3.37	8.32	3.17
	N	-0.05	0.17	0.52	4.04	-0.04	0.10
	κ	-53.32	70.30	0.76	7.81	-33.34	38.33
	Sx	1.56	11.46	1.03	4.28	-1.06	5.17
Glacier 2	z	2494.71	233.03	0.09	2.82	2306.90	93.74
	d_C	304.95	236.97	1.22	4.51	140.65	98.84
	α	0.59	0.43	-1.43	4.83	0.52	0.33
	m	13.02	9.48	1.08	3.00	6.54	2.24
	N	0.14	0.16	0.74	3.68	0.06	0.05
	κ	-18.40	91.35	1.30	6.83	-22.94	43.91
	Sx	-3.82	9.34	-0.18	6.09	-3.63	2.59
Glacier 13	z	2427.62	225.15	0.13	2.45	2219.45	82.25
	d_C	443.88	308.48	0.76	3.21	181.91	152.29
	α	0.55	0.49	-1.30	3.89	0.69	0.28
	m	13.36	10.13	1.15	3.51	5.10	1.98
	N	0.13	0.18	1.01	4.02	0.06	0.04
	κ	-13.31	89.16	1.24	6.65	-6.93	32.44
	Sx	3.69	12.08	0.97	3.68	-1.62	3.94

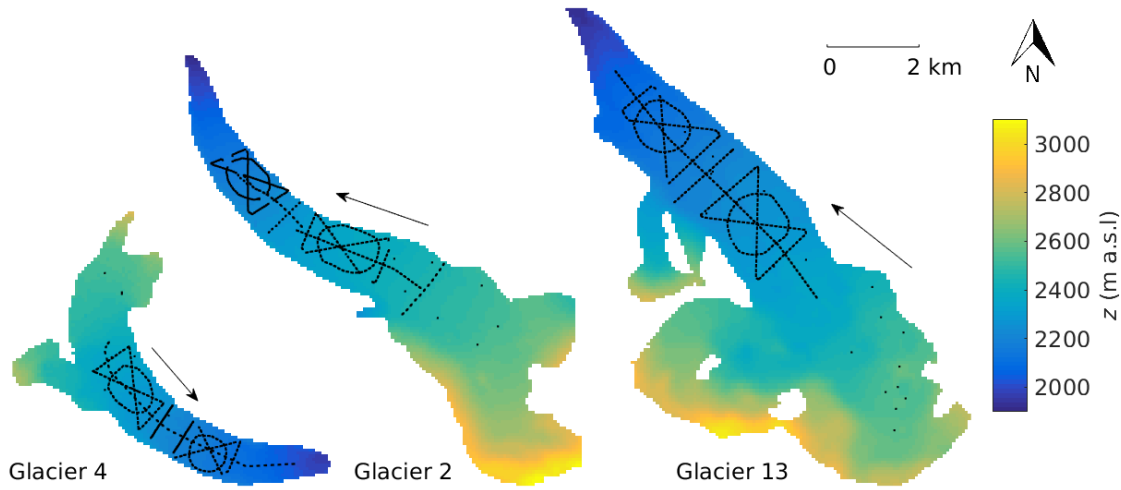


Figure 2.23: Distributions of elevation (z) used in the topographic regressions for the study glaciers. This DEM is derived from a SPOT5 satellite image and has a grid size of 40×40 m. Subsequent topographic parameters were derived from this DEM. Arrows indicate glacier flow direction and black dots show snow depth sampling locations.

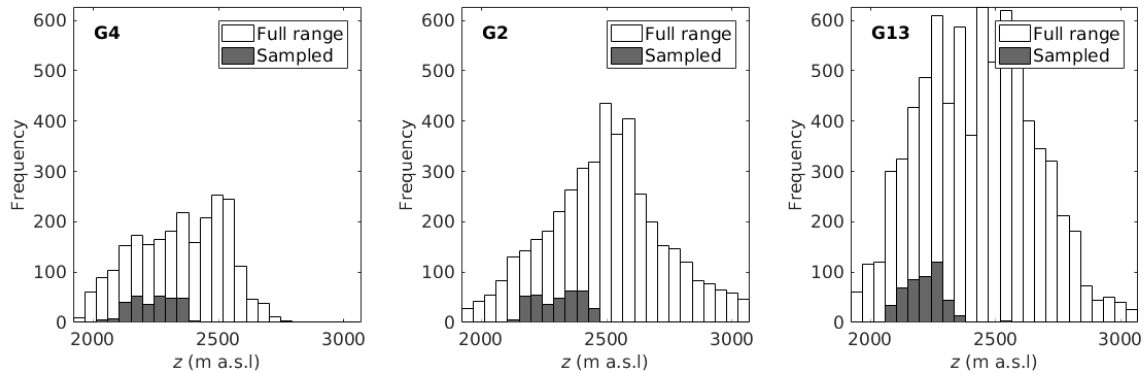


Figure 2.24: Histograms of elevation (z) sampled (black) as compared to total range of elevation (white) of study glaciers.

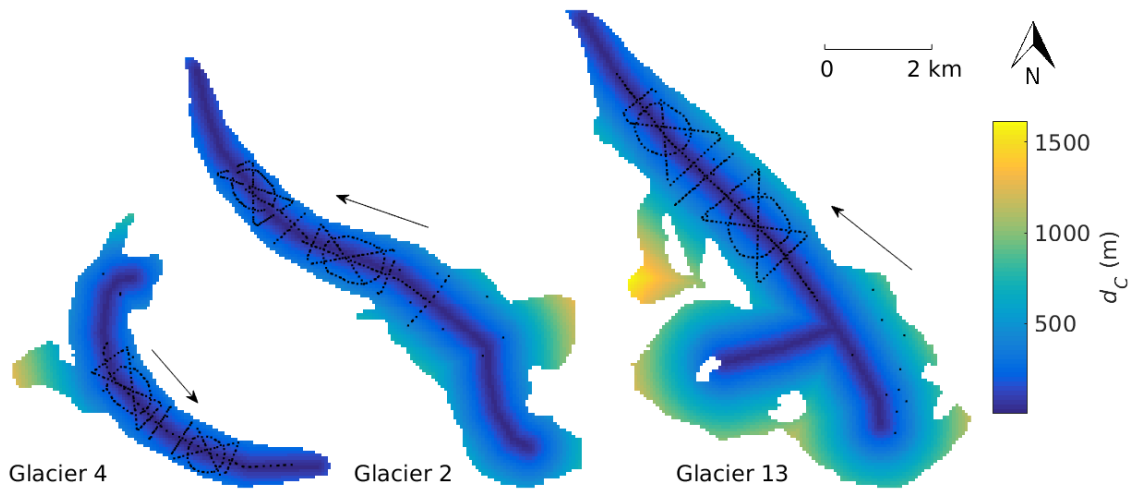


Figure 2.25: Distributions of distance from centreline (d_C) used in the topographic regressions for the study glaciers. Centreline was drawn by hand in QGIS. Arrows indicate glacier flow direction and black dots show snow depth sampling locations.

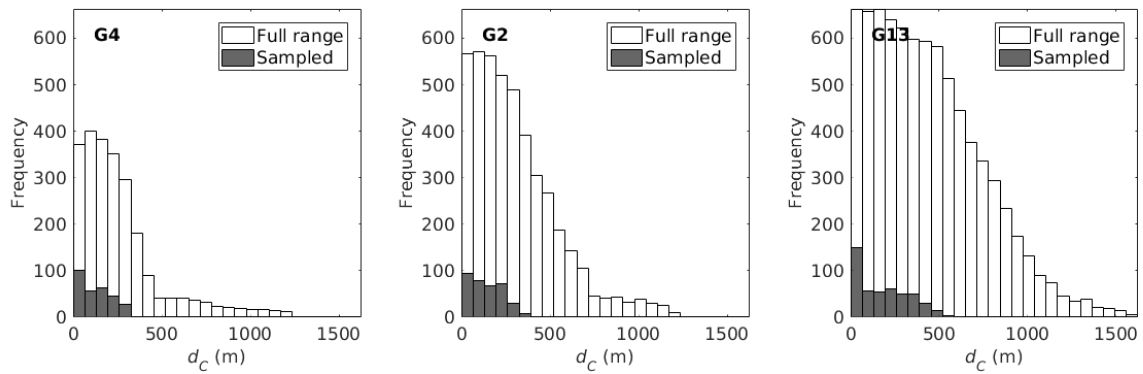


Figure 2.26: Histograms of distance from centreline (d_C) sampled (black) as compared to total range (white) of distance from centreline of study glaciers.

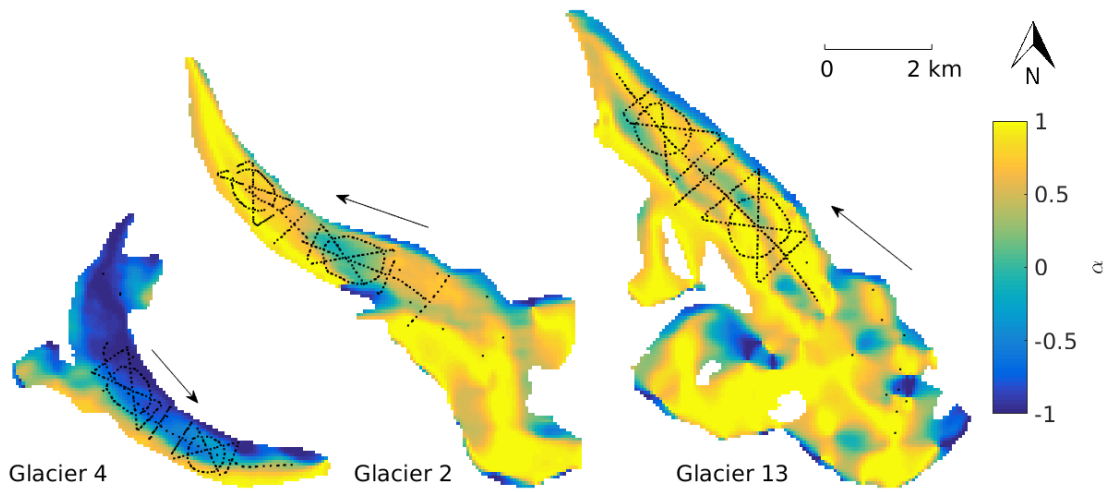


Figure 2.27: Distributions of the sine of aspect (α), which indicates north-south component of a slope (+1 defined as north), used in the topographic regressions for the study glaciers. Values are derived from a smoothed DEM. Arrows indicate glacier flow direction and black dots show snow depth sampling locations.

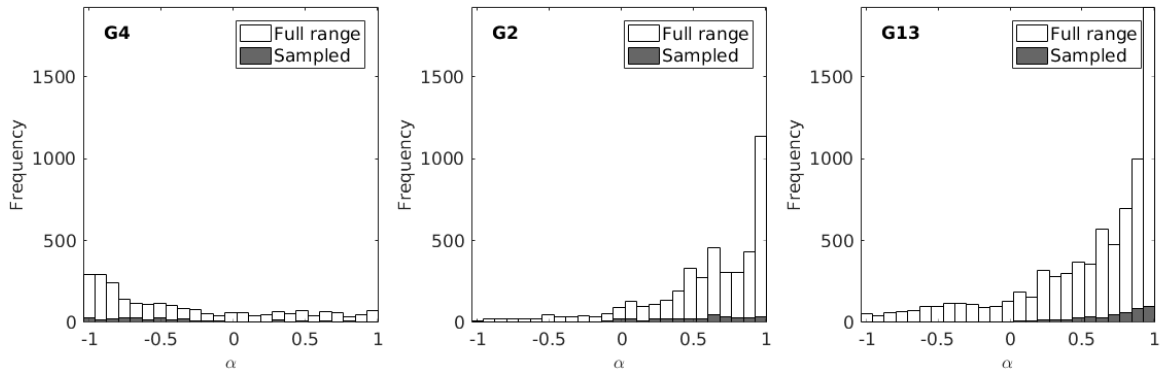


Figure 2.28: Histograms of aspect (α) sampled (black) as compared to total range (white) of aspect of study glaciers.

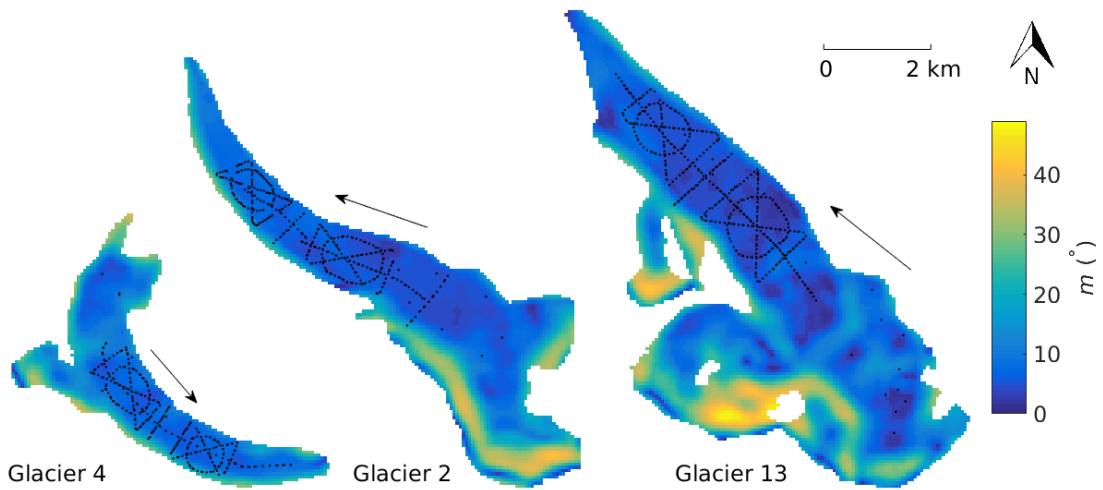


Figure 2.29: Distributions of slope (m) used in the topographic regressions for the study glaciers. Values were derived from a smoothed DEM (grid size of 40×40 m) in QGIS. Arrows indicate glacier flow direction and black dots show snow depth sampling locations.

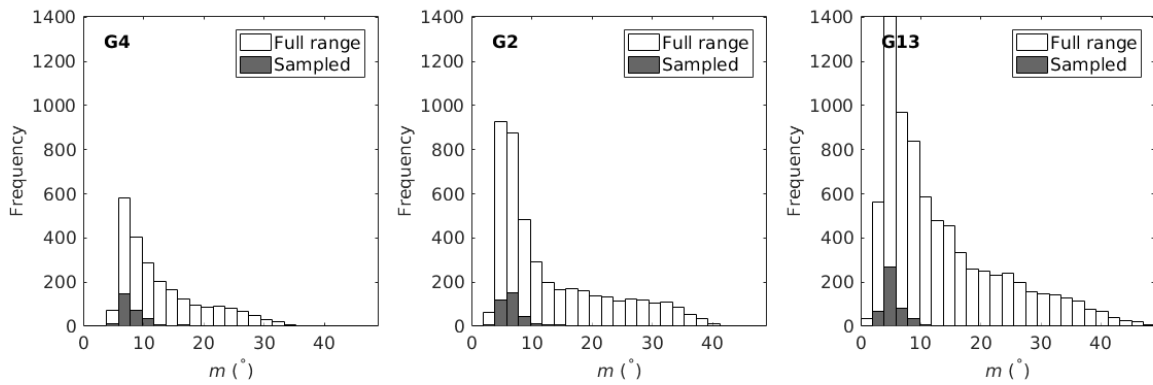


Figure 2.30: Histograms of slope (m) sampled (black) as compared to total range (white) of slope of study glaciers.

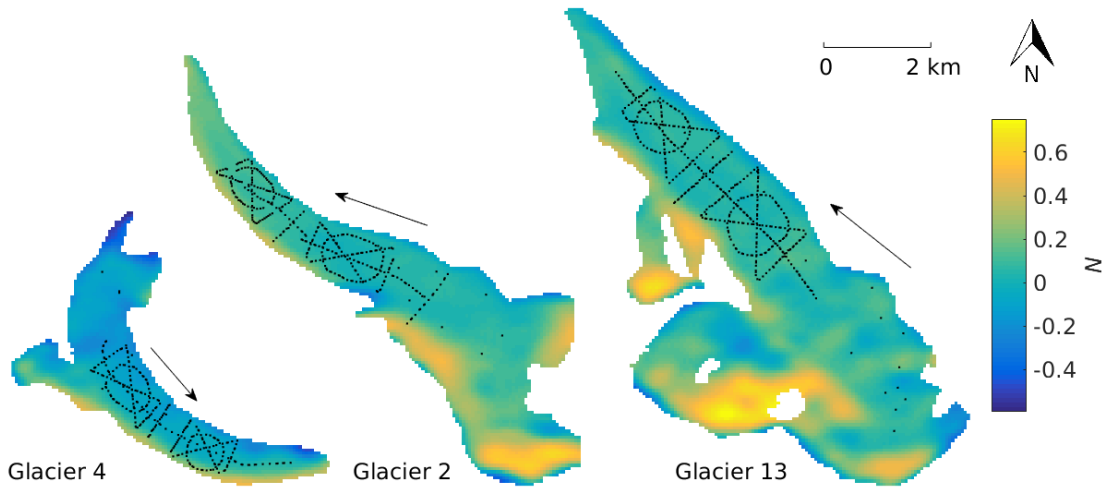


Figure 2.31: Distributions of “northness” (N) used in the topographic regressions for the study glaciers. “Northness” is defined as the product of the cosine of aspect and sine of slope. A value of -1 represents a steep, south facing slope, a value of +1 represents a steep, north facing slope, and flat surfaces yield 0. Values were derived from a smoothed DEM (grid size of 40×40 m) in QGIS. Arrows indicate glacier flow direction and black dots show snow depth sampling locations.

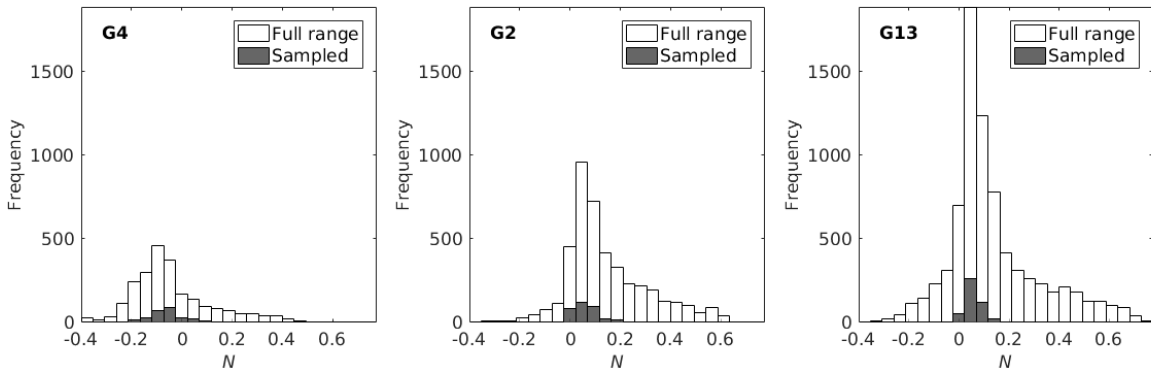


Figure 2.32: Histograms of “northness” (N) sampled (black) as compared to total range (white) of “northness” of study glaciers.

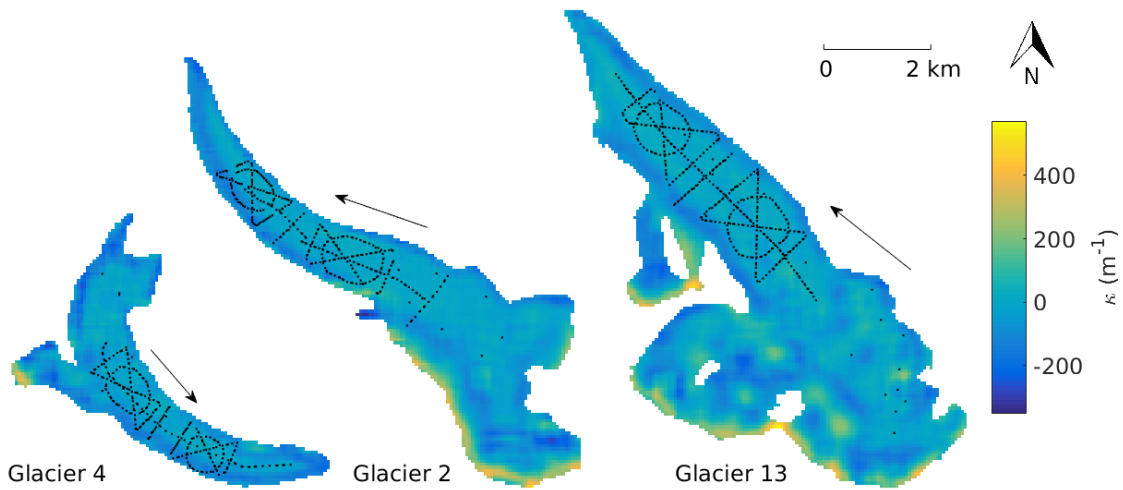


Figure 2.33: Distributions of curvature (κ) used in the topographic regressions for the study glaciers. Values were derived from a smoothed DEM (grid size of 40×40 m) in QGIS. Colour axis has been scaled to better resolve values close to zero. Arrows indicate glacier flow direction and black dots show snow depth sampling locations.

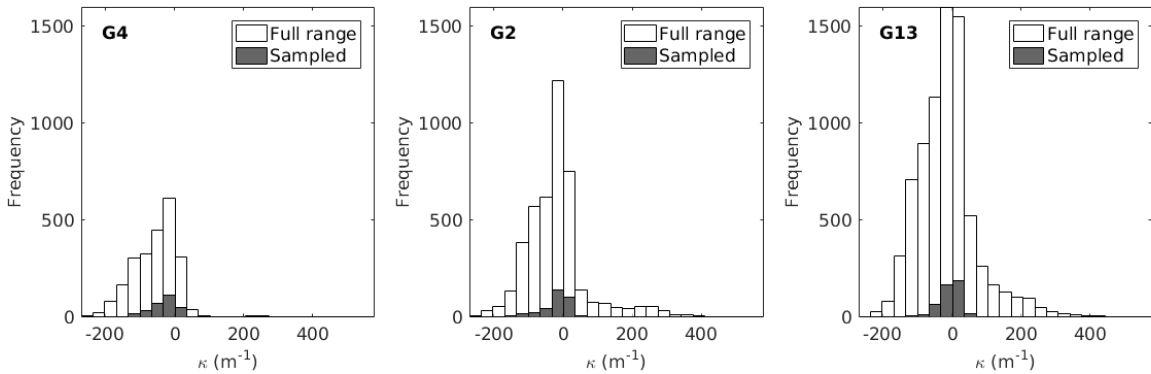


Figure 2.34: Histograms of curvature (κ) sampled (black) as compared to total range (white) of profile curvature of study glaciers.

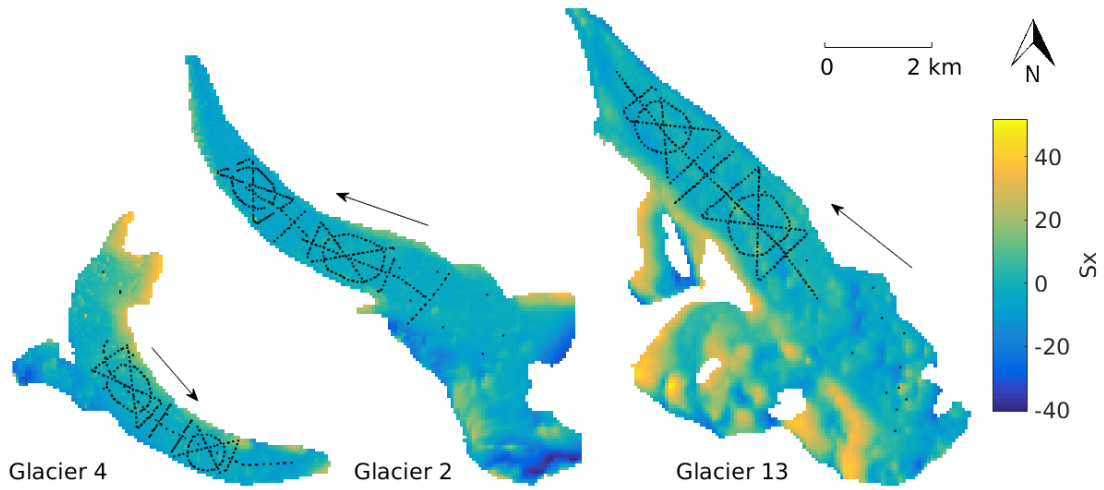


Figure 2.35: Distributions of S_x , which is a wind redistribution parameter, used in the topographic regressions for the study glaciers. See section 2.4.2 and the original paper by [130] for more details on calculation. See Table 2.6 for values of best correlated azimuth and maximum search distance for each glacier. Arrows indicate glacier flow direction and black dots show snow depth sampling locations.

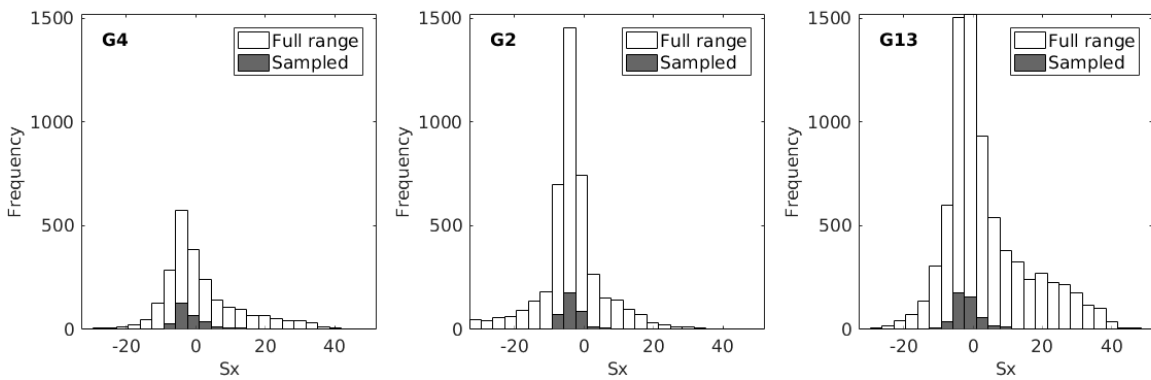


Figure 2.36: Histograms of S_x sampled (black) as compared to total range (white) of S_x of study glaciers.

2.5 Summary

Within this chapter, we describe the design and implementation of a snow survey on three glaciers as well as the initial data processing. The processing resulted in snow depth measurements at estimated transect measurement locations and extensive grid cell snow depth measurements obtained using zigzag snow surveys. Snow density values measured using a wedge cutter in snow pits as well as using a Federal Sampler are also presented. A number of methods used for interpolation of density values to obtain SWE values are then described.

The resultant data consists of eight different variations of SWE values at all measurement locations, each one calculated using a different density interpolation option. We also document the process of obtaining topographic parameters, which include elevation, slope, curvature, distance from centreline, aspect, “northness”, and wind redistribution, from a given DEM of the study area.

Chapter 3

Sampling

The sampling component of this thesis focuses on presenting observations from collected snow depth and density data. Basic statistics are used to examine variability snow depth at multiple scales as well as relationships between measured values. Section 3.1

3.1 Density

3.1.1 Basic statistics

The standard deviation of each type of density measurement is less than 10% of the mean density (Table 2.4). For snowpit derived densities, the mean density is within one standard deviation between glaciers. The densities estimated using the Federal Sampler differed between glacier within one standard deviation. Our density measurements on Glacier 2 were lower than those on Glacier 4, while density measurements taken on Glacier 13 were the same as Both Glaciers 2 and 4. The mean of all Federal Sampler derived density values was skewed by the proportionally large number of measurements obtained on Glacier 13.

3.1.2 Federal Sampler measurements and snow depth

There is a positive linear relation ($R^2 = 0.59$, $p < 0.01$) between measured snow density and depth for all Federal Sampler measurements (Figure 3.1). This positive relationship could be a result of physical processes, such as compaction, and/or artefacts during data collection; however, it seems more likely that this trend is a result of measurement artefacts for a number of reasons. First, the range of densities measured by the Federal sampler is large (225–410 kg m⁻³) and the extreme values seem unlikely to exist at these study glaciers, which experience a continental snowpack with minimal mid-winter melt events. Previous unpublished density measurements taken on Glacier 2 for five study years have a mean snow density of 298 kg m⁻³ and a standard deviation of 48 kg m⁻³ (range of 264–396 kg m⁻³ with a maximum density difference of 110 kg m⁻³ in any one year) (Flowers, 2016, personal communication). Second, compaction effects would likely be small at these study glaciers because of the relatively shallow snowpack (deepest measurement was 340 cm). Third, no

linear relationship exists between depth and snowpit-derived density ($R^2 = 0.05$) as can be seen in a plot of the depth-density relationship in snowpits in Figure 3.1. Together, these reasons lead us to conclude that the Federal Sampler measurements are biased. Linear detrending can correct the density data but it was decided to use uncorrected data for future analysis.

The Federal Sampler appears to oversample in deep snow and undersample in shallow snow. Oversampling by small diameter (area of 10–12 cm²) sampling tubes has been observed in previous studies, with a percent error between +6.8% and 11.8%[135, 40, 26]. Studies that use Federal Samplers often apply a 10% correction to all measurements [e.g. 88]. [34] attributed oversampling to slots “shaving” snow into the tube as it is rotated as well as cutter design forcing snow into the tube. [10] found that only when snow samples had densities greater than 400 kg m⁻³ and snow depth greater than 1 m, the Federal Sampler oversampled due to snow falling into the greater area of slots. Undersampling is likely to occur due to snow falling out of the bottom of the sampler [118]. It is likely that this occurred during our study since a large portion of the lower elevation snow on both Glaciers 2 and 13 was melt affected and thin, allowing for easier lateral displacement of the snow as the sampler was inserted. For example, on Glacier 13 the snow surface had been affected by radiation melt (especially at lower elevations where the snow was shallower) and the surface would collapse when the sampler was inserted into the snow. It is also difficult to measure the weight of the sampler and snow with the spring scale when there was little snow because the weight was at the lower limit of what could be detected by the scale.

3.1.3 Density uncertainties

Snowpit densities

Uncertainty in estimating density from snowpits stems from measurement errors and incorrect assignment of density to layers that could not be sampled (i.e. ice lenses and ‘hard’ layers). To determine a possible range of snowpit-derived integrated snow density values, the original data are used and three quantities are varied. Ice layer density is varied between 700 and 900 kg m⁻³, ice layer thickness is varied by ± 1 cm of the observed thickness, and the density of layers identified as being too hard to sample (but not ice) was varied between 600 and 700 kg m⁻³.

The range of integrated density values is always less than 15% of the reference density, with the largest ranges present on Glacier 2 (Table 3.1). Density values for shallow pits that contained ice lenses were particularly sensitive to changes in density and ice lens thickness.

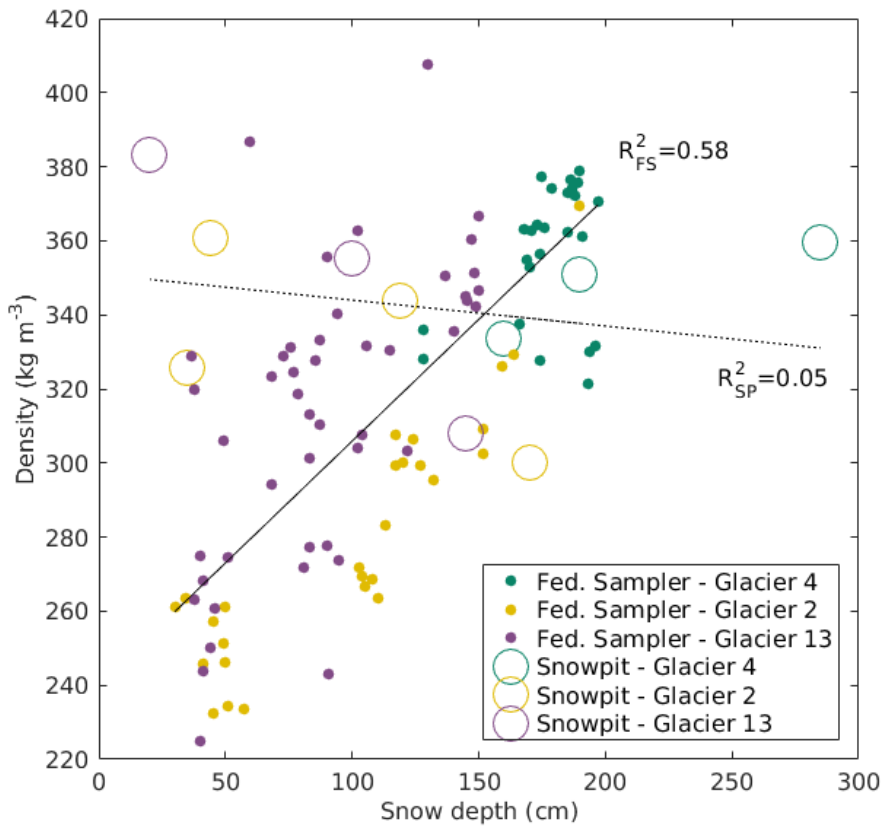


Figure 3.1: Relationship between measured density and snow depth for all Federal Sampler and snowpit locations. A linear regression of depth and density for Federal Sampler (FS) measurements is shown as a solid line and for snowpits (SP) is shown as a dashed line.

Table 3.1: Summary of reference and range of integrated snow density calculated from snowpit measurements. The reference density values are calculated with an ice layer density of 917 kg m⁻³ and a ‘hard’ snow density of 600 kg m⁻³. To determine the error in estimating integrated snow density, ice thickness, and the ‘hard’ layer density are varied between 700 and 917 kg m⁻³, ± 1 cm, and 500 and 600 kg m⁻³, respectively.

Snowpit Name	Depth (m)	Density (kg m ⁻³)			Range as % of reference value	Elevation (m a.s.l.)	Average Temperature (°)
		Reference	Minimum	Maximum			
Glacier 4, Lower	190	350.9	343.2	359.1	15.9	4.5	2154 – 4.3
Glacier 4, Upper	160	333.4	316.6	349.6	33.0	9.9	2298 – 5.7
Glacier 4, Accumulation	285	359.7	356.6	362.4	5.8	1.6	2482 – 6.8
Glacier 2, Lower	44	360.9	328.6	377.3	48.7	13.5	2175 – 3.7
Glacier 2, Zone 4A	35	325.8	307.9	344.7	36.8	11.3	2261 – 3.4
Glacier 2, Upper	119	344.0	327.1	361.9	34.8	10.1	2349 – 6.6
Glacier 2, Accumulation	170	300.2	298.6	303.1	4.5	1.5	2550 – 7.4
Glacier 13, Lower	20	383.0	383.0	383.0	0	0	2139 – 0.1
Glacier 13, Upper	100	355.4	345.6	366.9	21.3	6.0	2257 – 1.7
Glacier 13, Accumulation	145	307.8	306.4	308.2	1.8	0.6	2521 – 5.6

Federal Sampler densities

Mean Federal Sampler derived density has a larger range of values over the study glaciers when compared to snowpit densities (Table 3.2). The percent range is also larger than snowpit densities for many of the measurement locations.

3.1.4 Comparing density from snowpit and Federal Sampler measurements

To compare snowpit-derived densities and Federal Sampler-derived densities, eight Federal Sampler measurements were taken around two snowpit locations on each study glacier. The overall range of Federal Sampler-derived densities is larger than that of the snowpit-derived density values (Figure 3.2). Within the minimum and maximum snowpit-derived densities, the values are indistinguishable for all snowpit locations, except for the accumulation snowpit on Glacier 13 ('G13_ASP').

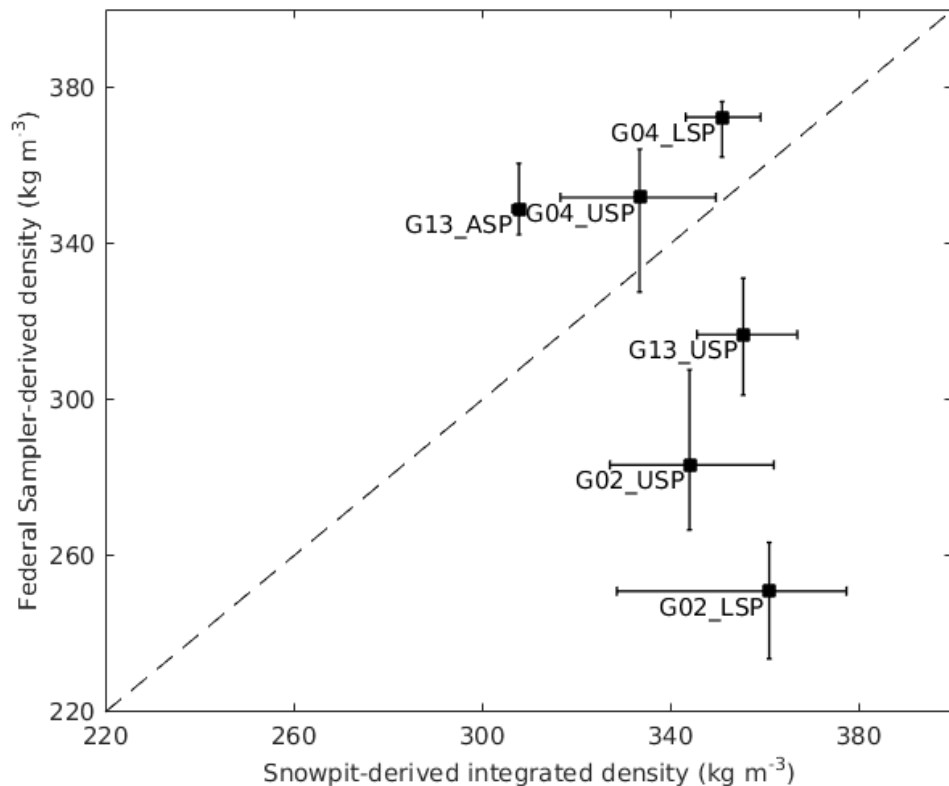


Figure 3.2: Comparison of integrated density estimated using wedge cutters in a snowpit and density estimated using Federal Sampler measurements for Glacier 4 (G04), Glacier 2 (G02) and Glacier 13 (G13). Error bars are minimum and maximum values for each estimate as reported in Table 3.1 and 3.2.

Table 3.2: Range of densities estimated from Federal Sampler measurements. The number (n) of reliable measurements, as well as the minimum, maximum, and mean density are shown. The density range, given as a percent of the mean density, is also shown. Location refers to the snowpit name as shown in Figure 2.9.

Location	<i>n</i>	Density (kg m⁻³)			Range as % of mean (%)	Elevation (m a.s.l)
		Mean	Minimum	Maximum		
G04_Z3A_SWE	3	334	309	358	14	2229
G04_USP	6	311	274	353	22	2298
G04_Z2A_SWE	3	360	303	431	35	2162
G04_LSP	7	272	250	297	13	2154
G04_Z5B_SWE	2	337	324	350	7	2360
G04_Z5A_SWE	3	311	275	351	21	2328
G04_Z5C_SWE	2	361	350	373	6	2332
G02_Z5C_SWE	2	296	245	347	28	2332
G02_USP	7	294	232	353	34	2349
G02_Z7A_SWE	3	326	304	349	12	2403
G02_Z7B_SWE	2	336	320	351	9	2458
G02_Z7C_SWE	3	351	338	365	7	2442
G02_Z3B_SWE	3	349	341	353	3	2172
G02_LSP_SWE	7	331	302	349	13	2175
G13_ASP	8	343	277	395	33	2521
G13_651	3	329	318	345	7	2574
G13_652	2	319	291	346	15	2542
G13_654	3	298	266	318	14	2571
G13_655	1	300	—	—	—	2561
G13_656	3	279	227	315	24	2541
G13_657	3	331	323	338	4	2483
G13_658	2	343	333	354	6	2427
G13_659	3	245	232	258	7	2327
G13_Z7C_SWE	2	270	253	287	9	2297
G13_USP	6	294	247	359	31	2258
G13_Z4C_SWE	4	342	334	350	5	2206
G13_744	3	323	298	347	14	2210
G13_Z3B_SWE	3	333	308	351	12	2156
G13_Z4B_SWE	2	332	312	351	11	2214
G13_Z5A_SWE	3	276	240	301	17	2271
G13_Z5B_SWE	2	255	254	257	1	2226

Table 3.3: Summary of linear regressions between integrated density and elevation (m a.s.l.).

Location	Snowpit Regression			Fed. Sampler Regression		
	Equation	R ²	n	Equation	R ²	n
Glacier 4	0.03z+274	0.16	3	-0.16z+714	0.53	7
Glacier 2	-0.14z+659	0.75	4	0.24z-282	0.72	7
Glacier 13	-0.20z+802	>0.99	3	0.12z+33	0.21	17
All	-0.12z+618	0.50	10	-0.14z+659	0.75	31

3.1.5 Density and elevation

A linear regression of density on topographic parameters is often used to interpolate density values between measurement locations [e.g. 37, 88, 126]. Since the density measurement locations spanned a large portion of the elevation range for each glacier, the density values are regressed on elevation only. Regression slopes differ in both magnitude and sign between snowpit-derived and Federal Sampler-derived densities (Table 3.3).

Snowpit-derived density decreases with elevation on Glaciers 2 and 13 and does not change with elevation on Glacier 4 (Figure 3.4). The lower elevation sites on Glaciers 2 and 13 could have been melt affected. Warmer mean snow temperatures at the lower sites (Table 3.1) indicate that melt has occurred, which would increase snow density. Glacier 4 was probably not affected by melt, as snow temperatures are cool at all snowpit sites.

Opposite relationships are seen in the regression of Federal Sampler-derived densities and elevation (Figure 3.5). Density increases with elevation on Glacier 2 and there is no relationship with elevation on Glacier 4 and 13. There is a positive relationship between snow density and snow depth (Section 3.1.2) and a positive relationship between snow depth and elevation (Figure 3.3) on Glacier 2, which results in a positive relationship between snow density and elevation. Since there is no significant relationship between snow depth and elevation on Glaciers 4 and 13, there is no relationship between snow density and elevation.

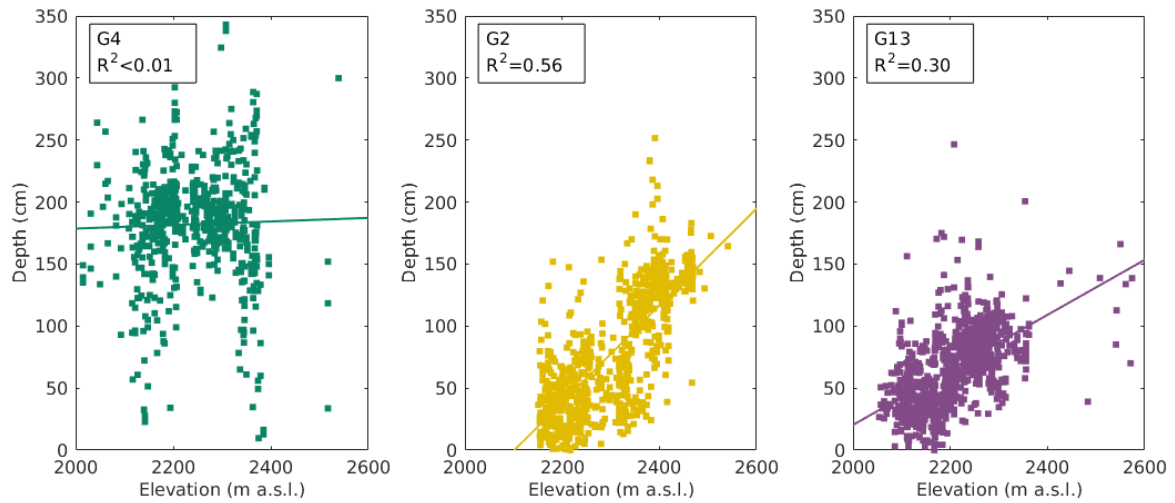


Figure 3.3: Relationship between measured snow depth and elevation at all sampling locations.

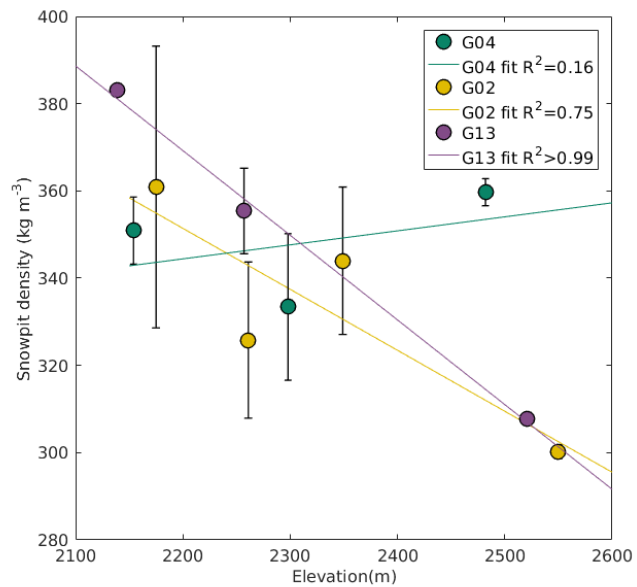


Figure 3.4: Relationship between snowpit-derived density and elevation for all study glaciers.

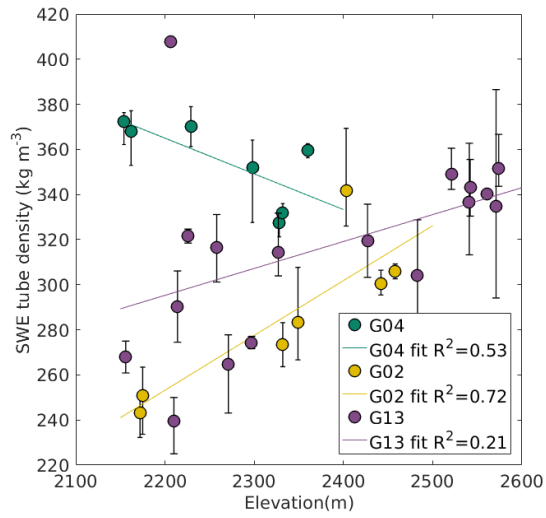


Figure 3.5: Relationship between Federal Sampler-derived density and elevation for all study glaciers.

3.2 Linear and curvilinear transect snow depth data

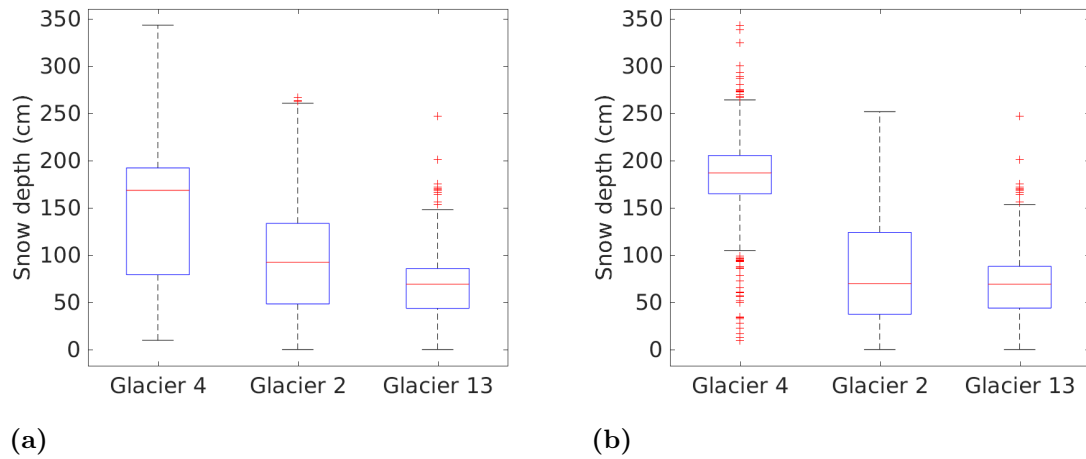


Figure 3.6: Boxplots of snow depth measured on study glaciers. All snow depth values shown in (a) and snow depth values only from transects (zigzag, snowpit and Federal Sampler measurements excluded) shown in (b). Red line indicates median, blue box shows first quartiles, bars indicate minimum and maximum values (excluding outliers), and red crosses show outliers, which are defined as being outside of the range of 1.5 times the quartiles (approximately $\pm 2.7\sigma$).

Glacier 4 has the largest median and range of snow depth values, while Glacier 13 has the smallest (Figure 3.6). The boxplot of snow depth on Glacier 4 has different characteristics when only transect data is plotted (zigzag, snowpit and Federal Sampler measurements excluded). The range and IQR are smaller and there are significantly more points that are considered outliers.

3.3 Zigzag snow depth data

A comparison of measured snow depth for each zigzag is shown in Figure 3.7. The zigzags on Glacier 4 show minimal variability with a small range of values observed and few outliers. The mean depth is significantly larger at the highest elevation zigzag. Zigzags on Glacier 2 show more variability. The range on the middle elevation is the largest of all the zigzags measured and the highest zigzag has many outliers. The zigzags on Glacier 13 do not vary considerably in range, although the lower zigzags show a large number of outliers which may be a result of these locations being close to a supraglacial meltwater channel.

The depths measured in each zigzag are shown in Figures 3.9, 3.10, and 3.11. There is considerable variability both between zigzags and within each zigzag. For example, snow depths in G04_Z5B are more uniform than in G04_Z3A (Figure 3.9).

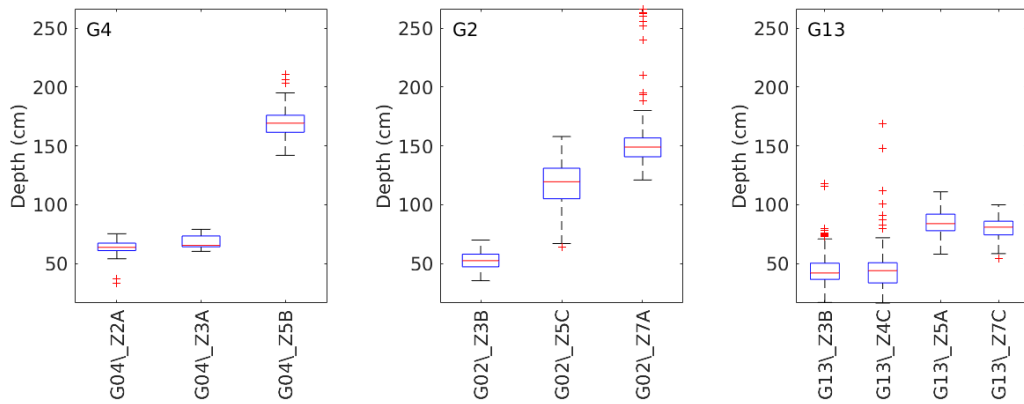


Figure 3.7: Boxplots of snow depth data measured at each zigzag location. See Figure 3.8 for locations of each zigzag.

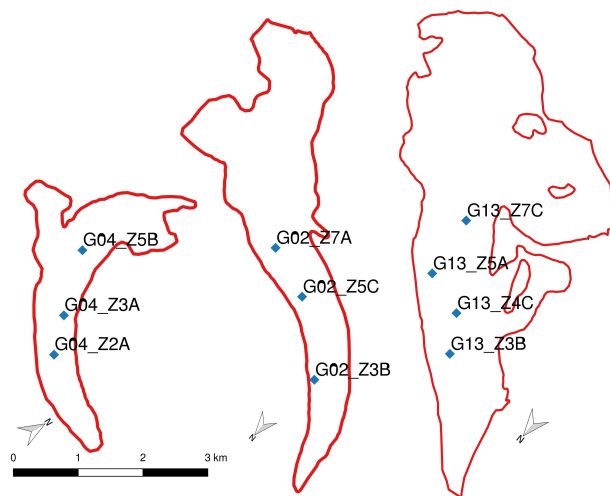


Figure 3.8: Map of zigzag locations on Glaciers 4, 2 and 13 (left to right).

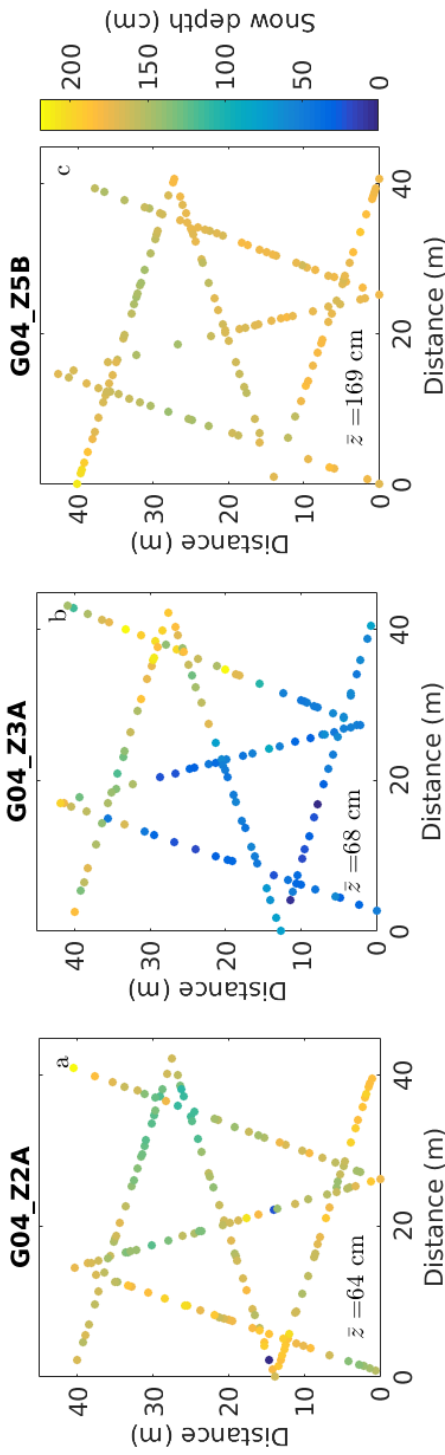


Figure 3.9: Snow depths measured in zigzags on Glacier 4. Mean depth (\bar{z}) is also reported. Zigzag elevations (left to right) are 2162, 2229 and 2360 m a.s.l. See Figure 3.8 for locations of each zigzag.

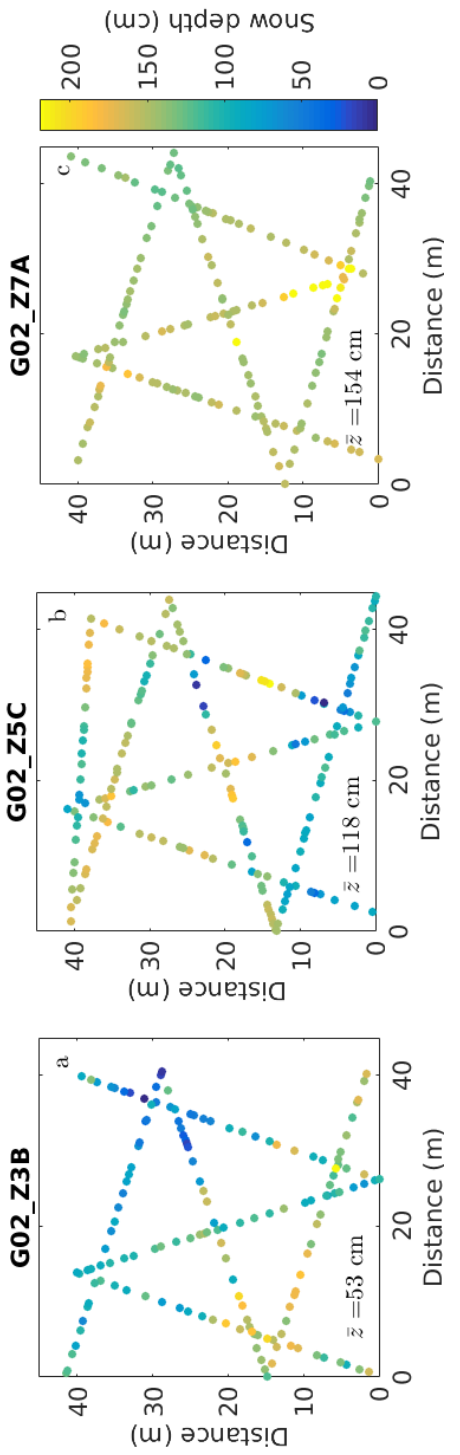


Figure 3.10: Snow depths measured in zigzags on Glacier 2. Mean depth (\bar{z}) is also reported. Zigzag elevations (left to right) are 2172, 2332 and 2403 m a.s.l. See Figure 3.8 for locations of each zigzag.

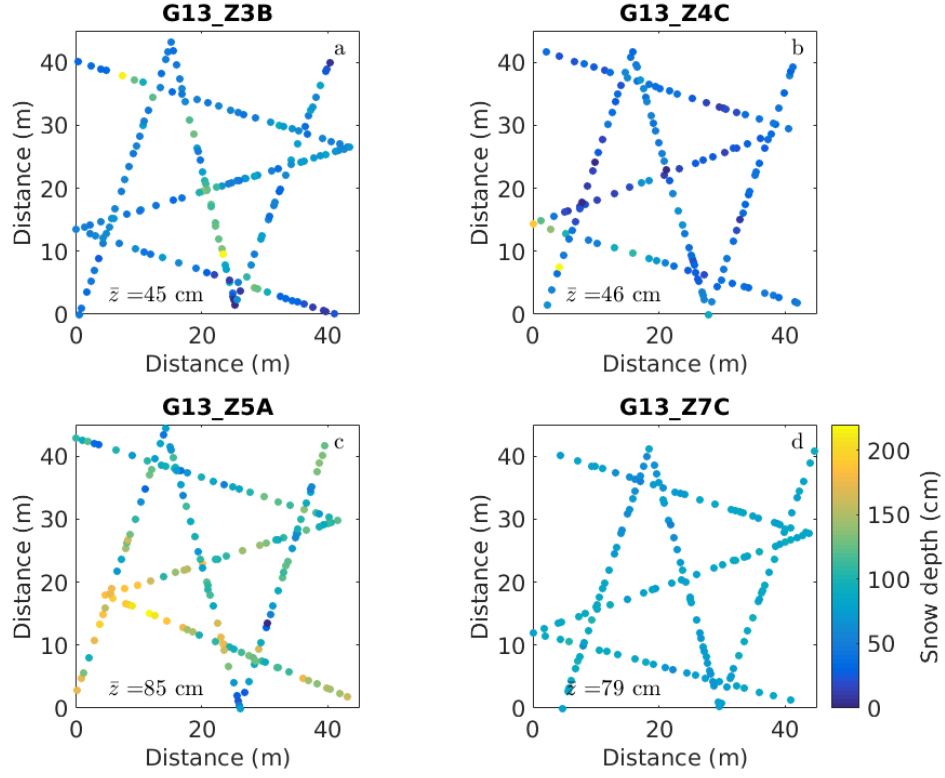


Figure 3.11: Snow depths measured in zigzags on Glacier 13. Mean depth (\bar{z}) is also reported. Zigzag elevations (a-d) are 2156, 2206, 2271 and 2297 m a.s.l. See Figure 3.8 for locations of each zigzag.

3.4 Snow water equivalent (SWE)

Snow water equivalent (SWE) at sampling locations is estimated using eight density options (Section 3.1). Estimates of SWE on each glacier are significantly different (Figure 3.12). Glacier 4 has two main groups of SWE estimates with a number of estimates that overlap (belong to group A and C). The estimate calculated using density F1 has a lower mean than the remaining estimates. Glacier 2 has four different grouping of SWE estimates but all estimates belong to multiple groups so there is no one estimate that differs from the rest. SWE estimates on Glacier 13 found using Federal Sampler-derived densities (Group B) have a higher mean SWE than those found using snowpit-derived densities (Groups A, C and D). The percent difference between the means of the SWE estimates are 12%, 18% and 19% for Glacier 4, 2 and 13, respectively.

Density option 3 (Figures 3.17 and 3.18), which uses a linear regression of density with elevation, is used in this study to examine how a regression based on topography could affect SWE estimates. Despite opposite relationships between density and elevation for Federal Sampler-derived densities and snowpit-derived densities (Table 3.3), the SWE estimates

do not differ significantly for Glaciers 4 and 2. On Glacier 13, these two SWE estimates do differ but all SWE estimates with density F differ from SWE estimates with density S. This systematic difference is perhaps a result of undersampling by the Federal Sampler on Glacier 13. Undersampling could have occurred because a considerable portion of the snowpack had undergone recent melt and snow depths were generally shallow, resulting in snow falling out of the sampling tube.

For all density options, SWE is highest on Glacier 4 and lowest on Glacier 13. Glacier 4 also shows considerable SWE variability within the basin, with both high and low values along a single transect (Figures 3.13 to 3.20). The lower, left side of Glacier 2 has low SWE with visible variability along transects. During field data collection, this area was observed to have dune-like ice features (~ 2 m) with alternating bare ice and wind-deposited snow patches.

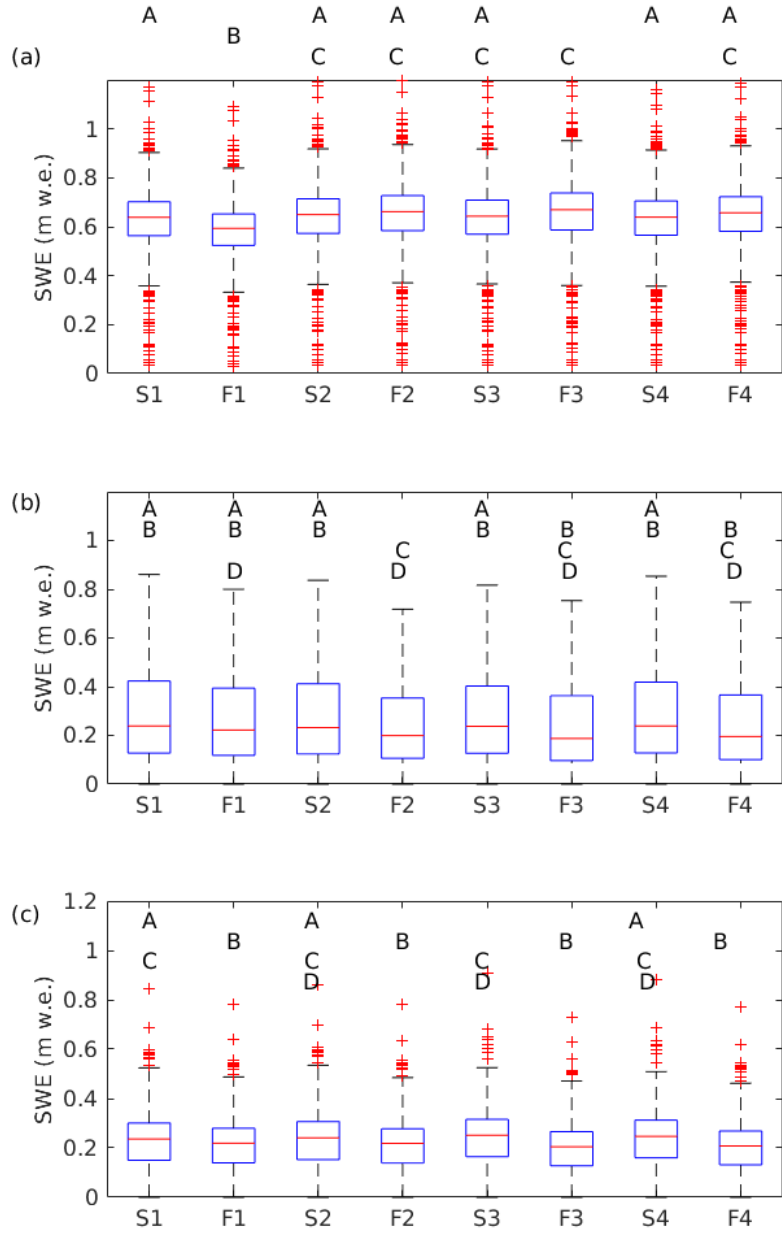


Figure 3.12: Boxplots of estimated SWE at sampling locations for Glacier 4 (a), Glacier 2 (b) and Glacier 13 (c). The density options using snowpit (S) or Federal Sampler (F) derived densities are mean from all glaciers (1), mean for individual glaciers (2), elevation regression (3) and inverse-distance weighting (4). SWE estimations using various density options were tested for differences using ANOVA ($p < 0.05$). SWE estimates that were not significantly different for each glacier are labelled with the same letter (e.g. all estimates with A on Glacier 4 are significant different than all estimates with B).

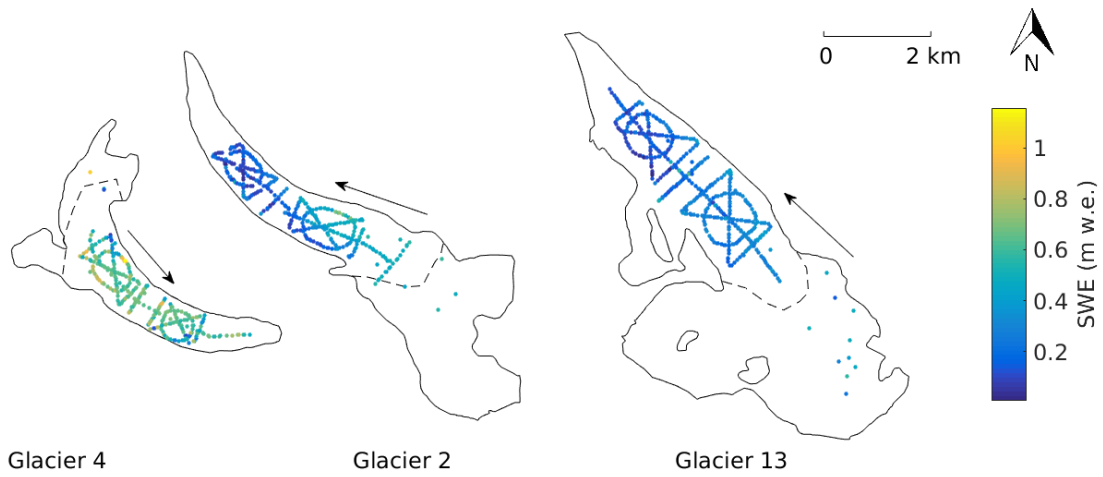


Figure 3.13: Estimated snow water equivalent (SWE) at measurement locations. Density was taken to be the mean value of all snowpit-derived densities from all glaciers (S1). Arrows show ice-flow direction and dashed lines show approximate ELA. Note that the individual measurement locations overlap on the figure.

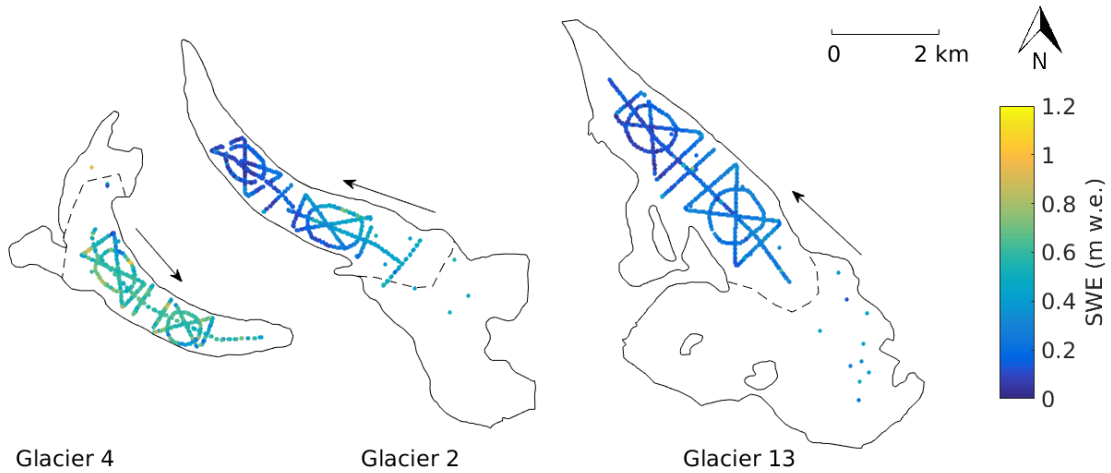


Figure 3.14: Estimated snow water equivalent (SWE) at measurement locations. Density was taken to be the mean value of all Federal Sampler-derived densities from all glaciers (F1). Arrows show ice-flow direction and dashed lines show approximate ELA. Note that the individual measurement locations overlap on the figure.

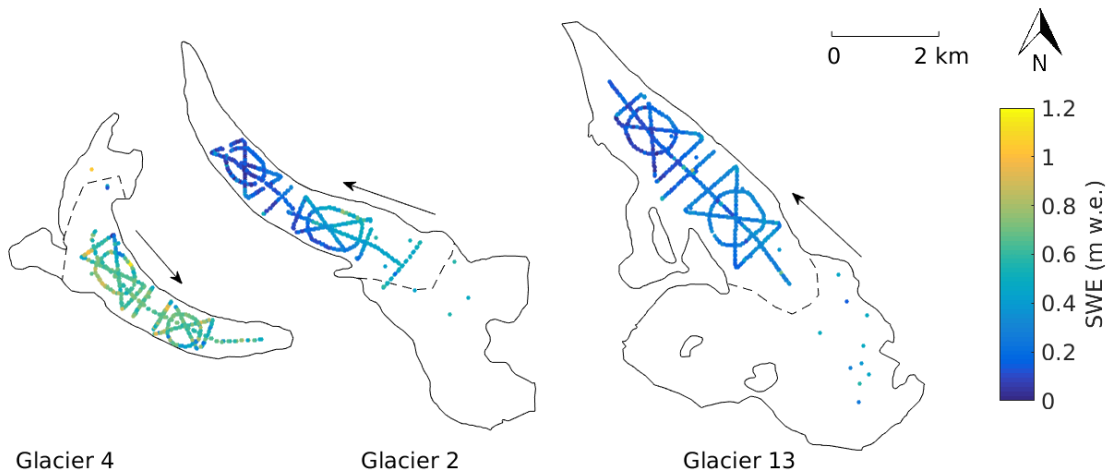


Figure 3.15: Estimated snow water equivalent (SWE) at measurement locations. Density for each glacier was taken to be the mean value of snowpit-derived densities from that glacier (S2). Arrows show ice-flow direction and dashed lines show approximate ELA. Note that the individual measurement locations overlap on the figure.

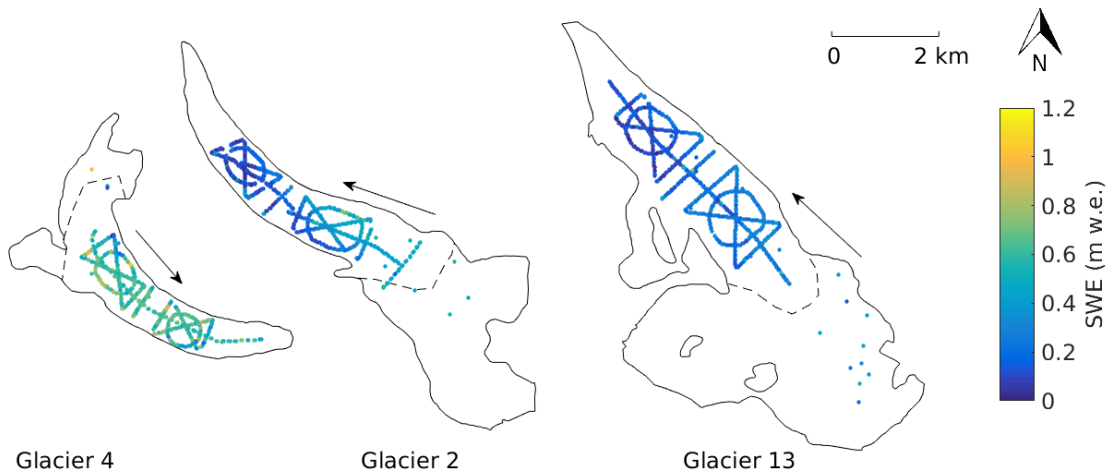


Figure 3.16: Estimated snow water equivalent (SWE) at measurement locations. Density for each glacier was taken to be the mean value of Federal Sampler-derived densities from that glacier (F2). Arrows show ice-flow direction and dashed lines show approximate ELA. Note that the individual measurement locations overlap on the figure.

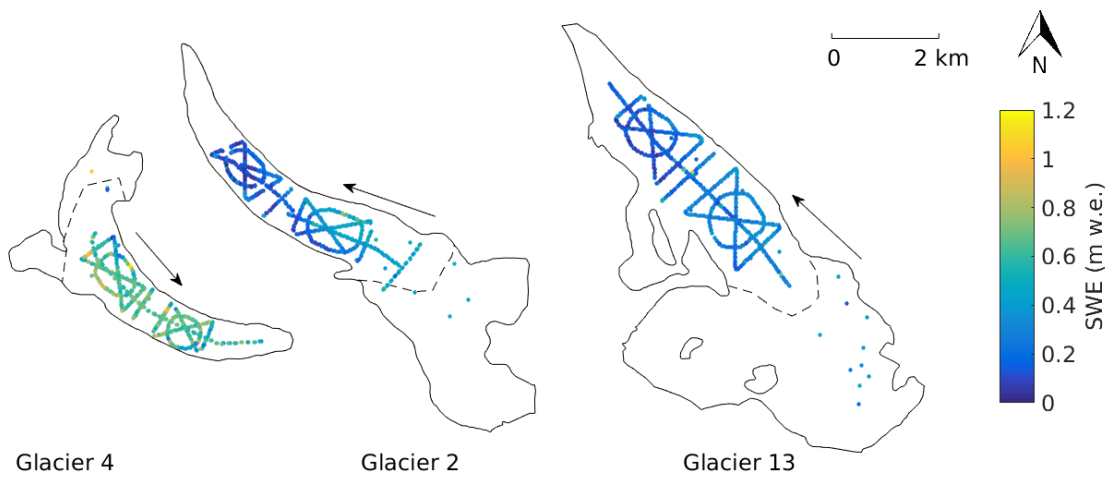


Figure 3.17: Estimated snow water equivalent (SWE) at measurement locations. Density was determined by using a linear fit between snowpit-derived density and elevation for each glacier (S3). Arrows show ice-flow direction and dashed lines show approximate ELA. Note that the individual measurement locations overlap on the figure.

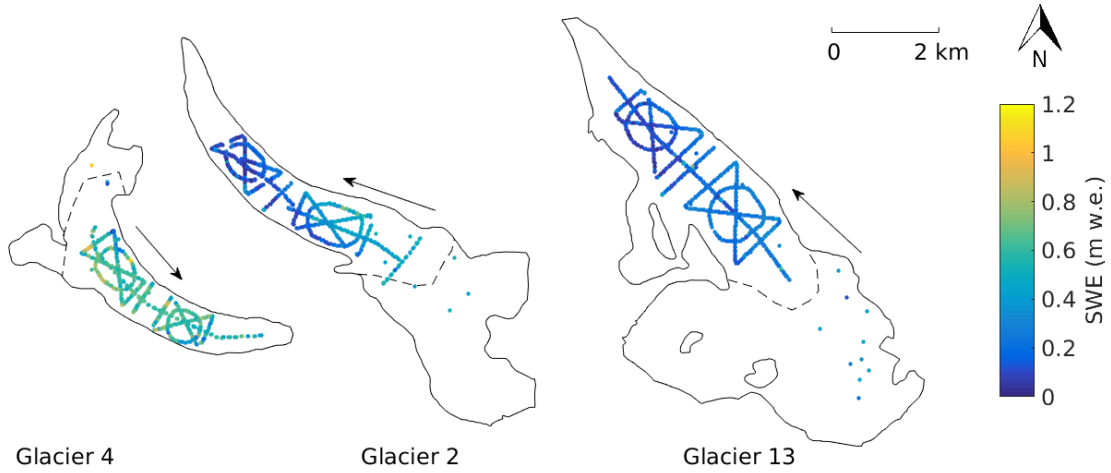


Figure 3.18: Estimated snow water equivalent (SWE) at measurement locations. Density was determined by using a linear fit between Federal Sampler-derived density and elevation for each glacier (F3). Arrows show ice-flow direction and dashed lines show approximate ELA. Note that the individual measurement locations overlap on the figure.

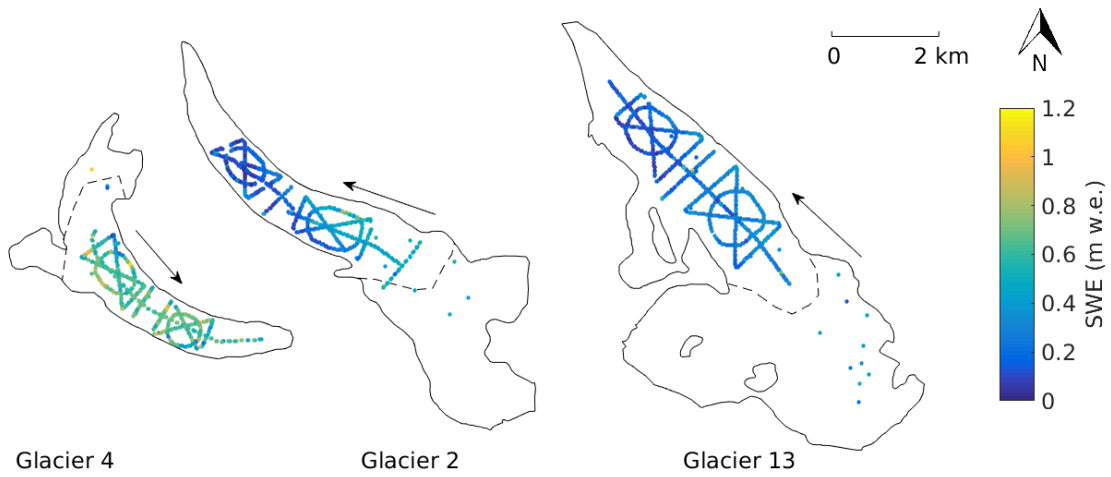


Figure 3.19: Estimated snow water equivalent (SWE) at measurement locations. Density was calculated using inverse distance weighting using all snowpit-derived densities (S4). Arrows show ice-flow direction and dashed lines show approximate ELA. Note that the individual measurement locations overlap on the figure.

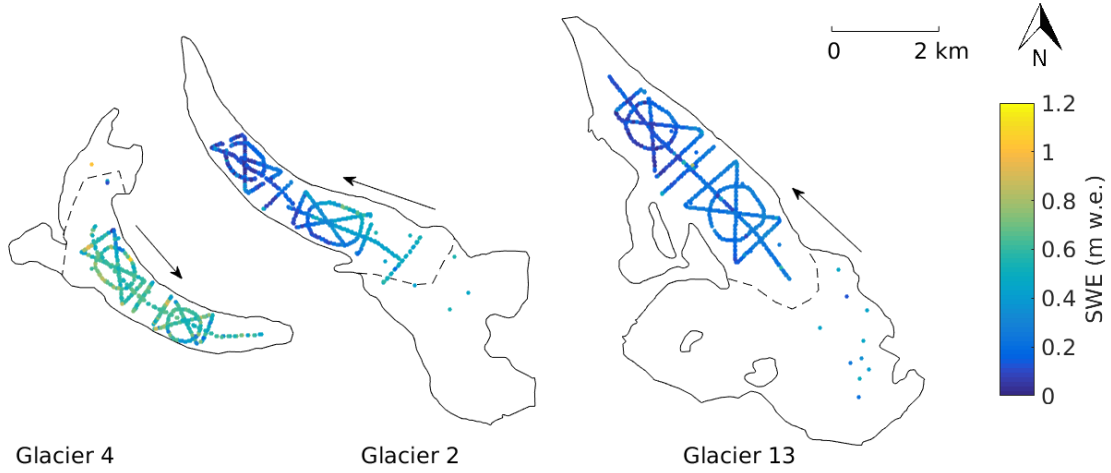


Figure 3.20: Estimated snow water equivalent (SWE) at measurement locations. Density was calculated using inverse distance weighting using all snowpit-derived densities (F4). Arrows show ice-flow direction and dashed lines show approximate ELA. Note that the individual measurement locations overlap on the figure.

3.5 Variability at multiple scales

In an attempt to compare sources of variability in values of observed SWE, a distribution of percent variability of measurements about a local mean is plotted at multiple scales. SWE variability (varswe) of observations (x), expressed as a percent of the local mean μ_{loc} is

calculated according to

$$\text{var}_{\text{SWE}} = \frac{x - \mu_{\text{loc}}}{\mu_{\text{loc}}}. \quad (3.1)$$

The coefficient of variation (CV), or relative standard deviation, is a standardized measure of data variability and is defined as

$$\text{CV} = \frac{\sigma}{\mu}, \quad (3.2)$$

where σ is the standard deviation and μ is the mean of a given data set. The ratio is often displayed as a percentage.

3.5.1 Point scale

The SWE variability at a single measurement location (Figure 3.21) varies considerably between glaciers (Table 3.4). Glacier 2 has the largest 2σ value, with SWE values varying by as much as 50% of the location mean. The map of coefficients of variation (Figure 3.22) show that the lower portion of Glacier 2, which corresponds to scoured ‘ice dunes’ observed during field work, has large variability. The lower portion of Glacier 13 also has higher variability. This area had shallow snow and bare ice was often observed. From these observations, it appears that areas with almost no snow have relatively high variability.

Table 3.4: 2σ values of SWE variability (%) distributions at the point and grid cell scale.

	Point Scale	Grid Cell Scale		
		<i>Zigzag data</i>	<i>Multiple measurement location data</i>	<i>Density Interpolation</i>
Glacier 4	13%	14%	15%	7%
Glacier 2	50%	26%	29%	17%
Glacier 13	28%	19%	57%	15%

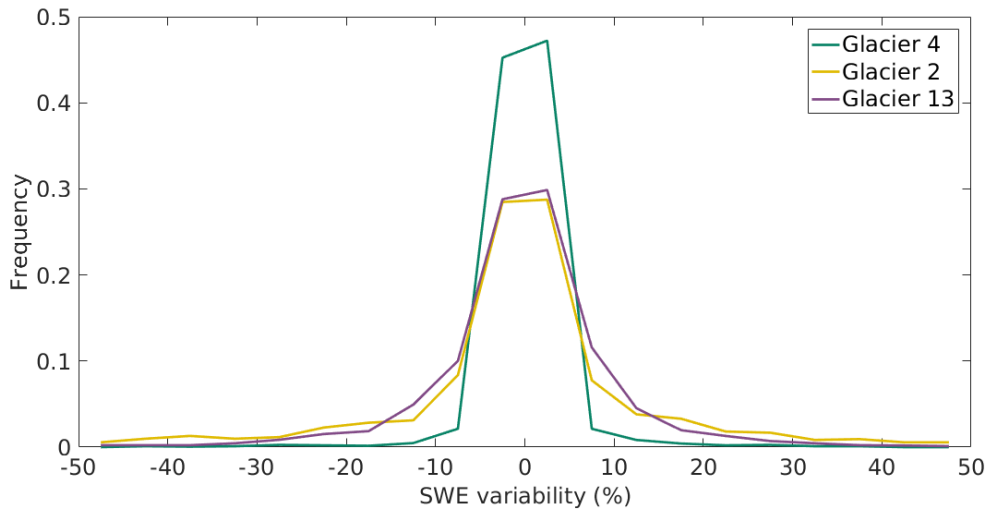


Figure 3.21: SWE variability at one measurement location. Three to four snow depth measurement were taken at each location and converted to SWE values using S1 density option.

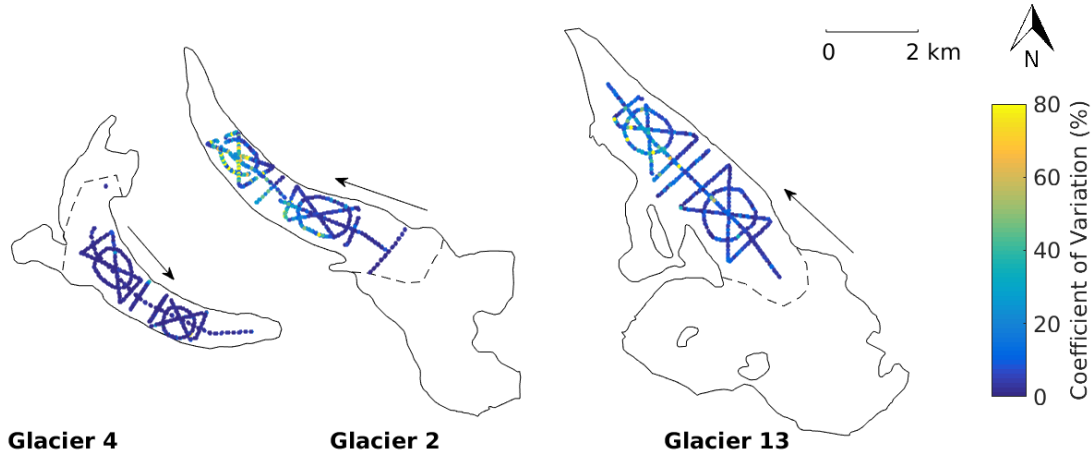


Figure 3.22: Coefficient of variation of observations at one measurement location. Three to four snow depth measurement were taken at each location and converted to SWE values using S1 density option.

3.5.2 Grid cell scale

Zigzag data

Two data sets are used to investigate grid cell scale variability. The first is zigzag data (Section 2.2.2), which contains extensive snow depth data within a 40×40 m area that corresponds to a DEM grid cell. Snow depth was converted to SWE by using the Federal

Sampler density measurement within the zigzag. Kruskal–Wallis test shows that zigzag variability (Figure 3.23) has the same distribution within each glacier ($p>0.05$), with the exception of G13_Z3B and G13_Z7C having different distributions. Since variability is consistent for each glacier, the distributions are combined to produce a grid cell scale SWE variability for each glacier (Figure 3.24). Glacier 4 has the lowest variability and Glacier 13 has the highest variability, with variation of more than 50% about the grid cell mean (Table 3.4).

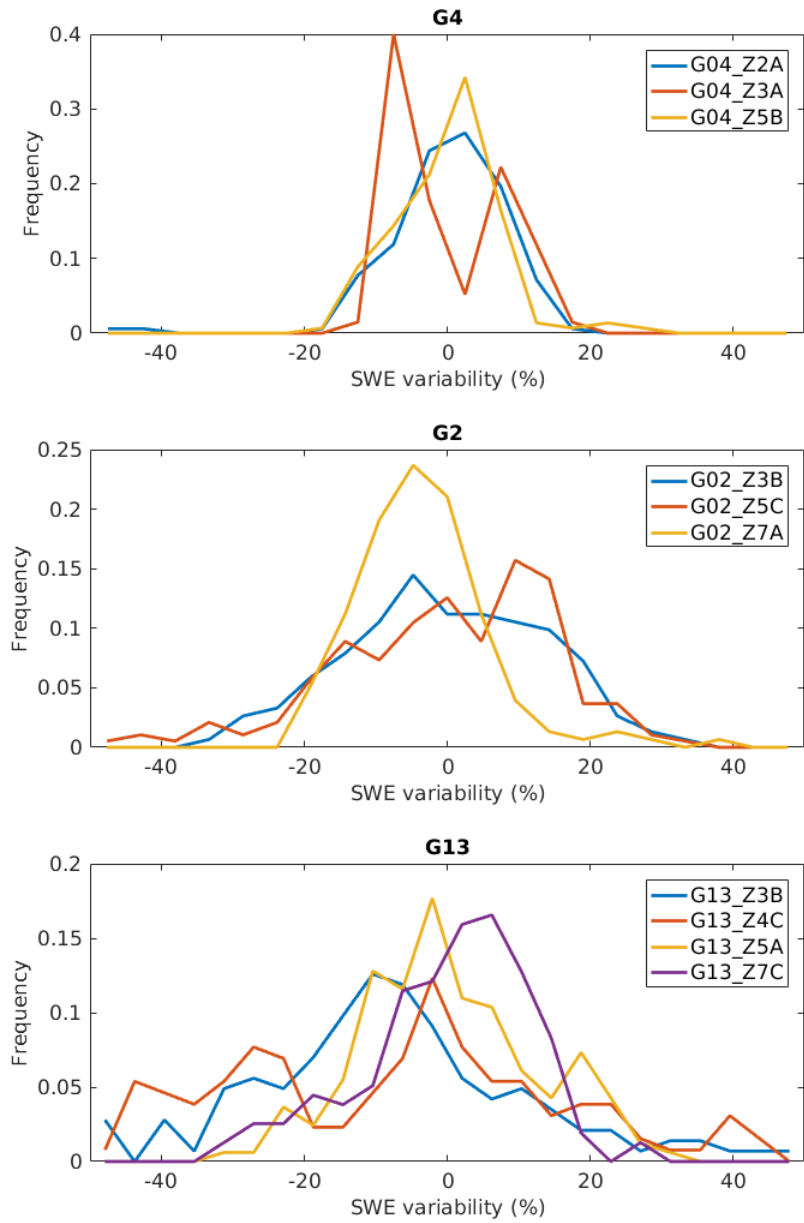


Figure 3.23: SWE variability for each set of zigzag measurements.

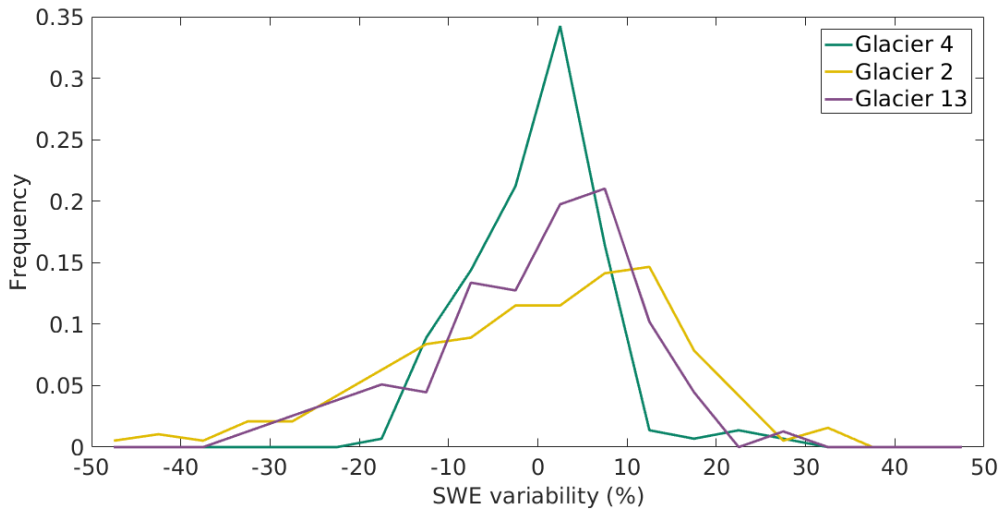


Figure 3.24: SWE variability at the grid cell scale based on zigzag measurements.

Multiple measurement location data

The second data set includes all grid cells that include more than one sampling location. These grid cells are distributed throughout the sampling area so they can provide insight into spatial changes in grid cell variability. Most grid cells with multiple measurements have two or three measurements (Figure 3.25) so variability values are limited by sample size and generally underestimate variability. The variability is similar between Glaciers 4 and 13 and largest for Glacier 2 (Figure 3.26). The 2σ values of the two grid cell scale data sets are similar for Glaciers 4 and 2, but the zigzag 2σ value on Glacier 13 is considerably larger than the multiple measurement value (Table 3.4). The spatial distribution of grid cell scale variability (Figure 3.27) closely resembles that of the point scale variability. Coefficient of variation values are highest in the ‘ice dune’ area of Glacier 2 and in the lower portion of Glacier 13.

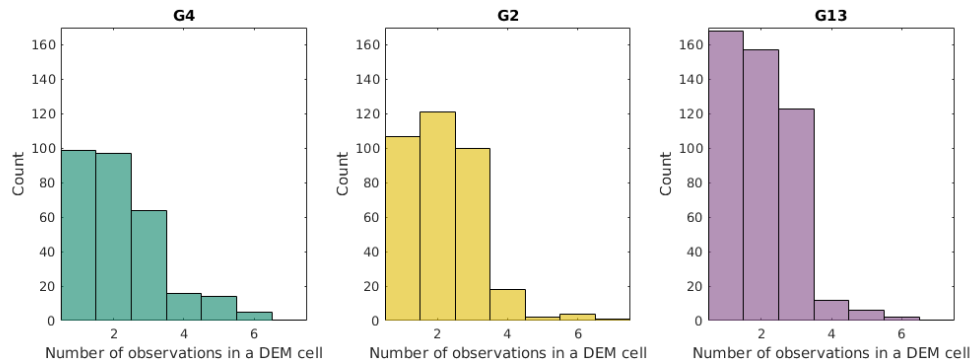


Figure 3.25: Number of measurements locations within DEM grid cells.

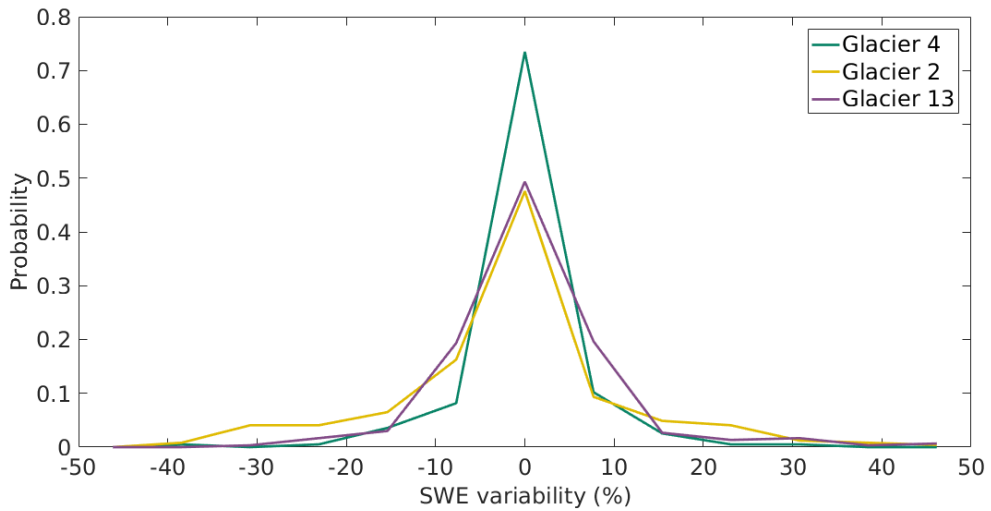


Figure 3.26: SWE variability at the grid cell scale based on multiple measurements in a DEM grid cell.

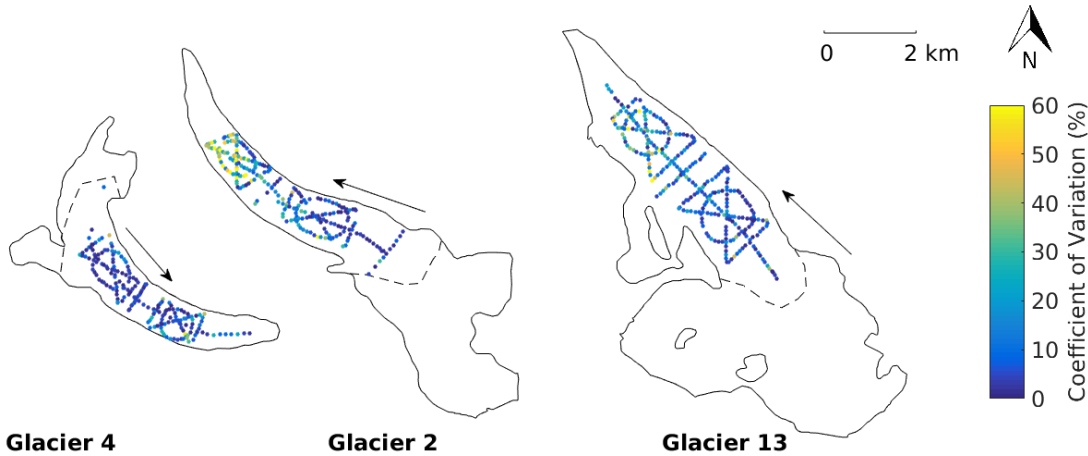


Figure 3.27: SWE variability at the grid cell scale based on zigzag measurements.

Density interpolation

Variability due to choice of density interpolation method is investigated at the grid cell scale. SWE variability is calculated using the SWE values estimated at each measurement grid cell using the eight density options (Section 4.1.3). The choice of density option does results in relatively low variability that is consistent between glaciers (Figure 3.28). However, there are noticeable spatial patterns in the coefficient of variation due to choice of density option that seems to closely follow the elevation gradient, with the lower portions of Glaciers 2 and 13 showing especially high variability (Figure 3.29). This spatial pattern likely arises from

the elevation dependent interpolation that results in low SWE estimates close to the glacier terminus. Despite this, the density variability has the lowest 2σ value of the investigated sources of variability (Table 3.4)

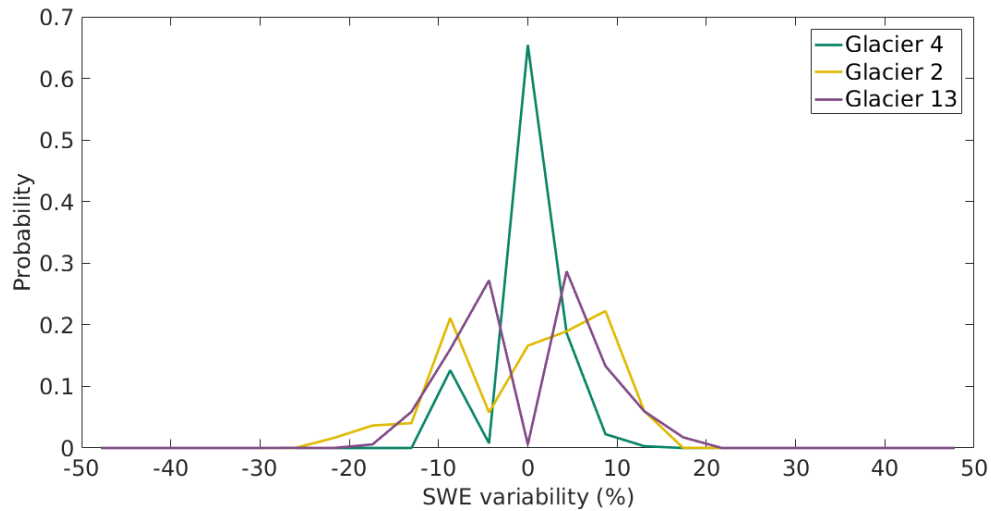


Figure 3.28: SWE variability at the grid cell scale based on eight different density interpolation methods in a DEM grid cell.

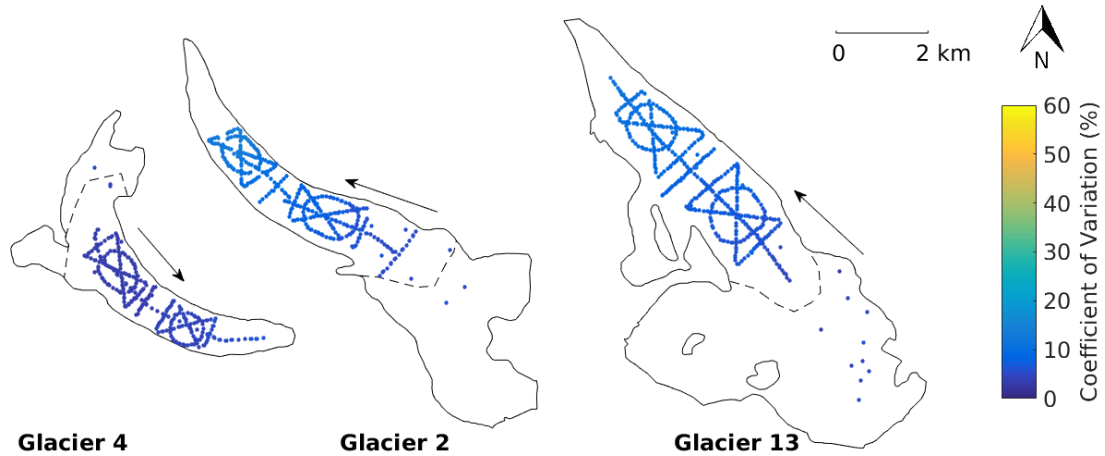


Figure 3.29: SWE variability at the grid cell scale based on eight different density interpolation methods.

Chapter 4

Interpolation

4.1 Linear topographic regressions

4.1.1 Background

Relating snow accumulation and terrain parameters to better predict accumulation within a basin has been employed for decades [e.g. 133, 88, 83]. The most common type of relation between topographic parameters and accumulation is a linear regression, where the observed snow water equivalent (SWE) is related to a linear combination of topographic parameters at each measurement location.

A linear regression takes the form

$$\mathbf{y} = \mathbf{X}\boldsymbol{\beta} + \boldsymbol{\varepsilon}, \quad (4.1)$$

where the matrix \mathbf{X} contains the set of independent regressors \mathbf{x}_i used to explain the dependant variable \mathbf{y} [e.g. 31]. The regression coefficient for each regressor is given by $\boldsymbol{\beta}$ and the error of the system is given by $\boldsymbol{\varepsilon}$. Applied to this study, the matrix of independent regressors (\mathbf{X}) contains the topographic parameters at the sampling locations, the dependent variable \mathbf{y} contains the observed SWE, and the $\boldsymbol{\beta}$ values are determined using a fitting model. While there are many types of fitting models, the ones employed in this study are multiple linear regression (MLR) and Bayesian model averaging (BMA).

To prevent over fitting of the data, regressions are calculated using cross validation. This means that for each regression, a randomly selected portion of the data is used to estimate regression coefficients and the coefficients are used to predict values that correspond to the remaining data [66]. The root mean squared error (RMSE) between the estimated and observed data is then calculated. This process was repeated 1000 times and the regression coefficients that resulted in the lowest RMSE are then chosen for that model.

In this study, regressions for all possible combinations of topographic parameters are calculated. The total number of models is 2^n , where n is the number of topographic parameters. Eight topographic parameters are used, resulting in $2^8 = 256$ models. Model

averaging is then used to determine the final regression coefficients. Model averaging is described in more details for multiple linear regressions (MLRs) in Section 4.1.4 and for Bayesian Model Averaging (BMA) in Section 4.1.5.

Once β values have been estimated, they can then be used to predict values of the dependent variable in other locations where regressors are known [31]. For each grid cell, known values of topographic parameters can be multiplied by their respective β coefficients and added together to obtain the modelled or predicted value of SWE.

4.1.2 Importance of variables in regression models

Regressions are used not only for estimating the response variable but also for assessing the relative importance of the regressors. Most types of regression models, including the ones used in this study, cannot be used to directly determine variable importance, so many additional metrics have been developed to address this need. [47] lists seven simple metrics for assessing variable importance in a univariate regression (one dependant variable). Two of these metrics, raw correlation and semi-partial correlation, are chosen for this study. For both metrics, a larger value indicates a larger influence of a regressor in the model.

The first metric is the square of the raw correlations between regressors and response variable [47]. Raw correlation values can aid in identifying important variables for explaining and interpreting results because it is ignorant of which other regressors are included in the model [30].

The second metric is the square of the semi-partial (or part) correlations for each regressor variable [47]. Semi-partial correlations are the correlation between the response variable and the residuals of the regression between each regressor and the remaining regressors. The value can be interpreted as the unique variance accounted for by x_1 in the presence of other predictors x_2, \dots, x_k [30, 18]. Semi-partial correlations are helpful in identifying a small number of regressors that have the most influence in the regression [46].

An assumption for semi-partial correlation is that regressors are independent of each other. When regressors are independent, the semi-partial correlations of all regressors sum to the total coefficient of determination (R^2) of the regression [47]. In this study, the regressors are all independent ($R^2 < 0.35$ for all glaciers) except for aspect and northness, which have R^2 values of 0.79, 0.83 and 0.64 for Glaciers 4, 2 and 13, respectively. Despite this correlation, semi-partial correlation is used because of its simplicity.

4.1.3 Snow density estimation methods

In this study, snow density was not measured at every location where snow depth was measured. Therefore, snow density values need to be estimated at snow depth measurement locations in order to estimate observed SWE values. There are a number of different methods for interpolating between snow density measurement locations. Four methods were chosen for this study and include (1) using a constant value, the mean of all observed snow

density values, for all measurement locations, (2) using a constant value (mean) for each glacier, (3) using a linear regression of elevation and snow density to interpolate for each glacier, and (4) taking an inverse-distance weighted mean of density observations. As discussed in Section 3.1, the snowpit-derived densities and Federal Sampler-derived densities are inconsistent so these two data set are kept separate for the analysis. In total there are eight different methods for estimating density, as summarized in Table 4.1.

Table 4.1: Description of density interpolation methods used to calculate SWE used in the topographic regression. Abbreviations with ‘S’ used snowpit-derived densities and abbreviations with an ‘F’ used Federal Sampler-derived densities.

	Source of snow density	Estimation method
	<i>Snowpit</i>	<i>Federal Sampler</i>
S1	■	
F1		■
S2	■	
F2		■
S3	■	
F3		■
S4	■	
F4		■

4.1.4 Multiple Linear Regression (MLR)

Background

Perhaps the most basic and well used method for relating SWE and topographic parameters is a multiple linear regression (MLR) [e.g. 25]. The best fit line of one type of MLR is the one described by coefficients that minimize the sum of squares of the vertical deviations of each data point (Y_i) from the estimated value according to the equation (\hat{Y}_i) [31]

$$\sum_{i=1}^n (\hat{Y}_i - Y_i)^2 = \text{minimum.} \quad (4.2)$$

Note that if a point falls on the line then the deviation is zero and the positive and negative deviations from the line do not cancel because the values are first squared and then summed. The residuals are simply the differences between the estimated and observed data values. To prevent over fitting of the data, cross validation is done for each MLR, as described in Section 4.1.

In this study, there are 2^8 models that encompass all possible linear combinations of topographic parameters. There is no reason to favour any of the models so a weighted sum

of all models is used to estimate regression coefficients. The Bayesian information criterion (BIC) value is used to assess the relative predictive success of each model.

A BIC value is found according to

$$\text{BIC} = -2 \ln L(\hat{\theta}_k|y) + k \ln(n), \quad (4.3)$$

where the values of $\hat{\theta}_k$, which are the model parameters, maximize the likelihood function for data y [19]. The likelihood function, $L(\hat{\theta}_k|y)$, is the probability of the model parameters occurring given the data. The number of data points is n and the number of regressors is k . BIC values are used to assess the relative predictive success of models while penalizing for overfitting of data. While the absolute BIC value is meaningless, models can be selected or averaged using the relative BIC values, with lower values indicating a better model [19].

The BIC value for each model (BIC_i) is used to determine the normalized weight of each model (w_i) relative to the best model (lowest BIC value indicated by BIC_{\min}) as defined by the equation [19]

$$w_i = \frac{e^{-0.5(BIC_i - BIC_{\min})}}{\sum_{i=1}^R e^{-0.5(BIC_i - BIC_{\min})}}. \quad (4.4)$$

Parameters not included in a particular model are assigned coefficients of zero. The sum of the weighted coefficients gives the final β values.

Methods

The MLR of SWE values and topographic parameters is done in Matlab (Appendix E). The best set of regression coefficients for each model is selected using cross-validation of a linear regression, with the coefficients chosen by minimizing the vertical sum of squares. Then, the regression coefficients from all models are weighted according to the BIC value of the model.

Results and Discussion

The importance of the various topographic parameters differs for the three study glaciers (Table 4.2). The regression for Glacier 2 explains a large portion of the variance ($R^2=0.66$), although the RMSE is higher than that of Glacier 13, for which the regression explains less variance ($R^2=0.40$) (Figure 4.1). Glacier 4 has the least variance explained by the regression ($R^2=0.12$) and the highest RMSE. The intercepts of the regression are similar for Glaciers 2 and 13 (~ 0.25 m w.e.) and these are much lower than the intercept for Glacier 4 (0.62 m w.e.). The discrepancy between intercept values is a result of the poor fit of the Glacier 4 regression - the value of the intercept approaches that of the data mean (0.63 m w.e.). The residuals for Glacier 4 have a larger range than those of Glacier 2 and 13 (Figure 4.3).

The most important regressor for Glacier 4 is Sx. The Sx regression coefficient is a factor of five larger than those of the remaining parameters for all density options (Table

Table 4.2: Mean MLR and BMA coefficients for topographic regression between measured SWE and standardized topographic parameters. Topographic parameters are distance from centreline (d_C), elevation (z), aspect (α), slope (m), northness (N), curvature (κ), and S_x . Since parameters are standardized, the magnitude of the coefficients is representative of their importance in predicting SWE. The root-mean-squared error (RMSE) between modelled SWE using those coefficients and observed SWE is also given. Semi-partial correlation is a metric that describes the increase in R^2 from the addition of a parameter to a regression that contains all other regressors. Raw correlation is the square of the Pearson correlation between a parameter and SWE.

		z	d_C	α	m	N	κ	S_x	Intercept	RMSE
Glacier 4	MLR Coefficient	0.008	-0.001	-0.012	-0.004	-0.002	0.016	-0.051	0.619	0.145
	BMA Coefficient	0.006	-0.001	-0.010	-0.007	-0.003	0.016	-0.050	0.619	0.106
	Semi-partial R^2	0.015	<0.001	<0.001	0.007	0.001	0.010	0.034	—	—
	Raw correlation	0.003	0.044	0.001	0.027	0.001	0.041	0.065	—	—
Glacier 2	MLR Coefficient	0.110	0.008	-0.010	0.026	0.011	0.001	0.036	0.262	0.089
	BMA Coefficient	0.111	0.008	-0.011	0.029	0.012	0.002	0.036	0.261	0.075
	Semi-partial R^2	0.205	0.014	0.004	<0.001	0.003	0.004	0.028	—	—
	Raw correlation	0.586	0.031	0.211	0.100	0.193	0.078	0.333	—	—
Glacier 13	MLR Coefficient	0.054	<0.001	<0.001	0.001	0.001	-0.021	0.003	0.229	0.076
	BMA Coefficient	0.054	<0.001	-0.001	<0.001	0.001	-0.019	0.003	0.228	0.060
	Semi-partial R^2	0.245	0.003	0.007	0.002	0.005	0.008	0.009	—	—
	Raw correlation	0.347	0.051	0.012	<0.001	0.022	0.040	0.083	—	—

Table 4.3: MLR coefficients for topographic regression between measured SWE and standardized topographic parameters. Topographic parameters are distance from centreline (d_C), elevation (z), aspect (α), slope (m), northness (N), curvature (κ), and Sx. Since parameters are standardized, the magnitude of the coefficients is representative of their importance in predicting SWE. The root-mean-squared error (RMSE) between modelled SWE using those coefficients and observed SWE is also given. See Table 4.1 for description of density options.

	Parameter	S1	F1	S2	F2	S3	F3	S4	F4
Glacier 4	z	0.011	0.006	0.008	0.009	0.018	<0.001	0.008	0.003
	d_C	<0.001	-0.002	<0.001	-0.002	-0.001	-0.001	-0.001	<0.001
	α	-0.021	-0.006	-0.024	-0.013	-0.016	-0.002	-0.008	-0.010
	m	-0.002	-0.004	-0.002	-0.005	-0.013	-0.002	-0.004	-0.003
	N	-0.002	-0.002	-0.002	-0.002	-0.004	-0.001	-0.001	-0.002
	κ	0.009	0.021	0.012	0.018	0.009	0.028	0.016	0.015
	Sx	-0.059	-0.046	-0.055	-0.053	-0.057	-0.051	-0.045	-0.042
	Intercept	0.617	0.567	0.626	0.631	0.621	0.642	0.618	0.633
	RMSE	0.144	0.134	0.146	0.149	0.146	0.148	0.144	0.147
Glacier 2	z	0.119	0.109	0.114	0.099	0.102	0.120	0.109	0.109
	d_C	0.009	0.021	0.008	0.003	0.007	0.002	0.011	0.001
	α	-0.011	-0.007	-0.019	-0.009	-0.013	-0.003	-0.011	-0.005
	m	0.030	0.024	0.023	0.023	0.025	0.029	0.022	0.029
	N	0.012	0.008	0.022	0.009	0.012	0.003	0.011	0.008
	κ	0.003	0.002	0.002	0.001	0.001	0.001	0.001	0.001
	Sx	0.040	0.036	0.040	0.031	0.035	0.027	0.040	0.037
	Intercept	0.287	0.263	0.275	0.235	0.273	0.240	0.282	0.238
	RMSE	0.096	0.089	0.093	0.081	0.093	0.082	0.096	0.084
Glacier 13	z	0.058	0.052	0.055	0.052	0.045	0.058	0.054	0.055
	d_C	<0.001	<0.001	0.001	0.001	<0.001	<0.001	<0.001	<0.001
	α	<0.001	<0.001	<0.001	<0.002	<0.001	<0.001	<0.001	<0.001
	m	0.001	<0.001	<0.001	0.001	0.001	0.001	<0.001	<0.001
	N	0.002	<0.001	<0.001	0.001	0.001	<0.001	<0.001	<0.001
	κ	-0.024	-0.020	-0.021	-0.019	-0.023	-0.018	-0.021	-0.020
	Sx	0.001	0.002	0.001	0.007	0.004	0.008	0.001	0.001
	Intercept	0.236	0.220	0.241	0.217	0.250	0.208	0.246	0.211
	RMSE	0.078	0.073	0.080	0.072	0.084	0.068	0.081	0.071

4.3) and for the mean of all density options (Table 4.2). Sx has the highest mean semi-partial correlation (0.034) and raw correlation (0.065) (Table 4.2). The Sx coefficient is negative, which indicates less snow in ‘sheltered’ areas. The negative correlation is counter intuitive so it is surprising that Sx is the best predictor for accumulation.

The map of estimated SWE for the entire glacier shows a relatively uniform SWE distribution over Glacier 4 (Figure 4.8), due to the large influence of the intercept on the regression. Areas with high Sx values (sheltered), especially in the accumulation area, have the lowest values of SWE. This regression indicates that the wind plays a role in snow distribution but since the valley in which the glacier sits is steep walled and curved, perhaps having a single cardinal direction for wind is inappropriate. Examining Sx values that assume wind moving up or down glacier and changing direction to follow the valley could allow the Sx parameter to explain more of the variance.

For Glacier 2, the most important regressor is elevation (Table 4.2). This coefficient is positive, which means that SWE will increase with elevation. The elevation regression coefficient is an order of magnitude larger than the other coefficients and has the highest semi-partial R^2 and raw correlation (Table 4.2). Sx is the second most important regresor and has a positive correlation, which indicates that ‘sheltered’ areas are likely to have high accumulation.

The map of modelled SWE on Glacier 2 closely matches that of elevation (Figure 2.23), which highlights the strong dependence of SWE on elevation. The range of predicted SWE is largest for Glacier 2 and it also has the highest SWE (1.92 m w.e) and the lowest SWE (0 m w.e.) values (Figure 4.2). Both extremes are perhaps unexpected on this glacier and are likely an artefact from extrapolating from the regression, which largely depends on elevation. The southwest region of the accumulation area with high estimated accumulation results from the combination of high elevation and Sx values. The low SWE values at the terminus are a result of low elevation values and Sx values that are close to zero.

The most important regressor for Glacier 13 is elevation (Table 4.2). The coefficient is positive, which means that cells at higher elevation had higher values of SWE. Despite a low value of raw correlation between elevation and SWE, the semi-partial R^2 value is the largest between the glaciers. The high semi-partial R^2 value indicates that when elevation is added to the regression the total variance explained increases considerably because the remaining regressors are not important. The map of estimated SWE on Glacier 13 (Figure 4.8) closely follows elevation although the range of SWE values is relatively small so the elevation effect is less pronounced than on Glacier 2.

Qualitatively, there is little variation in the fit between modelled and observed winter balance between the various density options for all glaciers and the residuals display a similar distribution between the density options (Figure 4.3). The semi-partial R^2 and raw correlation for each regressor also varies little between different density options (Figure 4.7).

The distribution of residuals from the MLR regression (Figure 4.4) differs between glaciers. The range is largest for Glacier 4 because of the poor regression and smallest for Glacier 2 for which the regression had high explanatory power. The map of residual values (Figure 4.5) shows high residual values (both negative and positive) on throughout the measurements on Glacier 4. The upper part of the upper hourglass has especially high and low values, indicating that there was significant variability over a short distance that was not captured by the regression. A few high residual values are seen on Glacier 13 as well, which correspond to a deep, snow-filled supraglacial channel.

The choice of density measurements and interpolation techniques does not affect the relative importance of regressors. Although there is a range of coefficient values that result from the choice of density options (Figure 4.6), the relative dominance of S_x for Glacier 4 and elevation for Glacier 2 and 13 is consistent. The largest range in semi-partial correlation is in elevation for Glaciers 2 and 13 (Figure 4.7). Estimating SWE using the linear elevation regression and Federal Sampler-derived density (F3) resulted in the highest semi-partial correlation for Glaciers 2 and 13 (0.24 and 0.30, respectively). Since the Federal Sampler derived densities are correlated with snow depth, which is correlated with elevation, it is likely that these density values amplify the elevation component of the regression.

The largest difference in estimated SWE between the various density options is found on Glacier 2 in the upper part of the accumulation area (Figure 4.9). Glacier 2 also has the lowest difference in estimated SWE, which result from all density options estimating values of 0 m w.e. at the terminus. The strong relationship between elevation and SWE makes the estimation of glacier-wise SWE sensitive to this parameter. The difference in estimated SWE expressed as a percent (Figure 4.10) is relatively consistent on each glacier. The mean percent difference is highest on Glacier 2 (25%) and slightly lower on Glaciers 4 and 13 (18% and 20%, respectively). Extreme values in percent difference are located in areas with low values of estimated SWE (small denominator), including the terminus of Glaciers 2 and 13 as well as parts of the accumulation area on Glacier 4.

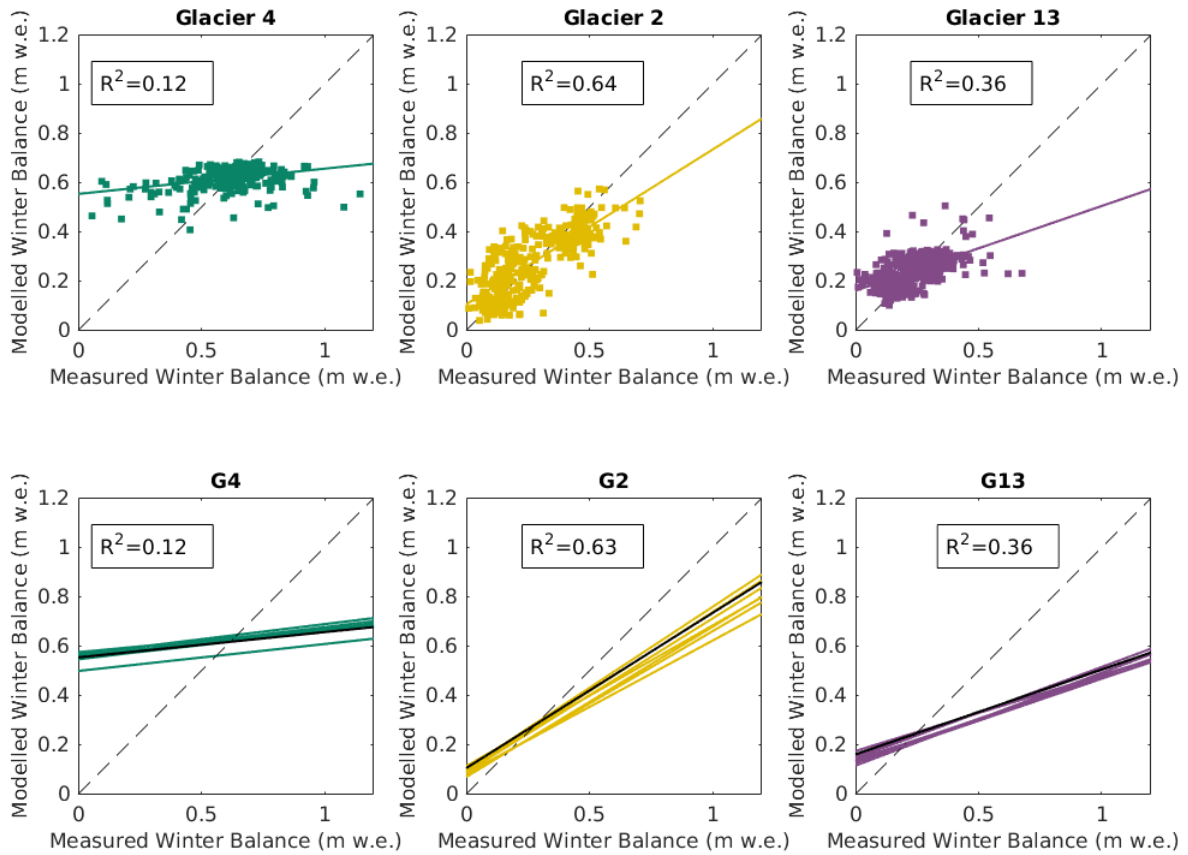


Figure 4.1: Top panel shows comparison of estimated (MLR) and observed (original) snow water equivalent (SWE) for three study glaciers. The SWE values were calculated using inverse-distance weighted snowpit densities (S4). Bottom panel shows plots of all linear fits between estimated and observed SWE using eight options for calculating density. Mean R^2 value is shown for each sub-plot and a reference 1:1 line is also provided. Black line highlights the S4 option from the top panel. See Figure 4.11 for a plot of all estimated SWE values.

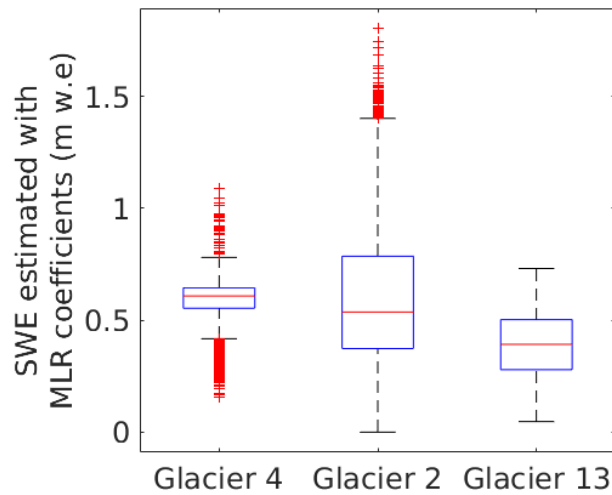


Figure 4.2: Summary of estimated SWE values found using MLR coefficients. Red line indicates median, blue box shows first quantiles, bars indicate minimum and maximum values (excluding outliers), and red crosses show outliers, which are defined as being outside of the range of 1.5 times the quartiles (approximately $\pm 2.7\sigma$).

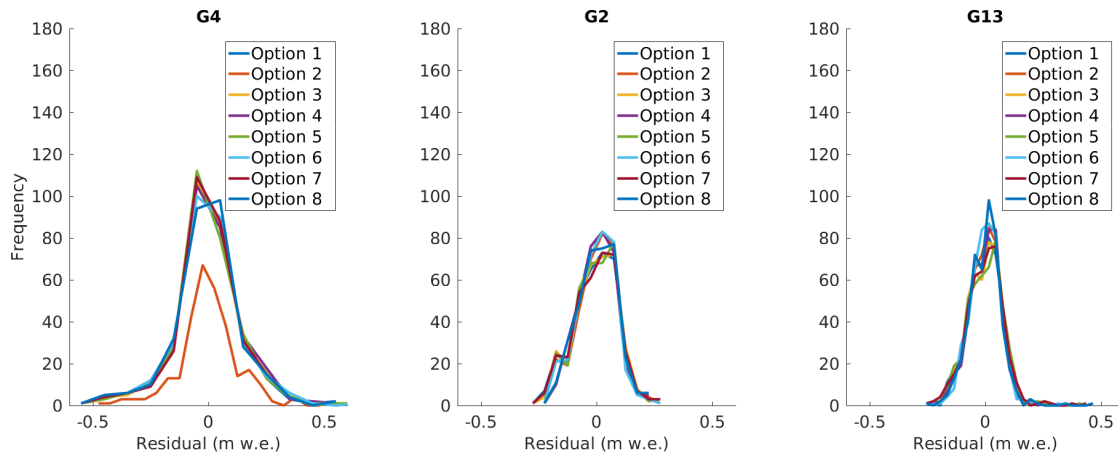


Figure 4.3: Residuals of SWE predicted using MLR for all options of estimating density.

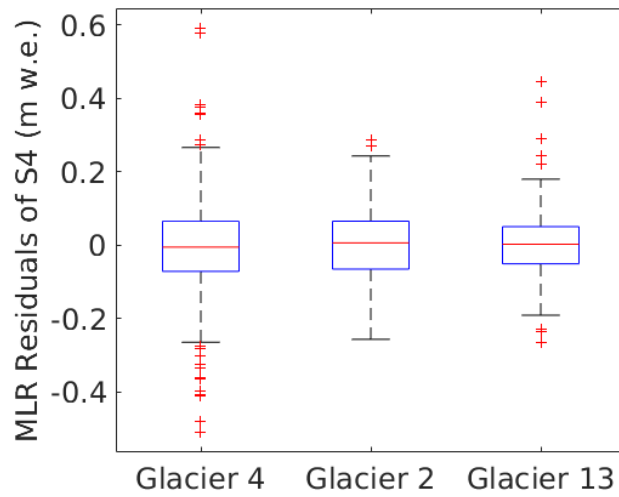


Figure 4.4: Summary of residuals from estimated SWE values found using MLR coefficients (S4). Red line indicates median, blue box shows first quantiles, bars indicate minimum and maximum values (excluding outliers), and red crosses show outliers, which are defined as being outside of the range of 1.5 times the quartiles (approximately $\pm 2.7\sigma$).

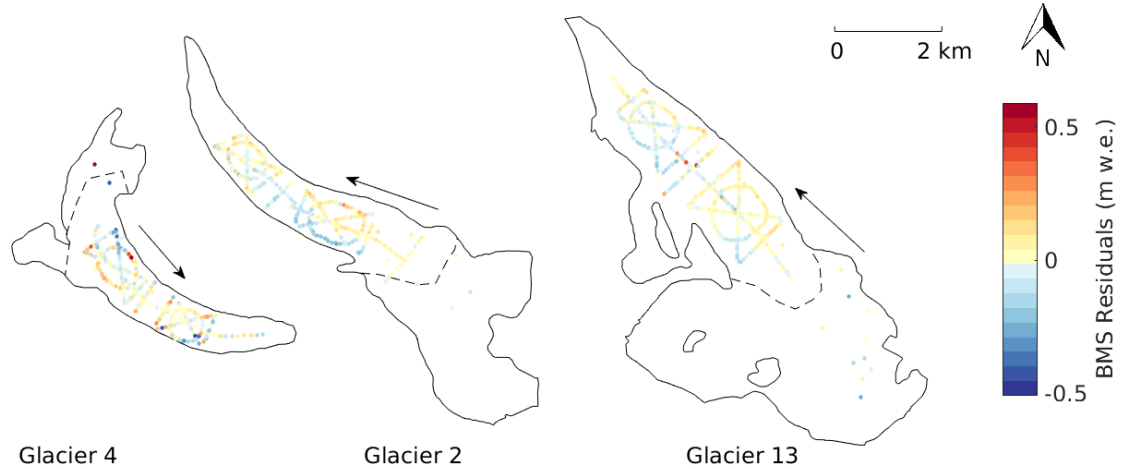


Figure 4.5: Map of the residuals from estimated SWE values found using MLR coefficients (S4) for each measurement location.

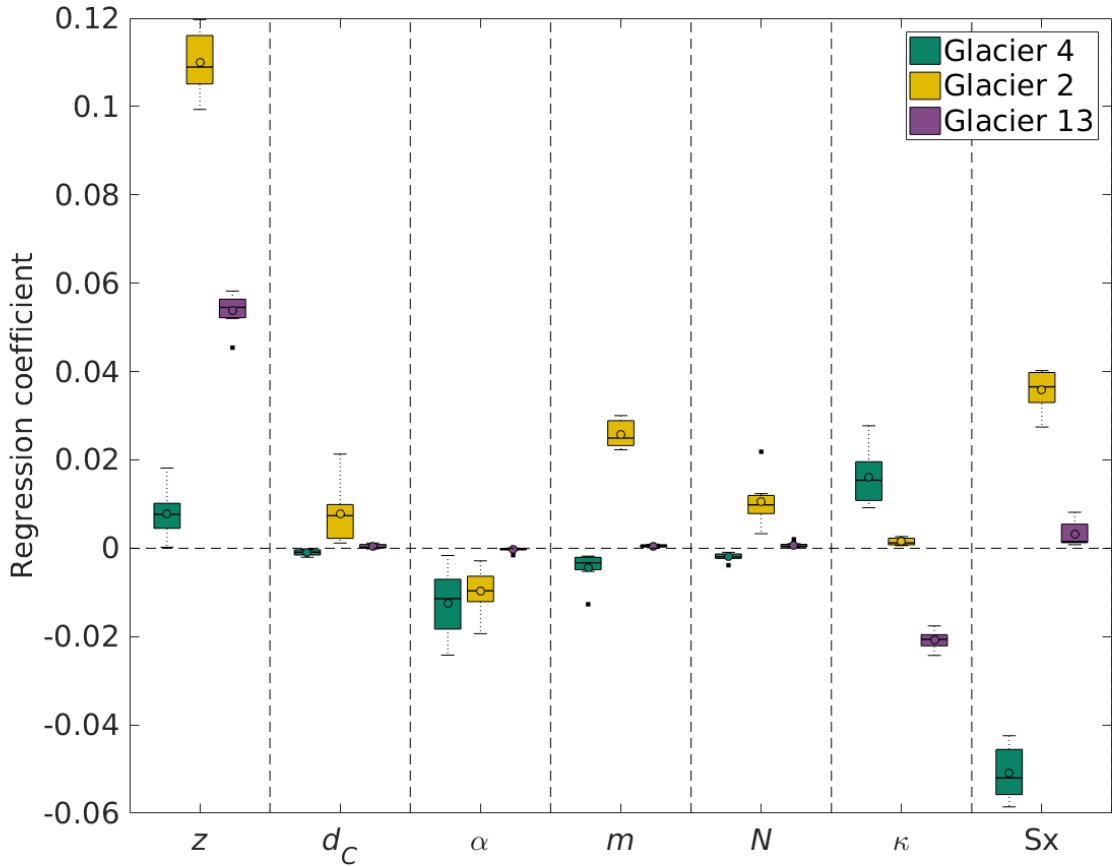


Figure 4.6: Boxplot showing the range of regressor coefficients explained by each topographic parameter for each option of estimating snow water equivalent (SWE). Topographic parameters are distance from centreline (d_C), elevation (z), aspect (α), slope (m), northness (N), curvature (κ), and Sx . Within each box, the mean is shown as a circle, the median as a horizontal line, the interquartile range (IQR) as a coloured box, two times the IQR as dashed lines beyond the box, and outliers as single points.

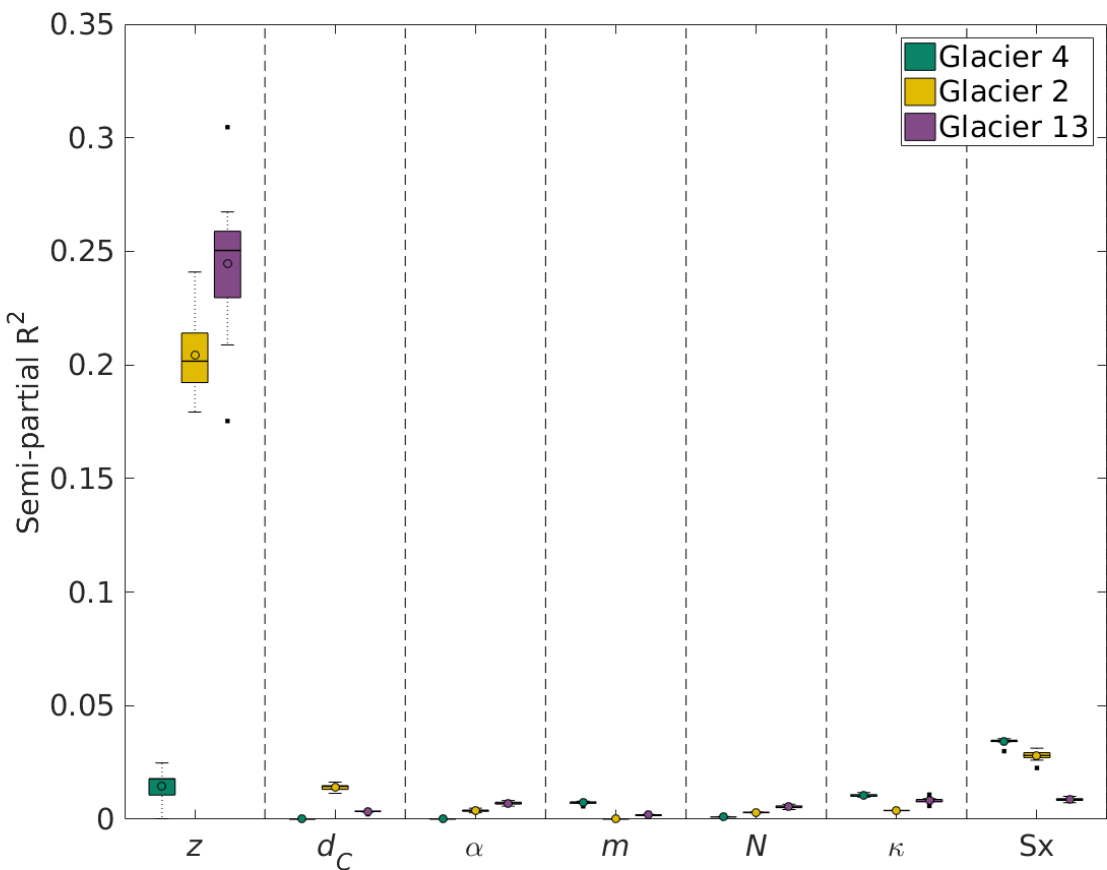


Figure 4.7: Boxplot showing the range of semi-partial correlation explained by each topographic parameter for each option of estimating snow water equivalent (SWE). Topographic parameters are distance from centreline (d_C), elevation (z), aspect (α), slope (m), northness (N), curvature (κ), and Sx . Within each box, the mean is shown as a circle, the median as a horizontal line, the interquartile range (IQR) as a coloured box, two times the IQR as dashed lines beyond the box, and outliers as single points.

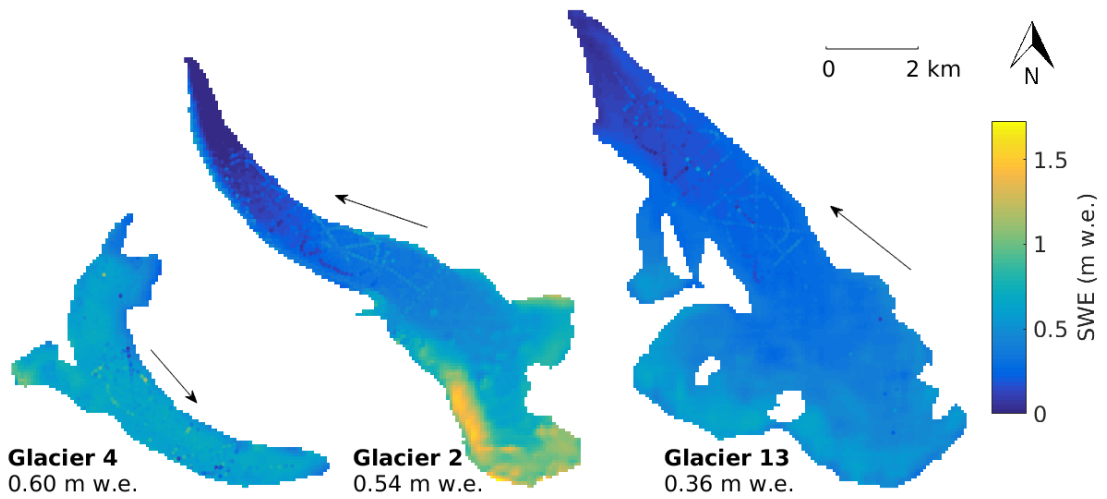


Figure 4.8: Modelled SWE using coefficients determined using MLR and density interpolated with inverse-distance weighting from snowpits (S4). Observed SWE values are overlain on the maps.

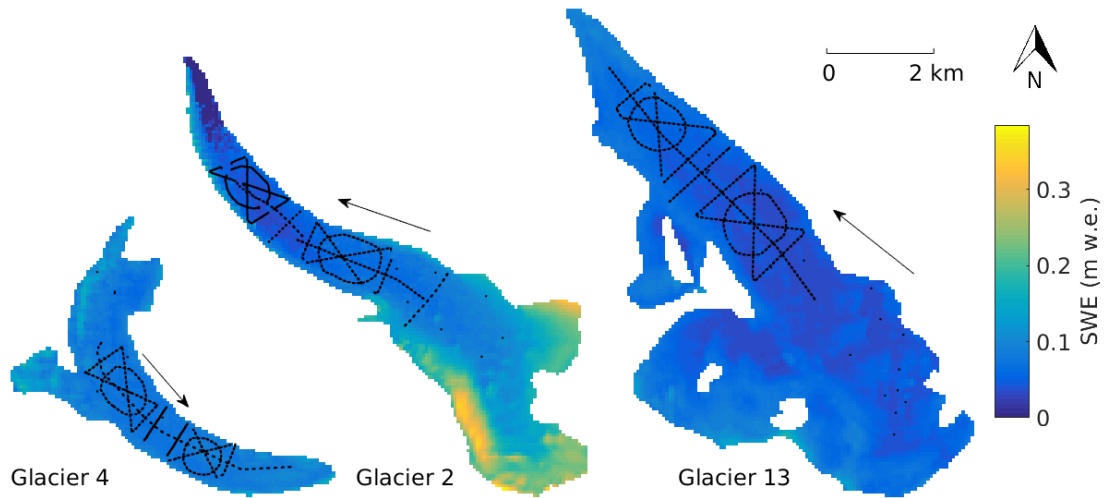


Figure 4.9: Map of the difference between maximum and minimum SWE values for each DEM cell between all density options using MLR coefficients. Observed SWE values are overlain on the maps.

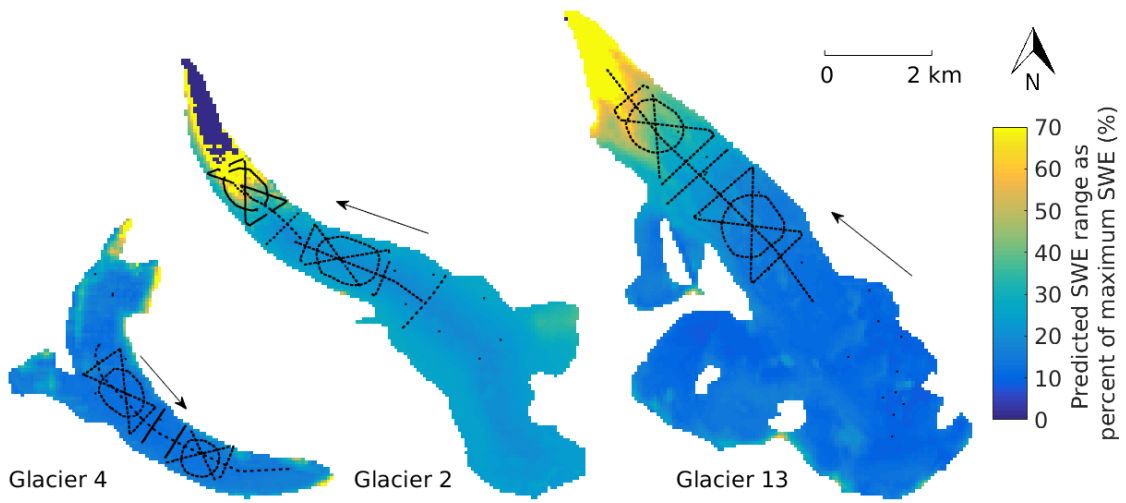


Figure 4.10: Map of the difference between maximum and minimum SWE values, expressed as a percent of the maximum SWE, for each DEM cell between all density options using MLR coefficients. The colours have been scaled to highlight difference in the main part of the glaciers. Values of zero are found where the minimum estimated SWE is zero m w.e. Observed SWE values are overlain on the maps.

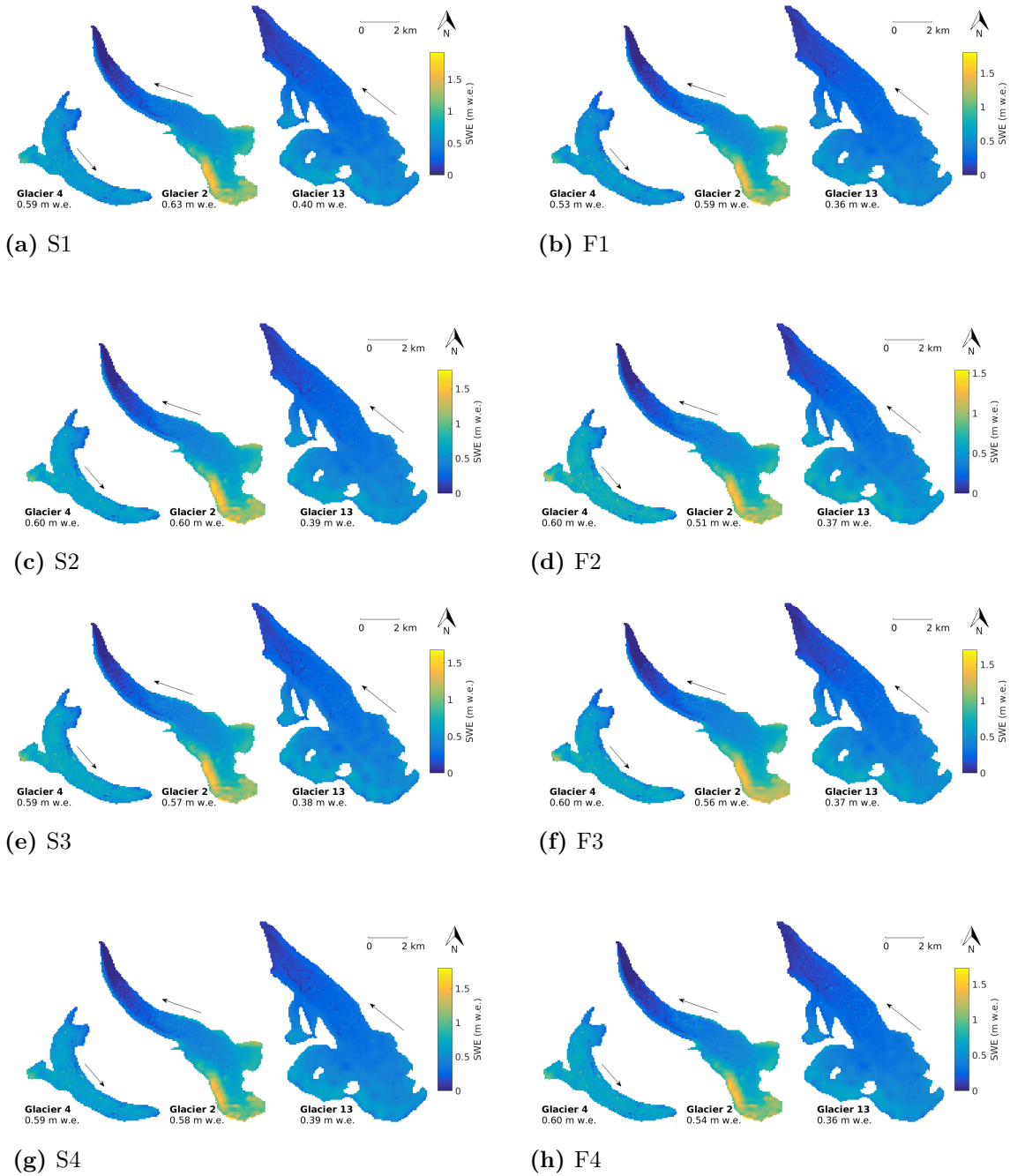


Figure 4.11: Map of modelled SWE using the MLR coefficient values for all density options. Measured SWE is plotted as overlaid filled circles. Glacier flow directions are indicated by black arrows and mean estimated SWE values for each glacier are shown.

4.1.5 Bayesian Model Averaging (BMA)

Background

Bayesian model averaging (BMA) is a method of estimating all possible linear combinations of predictor variables, in this case topographic parameters, and then averaging over all models [103, 123, 102]. This method is based on Bayesian principals in which the probability of an outcome is determined based on an initial probably distribution that is determined by the researcher, as well as the data provided. Given that the predictive outcome has a probability distribution of x given y , written as $P(x|y)$, we use Bayes' theorem to to write this as

$$P(x|y) = \frac{P(y|x)P(x)}{P(y)}. \quad (4.5)$$

$P(x|y)$ is often called the posterior model probability (PMP). The quantity $P(y|x)$ is the likelihood function, which determines unknown parameters from a known outcome (i.e. observed data). The term $P(x)$ is an observer determined prior probability distribution (typically just called a *prior*) and it reflects the prior knowledge of the system [103]. Choosing an appropriate prior is one of the most challenge components of Bayesian probability theory [123]. The $P(y)$ term can be obtained by integrating $P(y|x)P(x)$ over all x and is thus a constant for all models that is typically discarded [123].

Together then, the posterior model probability is a function of both the model prior, specified by the researcher, as well as the distribution of the observed data — the PMP is the transformation of the prior as a result of considering collected data [123]. This can be loosely expressed as

$$\text{posterior} \propto \text{prior} \times \text{likelihood}. \quad (4.6)$$

If the prior is uninformative then the posterior will be strongly influenced by the data [123]. An informative prior will result in a posterior that is a mix of the prior and the data. As the prior becomes more informative, the amount of data needed to transform the distribution increases. If there is a large amount of data then the prior will have little effect on the posterior. The final coefficients for the linear combination of predictor variables is often reported as posterior distribution means or values that maximize the log-likelihood.

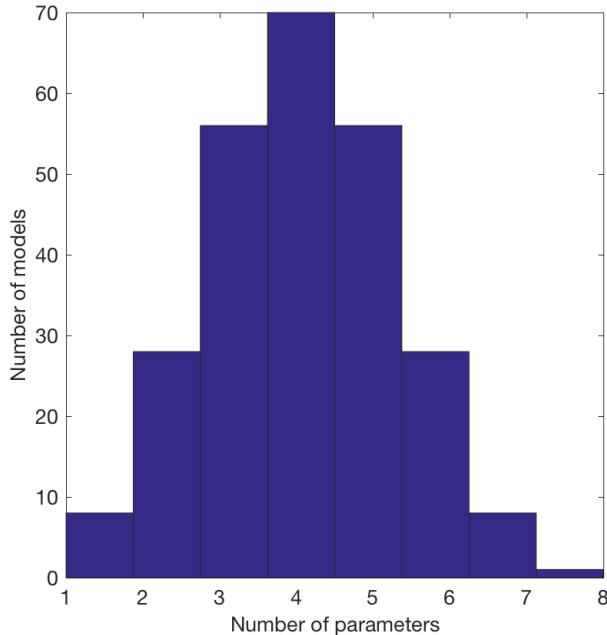


Figure 4.12: Uniform model prior for eight topographic regressors used in BMA.

distribution increases. If there is a large amount of data then the prior will have little effect on the posterior. The final coefficients for the linear combination of predictor variables is often reported as posterior distribution means or values that maximize the log-likelihood.

Within BMA, Bayes' theorem is used to find the posterior model probability and the PMP is used as a weight when averaging over all models [123]. The model weighted posterior distribution for the coefficients β of k models after normalization is given by

$$P(\beta|y, X) = \sum_{i=1}^{2^k} P(M_i|X, y)P(\beta|M_i, y, X), \quad (4.7)$$

where the responding variable is given by y and the matrix of variables is given by X [103]. Here, the model prior is $P(M_i|X, y)$ and the likelihood of the β coefficient is $P(\beta|M_i, y, X)$.

There are a number of different priors to describe model size distribution that have been applied in BMA. A commonly used prior is the ‘uniform’ prior, which assumes a normal model distribution with a total of 2^n models, where n is the number of regressors [123]. This model prior states that the observer has no knowledge of the system and all models are equally likely. The uniform prior has a prior model probability of the form $P(M_i) = 2^{-n}$ (Figure 4.12), which is symmetric about the mean $n/2$ [136]. This prior inherently favours models of an intermediate size.

Other types of priors include those that are skewed to favour smaller models, ones with equal probability for all model sizes, and ones with varying probability for individual regressors. In this project, a uniform prior was chosen for two reasons. First, there was no knowledge of the model distribution so we aim to minimize the observer influence on the final distribution. Second, the MLR estimation (Section 4.1.4) assumes a uniform distribution so choosing a uniform distribution for BMA allows for consistency between methods. Using a uniform distribution is commonly done in BMA [123].

With a small number of regressors, the posterior of all possible models can be determined. However, with a large set of regressors, this computation becomes increasingly expensive. To reduce computation time for a large set of regressors, BMA can use Markov chain Monte Carlo (MCMC) model composition to directly approximate the posterior distribution [123]. In our study, there are eight regressors so $2^8 = 256$ models. It is possible to visit all models and to obtain an exact solution so an MCMC model composition was not employed.

BMA allows for the calculation of a metric called the posterior inclusion probability (PIP), which is used to evaluate the importance of a regressor in explaining the observed data. PIP is the sum of all posterior model probabilities (PMP) where the variable was included in the model [136]. A higher PIP indicates that the regressor is more important in the regression.

Methods

The BMA process was implemented in R (Appendix F), using the Bayesian model statistics (BMS) package developed by [136]. The package computes the posterior distribution

mean value of all β coefficients for topographic parameters as well as the percent variance explained by each parameter.

Results and Discussion

The regression coefficients generated using BMA and their relative importance is similar to those generated by MLR. The most important topographic parameter is Sx on Glacier 4 and elevation (z) on Glaciers 2 and 13 (Tables 4.2 and 4.4). The variance explained by the BMA models is also comparable to that of the MLR models (Figures 4.13 and 4.14). The distribution of residuals is largest for Glacier 4 as a result of the poor fit of the regression (Figures 4.15). For a more detailed discussion of the regression of SWE and topographic parameters refer to Section 4.1.4.

The distribution of estimated glacier-wise SWE is different between glaciers but consistent with the distribution found using MLR (Figures 4.18). The estimated SWE range is greatest for Glacier 2 and there are a large number of outliers on Glacier 4. Mean estimated SWE decreases with distance from the topographic divide, which is consistent with the observed mean SWE (Figure 3.6). The distribution of residuals from the regression has a similar distribution between different density options (Figure 4.15) but it differs considerably between glaciers (Figure 4.16), which is similar to that of MLR. The largest residuals are found on Glacier 4 (Figure 4.17) because of the poor explanatory power of the regression. The range of regression coefficient values found using the different density options (Figure 4.19) and the semi-partial correlation range (Figure 4.20) are also similar to those found using MLR. The glacier wide estimates of SWE (Figure 4.21), difference between density option variation in SWE (Figure 4.22), and SWE difference as percent (Figure 4.23) resemble those of MLR. The mean percent difference is highest for Glaciers 2 and 13 (22%) and lowest for Glacier 4 (15%). For a more detailed analysis of estimated SWE found using the regression coefficients, see Section 4.1.4. These consistent results indicate that the choice of regression method does not strongly affect the final regression of SWE and topographic parameters.

Table 4.4: BMA coefficients for topographic regression between measured SWE and standardized topographic parameters. Topographic parameters are distance from centreline (d_C), elevation (z), aspect (α), slope (m), northness (N), curvature (κ), and Sx. Since parameters are standardized, the magnitude of the coefficients is representative of their importance in predicting SWE. The root-mean-squared error (RMSE) between modelled SWE using those coefficients and observed SWE is also given. See Table 4.1 for description of density options.

	Parameter	S1	F1	S2	F2	S3	F3	S4	F4
Glacier 4	z	0.007	0.010	0.004	0.003	0.014	-0.001	0.005	0.004
	d_C	<0.001	<0.001	-0.001	-0.002	-0.001	-0.002	<0.001	-0.001
	α	-0.022	-0.004	-0.008	-0.012	-0.015	-0.006	-0.007	-0.008
	m	-0.004	-0.003	-0.005	-0.004	-0.017	-0.007	-0.001	-0.013
	N	-0.006	-0.003	<0.001	-0.001	-0.005	-0.002	-0.003	<0.001
	κ	0.008	0.026	0.026	0.012	0.008	0.014	0.029	0.005
	Sx	-0.061	-0.044	-0.047	-0.047	-0.056	-0.051	-0.046	-0.052
Glacier 2	Intercept	0.618	0.578	0.623	0.631	0.618	0.635	0.614	0.637
	RMSE	0.104	0.099	0.104	0.098	0.110	0.110	0.108	0.112
	z	0.123	0.105	0.118	0.102	0.103	0.117	0.107	0.113
	d_C	0.005	0.015	0.010	0.006	0.011	0.003	0.009	0.004
	α	-0.010	-0.022	-0.014	-0.006	-0.018	-0.004	-0.006	-0.007
	m	0.035	0.018	0.024	0.033	0.033	0.030	0.031	0.028
	N	0.013	0.025	0.016	0.005	0.018	0.006	0.003	0.011
Glacier 13	κ	0.001	<0.001	0.002	0.002	0.006	0.004	0.001	0.002
	Sx	0.037	0.034	0.032	0.033	0.039	0.037	0.042	0.036
	Intercept	0.280	0.263	0.273	0.235	0.275	0.241	0.276	0.243
	RMSE	0.082	0.075	0.078	0.068	0.077	0.070	0.081	0.070
	z	0.061	0.054	0.056	0.057	0.044	0.056	0.054	0.054
	d_C	<0.001	<0.001	0.001	<0.001	<0.001	<0.001	<0.001	0.001
	α	-0.001	<0.001	-0.002	-0.002	<0.001	-0.002	<0.001	<0.001
Glacier 13	m	0.001	<0.001	0.002	-0.001	<0.001	<0.001	<0.001	0.001
	N	0.001	0.001	0.002	0.001	0.001	<0.001	0.001	<0.001
	κ	-0.021	-0.018	-0.016	-0.019	-0.021	-0.019	-0.023	-0.016
	Sx	0.003	0.003	0.007	0.001	0.006	0.005	0.001	0.002
Intercept	0.236	0.222	0.238	0.219	0.248	0.210	0.243	0.209	
	RMSE	0.063	0.056	0.063	0.058	0.068	0.056	0.067	0.052

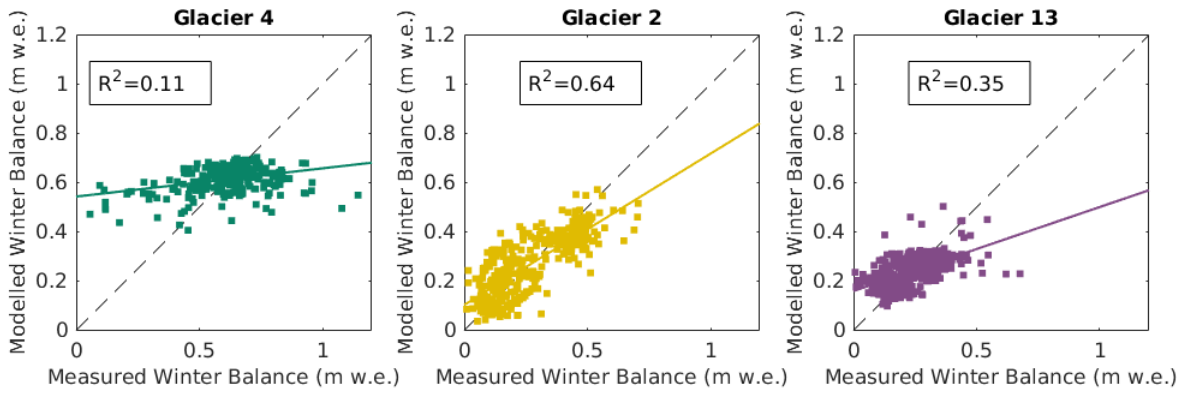


Figure 4.13: Comparison of predicted (BMA) and observed (original) snow water equivalent (SWE) for three study glaciers. The SWE values were calculated inverse distance weighted snowpit densities (S4).

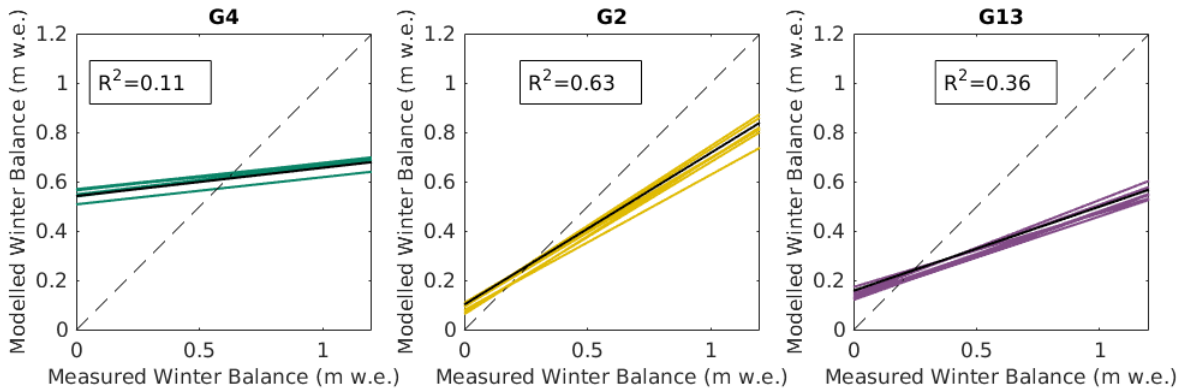


Figure 4.14: Plot of all linear fits between modelled (BMA) and observed SWE using eight options for calculating density. Mean R^2 value is shown for each sub-plot and a reference 1:1 line is also provided. See Figure 4.13 for a plot of the data.

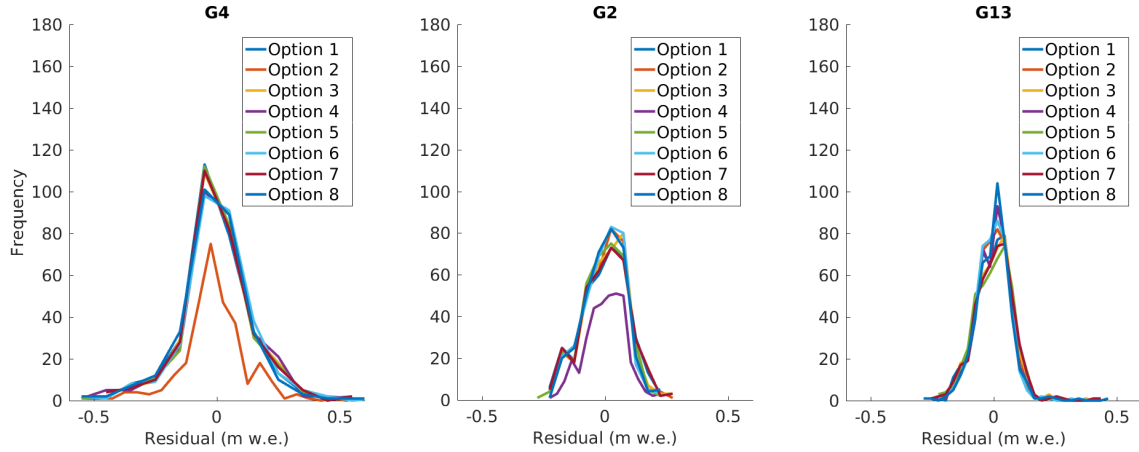


Figure 4.15: Residuals of SWE predicted using BMA for all options of estimating density.

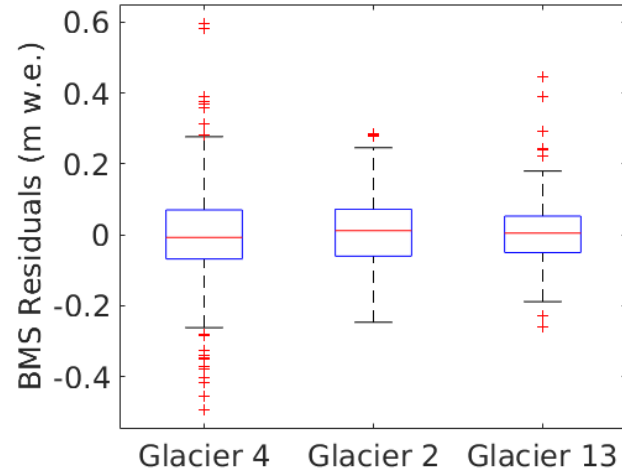


Figure 4.16: Summary of residuals from estimated SWE values found using BMA coefficients (S4). Red line indicates median, blue box shows first quantiles, bars indicate minimum and maximum values (excluding outliers), and red crosses show outliers, which are defined as being outside of the range of 1.5 times the quartiles (approximately $\pm 2.7\sigma$).

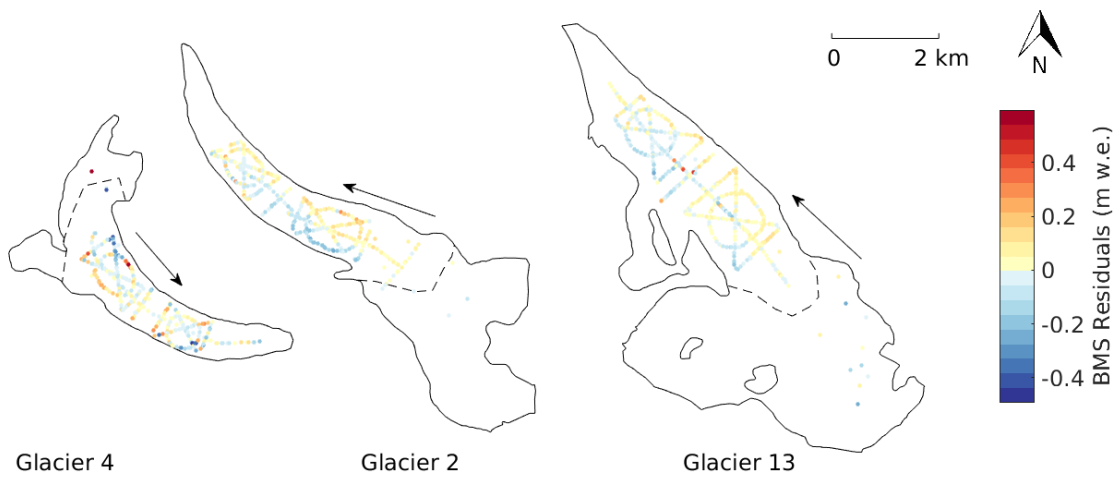


Figure 4.17: Map of the residuals from estimated SWE values found using BMA coefficients (S4) for each measurement location.

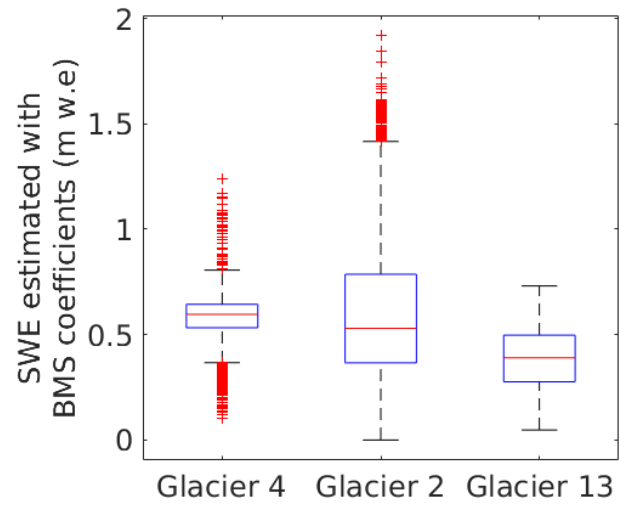


Figure 4.18: Summary of estimated SWE values found using BMA coefficients (S4). Red line indicates median, blue box shows first quantiles, bars indicate minimum and maximum values (excluding outliers), and red crosses show outliers, which are defined as being outside of the range of 1.5 times the quartiles (approximately $\pm 2.7\sigma$).

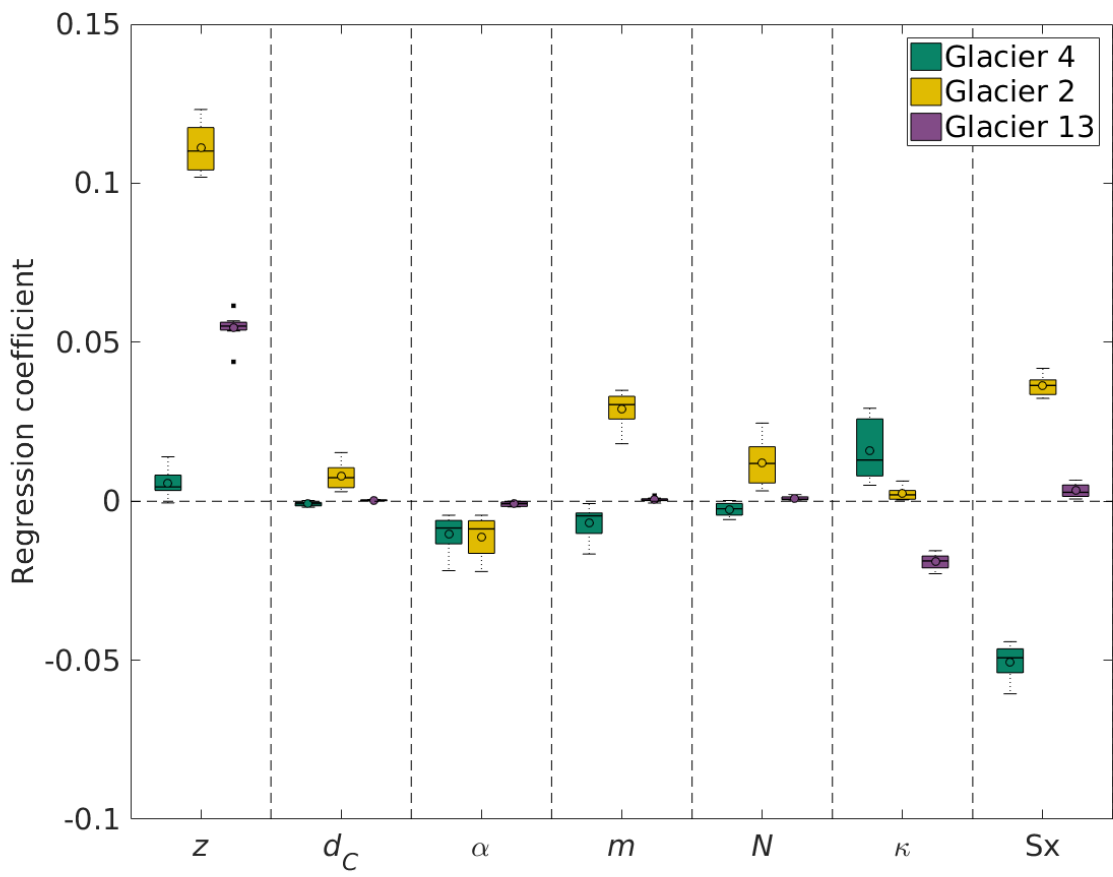


Figure 4.19: Boxplot showing the range of regressor coefficients explained by each topographic parameter for each option of estimating snow water equivalent (SWE) using BMA. Topographic parameters are distance from centreline (d_C), elevation (z), aspect (α), slope (m), northness (N), curvature (κ), and Sx. Within each box, the mean is shown as a circle, the median as a horizontal line, the interquartile range (IQR) as a coloured box, two times the IQR as dashed lines beyond the box, and outliers as single points.

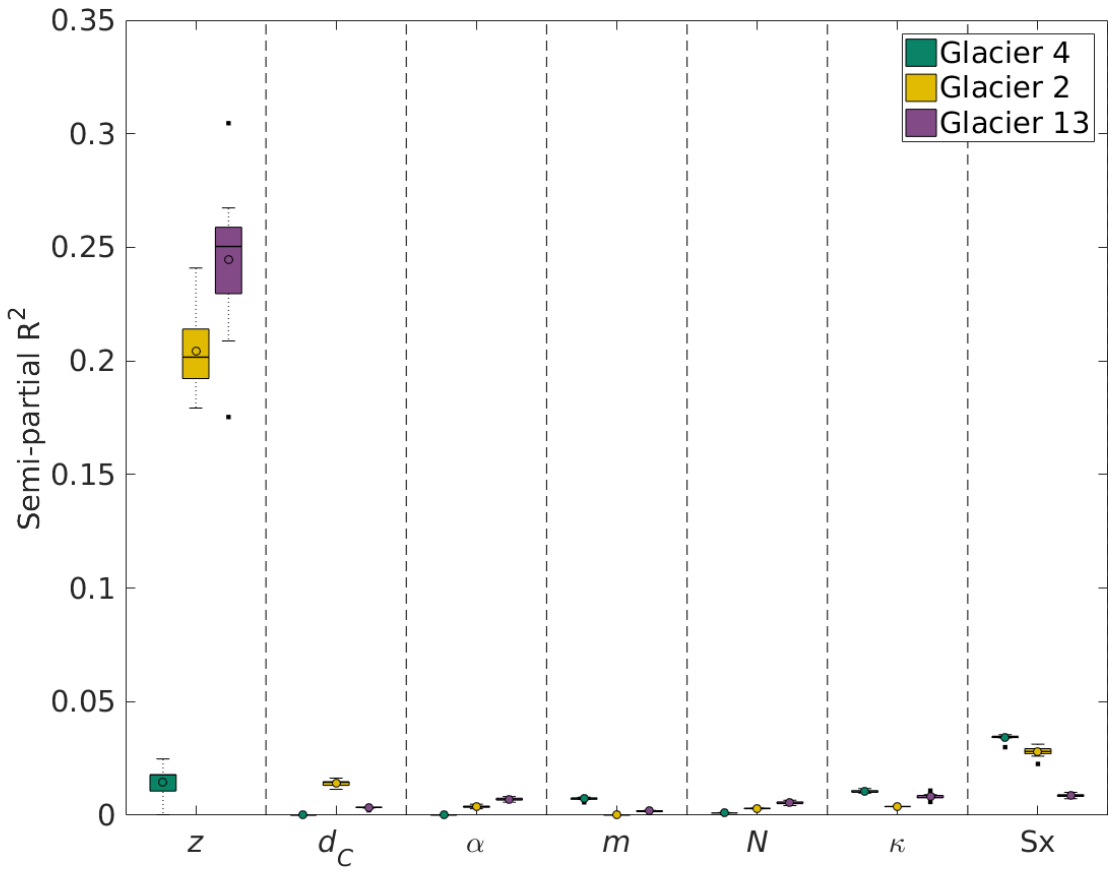


Figure 4.20: Boxplot showing the range of semi-partial correlation explained by each topographic parameter for each option of estimating snow water equivalent (SWE) using BMA. Topographic parameters are distance from centreline (d_C), elevation (z), aspect (α), slope (m), northness (N), curvature (κ), and Sx . Within each box, the mean is shown as a circle, the median as a horizontal line, the interquartile range (IQR) as a coloured box, two times the IQR as dashed lines beyond the box, and outliers as single points.

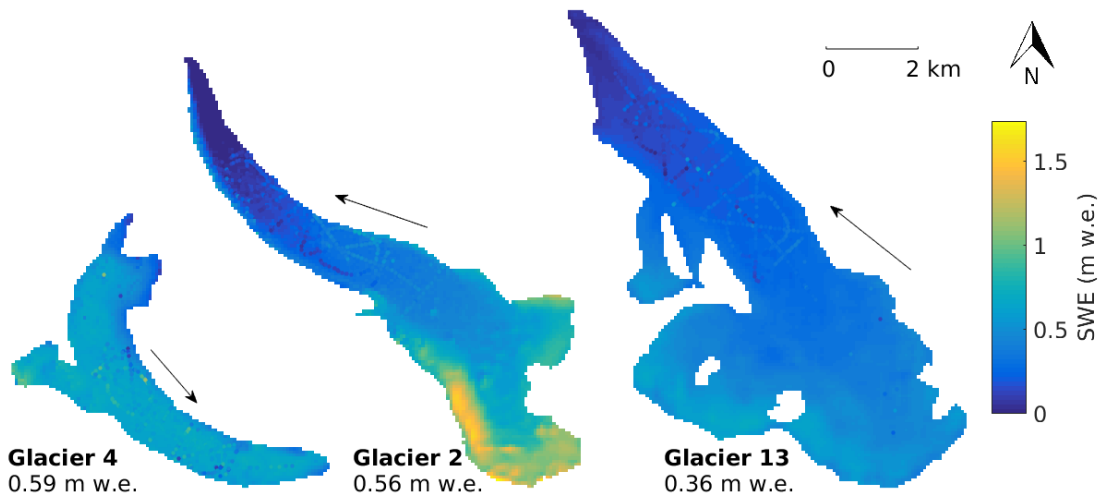


Figure 4.21: Modelled SWE using coefficients determined using BMA and density interpolated with inverse-distance weighting from snowpits (S4). Observed SWE values are overlain on the maps. Arrows indicate glacier flow direction and black dots show snow depth sampling locations.

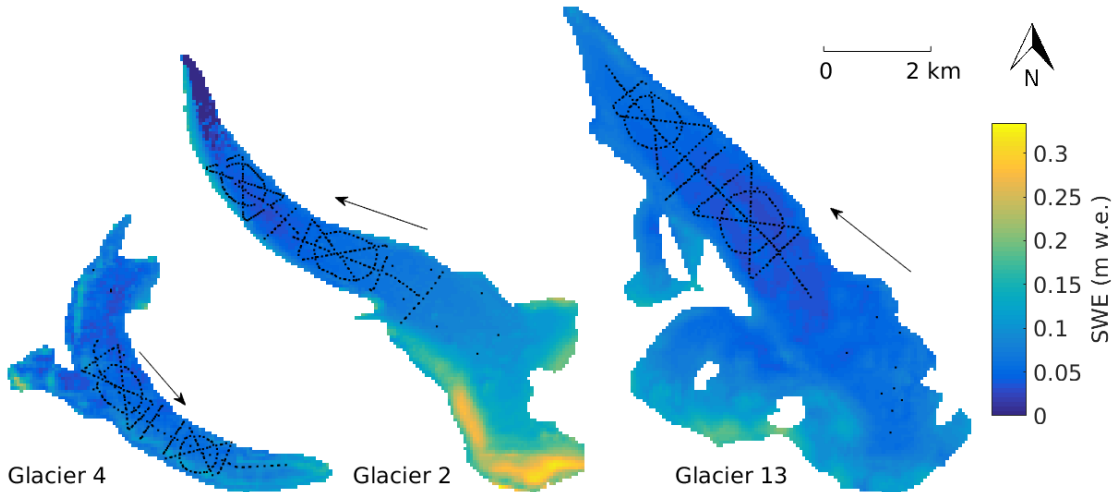


Figure 4.22: Map of the difference between maximum and minimum SWE values for each DEM cell between all density options using BMA coefficients. Arrows indicate glacier flow direction and black dots show snow depth sampling locations.

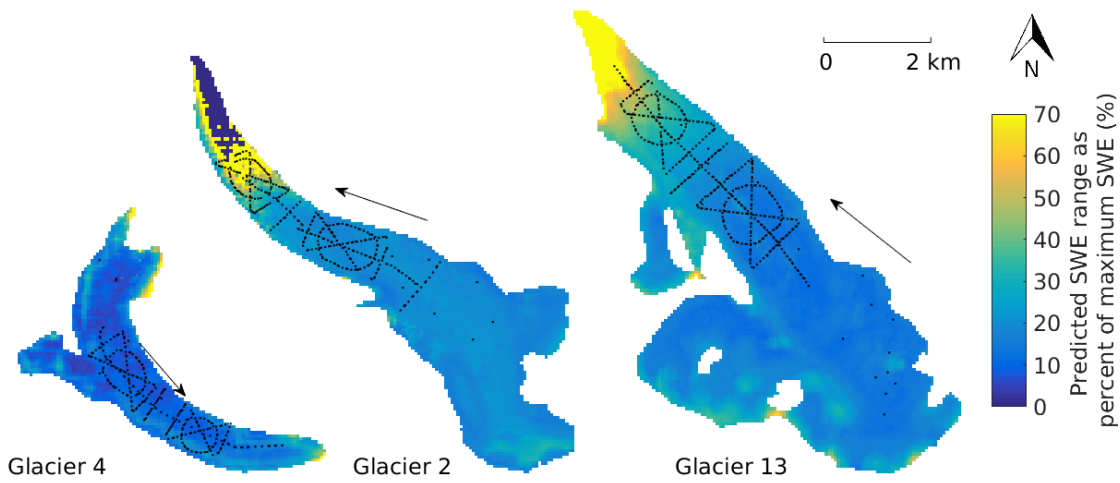


Figure 4.23: Map of the difference between maximum and minimum SWE values, expressed as a percent of the mean SWE, for each DEM cell between all density options using BMA coefficients. The colours have been scaled to highlight difference in the main part of the glaciers. Arrows indicate glacier flow direction and black dots show snow depth sampling locations.

4.1.6 MLR and BMA comparison

The range of coefficient values resulting from different choices in density interpolation found using MLR and BMA is similar for all glaciers (Figure 4.25). The range of coefficient value for all glaciers are not significantly different between MLR and BMA ($p>0.05$). Visually, these ranges always overlap, although the mean and median values can differ between these two methods. The range of unimportant variables is always small, indicating that for all density options these coefficients are small.

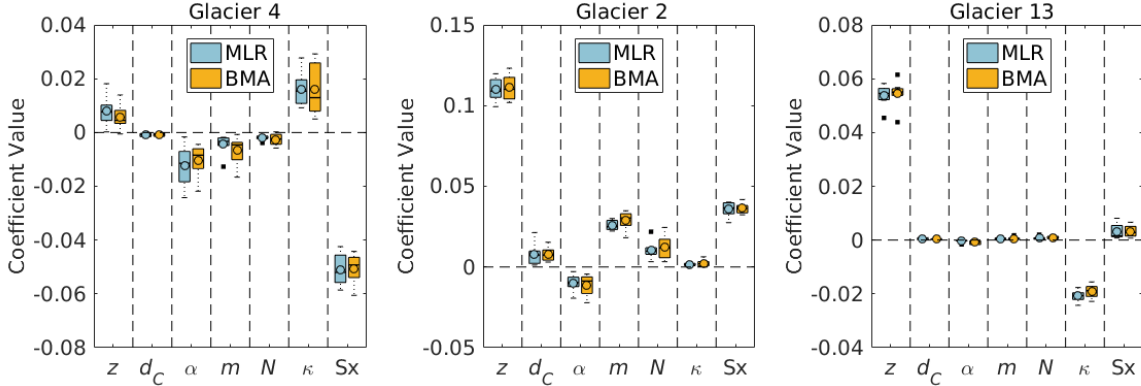


Figure 4.25: Boxplot showing the range of values of coefficients for each topographic parameter from both MLR and BMA analysis for Glacier 4 (left), Glacier 2 (middle), and Glacier 13 (right). Note the different y axes for the three glaciers. Topographic parameters are distance from centreline (d_C), elevation (z), aspect (α), slope (m), northness (N), curvature (κ), and Sx . Within each box, the mean is shown as a circle, the median as a horizontal line, the interquartile range (IQR) as a coloured box, two times the IQR as dashed lines beyond the box, and outliers as single points.

The aspect, curvature, and Sx coefficients for Glacier 4 have the largest range of coefficients. Regardless of the choice of density option, the relative importance of these coefficients is the same (i.e. Sx will always be the most important). For Glacier 4, the choice of density option has a negligible impact on modelled SWE values - the regression fit is so poor that the fit does not change with the choice of density interpolation method (Figure 4.1 and 4.14). MLR and BMA appear to have similar ranges of coefficient values, although the mean and median within each regression method differs for Sx and slope, with MLR producing larger coefficients.

The range of coefficient values for Glacier 2 and 13 is generally small for all parameters indicating that the choice of density option does not have a large impact on modelled SWE. The range is especially small for Glacier 13 and most coefficients are close to zero, with the exception of elevation and curvature. This highlights the large semi-partial correlation of elevation on Glacier 13. Further, the relative importance of the coefficients does not change

Table 4.5: ANOVA p-values between estimated SWE found using MLR and BMS regression coefficients for various density options. Significance is taken to be $p < 0.05$.

Density Option	Glacier 4	Glacier 2	Glacier 13
S1	0.03	0.14	<0.01
F1	<0.01	0.08	<0.01
S2	<0.01	0.37	<0.01
F2	0.97	<0.01	0.34
S3	<0.01	<0.01	<0.01
F3	0.02	0.84	<0.01
S4	0.04	0.93	0.14
F4	0.01	0.01	0.96

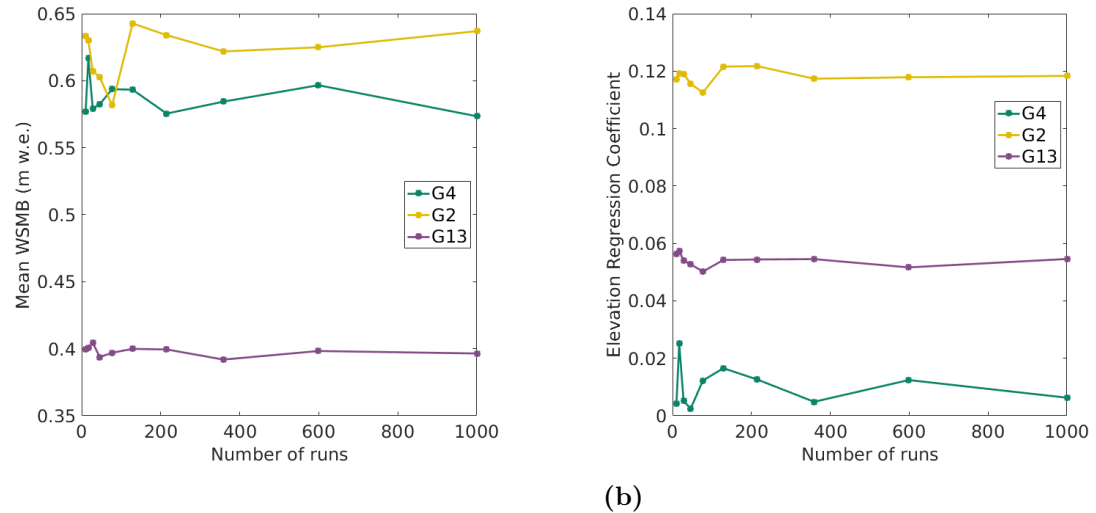


Figure 4.26: (a) Mean winter balance and (b) elevation regression coefficient found with varying number of runs for cross validation.

with choice of density option. The greatest range of coefficient values is for elevation, which is also the most significant coefficient. The type of regression model used does not appear to have a large impact on the coefficient values.

For all glaciers, the BMA regression produced a smaller RMSE and a slightly higher R^2 . It is not clear why the BMA regression is better at minimizing RMSE. For some density options, estimated values of SWE can be significantly different when found using either MLR- or BMA-derived coefficients (Table 4.5). Although the range of coefficients is not different between BMA and MLR, the resulting SWE values are significantly different.

4.1.7 Number of cross validation runs

Cross validation is used to prevent overfitting of the regression coefficients in both MLR and BMA. A random subset of the data is used to fit the regression and a RMSE is calculated using the remaining data. The process is repeated 1000 times and the coefficients with the lowest RMSE are chosen. The number of runs is large to ensure that the regression coefficients that result in the lowest RMSE are found. However, computational expense increases with the number of runs so it is desirable to determine the minimum number of runs that provide a reliable set of regression coefficients.

The mean winter balance for each glacier does not appear to vary after about 200 runs (Figure 4.26). The value of the elevation regression coefficient, which is the most important coefficient for Glaciers 2 and 13, also does not change considerably after 200 runs. A similar decrease in variation is seen for the remaining important regressors (not shown). Therefore,

the number of cross validation runs can be decreased to 200 for future analysis if decreased computational time is desired.

4.2 Kriging

4.2.1 Background

Physical surfaces vary continuously and must therefore be spatially correlated at short distance but statistically independent at large distances [31]. If sampling points are distributed throughout a surface, the degree of spatial correlation of the observed surface can be determined and the surface can then be interpolated between sampling points. Kriging is a geostatistical interpolation method that finds a set of optimal weights for the values at each sampling location based on the spatial correlation of measured values and then estimates values at unsampled locations [31, 73]. The kriging estimate (\hat{z}) at point x_0 is found using the equation

$$\hat{z}(x_0) - \mu = \sum_{i=1}^n \lambda_i [z(x_i) - \mu(x_0)], \quad (4.8)$$

where μ is a known stationary mean, λ_i is a kriging weight, $z(x_i)$ is the measured value of the surface at point x_i , n is the number of sampled points used to make the estimation (depends on size of sampling window), and $\mu(x_0)$ is the mean value of sampled points in the search window [120, 72]. Slight variations on Equation 4.8 result in various forms of kriging that are suited for different data sets. The kriging weights are estimated by minimizing the variance or the squared error, which is given by

$$\text{var}[\hat{z}(x_0)] = E[(\hat{z}(x_0) - z(x_0))^2] \quad (4.9)$$

$$= \sum_{i=1}^n \sum_{j=1}^n \lambda_i \lambda_j C(x_i - x_j) + C(x_0 - x_0) - 2 \sum_{i=1}^n \lambda_i C(x_i - x_0), \quad (4.10)$$

where $C(x_i - x_j) = \text{Cov}[z(x_i), z(x_j)]$ is the covariance of the surface [72]. Kriging assumes that the variance does not depend on the sample location, but depends only on distance between samples. Anisotropic kriging allows for variance to change with direction but the variance still does not depend on sample location. Isotropic variance was assumed in this study.

A physical surface is usually assumed to be noisy and this noise is captured by a “nugget” parameter that allows for the surface to vary smoothly and thus, not pass directly through each measured point. The nugget is a residual that encompasses sampling-error variance as well as the spatial variance at distances less than the minimum sample spacing [72]. Spatial correlation of data is estimated using imprecise variance and is often plotted in the form of a variogram (see Section ??).

There are many forms of kriging and each one is tailored to suit different data types (see [73]). The most appropriate type of kriging for this study is simple kriging.

Simple kriging is used to estimate residuals about a constant and stationary mean μ , which is typically calculated as the average of the data. Kriged estimates for simple kriging are found by slightly modifying Equation 4.8 to

$$\hat{z}(x_0) = \sum_{i=1}^n \lambda_i z(x_i) + \left[1 - \sum_{i=1}^n \lambda_i \right] \mu. \quad (4.11)$$

Larger values of $[1 - \sum_{i=1}^n \lambda_i]$ result in estimates that are closer to the data mean [72]. The value of $[1 - \sum_{i=1}^n \lambda_i]$ generally increases in poorly sampled areas.

4.2.2 Methods

Simple kriging is implemented using the R package **DiceKriging**, which approximates functions by first generating a kriging model from input data and then estimating data values at new locations based on their distance from observed data [106]. For the SWE data, a nugget value needs to be estimated by the **DiceKriging** package because the covariance length varies considerably over short distances. For this study, the kriged surface cannot not be estimated without a nugget, indicating that the function is not purely deterministic. Maximum likelihood is used to estimate both nugget and covariance values in **DiceKriging**. Negative values of kriged SWE were set to zero. For more details on implementation of **DiceKriging** see Appendix G.

4.2.3 Results

There are large differences in spatial patterns of interpolated SWE distributions for the three study glaciers found using simple kriging (Figure 4.27). The lower half of Glacier 4 has a relatively uniform SWE, while the accumulation area has both low and high values of SWE. The low density of sampling points in the accumulation area of Glacier 4 result in large gradients in SWE. Glacier 2 has two distinct and relatively uniform areas — the lower ablation area has low SWE (~ 0.1 m w.e.) and the upper ablation and accumulation areas have higher SWE values (~ 0.6 m w.e.). The boundary between two these zones closely follows the outline of the ice dune area observed during field data collection. Glacier 13 does not appear to have any strong patterns and accumulation is generally low ($\sim 0.1\text{--}0.5$ m w.e.).

The glacier-wide winter mass balance on each glacier (B_w), calculated as the mean SWE, that is found using simple kriging is considerably different to that found using a topographic regression (Figure 4.21). Accumulation on Glacier 4 is 0.09 m w.e. (15%) higher and has larger spatial gradients in SWE when simple kriging is used. Conversely, simple kriging estimates are 0.13 m w.e. (23%) and 0.08 m w.e. (22%) lower for Glaciers 2 and 13, respec-

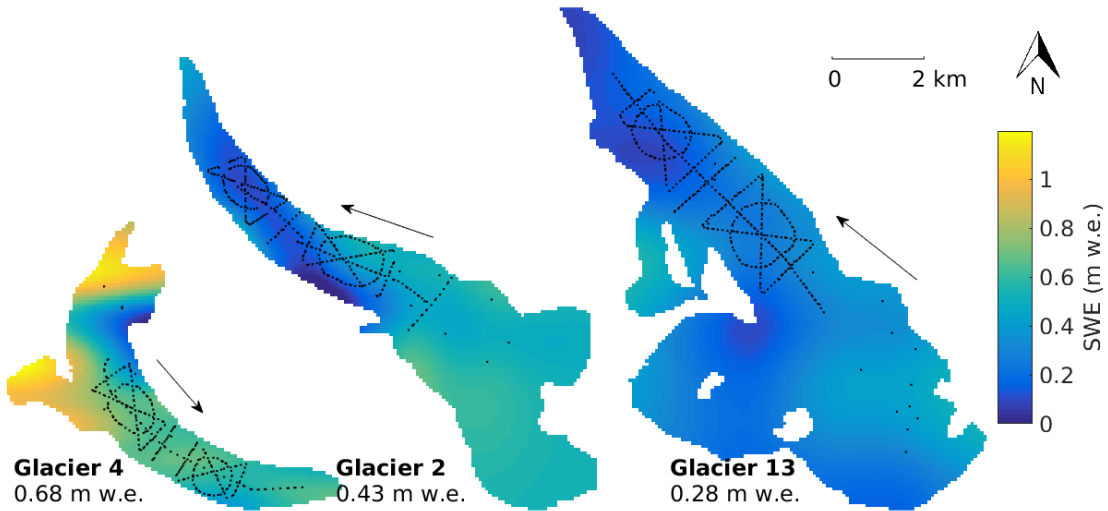


Figure 4.27: SWE distributions estimated by kriging. Arrows indicate glacier flow direction and black dots show snow depth sampling locations.

tively, and the range of SWE values is smaller. The accumulation distribution estimated by simple kriging and by regression is qualitatively similar for Glacier 13 but differs considerably for Glacier 4 and 2. Glacier 4 has large SWE values in the accumulation area when simple kriging is used, which contrasts strongly with the mostly uniform accumulation estimated with regression. The converse is observed on Glacier 2, where the simple kriging estimate has a small SWE range and two distinct regions of SWE values while the regression estimate has a large range and a significant elevation gradient in accumulation. These spatial patterns highlight that kriging is sensitive to individual observation values in areas with sparse sampling.

Estimates of the nugget found using maximum likelihood in the DiceKriging package also vary between glaciers (Table 4.6). Nugget values are small for both Glacier 2 and 13 (~ 0.004 m w.e.) and do not vary when different methods for interpolating snow density (Section 4.1.3) are used. The nugget values for Glacier 4 are an order of magnitude larger and vary by $\sim 80\%$ of the minimum nugget value for this glacier.

Comparing estimated and observed values of SWE (Figure 4.28) shows that kriging is best able to predict SWE values on Glacier 2 and that kriging has the lowest predictive power on Glacier 4. This is similar to topographic regression estimates (Figure 4.13), where the least variance was explained on Glacier 4 and the most variance was explained on Glacier 2. When compared to regression estimates, the R^2 values between SWE estimated using simple kriging and observed SWE are higher for all glaciers. Correlation values increase from 0.11, 0.63 and 0.36 to 0.25, 0.84 and 0.49 for Glaciers 4, 2 and 13, respectively. The largest difference in R^2 between these two methods is on Glacier 2, which also has the highest R^2 values. Note that the scatter of estimated and observed SWE values in Figure 4.28 is due

Table 4.6: Nugget ($\times 10^{-3}$ m w.e.) and range length (m) values for SWE data with various snow density interpolation schemes estimated using maximum likelihood in DiceKriging package. S = Snowpit density values, F = Federal Sampler density values. See Section 4.1.3 for details on density options.

Density Option	Nugget			Range length		
	G4	G2	G13	G4	G2	G13
S1	9.2	3.6	3.3	89	784	318
F1	8.0	2.7	2.9	89	364	318
S2	9.5	3.0	3.4	89	364	318
F2	9.9	2.6	3.3	89	1375	770
S3	9.5	3.1	3.8	91	350	279
F3	10.2	2.0	2.8	87	390	682
S4	9.4	3.6	3.6	88	884	294
F4	9.8	2.5	2.8	88	759	317

to the nugget, which encompasses sampling-error variance and variance at distances smaller than the sample spacing.

The confidence intervals for winter balance estimated using simple kriging are a large proportion of the estimated SWE values (Figure 4.29). The confidence interval range is at least half of the estimated SWE for all areas of the glacier, and in some areas, this proportion is more than four times the SWE estimate. The accumulation area, margin, and terminus of Glacier 2 all have especially high uncertainty.

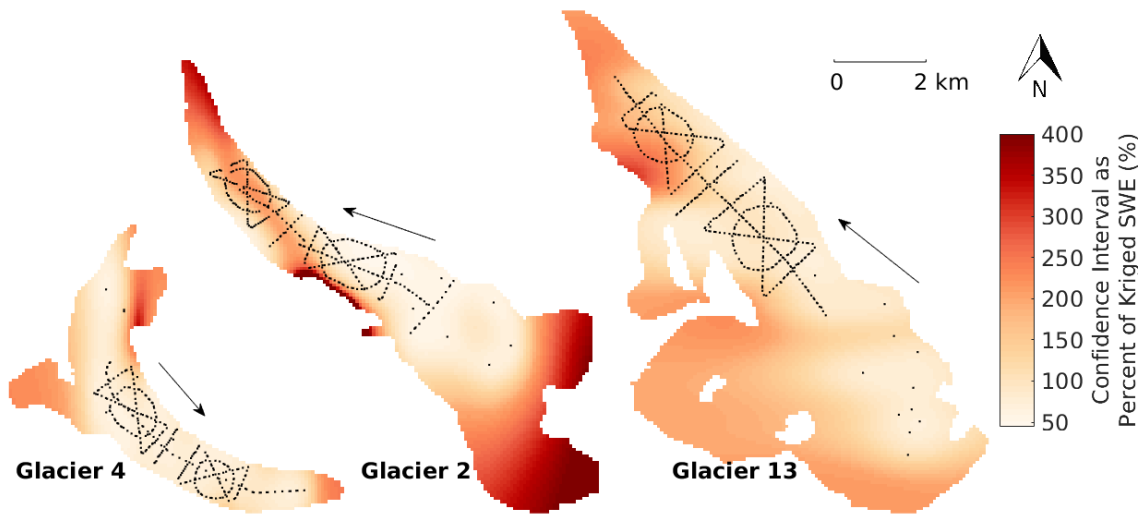


Figure 4.29: Simple-kriging winter-balance confidence interval (95%) as a percent of distributed SWE, found using kriging. The SWE value were estimated using density S4. Arrows indicate glacier flow direction and black dots show snow depth sampling locations.

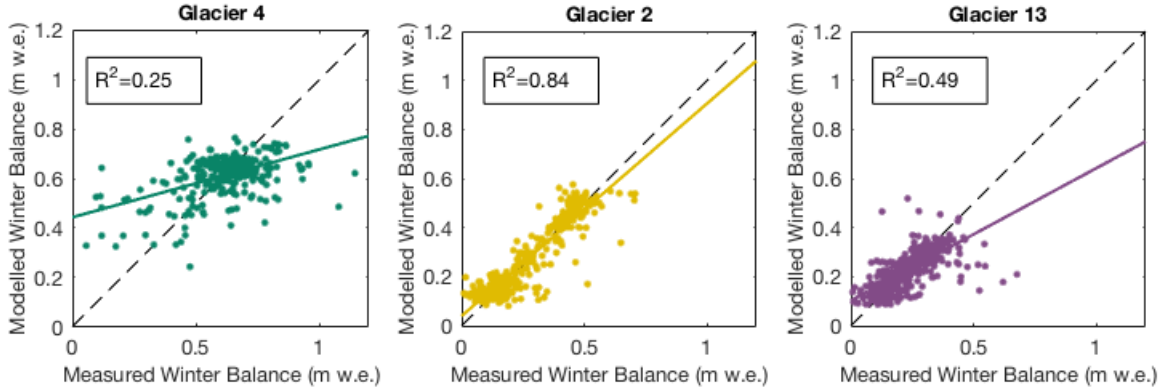


Figure 4.28: Comparison of estimated (simple kriging) and observed (original) snow water equivalent (SWE) for three study glaciers. The SWE values were calculated using inverse-distance weighted snowpit densities (S4).

4.3 Regression kriging

4.3.1 Background

Regression kriging estimates values between measurement locations by combining a regression estimate (see Section 4.1) with a kriged estimate of the regression residuals (see Section 4.2) [55]. First, the regression estimate is determined using auxiliary variables (e.g. terrain parameters such as elevation and slope). Then, simple kriging is used to interpolate regression residuals, which have assumed mean of zero. The two surface estimates are then added. The final estimate can be written as

$$\hat{z}(x_0) = \hat{m}(x_0) + \hat{e}(x_0) \quad (4.12)$$

$$= \sum_{k=0}^p \hat{\beta}_k \cdot q_k(x_0) + \sum_{i=1}^n \lambda_i \cdot e(x_i), \quad (4.13)$$

where $\hat{m}(x_0)$ is the regression estimate and $\hat{e}(x_0)$ is the interpolated residual, $\hat{\beta}_k$ are the estimated regression coefficients, $q_k(x_0)$ are the regressors, p is the number of regressors, λ_i are the kriging weights for the residuals, and $e(x_i)$ is the residual at x_i .

Regression kriging can be thought of as an intermediate between pure kriging (no regression) and pure regression (small residuals) and can be more strongly skewed to either end-member based on the strength of the regression correlation [55]. Regression kriging is mathematically equivalent to universal kriging, in which auxiliary variables are used directly to determine the kriging weights [55]. However, separating the trend analysis and kriging steps has the advantage of being able to test regression methods that go beyond a basic

linear trend. Kriging combined with regression has been found to produce better estimates of spatial fields when compared to simple kriging and co-kriging [65].

4.3.2 Methods

First, SWE values are estimated with a regression of topographic parameters, as described in Section 4.1. The BMA regression is used for regression kriging because it resulted in a better fit than MLR between estimated and observed SWE. Second, the BMA residuals at each measurement location are calculated and the distributed residuals are found using simple kriging, as described in Section 4.2. The BMA-estimated distributed SWE and kriging-estimated distributed residuals are then added together to obtain the final distributed winter balance.

4.3.3 Results

The range, magnitude and spatial pattern of estimated regression residuals found using simple kriging varies between the three study glaciers (Figure 4.30). Generally, the range of residual values is highest on Glacier 4 and lowest on Glacier 13. Extreme values are located in the accumulation area of Glacier 4 with both strongly negative and strongly positive residuals located within a kilometre of each other. The low density of sampling points in the accumulation area biases the interpolation of residuals to fit the over- and underestimation of SWE at the two uppermost sampling locations. Residuals show less variation on Glacier 2, although relatively large residuals of approximately ± 0.4 m w.e. are present in the upper ablation area along the ice margins. Glacier 13 has the smallest range of residuals but residual values are approximately equal to those of estimated SWE. The mean value of distributed residuals is positive for Glacier 4, indicating that the distributed residuals will increase the overall estimate of winter balance. Conversely, the mean residual for Glacier 2 is negative and will decrease the estimated winter balance.

The winter balance found using simple kriging and regression kriging (Figure 4.31) shows a gradient in accumulation across the mountain range. Glacier 4 has the highest mean SWE and Glacier 13 has the lowest mean SWE. However, the accumulation gradient is steeper for simple kriged estimates than for regression kriged estimates. Glacier 4 has a similar mean SWE between the two methods but mean SWE on Glaciers 2 and 13 are much lower. All three glacier have the largest values of SWE in the upper part of the accumulation areas.

SWE distribution estimated using regression kriging is similar to the winter balance estimated using topographic regressions for Glaciers 2 and 13 (Figure 4.31). The similarity is due to the relatively high explanatory power of the regressions, so the regression kriging estimate is closer to a pure regression. The distribution of SWE on Glacier 4 is more strongly affected by the kriged residuals because the regression had low explanatory power, resulting in larger residual values that changed the snow distribution, particularly in the accumulation area. The regression kriging for Glacier 4 is therefore closer to pure kriging.

Regression kriging produces the highest overall set of R^2 values (Figure 4.32). The correlation coefficient for Glacier 2 is especially high, with more than 80% of the variance in observed SWE explained by the regression kriging model. Glacier 4 has the lowest correlation coefficient but this value is considerably higher than that of topographic regression or simple kriging.

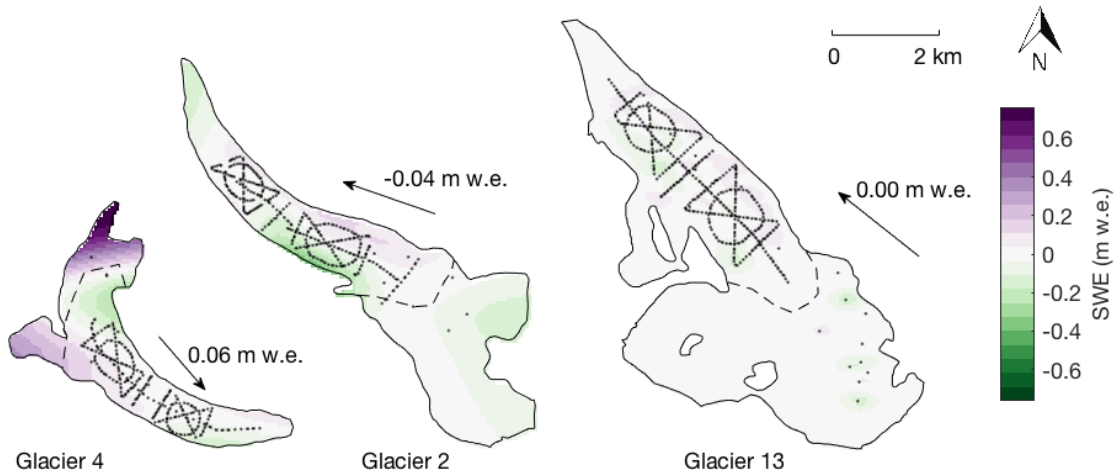


Figure 4.30: Distributed BMA residuals estimated by simple kriging. Arrows indicate glacier flow direction and black dots show snow depth sampling locations. Dashed line indicates approximate ELA.

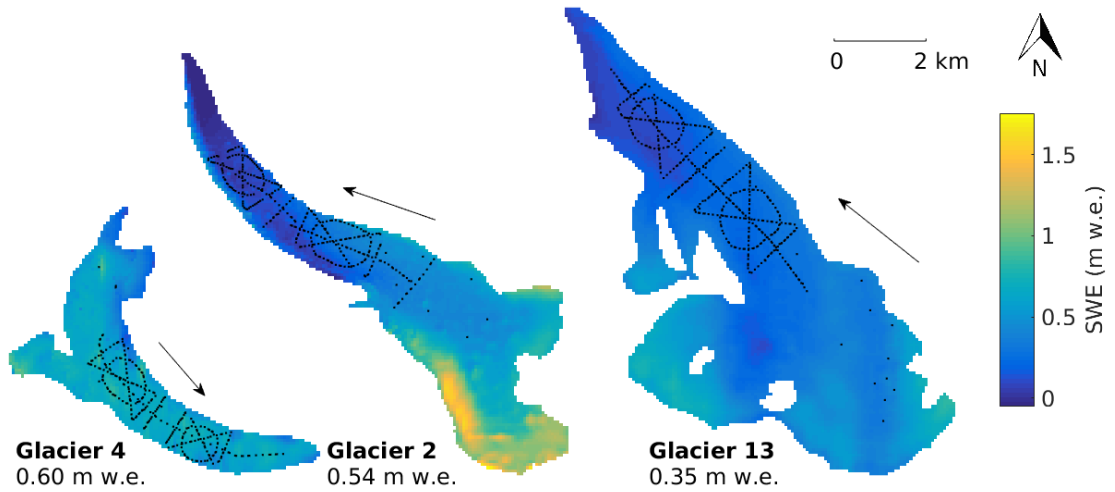


Figure 4.31: SWE distributions estimated by adding the kriged residuals to the SWE distributions estimated using topographic regression with BMA. Observed SWE values are overlaid on the maps. Arrows indicate glacier flow direction.

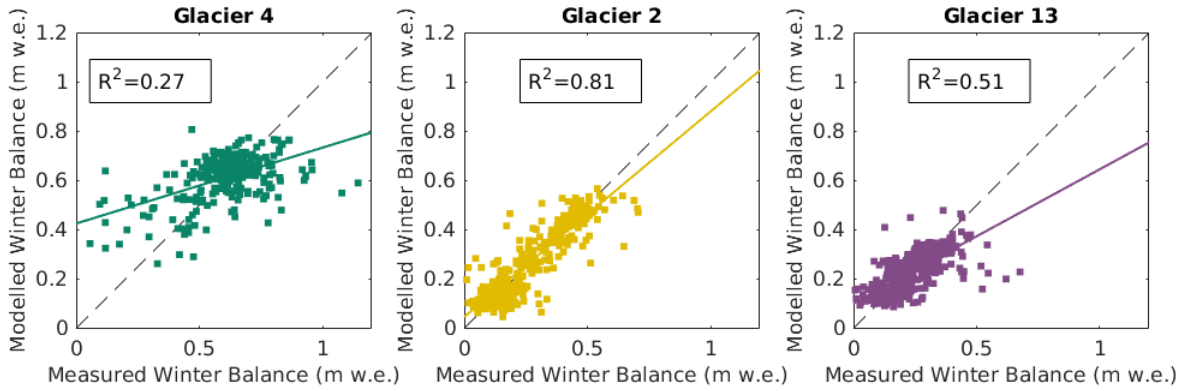


Figure 4.32: Comparison of estimated (regression kriging) and observed (original) snow water equivalent (SWE) for three study glaciers. The SWE values were calculated using inverse-distance weighted snowpit densities (S4).

4.4 Comparison of interpolation methods

The choice of interpolation method affects the mean winter balance (Figure 4.33). Kriging interpolation produces the highest mean value of SWE on Glacier 4. The estimates of SWE in the accumulation area are greatest when kriging is used because there is a single high SWE value in the accumulation area. Kriging is sensitive to outliers in areas with sparse sampling. However, the winter balance is similar between interpolation methods and mean of observed data for Glacier 4. This similarity arises from the low correlation coefficient for all methods, resulting in values closer to the data mean. The observed SWE mean values for Glaciers 2 and 13 are much lower than the estimated winter balance. Both glacier show a significant correlation between SWE and elevation, so limiting sampling to the ablation area skewed the observed values of SWE to be lower than the mean. Relative differences in mean SWE between the three interpolation methods are similar for Glacier 2 and 13, with topographic regression producing the highest mean SWE and kriging producing the lowest. Kriging estimates lower SWE in the accumulation area of both glaciers because elevation is not incorporated into the model. A mountain range accumulation gradient exists when looking at the mean SWE values found using kriging and regression kriging, as well as in the observed data, but Glaciers 4 and 2 have the sample winter balance when topographic regression is used.

For all glaciers, the topographic regression results in the lowest mean variance explained (Figure 4.34). The mean correlation coefficients for kriging and regression kriging are similar for all glaciers, with regression kriging being slightly lower than kriging. Variance explained on Glacier 4 is consistently the lowest, indicating that observed SWE values are highly

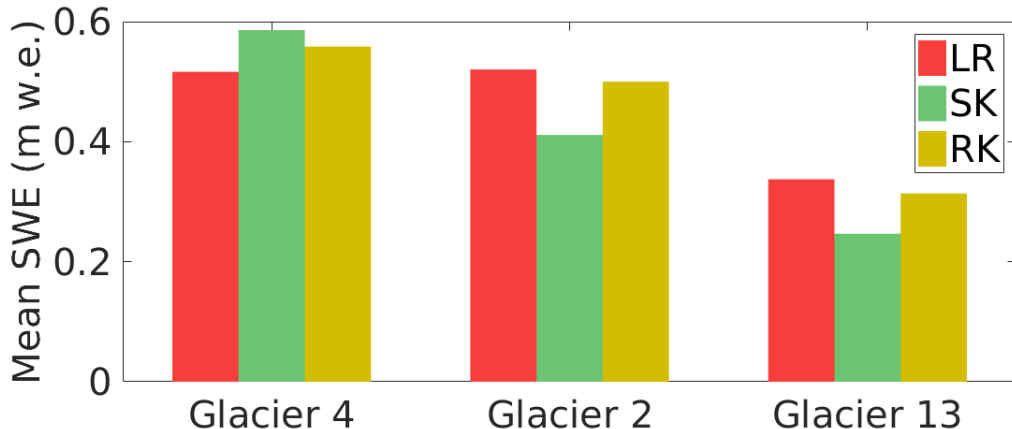


Figure 4.33: Mean observed SWE and estimated winter balance using topographic regression, kriging, and regression kriging , averaged over density options.

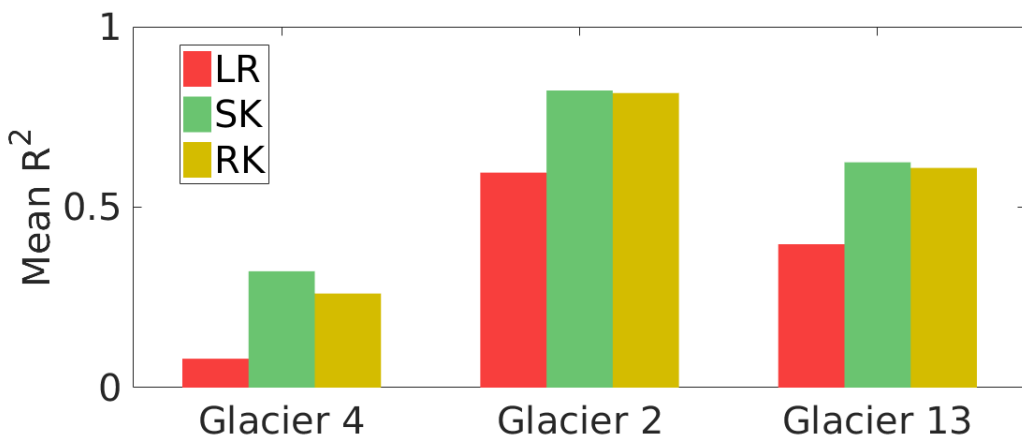


Figure 4.34: Mean correlation coefficient (R^2) between observed SWE and estimated winter balance using topographic regression, kriging, and regression kriging at sampling locations, averaged over all density options.

variable. The converse is seen on Glacier 2, where correlation coefficients are consistently high regardless of the interpolation method.

The choice of density interpolation method generally does not affect the mean SWE value and their relative magnitudes (Figure 4.35). The main exception to this is that of kriging interpolation on Glacier 2, where a difference of almost 0.25 m w.e. exists between F3 and F4. The F3 option uses a linear regression between Federal Sampler-derived density and elevation to interpolate density values. There is a positive relationship (Figure ??), which means that the elevation gradient in SWE is increased, resulting in higher SWE point measurements in the accumulation area. This in turn increases the kriging estimate for the accumulation area beyond these points and raises the mean SWE. Again, it is clear that kriging is sensitive to individual measurement in sparsely sampled areas. It is surprising

that the R^2 value for both these options is similar and high (Figure 4.36), indicating that both estimates of winter balance are equally good.

Regression kriging and kriging outperform topographic regression in predicting SWE at measurement locations (Figure 4.36). The correlation coefficient is similar for all density options on Glaciers 2 and 13. In all cases, R^2 values are highest for kriging and slightly lower for regression kriging (c.f. S3 on Glacier 13). However, the relative magnitude of R^2 values on Glacier 4 differs between kriging and regression kriging when different density options are chosen.

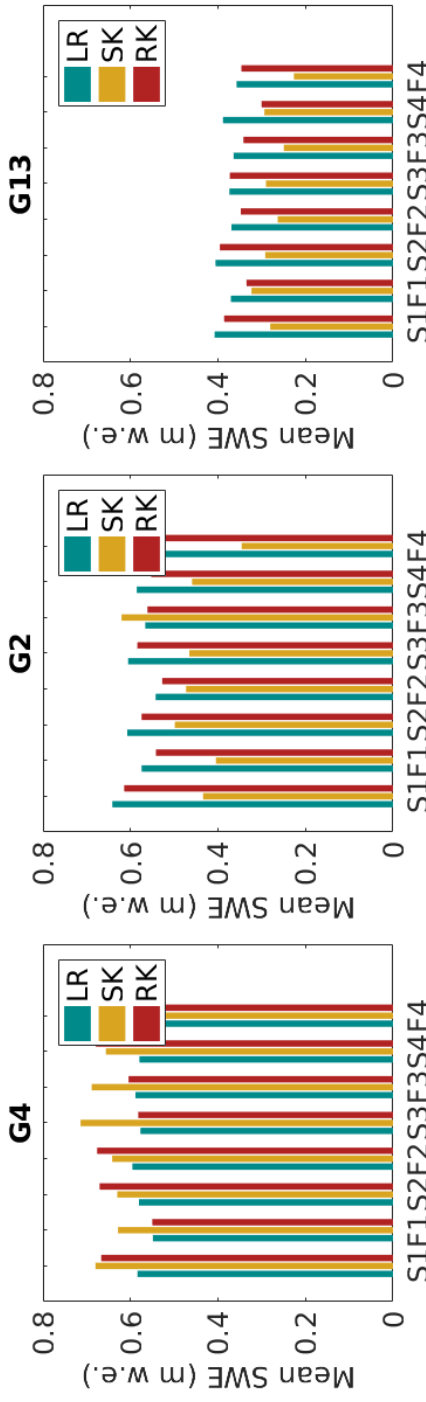


Figure 4.35: Mean SWE and mean estimated winter balance using topographic regression, kriging, and regression kriging.

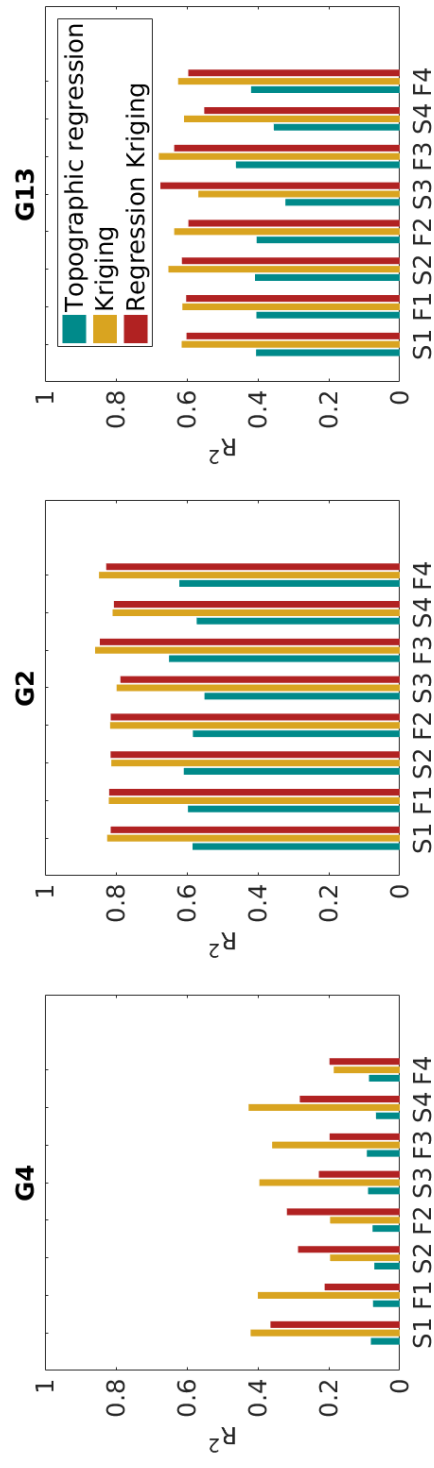


Figure 4.36: Correlation coefficient (R^2) between observed SWE and mean estimated winter balance using topographic regression, kriging, and regression kriging at sampling locations.

The two interpolation end-members, topographic regression and kriging, produce distributed fields that have different applications. Topographic regressions are, theoretically, both spatially and temporally transferable. If the field is relatively stationary then the topographic regression model can be applied to the same location at other times and/or at other locations. After the regression model is calculated, only a few measurements are needed to scale the regression values higher or lower to obtain a distributed field. Additionally, topographic parameters are chosen as proxies for physical processes so if the regression coefficients are physically realistic, extrapolation of the regression is likely to produce more realistic fields. Topographic regressions are also less sensitive to data outliers. When extreme values are present in a well sampled area, the regression will not significantly be affected, resulting in more realistic extrapolation. The main limitation of topographic regressions is that the field must be well sampled to initiate the model and the model is highly dependent on the accuracy and resolution of the DEM.

Kriging is, in theory, temporally transferable but not spatially transferable. Once kriging weights are calculated, they can be applied to the same area where the mean value is estimated with a few observations. Kriging weights cannot be applied to another location. A benefit of kriging is that the resulting field is not limited to the accuracy, resolution and availability of external data (i.e. DEM). Therefore, this interpolation technique is valuable in areas with no topographic data or at scales less than the resolution of available DEMs. Another benefit of kriging is that confidence intervals can easily be calculated for the field of interest, providing concrete bounds on the distribution of values. However, kriging often produces poor results when extrapolating data. The distributed field is highly sensitive to individual measurements with extreme values in sparsely sampled areas, so extrapolating past these points can result in unrealistic values and large confidence intervals (i.e. accumulation area of Glacier 2). Problems with extrapolation are especially prevalent when observations are locally dense but globally sparse.

4.5 Summary

??

Chapter 5

Winter Balance

5.1 Background

Winter surface mass balance is the net accumulation and ablation of snow over the winter season [24], which constitutes glacier mass input. We refer to this quantity as winter balance throughout the thesis. Accurate estimates of winter balance are critical for calculating glacier mass balance, not only because winter balance constitutes half of the glacier mass balance but also because the distribution of snow on a glacier initializes the summer balance and high snow albedo contributes to reduced summer melt [e.g. 57, 104]. Currently, uncertainty in winter balance estimates overshadow differences between melt models when estimating glacier mass balance [104]. The goal of this chapter is to show how snow variability, data error and our methodological choices interact to create uncertainty in our estimate of winter balance.

5.2 Methods

To quantify effects of uncertainty on the winter balance estimate, we conduct a Monte Carlo experiment, which uses repeated random sampling to calculate a numerical solution [85]. This random sampling process is done 1000 times, which results in a distribution of possible winter balance values based on uncertainty within the data processing steps. We quantify the effect of uncertainty as the standard deviation of the distribution. Three sources of uncertainty, which encompass error and uncertainty within each processing step, are considered: (1) density uncertainty, (2) SWE uncertainty and (3) interpolation uncertainty. Individual sources of uncertainty are propagated through the process of converting snow measurements to winter balance. Then, all three uncertainty sources are considered together and their combined effect on winter balance uncertainty is quantified.

5.2.1 SWE uncertainty

To estimate winter balance, we must represent SWE within a grid cell with a single value despite the fact that each grid cell contains a distribution of SWE values. The resulting uncertainty from this SWE representation is characterized by generating a normal distribution ($\mu = 0$), with a standard deviation equal to the mean standard deviation of all zigzags on each glacier ($\sigma_{G4} = 0.027$ m w.e., $\sigma_{G2} = 0.035$ m w.e., $\sigma_{G13} = 0.040$ m w.e.). For each iteration of the Monte Carlo, a set of random values is generated from the distribution and added to the observed SWE values. These perturbed SWE values are then used to estimate winter balance. The winter balance uncertainty due to SWE uncertainty (σ_{SWE}) is calculated as the standard deviation of the resulting distribution of winter balance estimates.

5.2.2 Density uncertainty

We incorporate uncertainty in interpolating density measurements by carrying forward all eight density interpolation options when estimating winter balance. The density measurement and interpolation methods used in our study encompass a broad spectrum of possible density values. The winter balance uncertainty due to density uncertainty (σ_ρ) is calculated as the standard deviation of winter balance estimates calculated using each density interpolation option.

5.2.3 Interpolation uncertainty

We represent the uncertainty in fitting an interpolation model to observed data in different ways for LR and SK. LR uncertainty is represented by obtaining a multivariate normal distribution of possible β_i values. The set of multivariate normal random regression coefficient distributions is found using the coefficient covariance and coefficient values from the linear regression using the built-in function `mvnrnd`. The covariance of regression coefficients is given by [6]:

$$\text{cov}(\boldsymbol{\beta}) = \sigma^2 (\mathbf{X}' \mathbf{X})^{-1} \quad (5.1)$$

where \mathbf{X} is the $n \times k$ matrix of predictor variables. The variance of the regression, σ^2 , is estimated using

$$\sigma^2 = \frac{\sum_{i=1}^n (\mathbf{y}_i - \bar{\mathbf{y}})^2}{n - k - 1} \quad (5.2)$$

The standard deviation of each distribution is calculated using the covariance of regression coefficients as outlined in [6]. The β_i distributions are randomly sampled and the new β_i values are used to estimate winter balance.

SK uncertainty is derived from the 95% confidence interval SWE surfaces generated within the `DiceKriging` package. The standard deviation of each grid cell is then calculated from the confidence interval surfaces and the glacier wide standard deviation is found by taking the square root of the average variance. The distribution of winter balance values is

Table 5.1: Standard deviation ($\times 10^{-2}$ m w.e.) of winter balance distributions arising from SWE (σ_{SWE}), density (σ_ρ) and interpolation (σ_{INT}) uncertainty. Result for Glacier 4 (G4), Glacier 2 (G2) and Glacier 13 (G13) are shown.

	Linear Regression			Simple Kriging		
	σ_ρ	σ_{SWE}	σ_{INT}	σ_ρ	σ_{SWE}	σ_{INT}
G4	1.90	0.86	2.13	2.15	0.85	14.05
G2	3.37	1.80	3.09	2.03	2.53	13.78
G13	1.68	1.12	2.80	1.27	1.15	9.65

centred at the SK winter balance estimate and has a standard deviation equal to the glacier wide standard deviation. For consistency, the standard deviation of winter balance values that result from either LR or SK interpolation uncertainty is referred to as σ_{INT} .

5.3 Results

5.3.1 Winter balance uncertainty

Specific winter balance is affected by uncertainty introduced when interpolating density (density uncertainty), when calculating grid cell SWE values (SWE uncertainty), and when interpolating observations (interpolation uncertainty). We find that when using LR and SK, interpolation uncertainty has a larger effect on winter balance uncertainty than density uncertainty or SWE uncertainty. The probability density function (PDF) that arises from SWE uncertainty is much narrower than the PDF that arises from interpolation uncertainty (Figure ?? and Table 5.1).

The total winter balance uncertainty from SK interpolation is 3 to 5 times greater than uncertainty from LR interpolation. The PDFs overlap between the two interpolation methods although the PDF modes have lower winter balance values when SK is used for Glaciers 2 and 13 and higher for Glacier 4. SK results in winter balance distributions that overlap between glaciers and there is also a small probability of estimating a winter balance value of 0 m w.e. for Glaciers 2 and 13. LR results in overlapping winter balance distributions for Glaciers 2 and 4, with the PDF peak of Glacier 4 being slightly higher than that of Glacier 2.

5.3.2 Spatial patterns of winter balance uncertainty

Density, SWE, and interpolation uncertainty all contribute to spatial patterns of winter balance uncertainty (Figure 5.2). For both LR and SK, the greatest uncertainty in estimated SWE occurs in the accumulation area. When LR is used, estimated SWE is highly sensitive to the elevation regression parameter. In the case of SK, uncertainty is greatest in areas far from observed SWE, which consist of the upper accumulation area on Glaciers 2 and 13. uncertainty is greatest on Glacier 4 when LR interpolation is used at the upper edges of

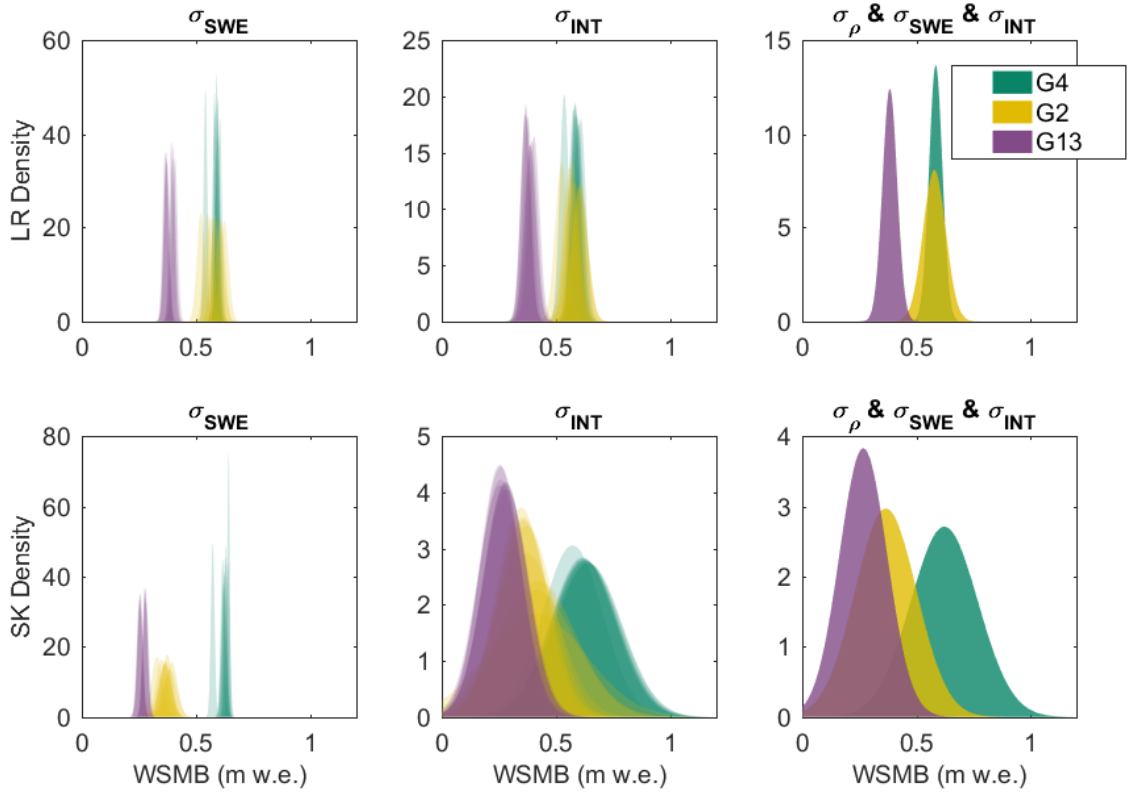


Figure 5.1: Probability density functions (PDFs) fitted to distributions of specific winter balance values that arise from (left) SWE uncertainty (σ_{SWE}), (middle) interpolation uncertainty (σ_{INT}) and (right) all three sources of uncertainty. Results from a linear regression interpolation (top panels) and simple kriging (bottom panels) are shown. Each PDF is calculated using one of eight density interpolation methods for Glacier 4 (G4), Glacier 2 (G2) and Glacier 13 (G13).

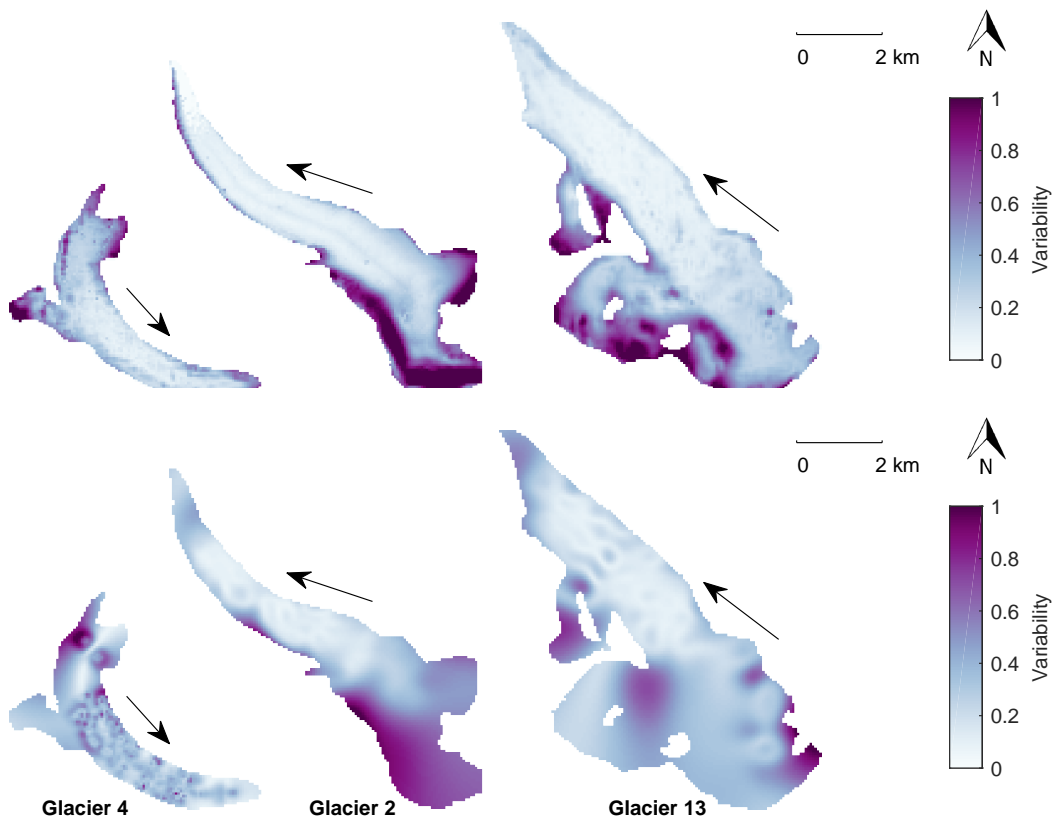


Figure 5.2: Uncertainty of SWE estimated using linear regression (top) and simple kriging (bottom). Uncertainty is a relative quantity measured by taking the sum of differences between one hundred estimates of distributed winter balance that include SWE uncertainty and, in the case of linear regression, regression uncertainty. The sum is then normalized for each glacier. Glacier flow directions are indicated by arrows.

the accumulation area, which correspond to the locations with extreme values of the wind redistribution parameter. When SK is used for interpolation on Glacier 4, uncertainty is greatest at the measured grid cells, which highlights the short correlation length and the large effect of density interpolation on the SK accumulation estimate.

5.4 Discussion

Interpolation uncertainty is the greatest contributor to winter balance uncertainty for both SK and LR. A large contributor to uncertainty arises from extrapolation beyond the sampled region, which results in high uncertainty in estimated SWE in the accumulation area. The winter balance distributions obtained using LR and SK overlap for each glacier but

the distribution modes differ, with SK generally estimating lower winter balance in the accumulation area, which lowers the overall winter balance estimate. It is important to note that although the distributions from LR are narrower than those from SK, that does not necessitate that LR is a more accurate method of estimating winter balance. Based on the sources of uncertainty chosen, LR appears to be more precise than SK but the methods of calculating interpolation uncertainty are different so the distributions should not be directly compared.

SWE uncertainty is the smallest contributor to winter balance uncertainty. Therefore, obtaining the most accurate value of SWE to represent a grid cell, even a relatively large grid cell, does not need to be a priority when designing a snow survey. Many parts of a glacier are characterized by a relatively smooth surface, with roughness lengths on the order of centimeters [57] resulting in low snow depth uncertainty. However, we assume that the sampled grid cells are representative of the uncertainty across the entire glacier, which is likely not true for areas with debris cover, crevasses and steep slopes.

Using a Monte Carlo experiment to propagate uncertainty allowed us to quantify effects of uncertainty on estimates of winter balance. However, our analysis did not include uncertainty arising from a number of data sources, which we assumed to contribute negligibly to the uncertainty in winter balance or to be encompassed by investigated sources of uncertainty. These sources of uncertainty include error associated with SP and FS density measurement, DEM vertical and horizontal error and error associated with estimating measurement locations.

Chapter 6

Regional Controls

6.1 Transferability of linear regression coefficients

To determine the spatial transferability of LR coefficients, the coefficients from each glacier are used to estimate winter balance on the remaining glaciers. All collected data is then used to generate LR coefficients, which are applied to the study glaciers to estimate winter balance.

6.1.1 Results

There are considerable differences in the spatial pattern and mean estimated winter balance found using transferred regression coefficients (Figure 6.1). The spatial patterns found using the Glacier 2 and Glacier 13 coefficients reflect the dominance of elevation within the regression. The uniform distributions found using Glacier 4 coefficients reflect the low regression coefficient values for the topographic parameters on Glacier 4.

The mean estimated winter balance differs considerably when the various LR coefficients are used. Glacier 4 coefficients result in the highest mean winter balance values because the mean value is approximately equal to the mean of the observed values on Glacier 4, which are higher than that of Glaciers 2 and 13. The range of mean winter balance between different coefficients is especially large for Glacier 4 (0.34 m w.e.).

The range-scale accumulation gradient (Glacier 4 highest accumulation, Glacier 13 lowest accumulation) is not present when using transferred coefficients. Glacier 4 coefficients result in an almost uniform snow distribution on all glaciers. Coefficients from Glaciers 2 and 13 result in Glacier 13 having the highest winter balance. For Glaciers 4 and 2, transferring coefficients decreases the mean winter balance and for Glacier 13, using transferred coefficients increases the mean winter balance. When using all the data to estimate a LR, the mean winter balance and spatial pattern of SWE on each glacier is similar to when Glacier 13 coefficients are used, but the larger LR intercept value results in a higher mean winter balance.

The winter balance is largely determined by the intercept of the LR used and the magnitude of the elevation regression coefficient (Table 6.1) because all other regressors have small coefficients. Therefore, estimating winter balance in the Donjek Range from transferred coefficients is especially sensitive to LR intercept value and magnitude of the elevation regression coefficient.

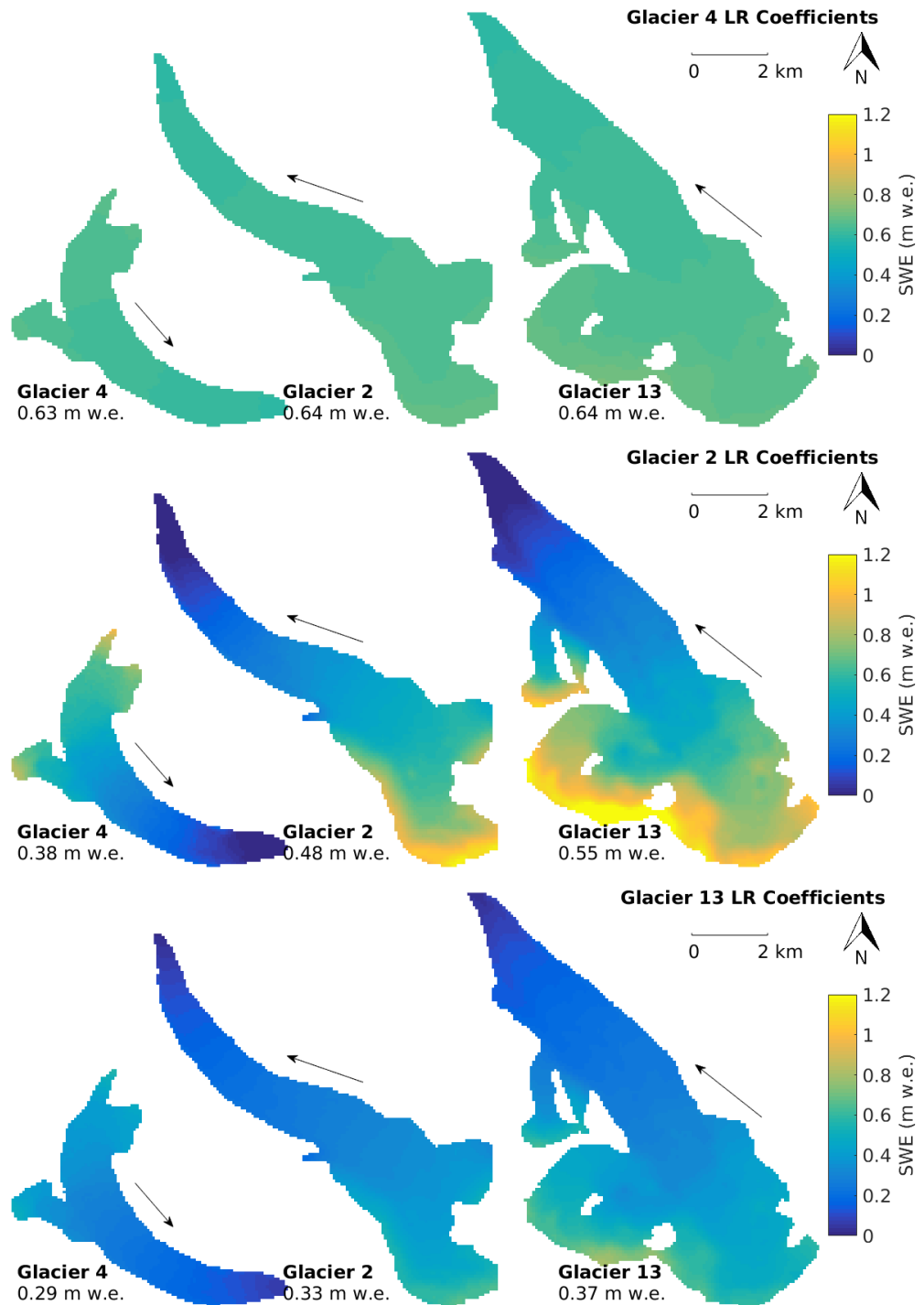


Figure 6.1: Transfer of LR coefficients to estimate distributed winter balance on study glaciers. winter balance found using Glacier 4 (top), Glacier 2 (middle) and Glacier 13 (bottom) regression coefficients. The mean SWE from all density interpolation options is shown. Arrows indicate glacier flow direction.

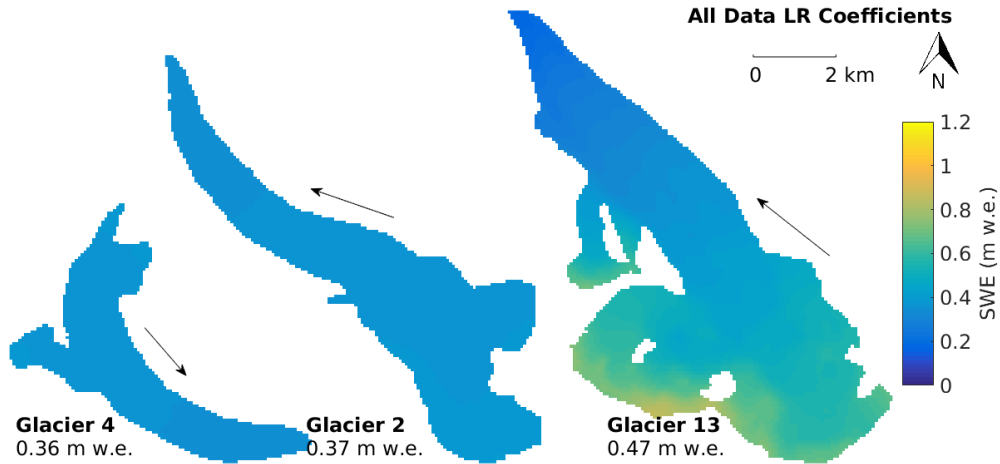


Figure 6.2: Transfer of LR coefficients to estimate distributed winter balance on study glaciers. Winter balance found using coefficients determined from all available SWE observations. The mean SWE from all density interpolation options is shown. Arrows indicate glacier flow direction.

Table 6.1: Elevation regression coefficients and intercepts used in linear regression transferability. The mean RMSE for all glaciers is also shown.

	Glacier 4 Coefficients	Glacier 2 Coefficients	Glacier 13 Coefficients	All Data Coefficients
Elevation Regression Coefficient	0.0082	0.1084	0.0510	0.0523
Intercept (m w.e.)	0.6217	0.2497	0.2247	0.3435
Mean RMSE (m w.e.)	0.3066	0.2065	0.2142	0.1994

The RMSE of estimated winter balance found using transferred coefficients is larger for all glaciers than when using glacier specific coefficients (Figure 6.3). Glacier 4 coefficients introduce a large RMSE for Glaciers 2 and 13, while all other coefficient sets result in large RMSE on Glacier 4. Glaciers 2 and 13 have relatively small changes in RMSE when coefficients from Glacier 2, Glacier 13 or all data coefficients are used. Interestingly, the lowest average RMSE for all glaciers occurs when all data coefficients are used (Table 6.1). Therefore, if transfer of coefficients is needed, using all the data to generate LR coefficients will result in the lowest error with observed values.

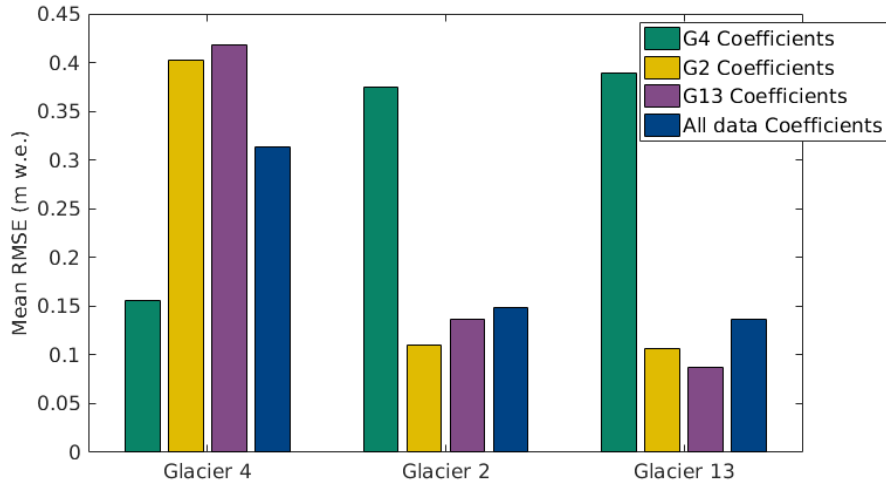


Figure 6.3: Root mean squared error (RMSE) at sampling locations when LR coefficients are transferred between glaciers. The mean RMSE from all density interpolation options is shown.

6.1.2 Accumulation gradient

An accumulation gradient is observed for the continental side of the St. Elias Mountains (Figure 6.4). Accumulation data are compiled from [115], the three study glaciers, as well as two snow pits we dug near the head of the Kaskawulsh Glacier in May 2016. The data show a linear decrease in observed SWE as distance from the main mountain divide (identified by [115]) increases, with a gradient of $-0.024 \text{ m w.e. km}^{-1}$. While the three study glaciers fit the regional relationship, the same relationship would not apply when just the Donjek Range is considered. Therefore, glacier location within a mountain range also affects glacier-wide winter balance. Interaction between meso-scale weather patterns and mountain topography is a major driver of glacier-wide accumulation. Further insight into mountain-scale accumulation trends can be achieved by investigating moisture source trajectories and orographic precipitation contribution to accumulation.

6.1.3 Limitations and future work

Extensions to this work could include an investigation of experimental design, examining the effects of DEM grid size on winter balance and resolving temporal variability. Our sampling design was chosen to extensively sample the ablation area and is likely too finely resolved for many future mass balance surveys to replicate. Determining a sampling design that minimizes error and reduces the number of measurements, known as data efficiency thresholds, would contribute to optimizing snow surveys in mountainous regions. For example, [76] concluded that 200–400 observations are needed to obtain accurate and robust snow distribution models.

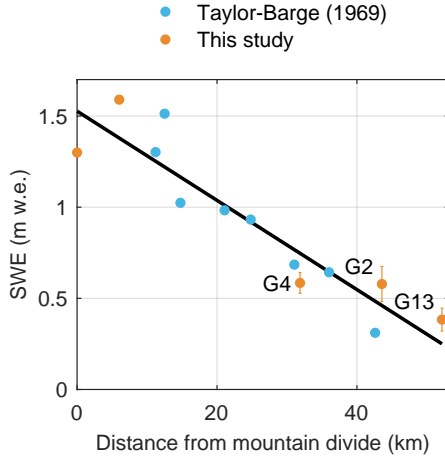


Figure 6.4: Relation between SWE and linear distance from St. Elias mountain divide, located at the head of the Kaskawulsh Glacier. Blue dots are snow pit derived SWE values from [115]. Orange dots furthest from the divide are mean winter balance from Glaciers 4, 2 and 13, with 95% confidence interval using a linear regression interpolation. Orange dots close to the divide are snow pit derived SWE value at two locations in the accumulation area of the Kaskawulsh Glacier collect in May 2016. Black line indicates line of best fit ($R^2 = 0.85$).

DEM grid cell size is known to significantly affect computed topographic parameters and the ability for a DEM to resolve important hydrological features (i.e. drainage pathways) in the landscape [137, 43, 51, 76], which can have implications for calculating a LR that uses topographic parameters. [137] found that a 10 m grid cell size is an optimal compromise between increasing resolution and large data volumes. Further, the importance of topographic parameters in predicting SWE is correlated with DEM grid size [e.g. 64, 76]. A decrease in spatial resolution of the DEM results in a decrease in the importance of curvature and an increase in the importance of elevation. A detailed and ground controlled DEM is therefore needed to identify the features that drive accumulation variability. Even with a high resolution DEM, microtopography that creates small scale snow variability cannot be resolved. For example, the lower part of Glacier 2 has an undulating ice surface (on the order of 5 m horizontal and 0.5 m vertical) that results in large variability in snow depth. Future studies could also evaluate the effects of DEM uncertainty on elevation and derived topographic parameters [e.g. 51, 125].

Temporal variability in accumulation is not considered in our study. While this limits the extent of our conclusions, a number of studies have found temporal stability in spatial patterns of snow accumulation and that terrain-based model could be applied reliable between years [e.g. 50]. For example, [122] analyzed more than 40 years of accumulation recorded

on two Norwegian glaciers and found that snow accumulation is spatially heterogeneous yet exhibits robust time stability in its distribution.

6.2 Conclusion

We estimate spatial accumulation patterns and specific winter balance for three glaciers in the St. Elias mountains from extensive snow depth and density sampling. Our objectives are to (1) examine methods and uncertainties when moving from snow measurements to estimating winter balance and (2) show how snow variability, data error and our methodological choices interact to create uncertainty in our estimate of winter balance.

We find that the method used to interpolate observations has a large effect on winter balance estimates and its associated uncertainty. On Glacier 4, winter balance estimates are consistent between linear regression (LR) and simple kriging (SK) but both explain only a small portion of observed variance, highlighting that although the winter balance estimates are relatively precise they may not necessarily be accurate. On Glaciers 2 and 13, LR and SK are better able to estimate observed SWE values but winter balance estimates differ considerably between the two interpolation methods due to extrapolation into the accumulation area. SK is a non-parametric interpolation method that relies heavily on regular and dense sampling so extrapolation is sensitive to marginal data values and the data mean. LR employs parameters that act as proxies for physical processes, which provides insight into drivers of SWE distribution, constrains extrapolation values and can be spatially transferred. It is therefore critical that future winter balance studies report which interpolation method is used to estimate winter balance, the ability for the model to estimate observed measurements and the uncertainty that results from fitting the interpolation model.

For our study glaciers, the total winter balance uncertainty ranges from 0.03 (8%) to 0.15 (54%) m w.e. depending primarily on the interpolation method. The smallest winter balance uncertainty source is the representation of grid cell SWE. Future studies could reduce winter balance uncertainty by increasing the spatial distribution of snow depth sampling rather than obtaining many measurements within a single grid cell. In our work, increased sampling within the accumulation area would better constrain SWE extrapolation and decrease uncertainty. Our results indicate that using extrapolated data to compare with winter balance estimates from remote sensing or modelling studies may produce misleading results. If possible, comparison studies should use observed SWE data rather than interpolated winter balance values.

Snow distribution patterns are found to differ considerably between glaciers, highlighting strong intra- and inter-basin variability and accumulation drivers acting on multiple scales. SWE distribution on Glacier 4 is highly variable, as indicated by shorter range distance, higher nugget value and lower explained variance. Glaciers 2 and 13 have lower SWE variability and elevation is the primary control of observed variation. Despite challenges

in accurately estimating winter balance, our data are consistent with a previously reported linear decrease in SWE with increased distance from the main topographic divide along the continental side of the St. Elias Mountains. This trend indicates that glacier location within a mountain range has a large influence on winter balance.

Bibliography

- [1] Donald Alford. Mountain hydrologic systems. *Mountain Research and Development*, pages 349–363, 1985.
- [2] Brian T Anderson, James P McNamara, Hans-Peter Marshall, and Alejandro N Flores. Insights into the physical processes controlling correlations between snow distribution and terrain properties. *Water Resources Research*, 50(6):4545–4563, 2014.
- [3] SP Anderton, SM White, and B Alvera. Evaluation of spatial variability in snow water equivalent for a high mountain catchment. *Hydrological Processes*, 18(3):435–453, 2004.
- [4] D Archer and D Stewart. The installation and use of a snow pillow to monitor snow water equivalent. *Water and Environment Journal*, 9(3):221–230, 1995.
- [5] Anthony A Arendt, Scott B Luthcke, Christopher F Larsen, Waleed Abdalati, William B Krabill, and Matthew J Beedle. Validation of high-resolution GRACE mascon estimates of glacier mass changes in the St Elias Mountains, Alaska, USA, using aircraft laser altimetry. *Journal of Glaciology*, 54(188):778–787, 2008.
- [6] Pantelis G Bagos and Maria Adam. On the Covariance of Regression Coefficients. *Open Journal of Statistics*, 5:680–701, 2015.
- [7] Benjamin Balk and Kelly Elder. Combining binary decision tree and geostatistical methods to estimate snow distribution in a mountain watershed. *Water Resources Research*, 36(1):13–26, 2000.
- [8] Tim P Barnett, Jennifer C Adam, and Dennis P Lettenmaier. Potential impacts of a warming climate on water availability in snow-dominated regions. *Nature*, 438(7066):303–309, 2005.
- [9] Alan Basist, Gerald D Bell, and Vernon Meentemeyer. Statistical relationships between topography and precipitation patterns. *Journal of climate*, 7(9):1305–1315, 1994.
- [10] Robert T. Beaumont and R. A. Work. Snow sampling results from three samplers. *International Association of Scientific Hydrology. Bulletin*, 8(4):74–78, 1963.
- [11] Sascha Bellaire and Jürg Schweizer. Deriving spatial stability variations from penetration resistance measurements. In *Proceedings ISSW*, pages 188–194, 2008.

- [12] Sascha Bellaire and Jürg Schweizer. Measuring spatial variations of weak layer and slab properties with regard to snow slope stability. *Cold Regions Science and Technology*, 65(2):234–241, 2011.
- [13] Etienne Berthier, Yves Arnaud, Rajesh Kumar, Sarfaraz Ahmad, Patrick Wagnon, and Pierre Chevallier. Remote sensing estimates of glacier mass balances in the Himachal Pradesh (Western Himalaya, India). *Remote Sensing of Environment*, 108(3):327–338, 2007.
- [14] Etienne Berthier, Eric Schiefer, Garry KC Clarke, Brian Menounos, and Frédérique Rémy. Contribution of Alaskan glaciers to sea-level rise derived from satellite imagery. *Nature Geoscience*, 3(2):92–95, 2010.
- [15] Günter Blöschl. Scaling issues in snow hydrology. *Hydrological Processes*, 13(1415):2149–2175, 1999.
- [16] Günter Blöschl and R Kirnbauer. An analysis of snow cover patterns in a small Alpine catchment. *Hydrological Processes*, 6(1):99–109, 1992.
- [17] Günter Blöschl, R Kirnbauer, and D Gutknecht. Distributed snow melt simulations in an alpine catchment. *Water Resources Research*, 27(12):3171–3179, 1991.
- [18] Johan Bring. A geometric approach to compare variables in a regression model. *The American Statistician*, 50(1):57–62, 1996.
- [19] Kenneth P. Burnham and David R. Anderson. Multimodel Inference: Understanding AIC and BIC in Model Selection. *Sociological Methods & Research*, 33(2):261–304, 2004.
- [20] Aristita Busuioc, Deliang Chen, and Cecilia Hellström. Performance of statistical downscaling models in GCM validation and regional climate change estimates: application for Swedish precipitation. *International Journal of Climatology*, 21(5):557–578, 2001.
- [21] Martyn P Clark, Jordy Hendrikx, Andrew G Slater, Dmitri Kavetski, Brian Anderson, Nicolas J Cullen, Tim Kerr, Einar Örn Hreinsson, and Ross A Woods. Representing spatial variability of snow water equivalent in hydrologic and land-surface models: A review. *Water Resources Research*, 47(7), 2011.
- [22] G. K. Garry KC Clarke and Gerald Holdsworth. Glaciers of the St. Elias Mountains. *US Geological Survey professional paper*, (1386J), 2002.
- [23] Garry KC Clarke, Sam G Collins, and David E Thompson. Flow, thermal structure, and subglacial conditions of a surge-type glacier. *Canadian Journal of Earth Sciences*, 21(2):232–240, 1984.
- [24] JG Cogley, R Hock, LA Rasmussen, AA Arendt, Andreas Bauder, RJ Braithwaite, P Jansson, G Kaser, M Möller, L Nicholson, et al. *Glossary of glacier mass balance and related terms*. UNESCO-IHP, Paris, 2011.
- [25] Jacob Cohen, Patricia Cohen, Stephen G West, and Leona S Aiken. *Applied multiple regression/correlation analysis for the behavioral sciences*. Routledge, 2013.

- [26] Steven M Conger and David M McClung. Comparison of density cutters for snow profile observations. *Journal of Glaciology*, 55(189):163–169, 2009.
- [27] Jeff W Crompton and Gwenn E Flowers. Correlations of suspended sediment size with bedrock lithology and glacier dynamics. *Annals of Glaciology*, 57(72):1–9, 2016.
- [28] R Dadić, R Mott, M Lehning, and P Burlando. Parameterization for wind-induced preferential deposition of snow. *Journal of Geophysical Research: Earth Surface*, 24(14):1994–2006, 2010.
- [29] Ryan K Danby, David S Hik, D Scott Slocombe, and Andrew Williams. Science and the St. Elias: an evolving framework for sustainability in North America’s highest mountains. *The Geographical Journal*, 169(3):191–204, 2003.
- [30] Richard B Darlington. Multiple regression in psychological research and practice. *Psychological bulletin*, 69(3):161, 1968.
- [31] John C Davis and Robert J Sampson. *Statistics and data analysis in geology*. Wiley New York et al., 2nd edition, 1986.
- [32] Jeffrey S Deems, Steven R Fassnacht, and Kelly J Elder. Fractal distribution of snow depth from LiDAR data. *Journal of Hydrometeorology*, 7(2):285–297, 2006.
- [33] Jeffrey S Deems and Thomas H Painter. Lidar measurement of snow depth: accuracy and error sources. In *Proceedings of the International Snow Science Workshop*, 2006.
- [34] David Dixon and Sarah Boon. Comparison of the SnowHydro snow sampler with existing snow tube designs. *Hydrological Processes*, 26(17):2555–2562, 2012.
- [35] Kelly Elder, Don Cline, Glen E Liston, and Richard Armstrong. NASA Cold Land Processes Experiment (CLPX 2002/03): Field measurements of snowpack properties and soil moisture. *Journal of Hydrometeorology*, 10(1):320–329, 2009.
- [36] Kelly Elder, Jeff Dozier, and Joel Michaelsen. Snow accumulation and distribution in an alpine watershed. *Water Resources Research*, 27(7):1541–1552, 1991.
- [37] Kelly Elder, Walter Rosenthal, and Robert E Davis. Estimating the spatial distribution of snow water equivalence in a montane watershed. *Hydrological Processes*, 12(1011):1793–1808, 1998.
- [38] Tyler A Erickson, Mark W Williams, and Adam Winstral. Persistence of topographic controls on the spatial distribution of snow in rugged mountain terrain, Colorado, United States. *Water Resources Research*, 41(4):1–17, 2005.
- [39] Jennifer Erxleben, Kelly Elder, and Robert Davis. Comparison of spatial interpolation methods for estimating snow distribution in the Colorado Rocky Mountains. *Hydrological Processes*, 16(18):3627–3649, 2002.
- [40] Phillip E Fames, NR Peterson, BE Goodison, and Robert P Richards. Metrication of Manual Snow Sampling Equipment. In *Proceedings of the 50th Western Snow Conference*, pages 120–132, 1982.

- [41] Daniel Farinotti, Jan Magnusson, Matthias Huss, and Andreas Bauder. Snow accumulation distribution inferred from time-lapse photography and simple modelling. *Hydrological Processes*, 24(15):2087–2097, 2010.
- [42] HJ Fowler, S Blenkinsop, and C Tebaldi. Linking climate change modelling to impacts studies: recent advances in downscaling techniques for hydrological modelling. *International Journal of Climatology*, 27(12):1547–1578, 2007.
- [43] J. Garbrecht and L. Martz. Grid size dependency of parameters extracted from digital elevation models. *Computers & Geosciences*, 20(1):85–87, 1994.
- [44] Alex S Gardner, Geir Moholdt, J Graham Cogley, Bert Wouters, Anthony A Arendt, John Wahr, Etienne Berthier, Regine Hock, W Tad Pfeffer, Georg Kaser, et al. A reconciled estimate of glacier contributions to sea level rise: 2003 to 2009. *Science*, 340(6134):852–857, 2013.
- [45] Mariusz Grabiec, Dariusz Puczko, Tomasz Budzik, and Grzegorz Gajek. Snow distribution patterns on Svalbard glaciers derived from radio-echo soundings. *Polish Polar Research*, 32(4):393–421, 2011.
- [46] Ulrike Grömping. Variable Importance Assessment in Regression: Linear Regression versus Random Forest. *The American Statistician*, 63(4):308–319, 2009.
- [47] Ulrike Grömping. Variable importance in regression models. *Wiley Interdisciplinary Reviews: Computational Statistics*, 7(2):137–152, 2015.
- [48] T Grünewald, Y Bühler, and M Lehning. Elevation dependency of mountain snow depth. *The Cryosphere*, 8(6):2381–2394, 2014.
- [49] T Grünewald, M Schirmer, R Mott, and M Lehning. Spatial and temporal variability of snow depth and ablation rates in a small mountain catchment. *Cryosphere*, 4(2):215–225, 2010.
- [50] T Grünewald, J Stötter, JW Pomeroy, R Dadic, I Moreno Baños, J Marturià, M Spross, C Hopkinson, P Burlando, and M Lehning. Statistical modelling of the snow depth distribution in open alpine terrain. *Hydrology and Earth System Sciences*, 17(8):3005–3021, 2013.
- [51] Tang Guo-an, Hui Yang-he, Josef Strobl, and Liu Wang-qing. The impact of resolution on the accuracy of hydrologic data derived from DEMs. *Journal of Geographical Sciences*, 11(4):393–401, 2001.
- [52] Alessio Gusmeroli, Gabriel J Wolken, and Anthony A Arendt. Helicopter-borne radar imaging of snow cover on and around glaciers in Alaska. *Annals of Glaciology*, 55(67):78–88, 2014.
- [53] I Hanssen-Bauer and EJ Førland. Long-term trends in precipitation and temperature in the Norwegian Arctic: can they be explained by changes in atmospheric circulation patterns? *Climate Research*, 10(2):143–153, 1998.
- [54] W Harrison. Seasonal accumulation and loss of snow from a block mountain catchment in central Otago. *Journal of Hydrology (NZ)*, 25(1):1–17, 1986.

- [55] Tomislav Hengl, Gerard B.M. Heuvelink, and David G. Rossiter. About regression-kriging: From equations to case studies. *Computers & Geosciences*, 33(10):1301–1315, 2007.
- [56] Michael M Herron and Chester C Langway Jr. Firn densification: an empirical model. *Journal of Glaciology*, 25:373–385, 1980.
- [57] Regine Hock. Glacier melt: a review of processes and their modelling. *Progress in Physical Geography*, 29(3):362–391, 2005.
- [58] J Hofierka, H Mitášová, and M Neteler. Geomorphometry in GRASS GIS. *Developments in Soil Science*, 33:387–410, 2009.
- [59] Gerald Holdsworth, Stephen Fogarasi, and HR Krouse. Variation of the stable isotopes of water with altitude in the Saint Elias Mountains of Canada. *Journal of Geophysical Research: Atmospheres (1984–2012)*, 96(D4):7483–7494, 1991.
- [60] Georg Kaser, J Graham Cogley, Mark B Dyurgerov, Mark F Meier, and Atsumu Ohmura. Mass balance of glaciers and ice caps: consensus estimates for 1961–2004. *Geophysical Research Letters*, 33(19), 2006.
- [61] Andrew Kasurak, Richard Kelly, and Alexander Brenning. Linear mixed modelling of snow distribution in the central Yukon. *Hydrological Processes*, 25(21):3332–3346, 2011.
- [62] Tim Kerr, Martyn Clark, Jordy Hendrikx, and Brian Anderson. Snow distribution in a steep mid-latitude alpine catchment. *Advances in Water Resources*, 55:17–24, 2013.
- [63] John W Kidson and Craig S Thompson. A comparison of statistical and model-based downscaling techniques for estimating local climate variations. *Journal of Climate*, 11(4):735–753, 1998.
- [64] Stefan Kienzle. The Effect of DEM Raster Resolution on First Order, Second Order and Compound Terrain Derivatives. *Transactions in GIS*, 8(1):83–111, 2004.
- [65] M. Knotters, D.J. Brus, and J.H. Oude Voshaar. A comparison of kriging, co-kriging and kriging combined with regression for spatial interpolation of horizon depth with censored observations. *Geoderma*, 67(3):227–246, 1995.
- [66] Ron Kohavi et al. A study of cross-validation and bootstrap for accuracy estimation and model selection. In *Proceedings of the Fourteenth International Joint Conference on Artificial Intelligence*, pages 1137–1145, 1995.
- [67] Jérôme Korona, Etienne Berthier, Marc Bernard, Frédérique Rémy, and Eric Thouvenot. SPIRIT SPOT 5 stereoscopic survey of Polar Ice: Reference images and topographies during the fourth International Polar Year (2007–2009). *ISPRS Journal of Photogrammetry and Remote Sensing*, 64(2):204–212, 2009.
- [68] Kalle Kronholm and Karl W Birkeland. Reliability of sampling designs for spatial snow surveys. *Computers & geosciences*, 33(9):1097–1110, 2007.

- [69] Kalle Kronholm, Martin Schneebeli, and Jürg Schweizer. Spatial variability of micropenetration resistance in snow layers on a small slope. *Annals of Glaciology*, 38(1):202–208, 2004.
- [70] Kristine M Larson, Ethan D Gutmann, Valery U Zavorotny, John J Braun, Mark W Williams, and Felipe G Nievinski. Can we measure snow depth with GPS receivers? *Geophysical Research Letters*, 36(17), 2009.
- [71] M Lehning, H Löwe, M Ryser, and N Raderschall. Inhomogeneous precipitation distribution and snow transport in steep terrain. *Water Resources Research*, 44(7):1–19, 2008.
- [72] Jin Li and Andrew D Heap. A review of spatial interpolation methods for environmental scientists. *Geoscience Australia*, page Record 2008/23, 2008.
- [73] Jin Li and Andrew D. Heap. Spatial interpolation methods applied in the environmental sciences: A review. *Environmental Modelling & Software*, 53:173–189, 2014.
- [74] Glen E Liston and Kelly Elder. A distributed snow-evolution modeling system (SnowModel). *Journal of Hydrometeorology*, 7(6):1259–1276, 2006.
- [75] Glen E Liston and Matthew Sturm. A snow-transport model for complex terrain. *Journal of Glaciology*, 44(148):498–516, 1998.
- [76] JI López-Moreno, J. Latron, and A. Lehmann. Effects of sample and grid size on the accuracy and stability of regression-based snow interpolation methods. *Hydrological Processes*, 24(14):1914–1928, 7 2010.
- [77] JI López-Moreno and D Nogués-Bravo. Interpolating local snow depth data: an evaluation of methods. *Hydrological processes*, 20(10):2217–2232, 2006.
- [78] Juan I López-Moreno, SR Fassnacht, Santiago Beguería, and JBP Latron. Variability of snow depth at the plot scale: implications for mean depth estimation and sampling strategies. *The Cryosphere*, 5(3):617–629, 2011.
- [79] H Machguth, Olaf Eisen, Frauke Paul, and M Hoelzle. Strong spatial variability of snow accumulation observed with helicopter-borne GPR on two adjacent alpine glaciers. *Geophysical Research Letters*, 33(13):1–5, 2006.
- [80] Wolf-Dietrich Marchand and Ånund Killingtveit. Statistical probability distribution of snow depth at the model sub-grid cell spatial scale. *Hydrological Processes*, 19(2):355–369, 2005.
- [81] Melvin G Marcus and Richard H Ragle. Snow accumulation in the Icefield Ranges, St. Elias Mountains, Yukon. *Arctic and Alpine Research*, pages 277–292, 1970.
- [82] James L McCreight, Eric E Small, and Kristine M Larson. Snow depth, density, and SWE estimates derived from GPS reflection data: Validation in the western US. *Water Resources Research*, 50(8):6892–6909, 2014.

- [83] Daniel McGrath, Louis Sass, Shad O’Neil, Anthony Arendt, Gabriel Wolken, Alessio Gusmeroli, Christian Kienholz, and Christopher McNeil. End-of-winter snow depth variability on glaciers in Alaska. *Journal of Geophysical Research: Earth Surface*, 120(8):1530–1550, 2015.
- [84] Malcolm Mellor. *A review of basic snow mechanics*. US Army Cold Regions Research and Engineering Laboratory, 1974.
- [85] Nicholas Metropolis and S. Ulam. The Monte Carlo Method. *Journal of the American Statistical Association*, 44(247):335–341, 1949.
- [86] Helena Mitášová and Jaroslav Hofierka. Interpolation by regularized spline with tension: II. Application to terrain modeling and surface geometry analysis. *Mathematical Geology*, 25(6):657–669, 1993.
- [87] Noah P Molotch and Roger C Bales. Scaling snow observations from the point to the grid element: Implications for observation network design. *Water Resources Research*, 41(11), 2005.
- [88] NP Molotch, MT Colee, RC Bales, and J Dozier. Estimating the spatial distribution of snow water equivalent in an alpine basin using binary regression tree models: the impact of digital elevation data and independent variable selection. *Hydrological Processes*, 19(7):1459–1479, 2005.
- [89] GWK Moore, Gerald Holdsworth, and Keith Alverson. Climate change in the North Pacific region over the past three centuries. *Nature*, 420(6914):401–403, 2002.
- [90] R Mott, M Schirmer, and M Lehning. Scaling properties of wind and snow depth distribution in an Alpine catchment. *Journal of Geophysical Research: Atmospheres*, 116(D6), 2011.
- [91] Rebecca Mott, Françoise Faure, Michael Lehning, Henning Löwe, Bernhard Hynek, Gernot Michlmayer, Alexander Prokop, and Wolfgang Schöner. Simulation of seasonal snow-cover distribution for glacierized sites on Sonnblick, Austria, with the Alpine3D model. *Annals of Glaciology*, 49(1):155–160, 2008.
- [92] Rebecca Mott, Michael Schirmer, M Bavay, T Grünewald, and M Lehning. Understanding snow-transport processes shaping the mountain snow-cover. *The Cryosphere*, 4(4):545–559, 2010.
- [93] Paul J Neiman, F Martin Ralph, Gary A Wick, Jessica D Lundquist, and Michael D Dettinger. Meteorological characteristics and overland precipitation impacts of atmospheric rivers affecting the West Coast of North America based on eight years of SSM/I satellite observations. *Journal of Hydrometeorology*, 9(1):22–47, 2008.
- [94] Markus Neteler and Helena Mitášová. *Open source GIS: a GRASS GIS approach*, volume 773. Springer Science & Business Media, 3 edition, 2008.
- [95] M Nolan, CF Larsen, and M Sturm. Mapping snow-depth from manned-aircraft on landscape scales at centimeter resolution using Structure-from-Motion photogrammetry. *The Cryosphere Discussions*, 9:333–381, 2015.

- [96] V Olaya. Basic land-surface parameters. *Developments in Soil Science*, 33:141–169, 2009.
- [97] Shad O’Neil, Eran Hood, Anthony Arendt, and Louis Sass. Assessing streamflow sensitivity to variations in glacier mass balance. *Climatic change*, 123(2):329–341, 2014.
- [98] Anja Pälli, Jack C Kohler, Elisabeth Isaksson, John C Moore, Jean Francis Pinglot, Veijo A Pohjola, and Håkan Samuelsson. Spatial and temporal variability of snow accumulation using ground-penetrating radar and ice cores on a Svalbard glacier. *Journal of Glaciology*, 48(162):417–424, 2002.
- [99] Laetitia De Paoli and Gwenn E Flowers. Dynamics of a small surge-type glacier using one-dimensional geophysical inversion. *Journal of Glaciology*, 55(194):1101–1112, 2009.
- [100] W Tad Pfeffer, Anthony A Arendt, Andrew Bliss, Tobias Bolch, J Graham Cogley, Alex S Gardner, Jon-Ove Hagen, Regine Hock, Georg Kaser, Christian Kienholz, et al. The Randolph Glacier Inventory: a globally complete inventory of glaciers. *Journal of Glaciology*, 60(221):537–552, 2014.
- [101] JW Pomeroy, Newell Hedstrom, and Jason Parviainen. The snow mass balance of Wolf Creek, Yukon: effects of snow sublimation and redistribution. *Wolf Creek, Research Basin: Hydrology, Ecology, Environment, edited by: Pomeroy, JW and Granger RJ*, pages 15–30, 1999.
- [102] Adrian E. Raftery, Tilman Gneiting, Fadoua Balabdaoui, and Michael Polakowski. Using Bayesian Model Averaging to Calibrate Forecast Ensembles. *Monthly Weather Review*, 133(5):1155–1174, 2005.
- [103] Adrian E. Raftery, David Madigan, and Jennifer A. Hoeting. Bayesian Model Averaging for Linear Regression Models. *Journal of the American Statistical Association*, 92(437):179–191, 1997.
- [104] Marion Réveillet, Christian Vincent, Delphine Six, and Antoine Rabatel. Which empirical model is best suited to simulate glacier mass balances? *Journal of Glaciology*, 63(237):1–16, Oct 2016.
- [105] Jesús Revuelto, Juan I López-Moreno, César Azorín-Molina, and Sergio M Vicente Serrano. Topographic control of snowpack distribution in a small catchment in the central Spanish Pyrenees: Intra-and inter-annual persistence. 2014.
- [106] Olivier Roustant, David Ginsbourger, and Yves Deville. DiceKriging, DiceOptim: Two R packages for the analysis of computer experiments by kriging-based metamodeling and optimization. *Journal of Statistical Software*, 21:1–55, December 2012.
- [107] Wendy A Ryan, Nolan J Doesken, and Steven R Fassnacht. Evaluation of ultrasonic snow depth sensors for US snow measurements. *Journal of Atmospheric and Oceanic Technology*, 25(5):667–684, 2008.

- [108] M Schirmer, V Wirz, A Clifton, and M Lehning. Persistence in intra-annual snow depth distribution: 1. Measurements and topographic control. *Water Resources Research*, 47(9), 2011.
- [109] Jürg Schweizer, Achim Heilig, Sascha Bellaire, and Charles Fierz. Variations in snow surface properties at the snowpack-depth, the slope and the basin scale. *Journal of Glaciology*, 54(188):846–856, 2008.
- [110] Jürg Schweizer, Kalle Kronholm, J Bruce Jamieson, and Karl W Birkeland. Review of spatial variability of snowpack properties and its importance for avalanche formation. *Cold Regions Science and Technology*, 51(2):253–272, 2008.
- [111] Cora Shea and Bruce Jamieson. Star: an efficient snow point-sampling method. *Annals of Glaciology*, 51(54):64–72, 2010.
- [112] Ronald B Smith and Idar Barstad. A linear theory of orographic precipitation. *Journal of the Atmospheric Sciences*, 61(12):1377–1391, 2004.
- [113] L Sold, M Huss, A Eichler, M Schwikowski, and M Hoelzle. Recent accumulation rates of an alpine glacier derived from firn cores and repeated helicopter-borne GPR. *The Cryosphere Discussions*, 8(4):4431–4462, 2014.
- [114] Leo Sold, Matthias Huss, Martin Hoelzle, Hubert Anderegg, Philip C Joerg, and Michael Zemp. Methodological approaches to infer end-of-winter snow distribution on alpine glaciers. *Journal of Glaciology*, 59(218):1047–1059, 2013.
- [115] Bea Taylor-Barge. *The summer climate of the St. Elias Mountain region*. Montreal: Arctic Institute of North America, Research Paper No. 53, 1969.
- [116] E Trujillo and Michael Lehning. Theoretical analysis of errors when estimating snow distribution through point measurements. *The Cryosphere*, 9(3):1249–1264, 2015.
- [117] Ernesto Trujillo, Jorge A Ramírez, and Kelly J Elder. Scaling properties and spatial organization of snow depth fields in sub-alpine forest and alpine tundra. *Hydrological processes*, 23(11):1575–1590, 2009.
- [118] J Turcan and HS Loijens. Accuracy of snow survey data and errors in snow sampler measurements. In *32nd Eastern Snow Conference*, 1975.
- [119] J van Pelt, J Ward, Rickard Pettersson, Veijo A Pohjola, Sergey Marchenko, Björn Claremar, and Johannes Oerlemans. Inverse estimation of snow accumulation along a radar transect on Nordenskiöldbreen, Svalbard. *Journal of Geophysical Research: Earth Surface*, 119(4):816–835, 2014.
- [120] Hans Wackernagel. *Multivariate geostatistics: an introduction with applications*. Springer Science & Business Media, 2013.
- [121] Cameron P Wake, Kaplan Yalcin, and Niels S Gundestrup. The climate signal recorded in the oxygen-isotope, accumulation and major-ion time series from the Eclipse ice core, Yukon Territory, Canada. *Annals of Glaciology*, 35(1):416–422, 2002.
- [122] Alexander Philip Unwin Walmsley. Long-term observations of snow spatial distributions at Hellstugubreen and Gråsubreen, Norway. Master’s thesis, 2015.

- [123] Larry Wasserman. Bayesian Model Selection and Model Averaging. *Journal of Mathematical Psychology*, 44(1):92–107, 2000.
- [124] Fred GR Watson, Thor N Anderson, Wendi B Newman, Susan E Alexander, and Robert A Garrott. Optimal sampling schemes for estimating mean snow water equivalents in stratified heterogeneous landscapes. *Journal of Hydrology*, 328(3):432–452, 2006.
- [125] Suzanne P. Wechsler and Charles N. Kroll. Quantifying DEM Uncertainty and its Effect on Topographic Parameters. *Photogrammetric Engineering & Remote Sensing*, 72(9):1081–1090, 2006.
- [126] Karl Wetlaufer, Jordy Hendrikx, and Lucy Marshall. Spatial Heterogeneity of Snow Density and Its Influence on Snow Water Equivalence Estimates in a Large Mountainous Basin. *Hydrology*, 3(3):1–17, 2016.
- [127] Brett A Wheler, Andrew H MacDougall, Gwenn E Flowers, Eric I Petersen, Paul H Whitfield, and Karen E Kohfeld. Effects of Temperature Forcing Provenance and Extrapolation on the Performance of an Empirical Glacier-Melt Model. *Arctic, Antarctic, and Alpine Research*, 46(2):379–393, 2014.
- [128] Martin Widmann, Christopher S Bretherton, and Eric P Salathé Jr. Statistical precipitation downscaling over the Northwestern United States using numerically simulated precipitation as a predictor. *Journal of Climate*, 16(5):799–816, 2003.
- [129] Robert L Wilby and TML Wigley. Precipitation predictors for downscaling: observed and general circulation model relationships. *International Journal of Climatology*, 20(6):641–661, 2000.
- [130] Adam Winstral, Kelly Elder, and Robert E Davis. Spatial snow modeling of wind-redistributed snow using terrain-based parameters. *Journal of Hydrometeorology*, 3(5):524–538, 2002.
- [131] Adam Winstral, Danny Marks, and Robert Gurney. Simulating wind-affected snow accumulations at catchment to basin scales. *Advances in Water Resources*, 55:64–79, 2013.
- [132] JG Winther, O Bruland, K Sand, A Killingtveit, and D Marechal. Snow accumulation distribution on Spitsbergen, Svalbard, in 1997. *Polar Research*, 17:155–164, 1998.
- [133] Ming-Ko Woo and Philip Marsh. Analysis of Error in the Determination of Snow Storage for Small High Arctic Basins. *Journal of Applied Meteorology*, 17(10):1537–1541, 1978.
- [134] Walter A Wood. Project “Snow Cornice”: the establishment of the Seward Glacial research station. *Arctic*, 1(2):107–112, 1948.
- [135] R.A. Work, H.J. Stockwell, T.G. Freeman, and R.T. Beaumont. *Accuracy of field snow surveys*. Cold Regions Research & Engineering Laboratory, 1965.
- [136] Stefan Zeugner and Martin Feldkircher. Bayesian Model Averaging Employing Fixed and Flexible Priors: The BMS Package for R. *Journal of Statistical Software*, 68(4):1–37, 2015.

- [137] Weihua Zhang and David R. Montgomery. Digital elevation model grid size, landscape representation, and hydrologic simulations. *Water Resources Research*, 30(4):1019–1028, 1994.
- [138] Eduardo Zorita and Hans Von Storch. The analog method as a simple statistical downscaling technique: comparison with more complicated methods. *Journal of Climate*, 12(8):2474–2489, 1999.

Appendix A

GPS Waypoint Creation and Upload to GPS Device

To create the desired **transect** waypoints and enter them into the handheld GPS devices (Garmin GPSMAP 64s) the following steps were taken:

1. In QGIS, the outline of the glacier was selected from the Randolph Glacier Inventory (RGI 5.0) [100] and a recent, end-of-summer Landsat image was downloaded (LC80620172013248LGN00 image courtesy of the U.S. Geological Survey).
2. The ELA was estimated by tracing out the snow line from the Landsat image.
3. The desired transects were traced out in QGIS within the intended area. The tool ‘QChainage’ was then used to divide the line into points that were spaced every 30 m. Note that the shape file of the transect lines was projected into UTM coordinates to space points using units of metres.
4. The new point file was then saved as a comma-separated value file (‘.csv’) and opened in Excel. Note that the projection of the file was WGS84 so that the exported file had latitude and longitude values, which were needed for the GPS software.
5. The points were then named according to their location, area, transect, and point order. A column was made for ‘Glacier’ and ‘Transect’ and filled in for each point (using the drag function in Excel). This required identifying the range of points in QGIS (which were numbered) that corresponded to each transect and relating them to the numbered points in the Excel file (this was a bit cumbersome). The two columns were then combined and a sequential number added to the end. This column requires the header ‘name’ to be correctly identified as the name of the point in the GPS software.
6. The file with the point names was then imported into to the Garmin software *Base-Camp* and the waypoints were transferred to the GPS devices using this software.

To create the desired **zigzag** waypoints and enter them into the GPS devices the following steps were taken:

1. As described above, the outline of the glacier was selected from the RGI and a recent, end-of-summer Landsat image was downloaded. The ELA was estimated by tracing out the snow line from the Landsat image.
2. The ablation area was then divided into 7 zones that had approximately equal area (estimated by eye) and a polygon was traced out for each zone (within one shape file).
3. In QGIS, the tool ‘Random Points’ was then used to choose three random locations in each polygon. This was the location of the SWE measurements A, B, and C in each zone.
4. The file with the SWE measurement locations was saved as a ‘.csv’. The points were then named in Excel and exported to the GPS device as described above.
5. A new shape file was then created for the vertices of the zigzag. The vertices were created (in sequential order) so that they fit along the edges of one cell of the SPOT5 DEM. This was done by actually looking at one cell and placing the points along the edges at the intended locations. As a result, the SWE measurement location within the zigzag was not the same between zigzags.
6. Once all the zigzag point groups were created, the file was saved as a ‘.csv’, points named accordingly, and then exported to the GPS device as described above.

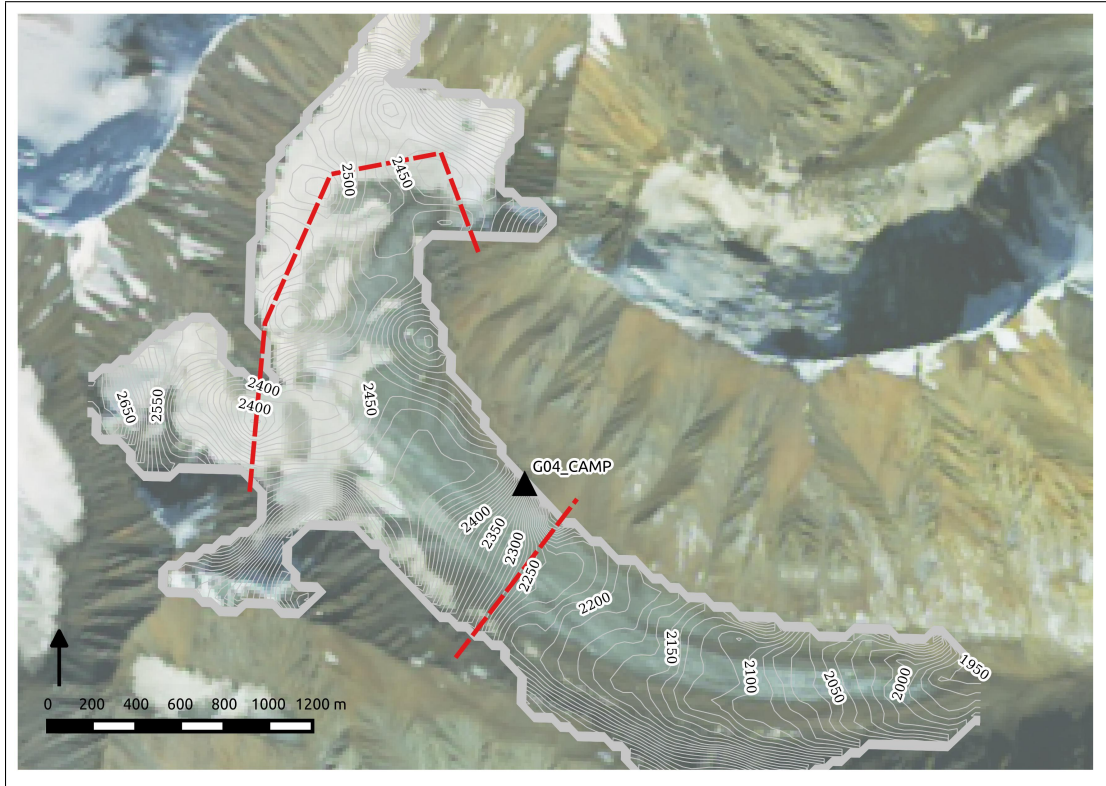
The locations of snowpits and snow cores were chosen by hand in a separate shape file. This file was then saved as a ‘.csv’, the points named, and the file exported to the GPS devices as described above.

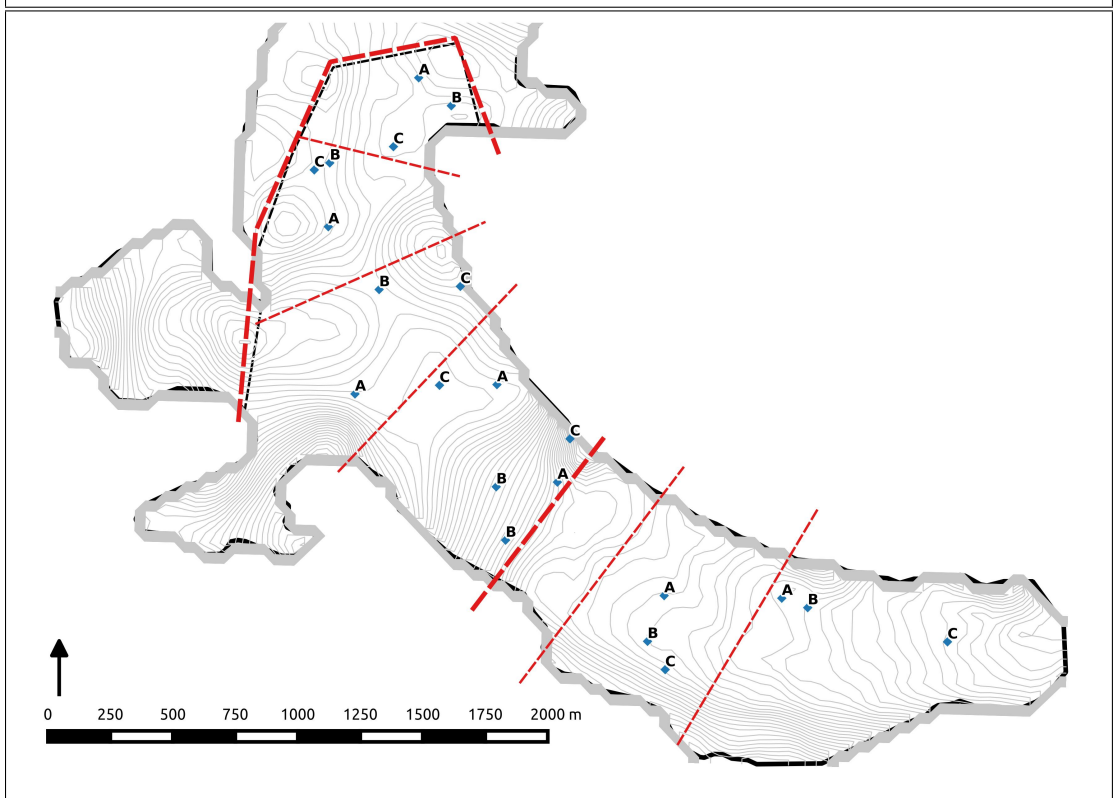
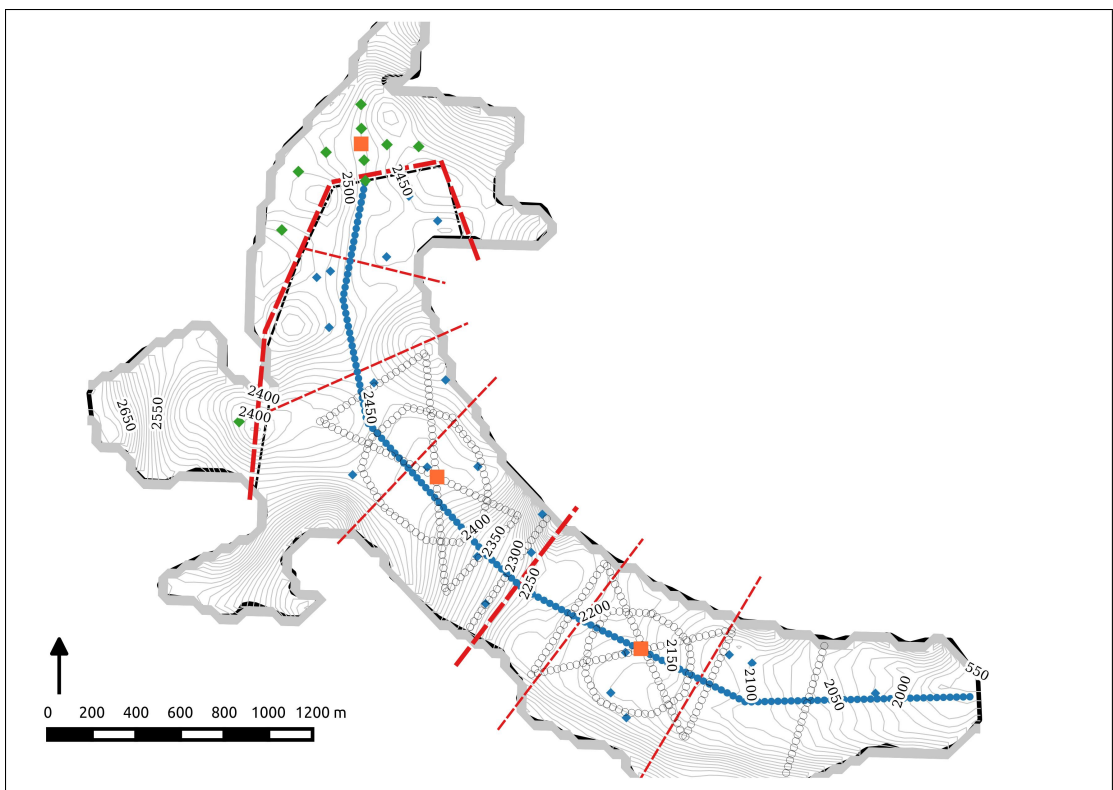
The files that had the names of the points were then imported back into QGIS so that the maps with point labels could be created. Since the order of completing measurements was determined in the field, these maps helped to quickly decide on the most efficient plan because they aided in determining the relative location of zigzags and transects.

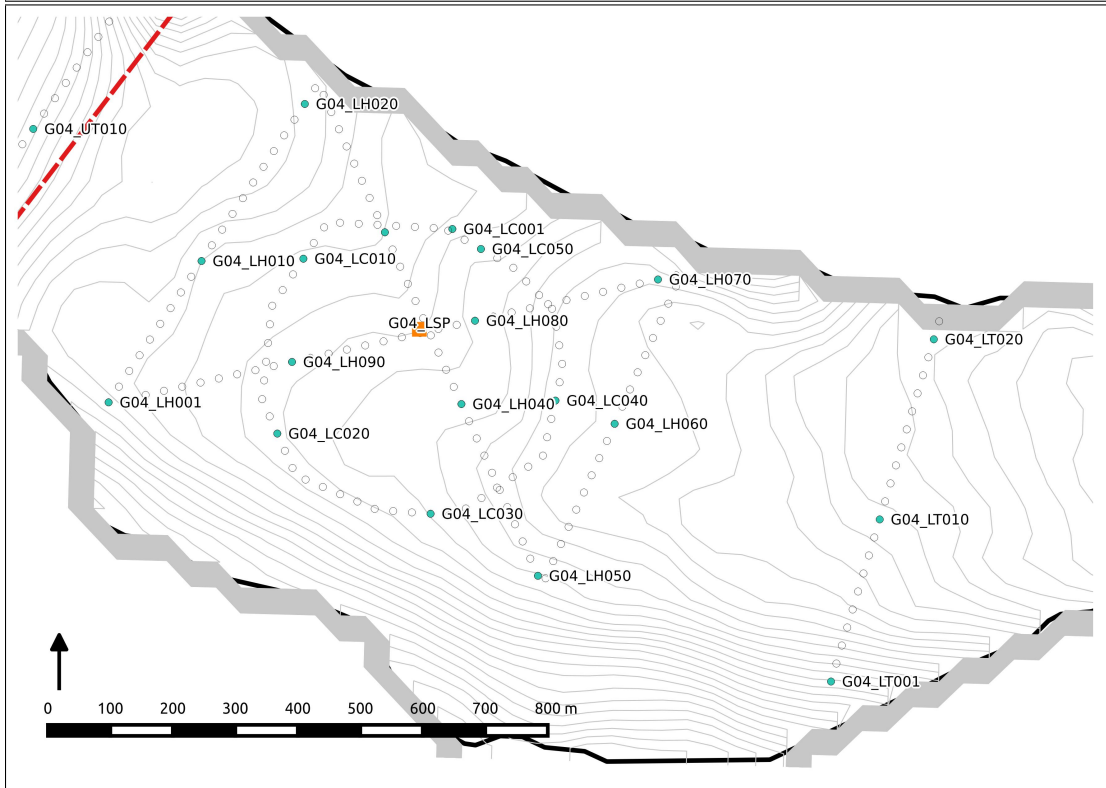
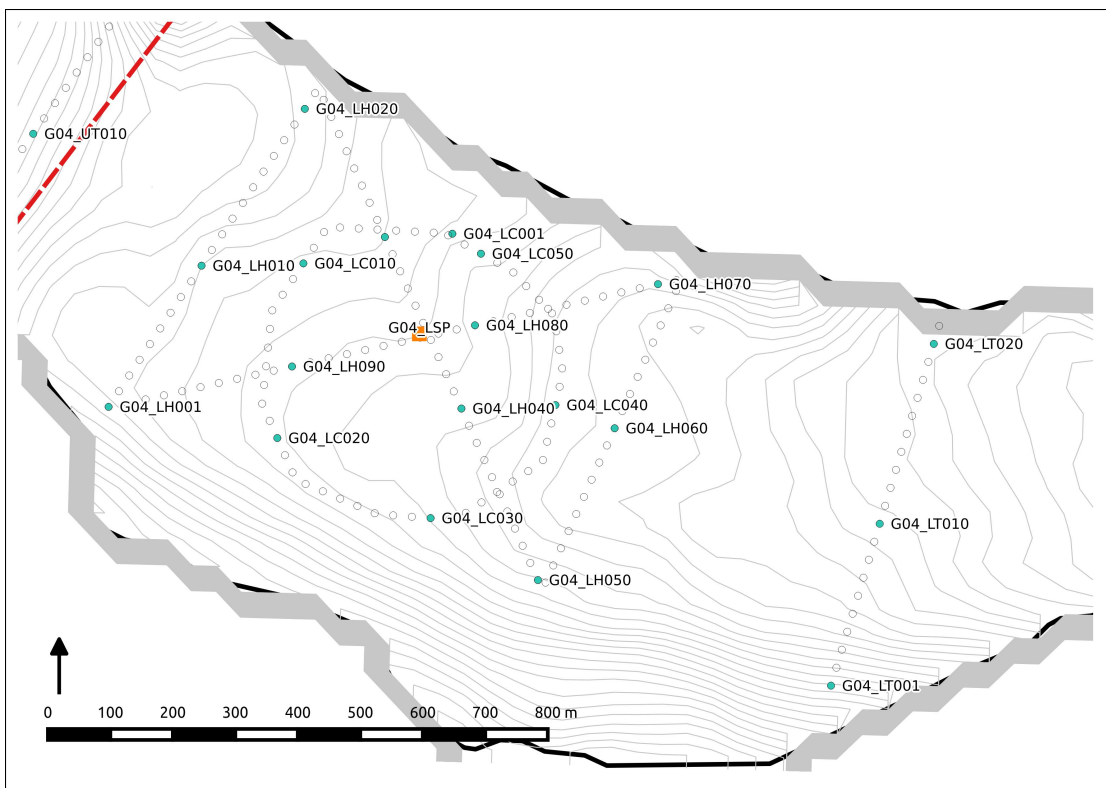
Appendix B

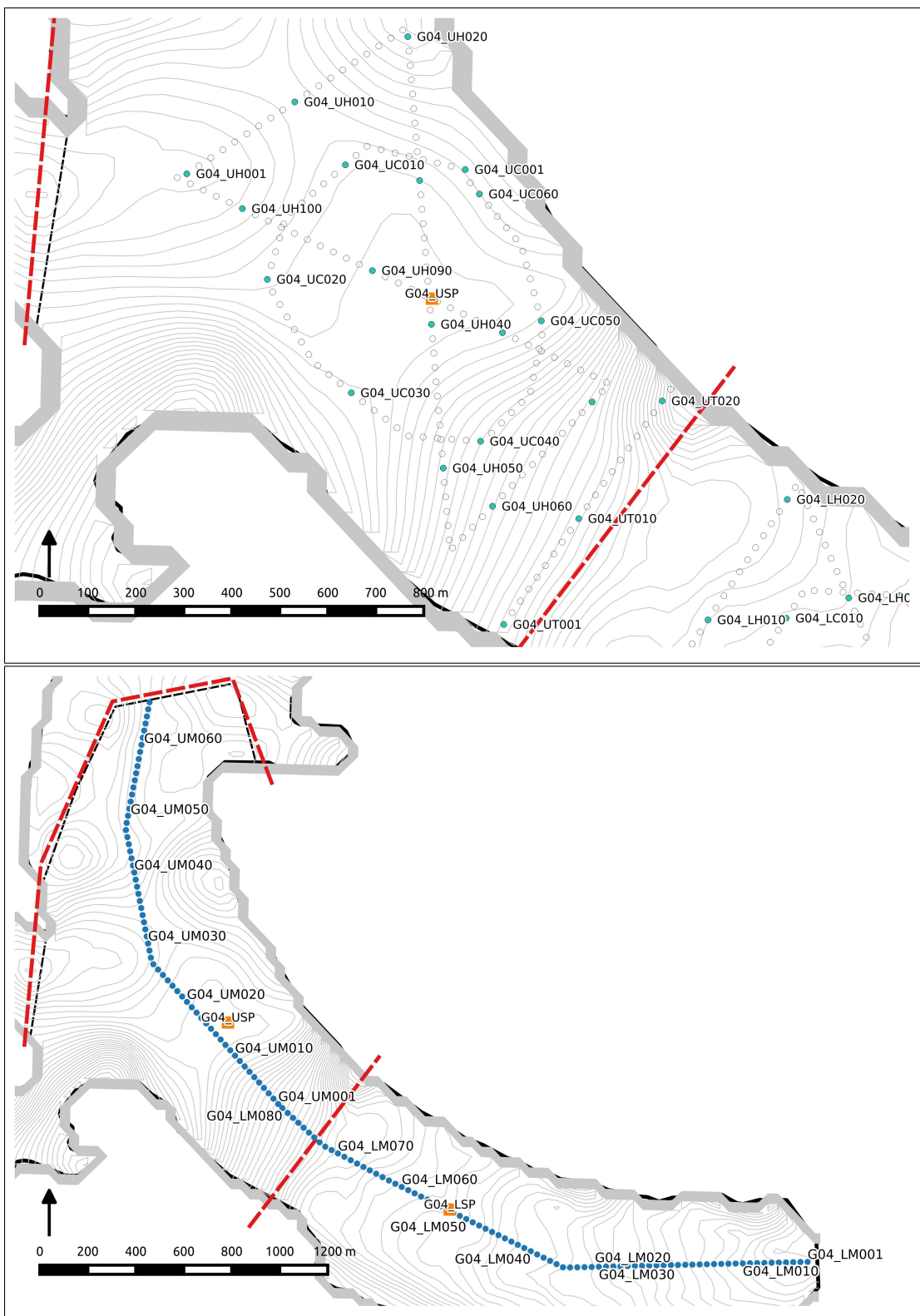
Field Maps

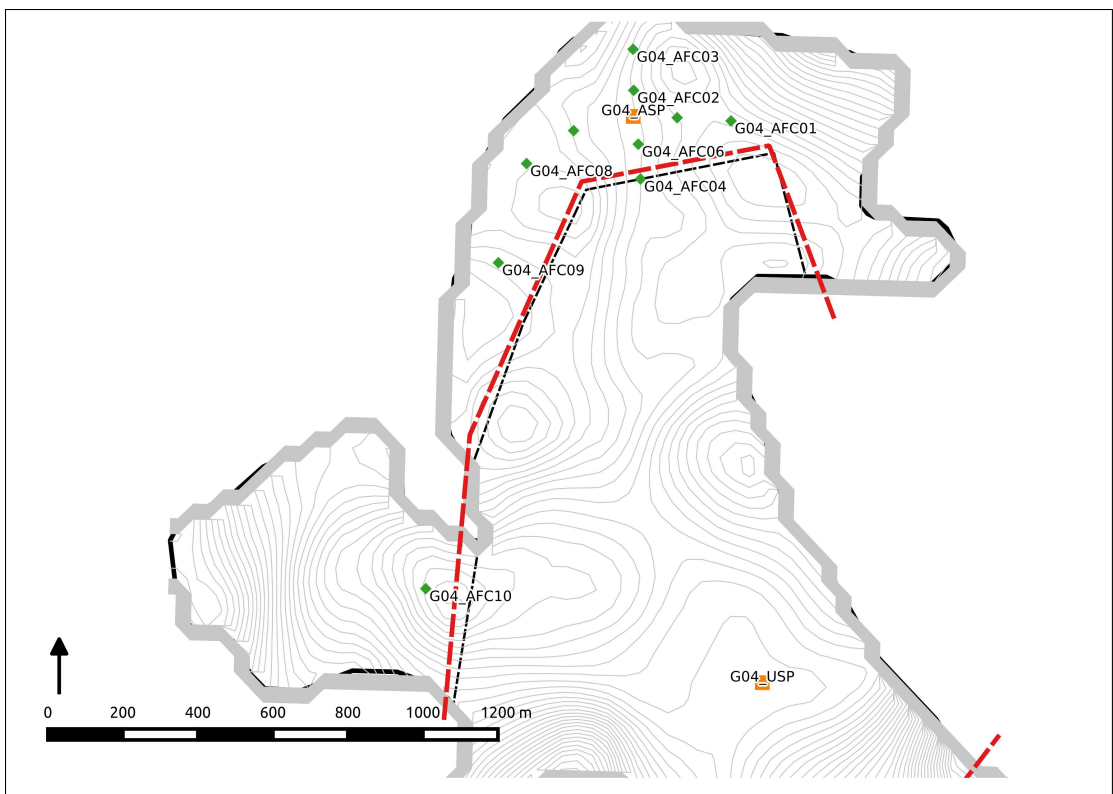
Glacier 4



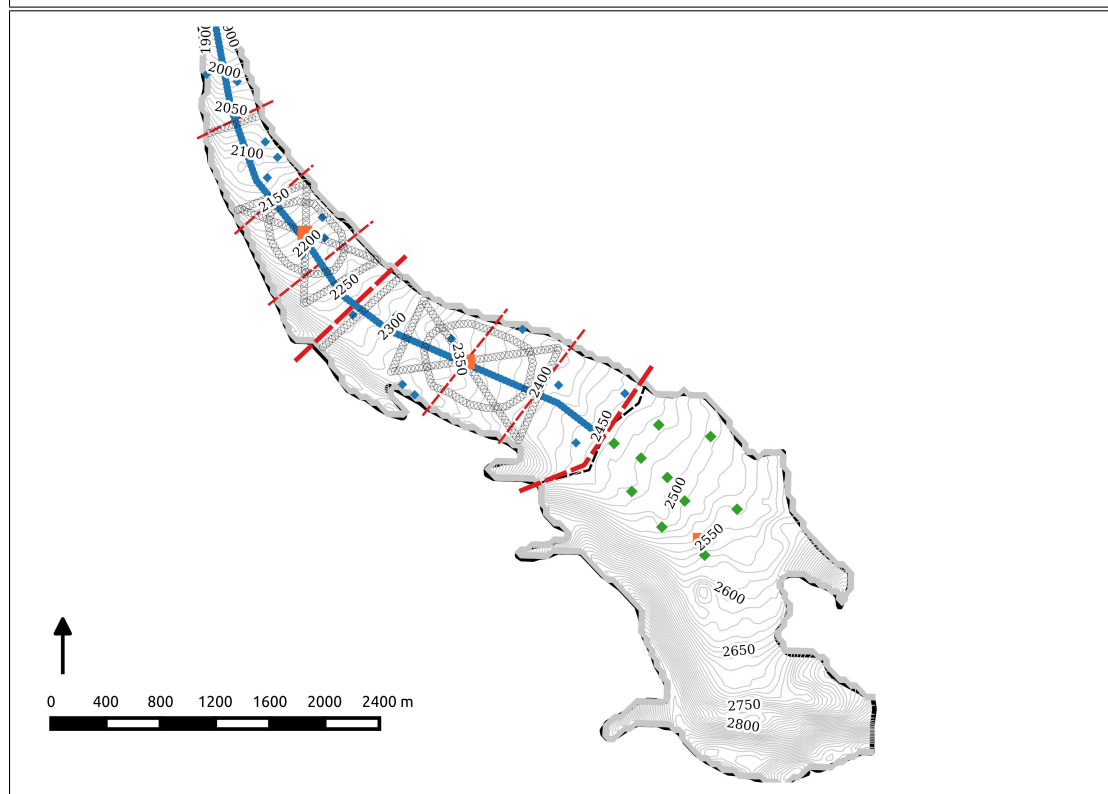
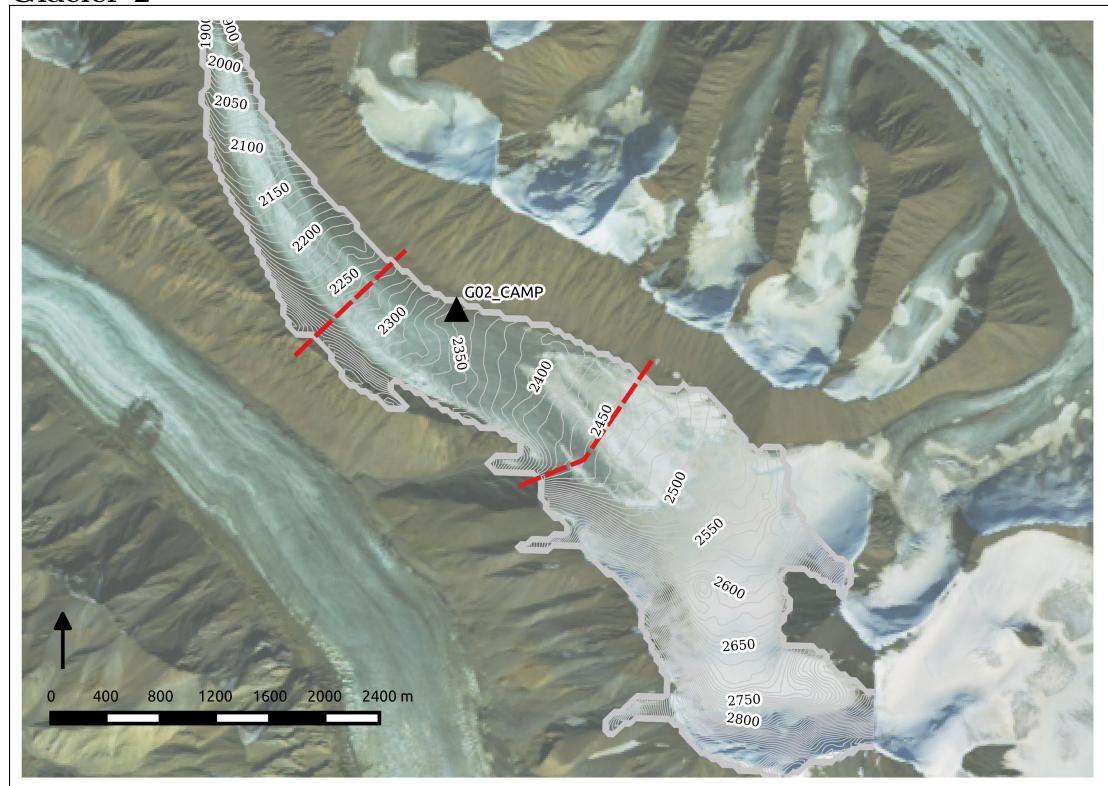


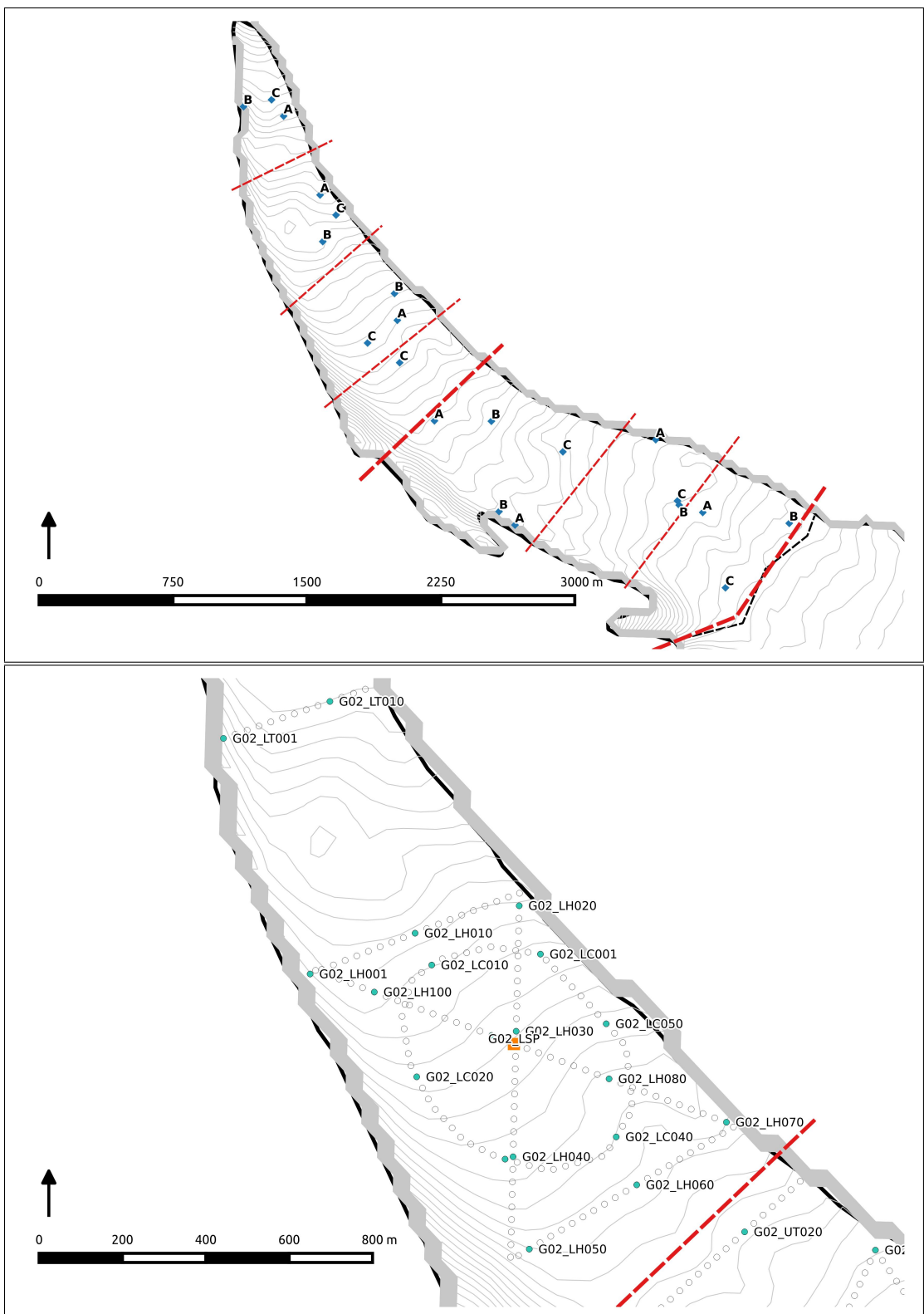


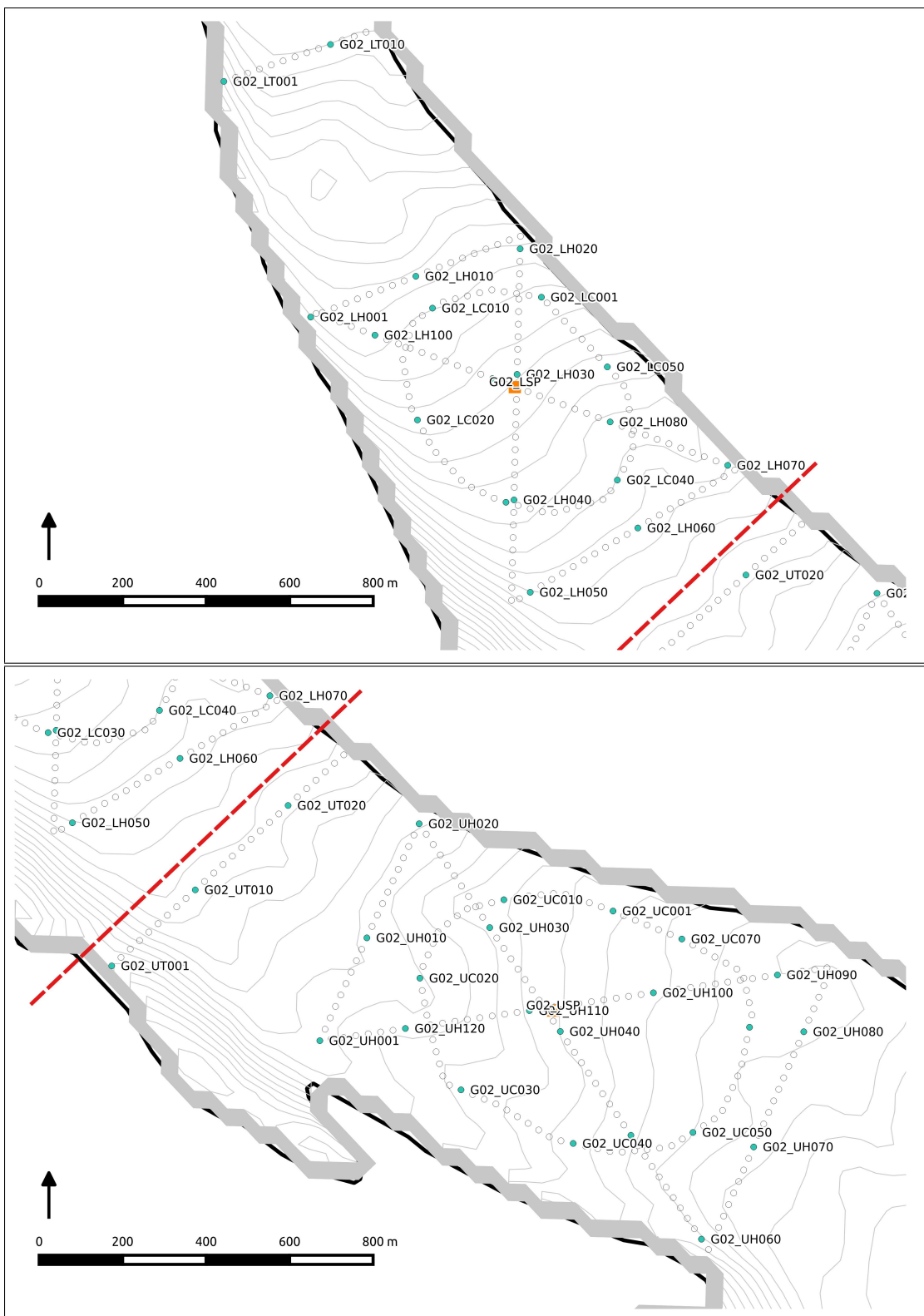


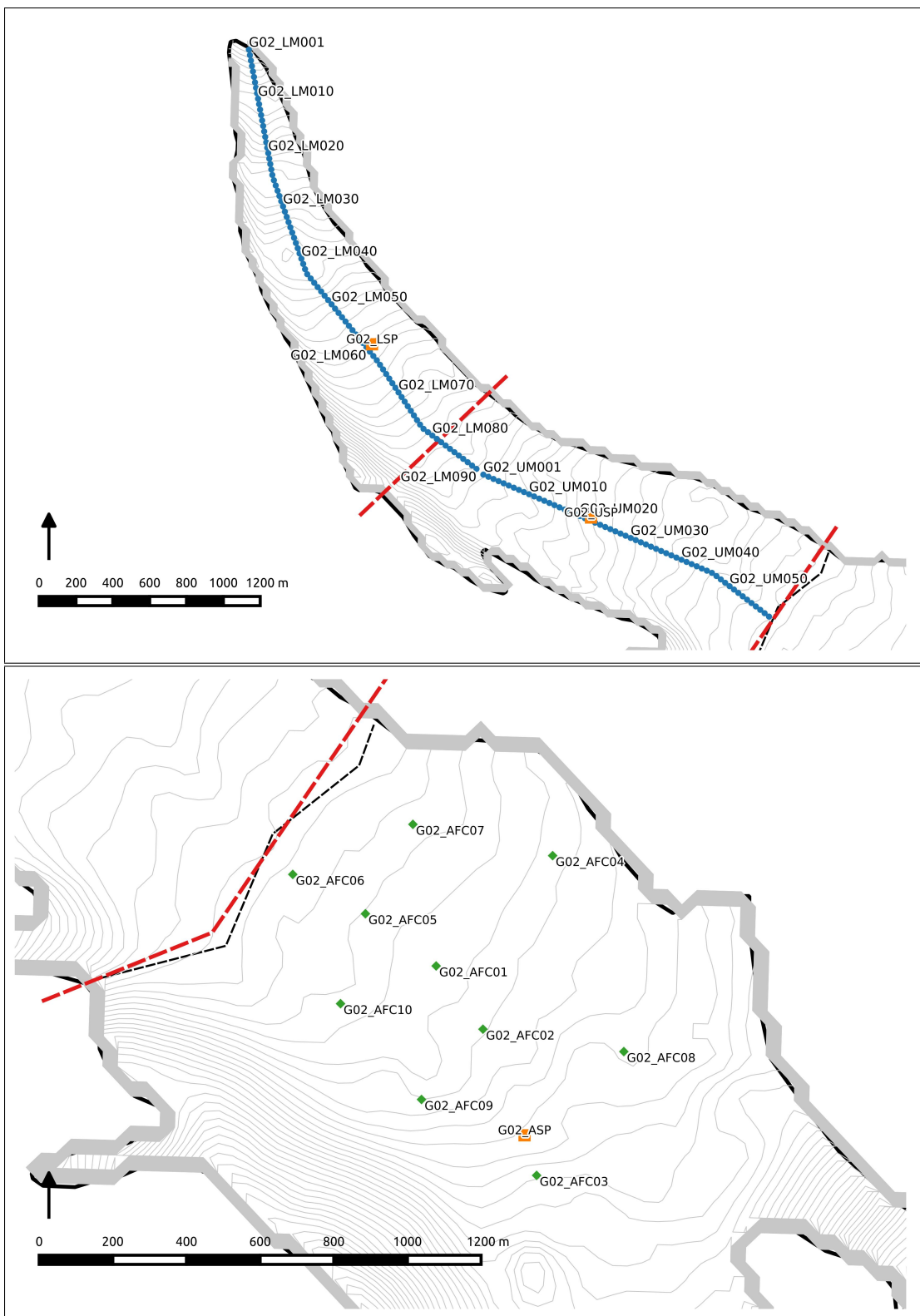


Glacier 2

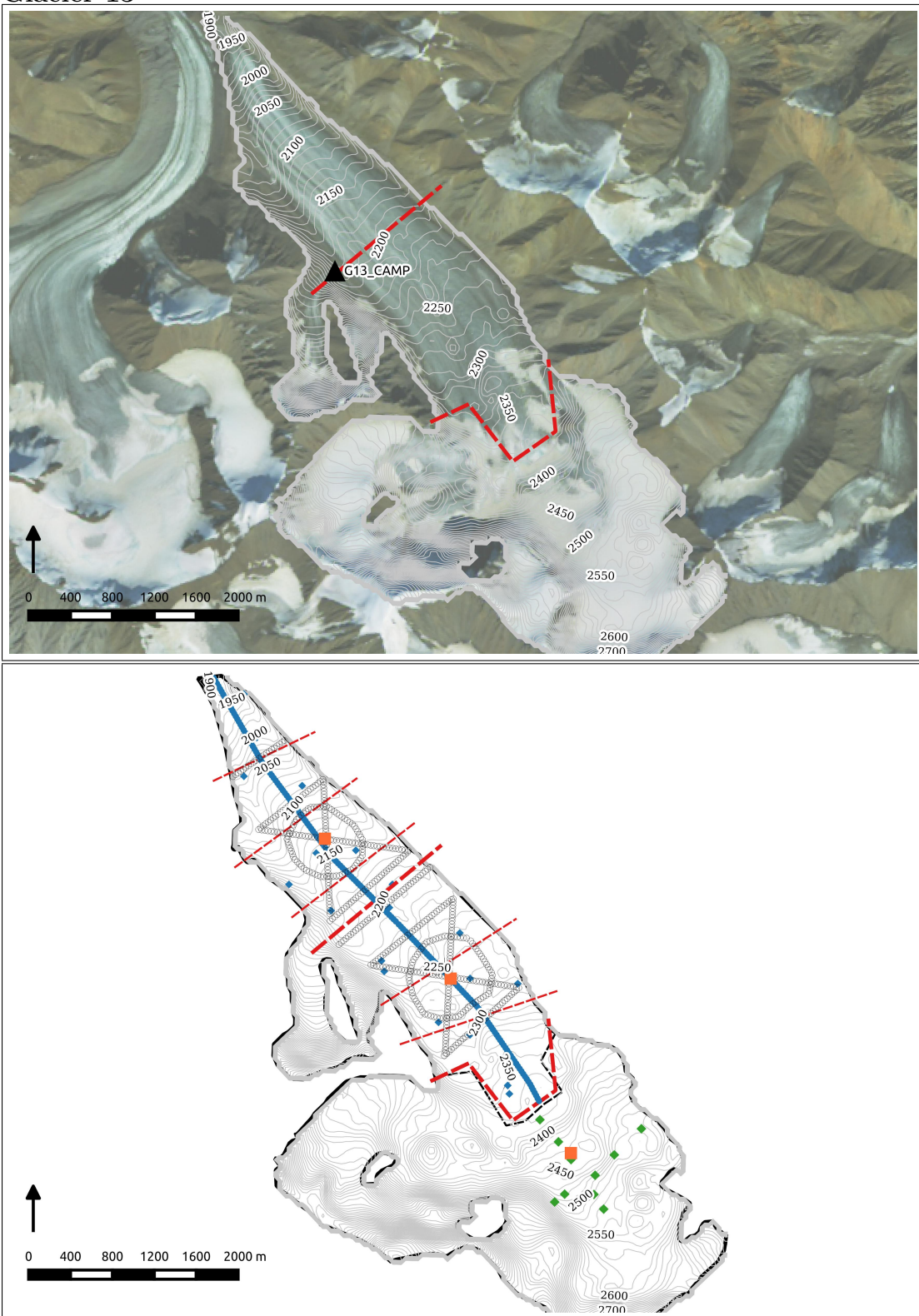


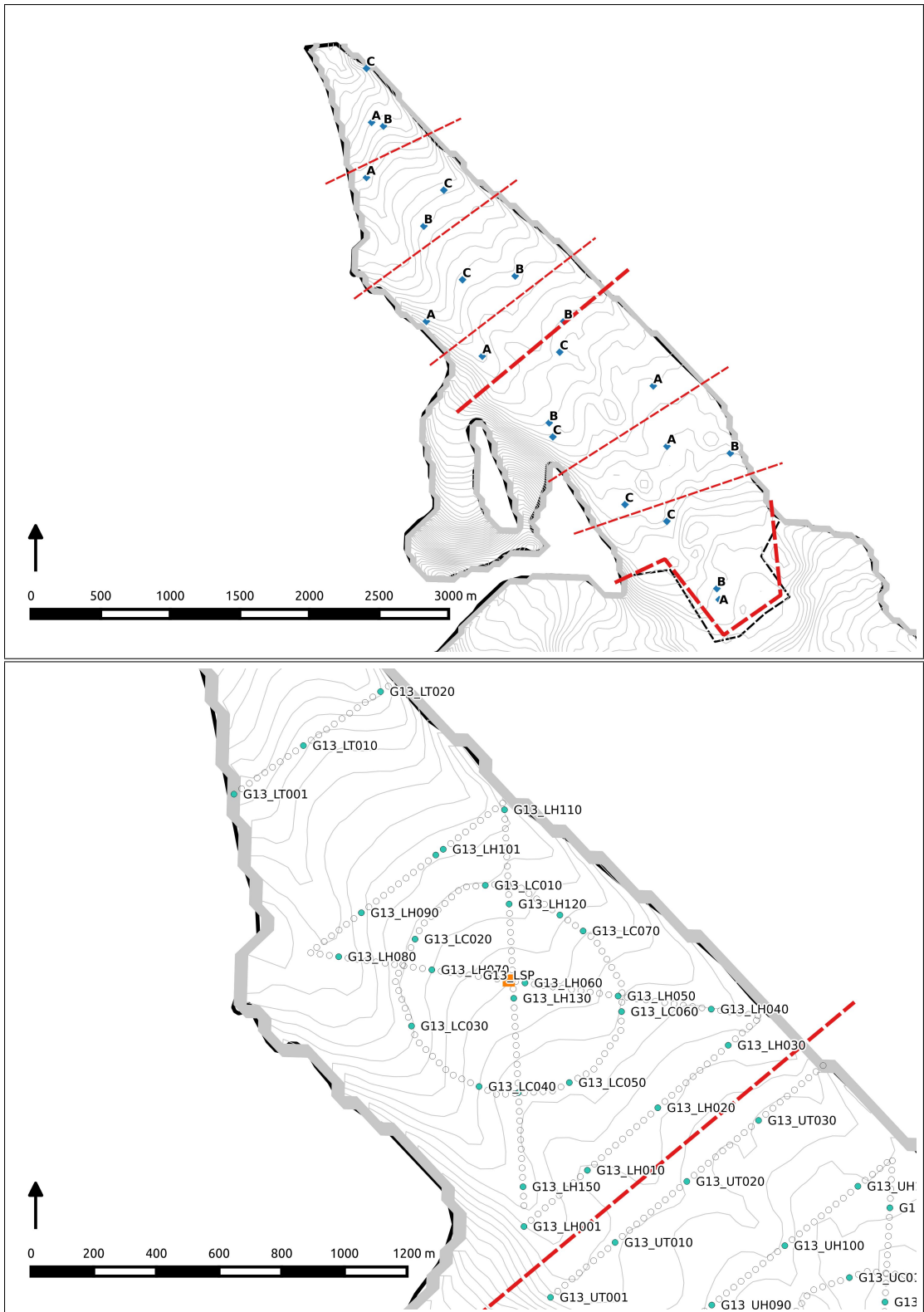


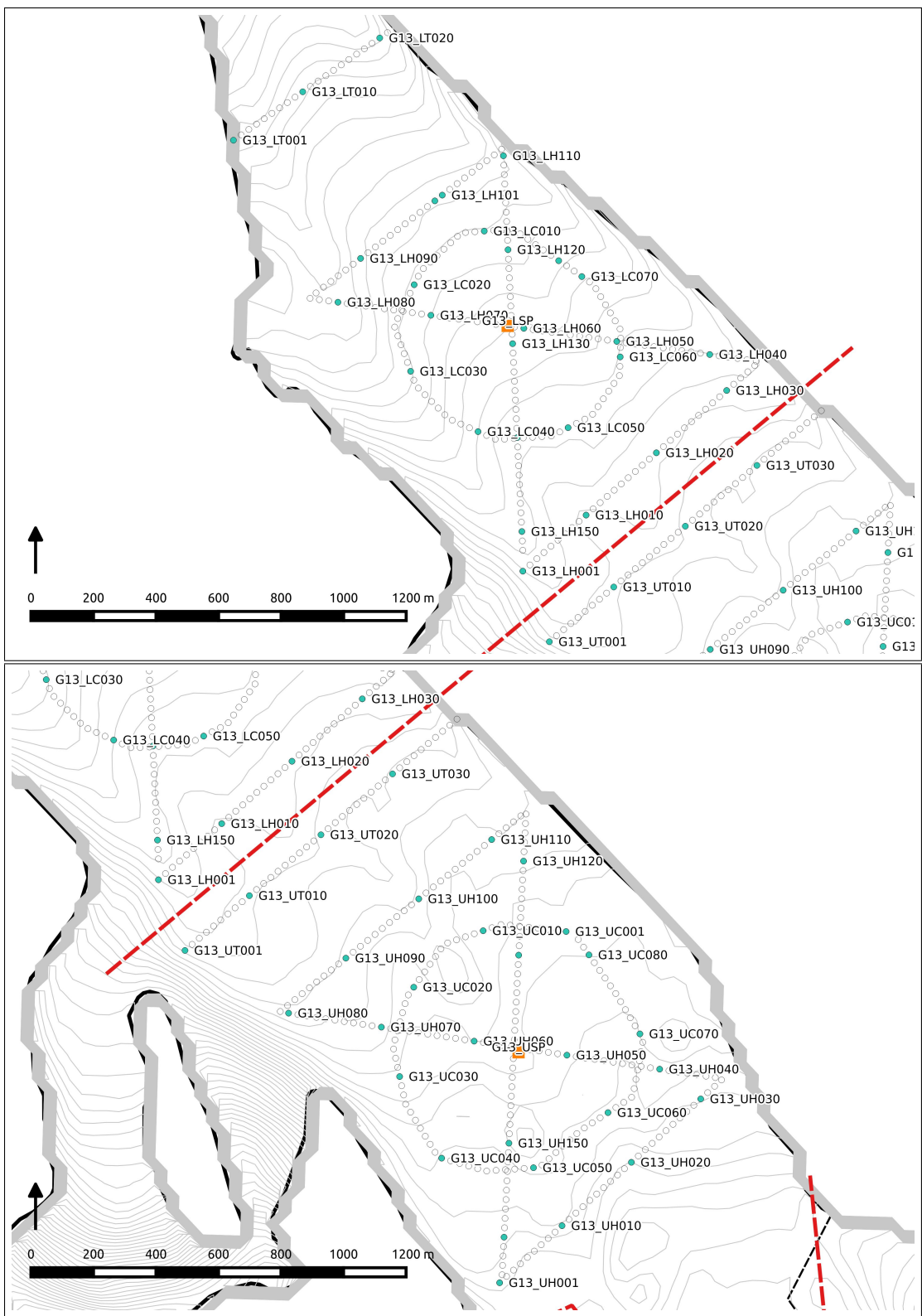


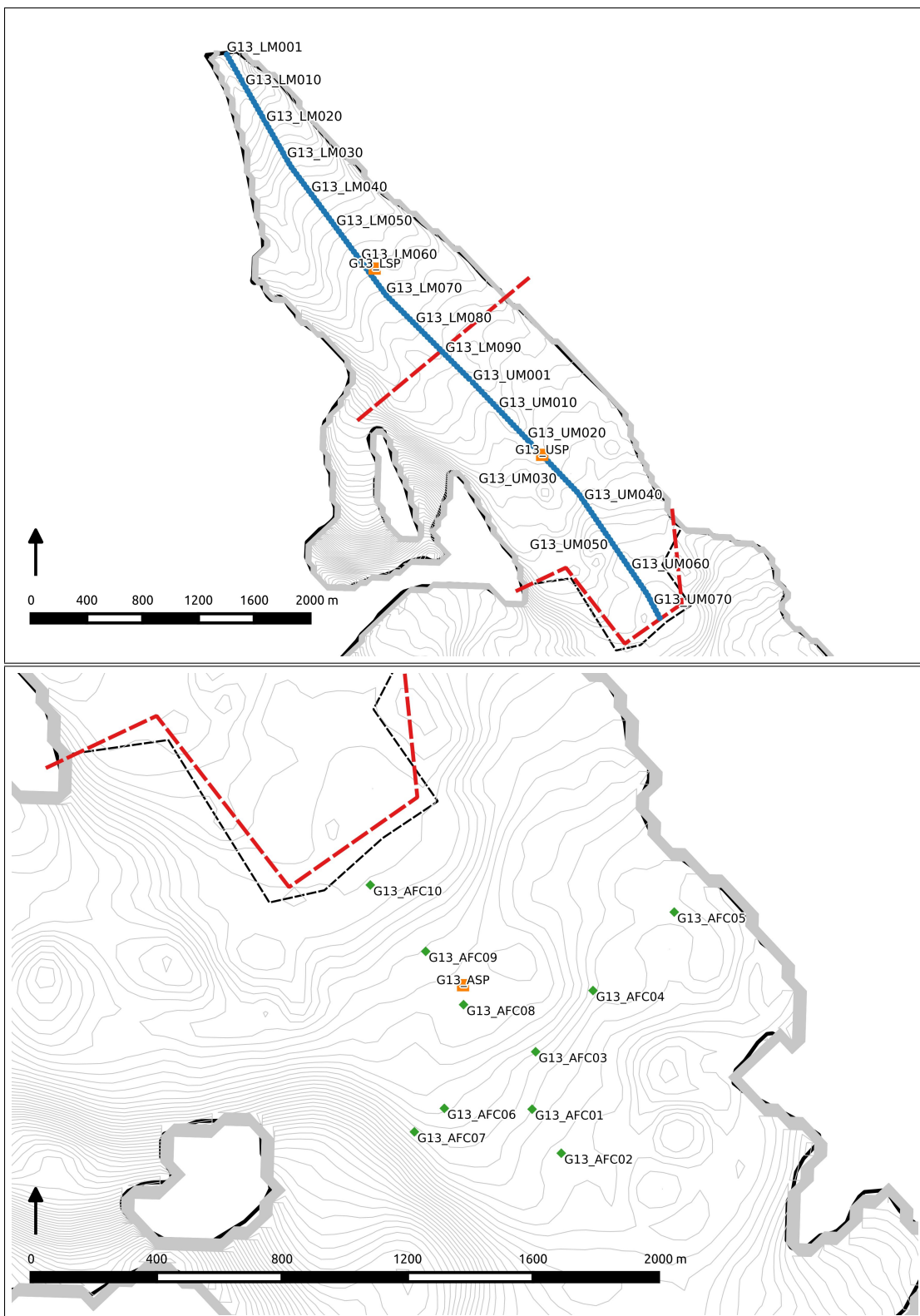


Glacier 13









Appendix C

Data Processing Scripts

Converting snow depth and density measurements to usable values of snow water equivalent (SWE) is done using a number of scripts written in Matlab. Since there are a number of possible variations for how SWE is estimated, various options are outlined in the ‘OPTIONS.m’ script. To run the entire data processing framework first ensure your desired SWE estimation options are reflected in the ‘OPTIONS.m’ script and then run both ‘OPTIONS.m’ and ‘MAIN.m’

C.1 Snow depth measured with graduated avalanche probe

C.1.1 Linear and curvilinear transect surveys

The following methodology was used to determine measurement locations along transects (each step corresponds with a section of the Matlab code ‘MeasurementLocations.m’):

1. Waypoint (WP) locations were exported from the GPS units using the Garmin BaseCamp program. They were then imported to QGIS and exported with UTM coordinates in the file ‘GlacierWP_UTM.xlsx’.
2. In order to obtain the measurement locations for the first WPs of each pattern, a fictitious WP was created that was along the line between the first and second WPs, but located ahead of the first WP. These fictitious waypoints were then inserted into the original data.
3. A set of 1000 equally spaced points was created along a straight line between each set of subsequent of WPs (including the fictitious WPs from the previous step) using the function `linspaceNDim.m` created by Steeve Ambroise and downloaded from the MathWorks File Exchange. The Euclidean distance between these interpolated points and the marked WP was then calculated and the points with distances closest to the assumed separation between observers were retained. A matrix was then created, which has the UTM Zone 7N Easting and Northing of

each measurement location and is labelled with the marked WP and a decimal that corresponds to the relative observer (e.g. label 45.2 means that the location was determined from the marked WP #45 and is 20 m behind this WP because it is the second observer).

Data recorded by each observer in the field books were entered into a spreadsheet format and then imported and processed in Matlab according to the following steps (each step corresponds with a section of the Matlab code ‘Import_Transect.m’):

1. A spreadsheet was created with a sheet for data from each snow depth (SD) field book (SD#1, SD#2, SD#3, and SWEDepth). For each reference WP there were values for all snow depth measurements and their quality (1 for good, 0 for bad or uncertain), written comments, field book name, glacier number, observer, transect, and date collected.
2. The quality, comments, book name, glacier name, observer, pattern, and date entries were turned into categorical variables (data type in Matlab), allowing for efficient grouping and data searching in future analysis.
3. Each depth measurement was then assigned the corresponding measurement location UTM from the ‘MeasurementLocations.m’ script. This was done by matching the WP number from the field books and that of the marked WPs and then assigning the coordinates from the WP ending with .1 to depths recorded in book SD#1, and likewise for the remaining books. The data sets from each field book were then made to be the same dimensions by inserting empty cells for WPs where no data were recorded in that set of observations.
4. The data were then arranged in a structure variable (called SD) with rows corresponding to each book (e.g. row 1 is data from book SD#1) and columns corresponding to the various types of data (e.g. depth values or glacier name). For example, the matrix with the glacier name for each value recorded in the book SD#1 can be accessed with ‘SD(1).glacier’.

Subsets of the transect data can be pulled using the function ‘pulldata.m’. The function is called with `pulldata(data, book, glacier, person, pattern, quality, format)`. Here, `data` is the full SD structure, `book`, `glacier`, `person`, and `pattern` are all strings that refer to desired categories, `quality` differentiates between good (1), bad (0), or ‘all’ data, and `format` specifies the formatting of the full depth matrix as being either a column vector (‘skinny’) or a matrix with depth values for one WP in a single row.

C.1.2 Zigzag surveys

Data from zigzag surveys, which include the measured snow depths and distances between adjacent measurement points, were entered to a spreadsheet. The data were then processed using the following procedure (each step corresponds with a section of the Matlab code ‘Import_Zigzag.m’):

1. Data were imported into Matlab.
2. Categorical data, including glacier number, zigzag zone label, reference vertex, data quality, observer name, date collected, and book name, were created.
3. A structure that contained the depth data and categorical variables was created.
4. The distance of each measurement point from its reference vertex was then calculated (Figure 2.12). These locations were assumed to be a cumulative sum of distances in a straight line between two subsequent vertices. Two options exist for determining the location of the reference vertex:
 - (a) Option 1 calculates the distance of each point from the UTM coordinates of the reference vertex.
 - (b) Option 2 calculates the distance of each point from the end of the previous line of measurements. The coordinates of the vertices were used for the start of each ‘Z’ shape (ZZ01 and ZZ05).
5. The final processing removes poor quality data and converts snow depth to snow water equivalent (SWE) based on the density calculated from the average SWE values measured with the Federal Sampler in each zigzag (see Section 3.1).

C.2 Snow density

Snow density data were first entered into and organized in a spreadsheet then processed in Matlab as follows (each step corresponds with a section of the Matlab code ‘Import_Density.m’):

1. Snow density data were imported into Matlab and poor quality data were removed.
2. Snowpit-derived snow density values were assigned to their respective location names and coordinates.
3. For each zigzag survey, the mean snow density (Federal Sampler), snow density standard deviation, and number of good quality measurements were calculated.
4. For remaining Federal Sampler measurement locations, the mean snow density, snow density standard deviation, and number of good quality measurements were calculated.
5. A structure with the processed data was created (**Density**).

The final version of the **Density** structure includes five fields:

Density.snowpit contains snow density data from snowpits. Columns correspond to snowpit label, integrated density, Easting, Northing, elevation, minimum density, maximum density, snow depth.

Density.pitANDtube includes data from locations where measurements were taken in a snowpit and with a Federal Sampler. Columns correspond to snowpit label, Federal Sampler mean density, standard deviation, minimum Federal Sampler-derived density, maximum Federal Sampler-derived density, number of observations, snowpit-derived density, site elevation, minimum snowpit density, and maximum snowpit density.

Density.tube includes Federal Sampler data. Columns correspond to location label, density mean, standard deviation, minimum and maximum, number of good quality observations, Easting, Northing, elevation, and snow depth.

Density.zigzagtube includes density values at each zigzag location estimated using a Federal Sampler. Columns correspond to zigzag label, mean density, standard deviation, number of observation, and site elevation.

Density.SWEdepth is a summary of all the Federal Sampler derived density data and corresponding snow depth measurements. Columns correspond to location label, mean probe depth, depth measured by the Sampler, and snow density measured using the Federal Sampler.

C.3 Snow water equivalent (SWE)

The final SWE values for each measurement location are calculated in Matlab using the following steps (this corresponds to the script ‘Import_SWE.m’):

1. The desired density interpolation method is selected in the ‘OPTIONS.m’ script.
2. Snow depth values from transects, zigzags, and extra measurements is complied into a single structure called ‘SWE’.
3. The elevation of each measurement location according to the SPOT5 DEM was found in QGIS and the elevations are imported to Matlab and assigned to their respective depth measurement values.
4. The density values for each snow depth measurement location were estimated according to the chosen method. SWE was then calculated.

To select the desired density calculation option (or to cycle through all options), change the value of `options.DensitySWE` to the appropriate option number.

The final version the `SWE` structure includes three rows, which correspond to Glacier 4, 2, and 13, and ten fields. The fields are:

- `book` (field book where measurement is written)
- `comments` (any comments noted by observer)
- `density` (the density value used to calculate SWE)

- **depth** (mean depth measured at each sampling location, $n = 3$ usually)
- **glacier** (glacier number where measurement was taken)
- **label** (measurement point reference label; for transects this is the waypoint number and relative position, for other measurements this is a label associated with transect and location)
- **pattern** (transect, or set of transects, that include the measurement)
- **person** (initials of observer)
- **swe** (estimated SWE value)
- **utm** (the Easting and Northing for the measurement location as well as the DEM elevation).

For example, to access the SWE values for Glacier 2, one would type `SWE(2).swe`.

The `SWE` structure includes all data that is collected for each glacier. If there is a need to remove the zigzag data or keep only the zigzag data, the script ‘ZigzagRemoval.m’ can be run. Set the option for including or excluding zigzag data in the script ‘OPTIONS.m’.

Appendix D

Topographic parameters from QGIS to Matlab

The value of each topographic parameter at the sampling location is determined in QGIS. The sampling locations are imported to QGIS and the Point Sampling Tool is used to determine the value of the topographic parameter raster cell at each measurement location. The set of parameters that corresponds to each location is then exported to a .csv file and imported into Matlab with the script ‘Import_Topo.m’. Note that selection of Sx values is completed first, as described in Section 2.4.2. The Sx map made with the combination of d_{max} and azimuth values that produces Sx values most strongly correlated with SWE is exported.

After importing values of sampled topographic parameters to Matlab, the sets of parameter values (x_p) are standardized (x_s) by $x_s = \frac{x_p - \mu}{\sigma}$. The resulting structure is called `topo_sampled` and is used in the regression to be able to compare the explanatory power of each parameter (Section 4.1.4 and 4.1.5). A non-standardized copy of the topographic parameters at the sampling locations is also kept for plotting purposes and is called `topo_sampled_ns`. Both structures are organized as a vector of values corresponding to the vectors in the `SWE` variable.

The topographic parameter rasters are also exported from QGIS as a .csv file and then imported into Matlab with the script ‘Import_Topo.m’. The values are stored in the structure `topo_full`, where each cell corresponds to one DEM cell. Cells outside of the glacier outline have no value (`NaN`). The raster values were standardized using the mean and standard deviation of the sampled topographic parameters so that this set of full topographic parameters could be used for modelling SWE using the regression. A copy of the non-standardized values was stored as `topo_full_ns`.

Appendix E

MLR software

The MLR was completed with the following steps (executed using the function 'MLRcalval.m'):

1. The topographic parameters are imported to Matlab using the script 'Import_Topo.m'.
2. The `topo_sampled` structure for one glacier as well as the `SWE` structure is passed into the function.
3. A set of initializations is completed. This includes 1) creating a logical matrix to choose all linear combinations of topographic parameters, 2) selecting the number of runs, 3) creating a matrix of random numbers for selecting data points in the cross validation procedure, 4) initializing matrices, and 5) converting the input structure to a table.
4. For each linear combination of topographic parameters, 1000 runs of a cross validation MLR are then executed. Two-thirds of the total data is randomly selected [66] to use for calculating the regression (using the function `regress()` which is a basic regression function with fast execution). The MLR equation is used to predict the SWE using the remaining one-third of the topographic parameters. The root-mean-squared error (RMSE) between the predicted and observed SWE values is then calculated and the set of regression coefficients that produce the lowest RMSE are then chosen for that combination of topographic parameters. The function `fitlm()` is then used to calculate the MLR from the set of data that gave the lowest RMSE. This function is slower but calculates a number of additional values that characterize the fit of the model. One of these values is the Bayesian information criterion (BIC), which allows for model selection among a finite set of models [19]. The BIC from the best model for each combination of topographic parameters is saved.
5. A weighted sum of all models found using linear combinations of topographic parameters was then found. The BIC values for each model (BIC_i) were used to determine the normalized weight of each model (w_i) relative to the best model (lowest BIC value BIC_{min}) according to Eq. 4.4.

6. The percent variance ($var\%$) explained by each parameter was calculated using the equation $var\% = \frac{SSr}{SSt} \times 100$, where SSr is the sum of squares of the residual (fitted topographic parameters) and SSt is the total sum of squares (SWE observations). The final coefficients and the percent variance explained by each one can be found in the `coeffs_final` table within the function and in the `m1r` structure when run for all density options and glaciers in the main script ‘TopoRegression.m’.
7. The residuals of the fit have also been calculated as a separate variable that can be returned when the function is called. The residual is calculated as the difference between the estimated SWE value and observed value.

Appendix F

BMA software

The BMA process was implemented in R, using the Bayesian model statistics (BMS) package developed by [136]. The function `BMS_R()` computes the posterior distribution mean value of all β coefficients for topographic parameters as well as the percent variance explained by each parameter using the following steps:

1. A portion of the data (2/3 as suggested by [66]) is randomly chosen as the calibration set and saved as a .mat file.
2. The Bayesian model statistics (BMS) package developed by [136] is run in R (called through an operating system command in Matlab)
 - (a) The R script imports the .mat file with SWE and topographic parameter values. It then creates a data frame with the SWE values as the first column and the topographic parameters as the remaining columns.
 - (b) The BMS package is used to complete BMA for the imported values. A uniform model prior was chosen. The mean coefficient value, coefficient standard deviation, PIP, and the posterior probability of a positive coefficient (how probable it is for the sign of the coefficient to be positive) were computed.
 - (c) The coefficients are saved as a .mat file.
3. Regressor coefficient values calculated in R are loaded into Matlab and a data table is created with the coefficients.
4. The remaining portion of the data (1/3) are then used to calculate a modelled value of SWE at those locations. These are compared to the observed SWE values and a RMSE value is determined.
5. The above steps are completed 1000 times and the coefficients associated with the lowest RMSE are chosen.
6. Percent variance explained by each parameter is then calculated in the same way as for the MLR (see Section E).

7. The final table of values includes the coefficients and percent variance explained for all topographic parameters associated with the lowest RMSE. It also includes the intercept and the actual RMSE value. This table is returned from the function.
8. The residuals of the best BMA fit are also calculated and can be return from the function.

Appendix G

Kriging software

Kriging is executed using the DiceKriging package in R [106]. The author-written Matlab function `KrigingR()` moves SWE data to R and then uses DiceKriging to find the estimated kriged surface, the upper and lower confidence intervals, the cross-validated (leave-one-out) estimates of SWE, as well as parameters that describe the kriging model fit (nugget, maximum log likelihood and mean constant). Input parameters of `KrigingR()` are the snow data (e.g. SWE values), locations of measurements, and the name of the relevant glacier. The function follows these steps:

1. The working directory is changed to the ‘Kriging’ folder
2. The DiceKriging.R script is run
 - (a) The function `km()` estimates the best fit kriging model with a constant mean using the Matérn $\nu = 3/2$ covariance kernel. The maximum log likelihood, model intercept (mean) and nugget estimates from the model are then extracted.
 - (b) Leave-one-out cross validation is then applied to estimated values using the built-in DiceKriging function `leaveOneOut.km()`.
 - (c) Surface prediction is then done for the entire glacier. First, a grid that replicates the glacier DEM is created (point spacing every 40 m to match the size of the DEM). Then, the built-in DiceKriging function `predict()` is used to predict the surface values at all grid locations. The predicted values, as well as the upper and lower 95% confidence intervals are returned.
 - (d) All returned values are then saved as a .mat file.
3. The .mat file is imported into Matlab and the data are organized into a structure. Cells outside of the glacier outlines are set to `NaN` and negative SWE values are set to zero. The final data are then output from the Matlab function.

Appendix H

Variability of data at various scales

H.1 Point Scale

This section details basic statistical results of the snow depth data at the point scale. The goal of these analyses is to examine variability of single measurements and to determine whether any correction need to be made to the collected data for future analysis.

H.1.1 Data normality

A χ^2 test is done to test whether the collected snow depth data are normally distributed. Generally, the transect snow depth data are not normally distributed and are even further from normality (larger χ^2 values) for data grouped by glacier (Table H.1). However, we chose to not transform the data in order to maintain its original context and because transformation of snow depth data is not typically done.

H.1.2 Observer differences

An ANOVA for each transect of snow depth measurements taken by different observers shows that there are no differences between observers ($p > 0.05$) (data not shown). The only exception is the Lower Hourglass on Glacier 4, where snow depth values collected by one observer were, on average, greater than the snow depth measurements taken by the other two observers ($AC > AP = CA$ with $p < 0.01$). Since this was the first transect completed and the only one to show differences by observer, this difference can be considered an anomaly. This result shows that observer bias is likely to not affect the results of this study and no corrections to the data based on observer were applied.

H.1.3 Standard deviation of snow depth along linear and curvilinear transects

The mean standard deviation of snow depth measurements collected at each location within various transects was found by calculating the standard deviation of the three to four measurements made by each observer at each measurement location (Table H.2). The mean of these standard deviations for each grouping (Table H.2) represents the variability in snow depth for the sampling locations. It can be used to evaluate the representativeness of the mean snow depth values that were used in the analysis at larger scales.

The overall standard deviation of all measurements was calculated by taking all the depth measurements within a subset of the data and then calculating the standard deviation (Table H.3). The overall standard deviation represents the variability in the depth field.

The mean standard deviation varies between glaciers, transects, and observers but generally, the reproducibility of depth measurement is on the order of centimetres (10^0). The overall standard deviation of measurements over the study area is on the order of 10^1 . Therefore, the standard deviation of a snow depth measurement is small compared to the standard deviation of all snow depth measurements. When expressed as a percentage of the mean, the overall standard deviation (Table H.3) is also larger than that of the mean standard deviation (Table H.2). This shows that variability at the point scale (a single measurement location) is an order of magnitude smaller than the variability of the depth field for the length of a transect, so the use of the mean snow depth at each measurement location is a valid value to carry forward in the analysis.

Variability in snow depth differs considerably between glaciers (Figure H.1). Both the range and mean depth are largest for Glacier 4 and smallest for Glacier 13. Glacier 13 has the most outliers ($>1.5 \times$ inner quartile range). The standard deviation of all

Table H.1: Normality of data with various sub-groups. χ^2 values are shown and normally distributed data is bold ($p < 0.05$). Data for each glacier are divided into lower hourglass (LH), lower circle (LC), lower midline (LM), upper hourglass (UH), upper circle (UC), upper midline (UM), and upper transect (UT).

Glacier	Transect	χ^2
Glacier 4	LH	14.9
	LC	17.3
	LM	6.6
	UH	52.1
	UC	5.9
	UM	1.4
	UT	15.7
Glacier 2	LH	27.8
	LC	5.0
	LM	6.2
	UH	43.8
	UC	13.1
	UM	31.3
	UT	0.1
Glacier 13	BT	13.1
	LH	32.1
	LC	11.4
	LM	18.1
	UH	12.8
	UC	17.6
	UM	9.7

measurement taken on a glacier (Table H.3) is lowest for Glacier 13 and highest for Glacier 2, with the standard deviation of Glacier 4 being close to that of Glacier 2.

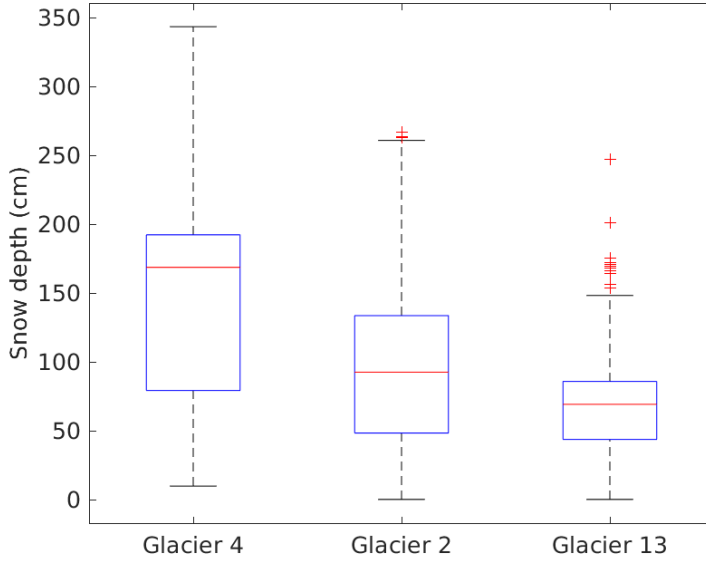


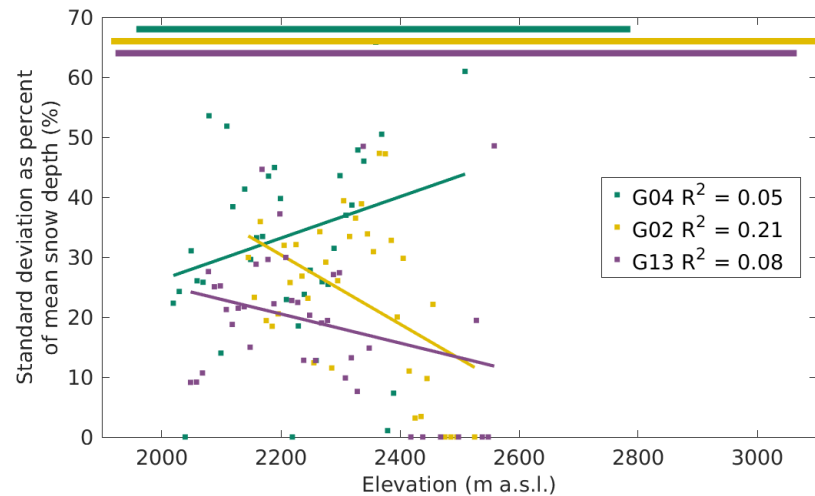
Figure H.1: Variability in all snow depth measurements taken at each glacier. Red line indicates median, blue box shows first quantiles, bars indicate minimum and maximum values (excluding outliers), and red crosses show outliers, which are defined as being outside of the range of 1.5 times the quartiles (approximately $\pm 2.7\sigma$).

elevations, which may skew the trend of higher variability close to the terminus.

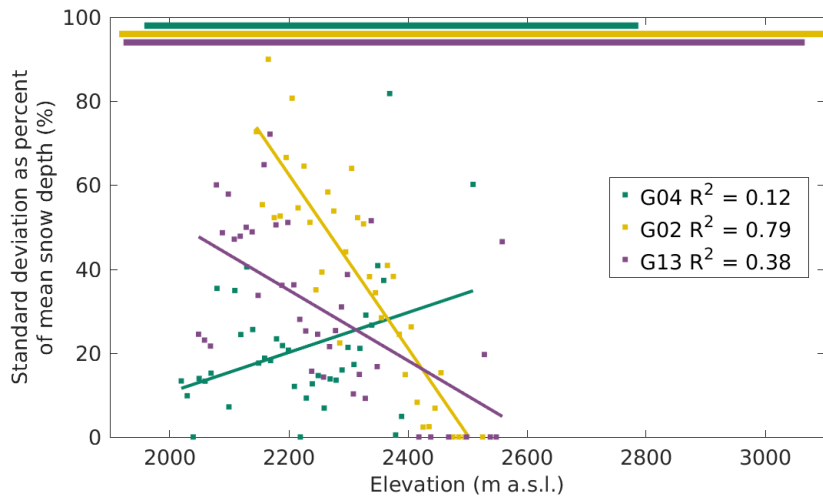
The standard deviation as a function of binned elevation show that the standard deviation decreases with elevation on both Glacier 2 and 13 but it increases with elevation on Glacier 4 (Figure H.2). The regression of elevation and standard deviation as percent of the mean is strong for Glacier 2 ($R^2 = 0.79$) and weak for Glacier 13 ($R^2 = 0.38$) and Glacier 4 ($R^2 = 0.12$). Therefore, the variability is higher closer to the terminus of the Glacier 2 and there is no significant trend on Glacier 4 and 13. However, there are comparatively fewer depth measurements taken at higher elevations.

H.1.4 Standard deviation of SWE in DEM cell

The chosen sampling design (Section 2.1) resulted in areas that correspond to a single DEM cell containing multiple SWE measurement locations. To extrapolate SWE over the glacier it is valuable to have one value of SWE for each DEM grid cell. Therefore, the mean SWE was used for a DEM cell with multiple observations. Using the mean value is supported by the small standard deviation of SWE within one DEM cell for all glaciers (Figure H.3). The mean standard deviation is 0.03 m w.e., which is low compared to the variability of SWE over the entire glacier (Section H.1.3). Extreme standard deviation values result from highly variable locations such as transects across deep supra glacier streams (Glacier 13) or on debris covered ice or ice-cored moraines (Glacier 4). However, the mean standard deviation is small so future analyses use the mean SWE value within one DEM cell.



(a)



(b)

Figure H.2: Standard deviation (a) and standard deviation as percent of mean (b) of all snow depth measurements binned in elevation bands of 10 m. Bars at the top of the figure indicate the elevation ranges of the three study glaciers. The regression of elevation and standard deviation of snow depth is shown as a coloured line within the data.

Table H.2: Mean standard deviation (cm) of snow depth measurements for the entire glacier (Overall Glacier), different transects (Overall Transect), and each observer. Standard deviation as a percent of the mean snow depth is shown in brackets. Data for each glacier are divided into lower hourglass (LH), lower circle (LC), lower midline (LM), upper hourglass (UH), upper circle (UC), upper midline (UM), and upper transect (UT).

Transect	Overall Glacier	Overall Transect	Observer		
			AP	GF	CA
Glacier 4	3.5 (2%)	LH	5.1 (3%)	4.8 (3%)	—
		LC	4.7 (3%)	4.3 (3%)	—
		LM	3.7 (2%)	—	4.7 (3%)
		UH	2.6 (1%)	3.4 (1%)	2.2 (1%)
		UC	1.9 (1%)	1.9 (2%)	2.3 (1%)
		UM	1.9 (1%)	—	1.5 (1%)
		UT	3.9 (2%)	3.7 (2%)	2.4 (1%)
Glacier 2	5.1 (7%)	LH	5.4 (11%)	4.8 (9%)	6.1 (13%)
		LC	5.0 (12%)	3.9 (11%)	6.2 (15%)
		LM	6.5 (17%)	—	6.5 (18%)
		UH	4.1 (7%)	3.5 (5%)	4.5 (9%)
		UC	7.0 (4%)	5.5 (3%)	8.7 (4%)
		UM	4.2 (4%)	3.2 (3%)	4.1 (4%)
		UT	5.6 (10%)	3.2 (6%)	8.2 (13%)
Glacier 13	4.2 (6%)	BT	2.2 (2%)	2.2 (2%)	3.0 (2%)
		LH	3.8 (10%)	3.1 (6%)	4.0 (13%)
		LC	4.5 (8%)	2.9 (6%)	5.8 (8%)
		LM	6.6 (13%)	4.6 (10%)	7.7 (16%)
		UH	3.5 (4%)	3.4 (4%)	3.4 (5%)
		UC	3.8 (4%)	3.4 (4%)	4.0 (4%)
		UM	4.8 (6%)	4.4 (5%)	4.4 (5%)
		UT	4.1 (6%)	2.7 (4%)	4.6 (7%)

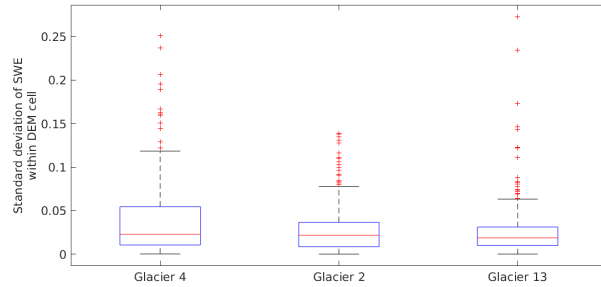


Figure H.3: Boxplot of the standard deviation of measured SWE in one DEM grid cell. Red line indicates median, blue box shows first quantiles, bars indicate minimum and maximum values (excluding outliers), and red crosses show outliers, which are defined as being outside of the range of 1.5 times the quartiles (approximately $\pm 2.7\sigma$).

Table H.3: Overall standard deviation (cm) of snow depth measurements for the entire glacier (Overall Glacier), different transects (Overall Transect), and each observer. Standard deviation as a percent of the mean snow depth is shown in brackets. Data for each glacier are divided into lower hourglass (LH), lower circle (LC), lower midline (LM), upper hourglass (UH), upper circle (UC), upper midline (UM), and upper transect (UT). The standard deviation of all transect data was 64.6 cm.

Glacier	Pattern	Overall	Overall	Person			AC
		Glacier	Pattern	AP	GF	CA	
Glacier 4	LH	44.7 (25%)	51.3 (28%)	51.4 (29%)	—	54.8 (32%)	45.7 (24%)
	LC		45.2 (26%)	50.5 (30%)	—	44.1 (25%)	39.8 (23%)
	LM		27.2 (15%)	—	21.6 (11%)	36.3 (19%)	22.5 (12%)
	UH		48.5 (28%)	48.6 (28%)	51.2 (29%)	—	45.8 (27%)
	UC		44.2 (23%)	44.8 (23%)	38.2 (21%)	—	48.2 (26%)
	UM		22.5 (13%)	—	24.1 (14%)	20.7 (12%)	22.7 (13%)
	UT		26.0 (13%)	25.1 (13%)	—	25.1 (13%)	27.7 (14%)
Glacier 2	LH	49.3 (62%)	29.9 (67%)	29.2 (63%)	—	30.6 (71%)	—
	LC		29.3 (61%)	28.6 (63%)	—	30.1 (59%)	—
	LM		18.4 (43%)	—	20.8 (45%)	15.5 (39%)	18.1 (43%)
	UH		42.0 (39%)	39.1 (37%)	41.6 (38%)	45.6 (42%)	—
	UC		55.0 (52%)	55.3 (53%)	55.2 (52%)	56.1 (52%)	—
	UM		35.1 (29%)	38.4 (33%)	34.5 (29%)	31.8 (27%)	—
	UT		36.4 (61%)	27.3 (51%)	—	43.9 (70%)	—
Glacier 13	BT	30.5 (46%)	20.8 (14%)	13.8 (10%)	—	13.7 (9%)	30.4 (22%)
	LH		27.4 (56%)	25.7 (53%)	27.5 (58%)	28.9 (57%)	—
	LC		27.1 (59%)	25.8 (57%)	21.4 (52%)	32.6 (68%)	—
	LM		24.9 (52%)	22.8 (60%)	27.5 (56%)	23.6 (42%)	—
	UH		21.0 (25%)	21.1 (25%)	21.4 (25%)	20.4 (24%)	—
	UC		16.3 (18%)	17.6 (21%)	14.5 (16%)	16.6 (18%)	—
	UM		29.4 (34%)	26.6 (32%)	33.4 (39%)	28.0 (33%)	—
	UT		32.7 (50%)	21.5 (31%)	44.4 (63%)	26.4 (42%)	—

Appendix I

Winter surface mass balance distribution

I.1 Linear regression winter balance distribution

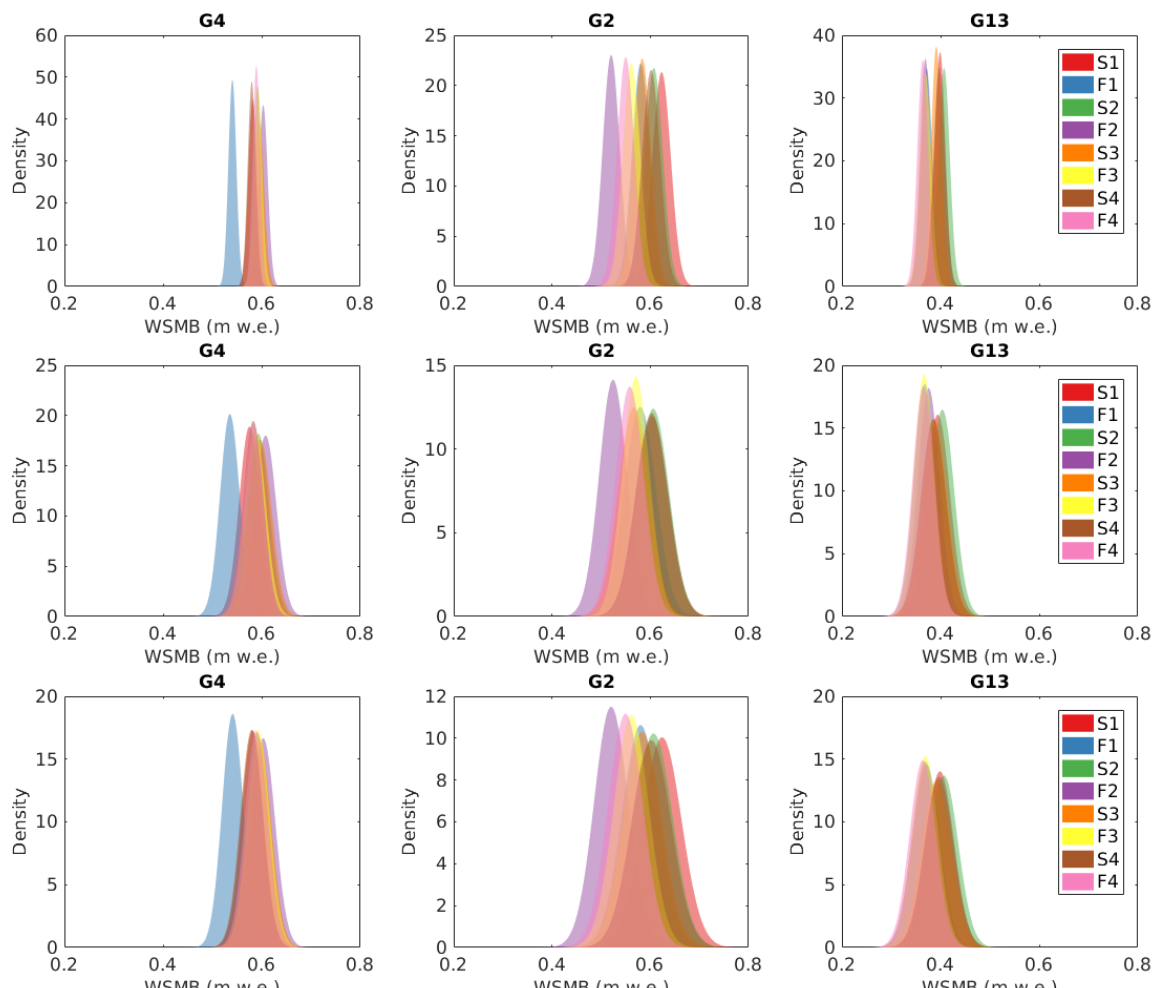


Figure I.1: Distribution of winter balance obtained using linear regression. (Top) Winter balance values obtained from a Monte Carlo sampling of normally distributed SWE variation (obtained from zigzag measurements) about the local SWE value. (Middle) Winter balance values obtained from a Monte Carlo sampling of normally distributed regression coefficients. (Bottom) Winter balance values obtained using both SWE variability and re-

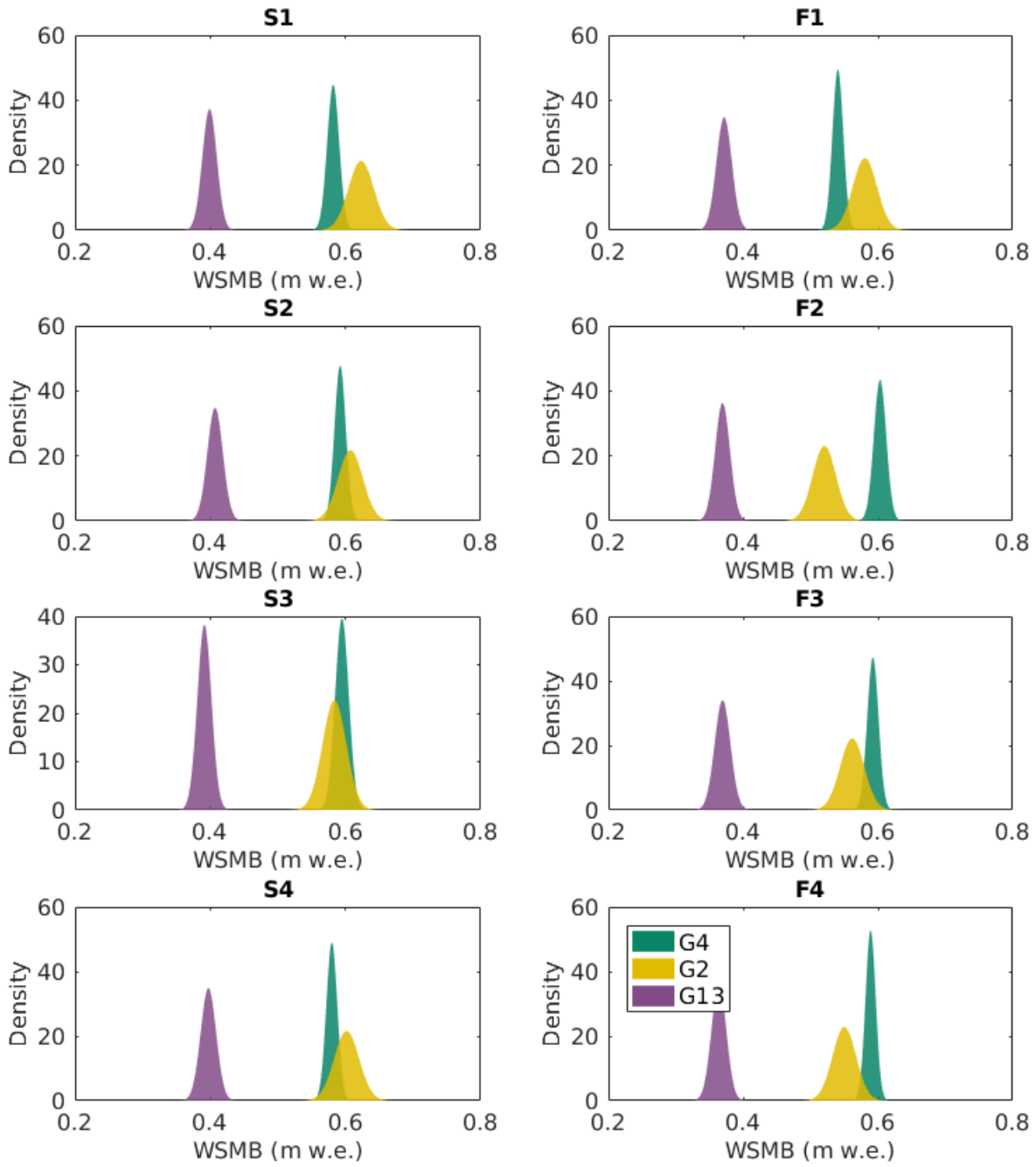


Figure I.2: Winter surface mass balance distribution obtained using linear regression for eight density interpolation options when variation due to SWE measurement (σ_{ZZ}) is included.

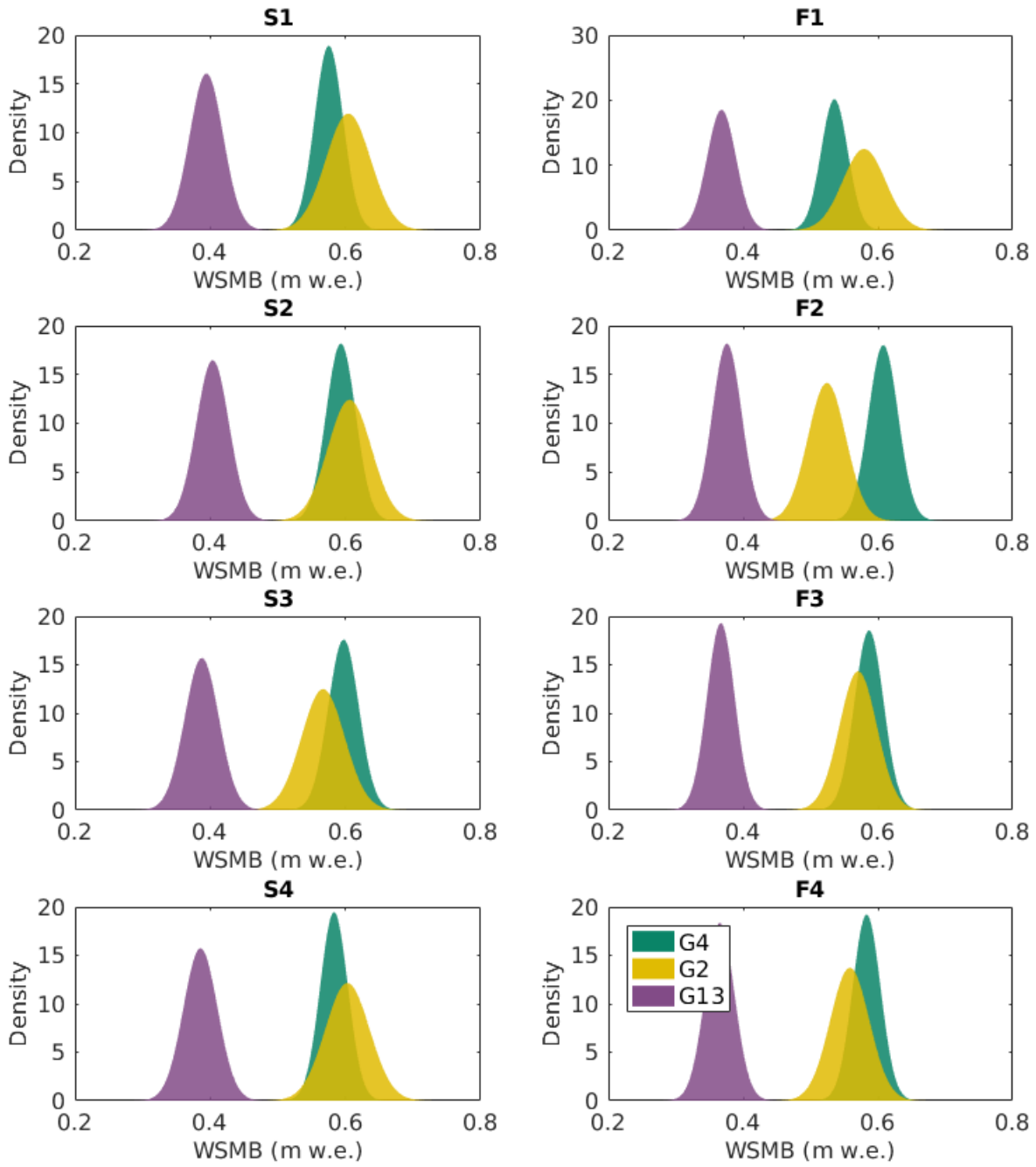


Figure I.3: Winter surface mass balance distribution obtained using linear regression for eight density interpolation options when variation due to regression coefficient estimation (β) is included.

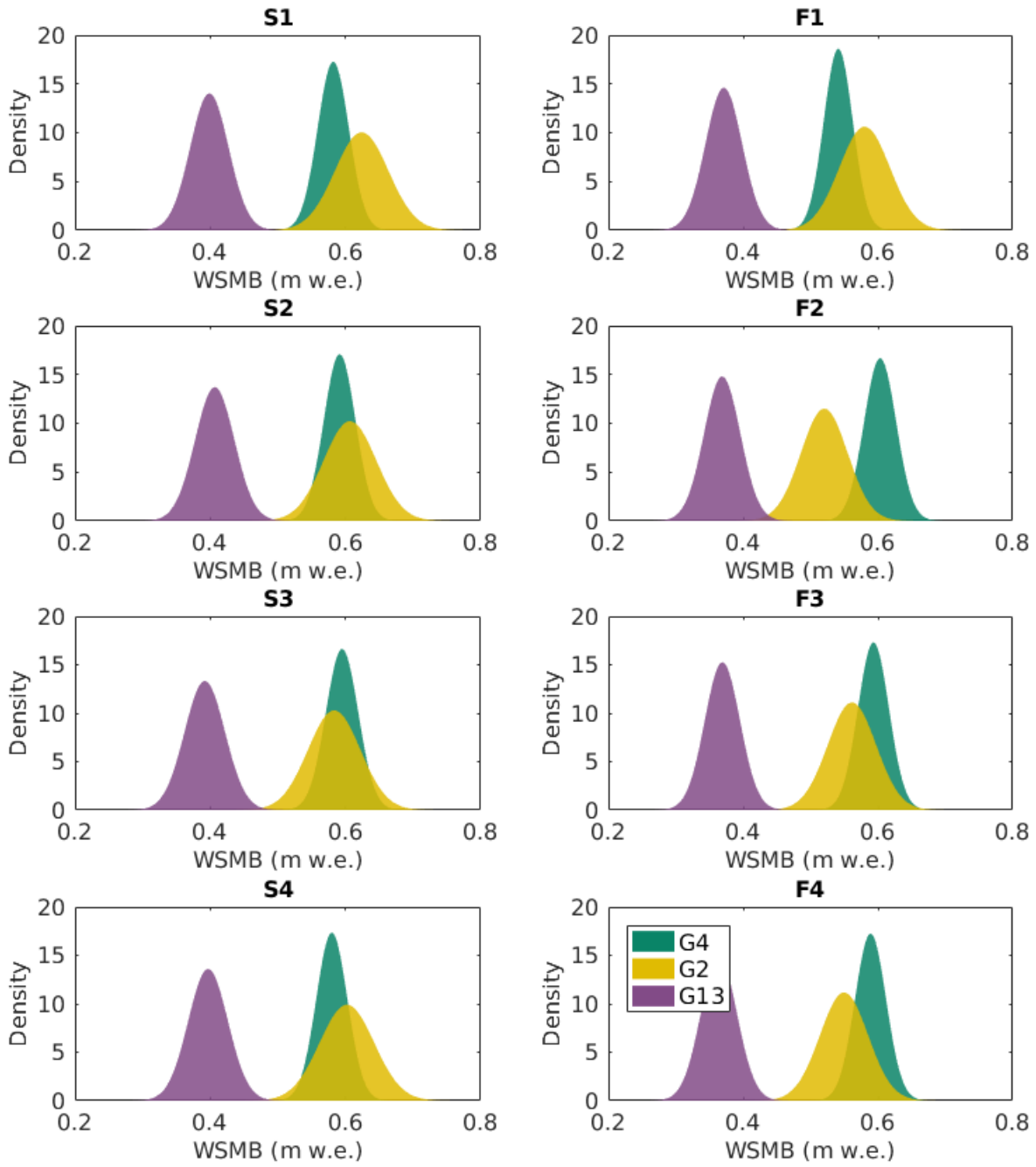


Figure I.4: Winter surface mass balance distribution obtained using linear regression for eight density interpolation options when variation due to regression coefficient estimation and SWE measurement (β and σ_{ZZ}) is included.

I.2 Simple kriging winter balance distribution

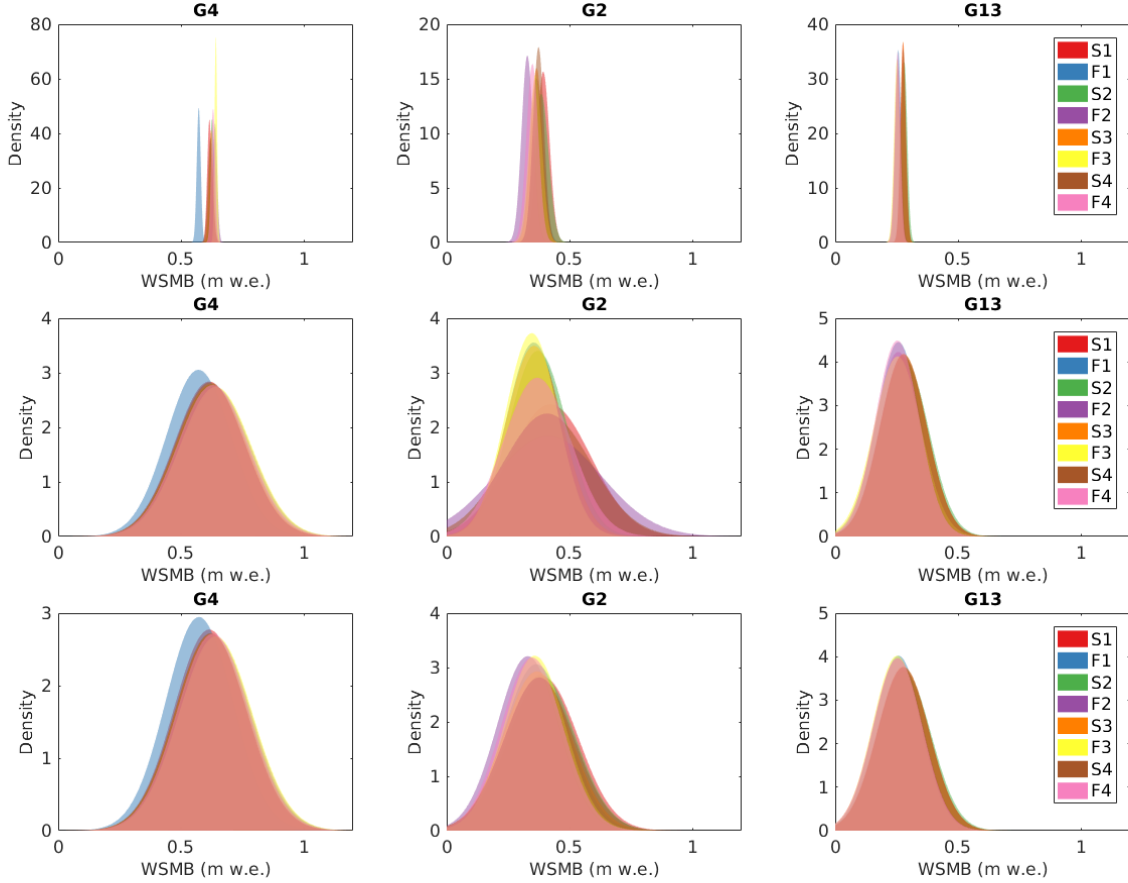


Figure I.5: Distribution of winter balance obtained using simple kriging. (Top) Winter balance values obtained from a Monte Carlo sampling of normally distributed SWE variation (obtained from zigzag measurements) about the local SWE value. (Middle) Winter balance values obtained from a Monte Carlo sampling of normally distributed regression coefficients. (Bottom) Winter balance values obtained using both SWE variability and regression coefficient variability. Eight different density interpolation methods are used to obtain SWE values used in the regression.

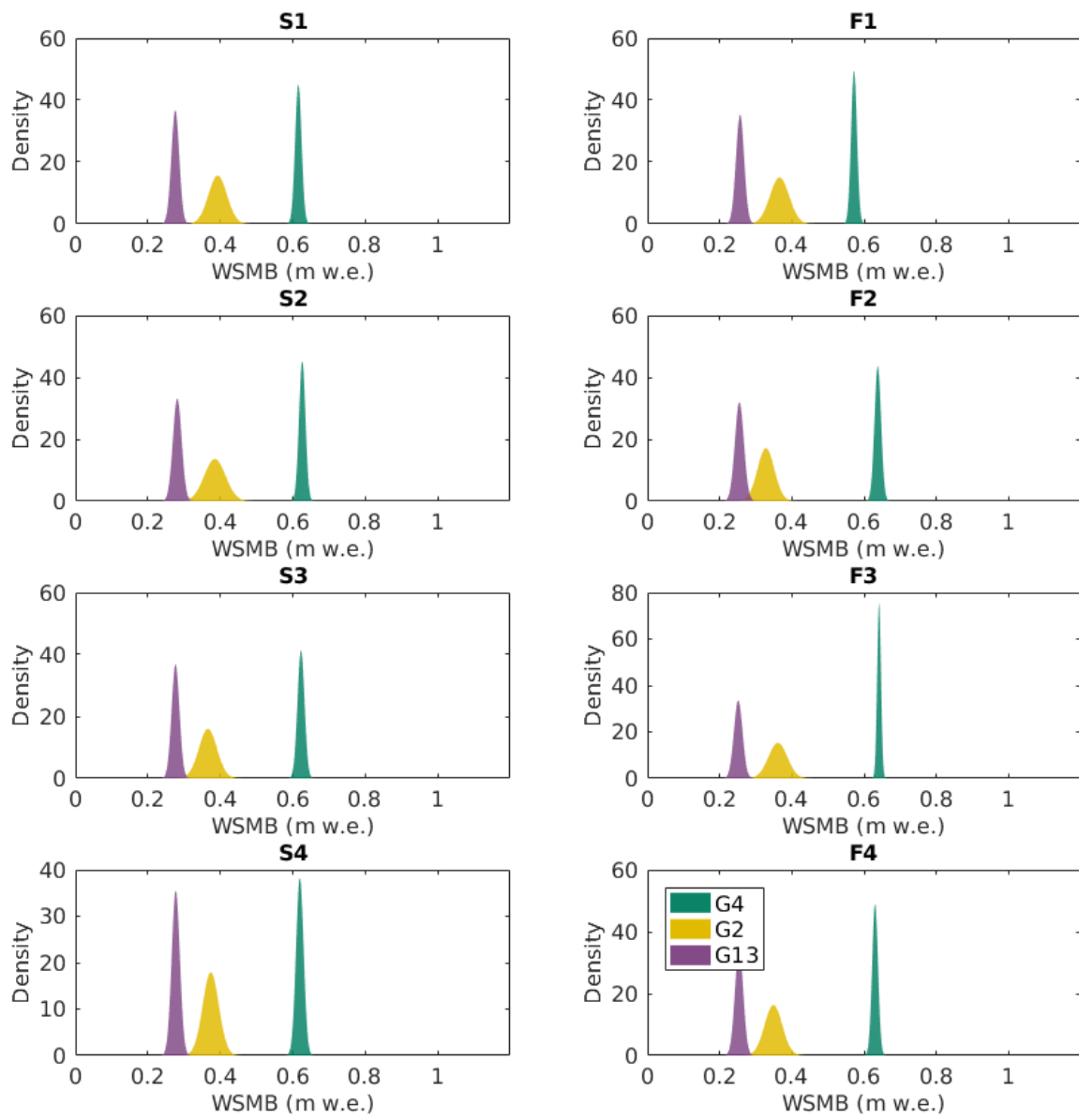


Figure I.6: Winter surface mass balance distribution obtained using simple kriging for eight density interpolation options when variation due to SWE measurement (σ_{ZZ}) is included.

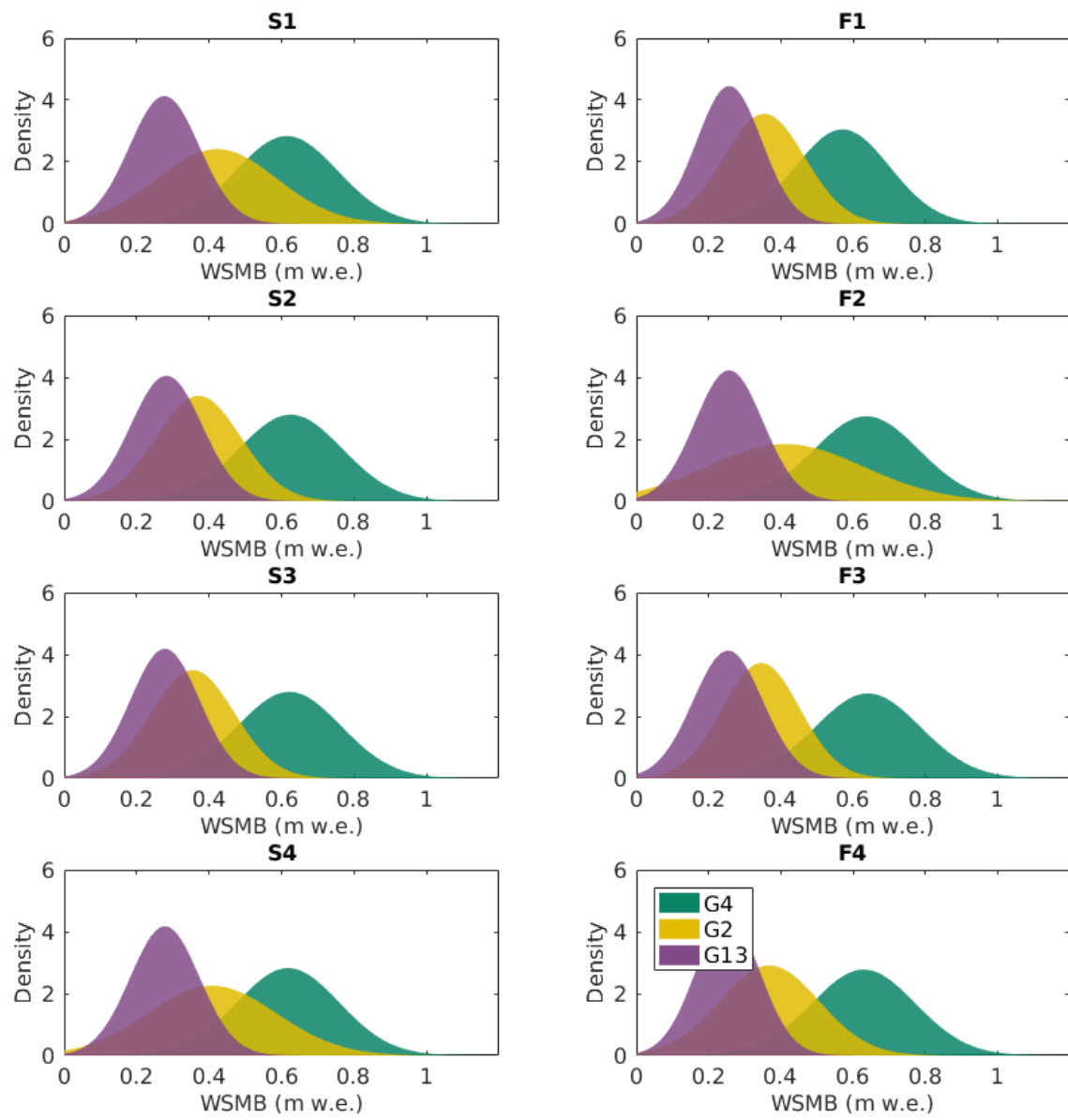


Figure I.7: Winter surface mass balance distribution obtained using simple kriging for eight density interpolation options when variation due to regression coefficient estimation (β) is included.

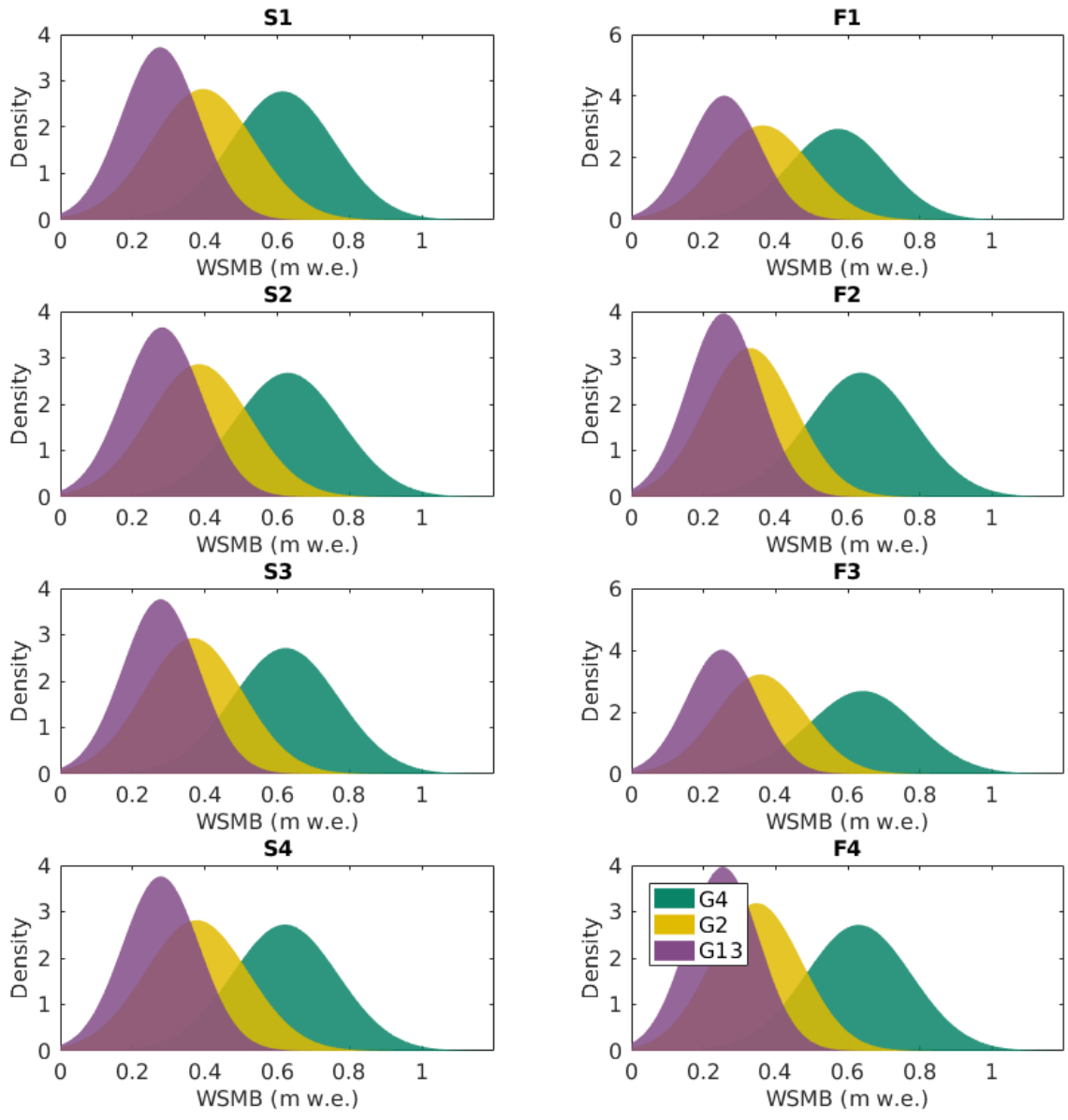


Figure I.8: Winter surface mass balance distribution obtained using simple kriging for eight density interpolation options when variation due to regression coefficient estimation and SWE measurement (β and σ_{ZZ}) is included.